Lattice softening and the martensitic transition in indium thallium alloys

Gunton, David John

LATTICE SOFTENING AND THE MARTENSITIC TRANSITION IN INDIUM - THALLIUM ALLOYS

A thesis

by

DAVID JOHN GUNTON B.Sc. (Dunelm)

of

Grey College

in candidature for the degree of

Doctor of Philosophy

at the University of Durham

November 1973

Department of Applied Physics and Electronics,

Science Laboratories, South Road, Durham City.

D J Coulter

30/11/73

ABSTRACT

Indium-thallium alloys in the composition range 16 to 31 at.% Tl undergo a martensitic phase transition from the higher temperature fcc form to the lower temperature fct one. Certain lattice properties of these alloys have been investigated in the region of the phase boundary. The alloys studied were in single crystal form and comprised of two (11.5 and 15 at.% Tl) which always had a tetragonal structure, and two (25 and 27 at.% Tl) which on cooling transformed from fcc to fct at 195 and 125K, respectively. Ultrasonic wave velocities and attenuation have been measured by pulse methods in the temperature range 4 to 423K (melting point $\simeq$427K). In addition, thermal expansion data for the alloys have been obtained. The temperature variation of the elastic constants, determined from the sound velocity results, is discussed with reference to effects associated with the martensitic transition. One elastic constant combination — $\frac{1}{2}(C_{11} - C_{12})$ — has been shown to approach zero at the transition; theoretical calculations of elastic constants from phonon dispersion curves computed from the optimised model potential theory show a similar result, and the mechanism of the transition is interpreted as the collapse of the slow transverse acoustic phonon mode propagating in the [110] direction. Crystal stability conditions have enabled the limiting values of Poisson's ratio to be derived, and the variation of that ratio and its limits has been investigated as the phase boundary is approached. The order of the phase transition is discussed; a second order process is suggested by the results obtained.

Acknowledgements

Many people have been involved in some way in the preparation of this thesis, and in the work and thought that lies behind its contents.

My supervisor, Dr. G A Saunders must come first: his sustained encouragement, advice and criticism has been of inestimable value during the three years of study. My thanks go, too, to my colleagues in Dr. Saunders' research group for the many useful discussions on topics dealt with herein. Certain matters related to the theoretical work described in Chapter 7 benefitted greatly from discussions and correspondence with M W Finnis, of the Cavendish Laboratory, Cambridge, and for which I am most grateful. A very useful discussion took place also with D Budgen.

And then there is the large group of people, too numerous to mention individually, of friends and acquaintances with whom I have been able to discuss the mathematical, chemical and other aspects of my work.

I am grateful for the help and assistance of Prof. D A Wright in making available the facilities of the Department of Applied Physics and Electronics, and also to Mr. F Spence and his team of technicians, particularly Mr. Ron Waite, whose patience and skill have considerably eased the production of apparatus.

This work was made possible for me through the award of a research studentship by the Science Research Council.

Finally, may I thank Miss A K McGregor and Mr. J R Cutter for their part in reading the proofs.

Contents

CHAPTER 1

INTRODUCTION

Indium and thallium are two metals in group III B of the periodic table; indium (atomic number 49) is immediately above thallium (atomic number 81). Their atomic weights are 114.82 and 204.37, respectively; they are each trivalent and their atomic volumes differ by only about 10%. Indium has a face-centred tetragonal (fct) structure, with c/a ratio of 1.08, while thallium is hexagonal close packed at room temperature. The two metals mix to form disordered alloys over the whole of the composition range. Of particular interest to this work is the indium-rich end of the phase diagram where the fct structure is found at room temperature in alloys containing up to 22.5 at.% Tl, and a face-centred cubic (fcc) one from that composition to 59 at.% Tl. The position of the fcc/fct phase boundary is temperature dependent, and varies from just over 15 at.% Tl at the melting point ($\simeq$427K) to about 31 at.% Tl at 0 K. This transformation is diffusionless and proceeds by a lattice shear process: it is thus of the martensitic type.

Martensite was the name originally given to a form of a high carbon steel which had transformed from austenite on quenching; the term martensitic transformation now applies to a wider range of transitions than to just that in steel. The diffusionless nature and the lattice shear process are its distinguishing features.

In order to study the physical processes taking place at and in the vicinity of such a phase transition it is an advantage, and for some properties essential, to make measurements on single crystal material. The indium-thallium alloys were chosen for study because preparation in single crystal form is relatively easy; various other martensites, such as steel itself and also nitinol (TiNi), are precluded for this reason. A second advantage in an experimental study is to have the phase transition occurring in a temperature range easily accessible by normal laboratory methods. In this respect, too, the indium-thallium system is eminently suitable, for the temperatures involved lie between 0 K and about 427K, depending on the composition of the alloy. Thus, by selecting a suitable alloy composition it is possible to arrange for the martensitic transformation to take place at a predetermined temperature. Furthermore, it is possible to produce crystals of either modification at room temperature. These in themselves are features of the indium-thallium system which make possible a more detailed investigation of the transition than can be achieved in almost any other martensite. (With a system such as Au-47.5 at.% Cd, or with elements such as Na or Li, T_c is fixed for a given pressure.)

One possible drawback of In-Tl alloys concerns the toxicity of thallium or, more exactly, of the Tl^{++} and Tl^{+++} ions. One or other of these ions is produced when thallium metal comes into contact with skin, and the oxide or some other salt results. Consequently great care must be exercised in the handling of the metal. The alloys are less dangerous in this respect, though, for the thallium is diluted by indium, a less toxic material.

In appearance indium-thallium alloys are bright and silvery after a short etch in dilute nitric acid, but soon become dulled and slightly grey in colour because of the formation of a thin layer of oxide. The oxidation is not extensive, however, and does not impede bulk ultrasonic measurements.

Considerable effort has gone into a determination of the crystallography of the fcc to fct transition, starting with the work of Bowles et al. (1950), and later by Burkart and Read (1953) and Basinski and Christian (1953). However, the underlying mechanism causing the transformation is only now being resolved, and the major aim of this thesis is to investigate the suggested mechanism — the collapse of a soft acoustic phonon mode — from experimental and theoretical approaches. Hopefully the results for the indium-thallium case could be applied to other martensitic systems for which there are fewer easily controllable variables to ease an experimental investigation, and also for those involving metals which, by their nature, cannot easily be modelled by existing theoretical methods. (The latter includes those containing iron, nickel, gold or other noble or transition metals.)

Ultrasonic techniques have been largely used in this study. The propagation of a stress wave through a solid and a determination of its velocity and attenuation in the medium provide information concerning basic lattice properties of the material. In particular, the elastic constants can be found and, since these are related to the binding energy of the lattice, their variation with temperature gives information concerning the extent of the contribution to that energy which is anharmonic in the strain. The behaviour of the elastic constants and ultrasound attenuation are of particular interest in the study of any phase transition. In the present work we have attempted to relate the results of the elastic data to the behaviour of the crystal lattice in the vicinity of the martensitic transition. Results of thermal expansion measurements have also been used to that end. Further, ultrasonic methods allow of a direct investigation of the softening of an acoustic phonon mode through the propagation characteristics of an appropriately polarised wave.

CHAPTER 2

THE MARTENSITIC TRANSFORMATION AND ITS EFFECT ON PHYSICAL PROPERTIES OF INDIUM - THALLIUM ALLOYS

Introduction

This chapter sets out to review the main physical properties of indium-thallium alloys, with particular reference to those concerning the martensitic phase transition. The theories of the mechanism of the phase transition are outlined, both from the standpoint of the atomic motion involved, and from that of the possible underlying reason for the instability in terms of the collapse of a soft acoustic phonon mode. The elastic and ultrasonic data available are described, and a brief account is given of studies of other, less related, observed properties of this alloy system. The concern throughout has been to show the relationship between the present work and the knowledge available from previous studies of the alloys.

2.1 Martensitic transformations

2.1.1 General characteristics

Structural phase transitions can take place by either civilian or military processes, in the terminology suggested by Frank. In a transformation of the former type the atoms move independently of each other, while in the latter type the motion is co-ordinated and much more well-defined. The displacement undergone by any particular atom in a military transformation can be specified beforehand; such displacements are fractions of the inter-atomic spacing compared with a possible atomic movement over several inter-atomic distances in a civilian transformation. Diffusion plays no part in a military transformation; martensitic transformations are of this type.

Originally the term martensite was used to describe quenched high-carbon steel, in which the transformation from the face-centred cubic (fcc) austenite to body-centred tetragonal (bct) martensite occurred on rapid cooling, and which was accompanied by an increase in the hardness of the alloy. The name was given by Floris Osmond in 1895 to commemorate the work of Adolf Martens, a metallographer who had worked on the structure of steels. Since then many other materials have been found which have similar transformation properties: so wide is the range that it becomes difficult to find an all-embracing definition of a martensitic transformation. Petty (1970) gives the following: 'A martensitic transformation involves the coherent formation of one phase from another of the same composition by a diffusionless, homogeneous lattice shear process.'

Other important characteristics include:

(i) The process of formation of martensite is athermal, that is, it only occurs on cooling and not when the temperature is held constant.

(ii) A start temperature M_s and a finish temperature M_f are found. The temperature separation of M_s and M_f differ between materials, and in the case of an alloy can be affected by composition.

(iii) Thermal stabilisation can occur if the temperature is held between M_s and M_f. Undercooling is needed to restart the reaction.

(iv) Transformations are reversible with a temperature hysteresis.

(v) The shear responsible for the transformation takes place on a habit plane peculiar to any given material. For a homogeneous shear the habit plane itself is undistorted.

(vi) There is a definite relationship between planes and directions in the parent and the martensite phases. A transformation matrix can be written down to describe the strains involved in a particular transition (Wechsler, Lieberman and Read, 1953).

All of these characteristics have been observed in the phase transition found in indium-thallium alloys. A collection of data for other non-ferrous metals and alloys which also undergo a martensitic transformation is presented in Table 2.1 (Garwood, 1970).

2.1.2 The fcc to fct transition in indium-thallium alloys

2.1.2.1 The phase diagram

The phase diagram of the indium-thallium system is given in figure 2.1(a). This is a composite diagram given by Hansen and Anderko (1958) from the collected work of Valentiner (1940), Guttman (1950), Lipson and Stokes (1941). (See also Meyerhoff and Smith (1963) and Stout and Guttman (1952).) The region of the fcc to fct phase boundary is shown enlarged in figure 2.1(b), and is due to Pollock and King (1968).

TABLE 2.1

Martensitic transformations occurring in non-ferrous metals and alloys*

Metal or alloy	Structure change
Ti	BCC to HCP
Ti-11% Mo	BCC to HCP
Ti-5% Mn	BCC to HCP
Zr	BCC to HCP
Li	BCC to HCP (faulted) BCC to FCC (stress induced)
Na	BCC to HCP (faulted)
Cu-40% Zn	BCC to FCT (faulted)
Cu-Sn	BCC to orthorhombic BCC to FCC (faulted)
Cu-Ga	BCC to FCC (faulted) BCC to orthorhombic
Au-47.5% Cd	BCC to orthorhombic
Au-50% Mn	BCC to orthorhombic
Hg	rhombohedral to BCT
In-15 to 31% Tl	FCC to FCT

BCC body-centred cubic
FCC face-centred cubic
FCT face-centred tetragonal
HCP hexagonal close-packed
BCT body-centred tetragonal

* From Garwood (1970). This list is not exhaustive.

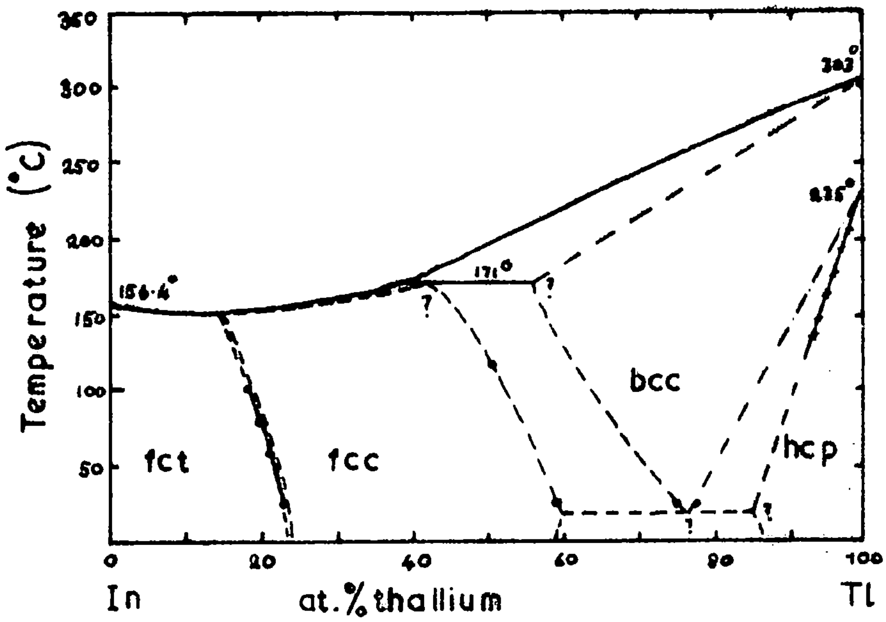

(a)

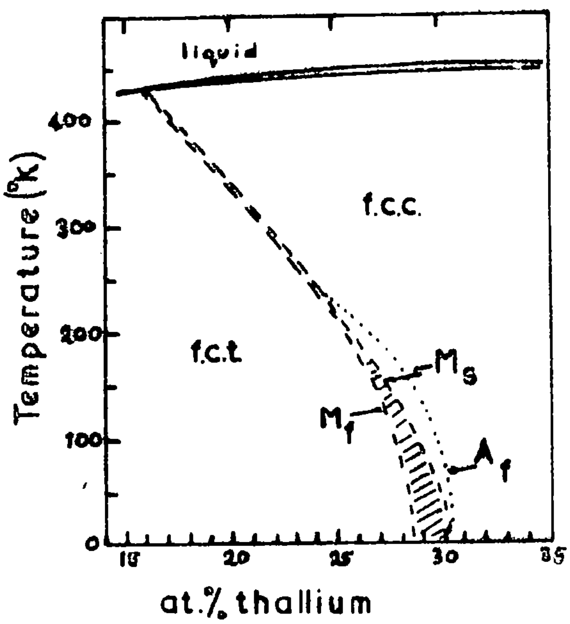

(b)

Figure 2.1 (a) The phase diagram of the indium-thallium system (after Hansen, 1958).

(b) The fcc to fct transition region (after Pollock and King, 1968).

The phase division line meets the solidus at just over 15 at.% Tl, and reaches OK at about 31 at.% Tl. Between these two points on the diagram there is a continuous variation of transition temperature with composition. A 22.5 at.% Tl alloy transforms at room temperature (290K). It is interesting to note that the solidus and liquidus are very close together for compositions up to about 40 at.% Tl. This means that a melt containing up to that amount of thallium gives a solid of much the same composition — a most useful property where sample preparation is concerned, and uniformity of composition is desired. A two-phase region is shown in figure 2.1(b). There has been much discussion on the existence and possible meaning of this region, especially with regard to the thermodynamics of the transition. Pollock and King (1968) describe this section of the phase diagram as a 'realisation' diagram, rather than an equilibriun one, and ascribe the difference between M_s and M_f as found in their polycrystalline samples to the effects of stress and strain in the sample and at the transition interface, thus bringing the pressure variable into play. Guttman (1950) concluded that there was in reality no two-phase region because his X-ray photographs showed lines from one or other of the two structures as the transition proceeded, and never from both. It is likely that if an actual piece of either single or polycrystal is considered as a whole, then the effect of stress within it acts to cause certain regions or grains to transform before others, thus giving rise to start and finish temperatures. But if one grain or region is considered, then the transformation occurs at one temperature set by the conditions of temperature and pressure within it.

2.1.2.2 The crystallography of the transformation

The first description of the crystallography of the fcc to fct transition in In-Tl alloys has been given by Bowles, Barrett and Guttman (1950). The experimental observations which they attempt to explain consist of micrographs of the surfaces of single crystal alloys which show that, after transformation, a previously smooth surface becomes corrugated, and a banded structure is observed. Further, each band has sub-bands across it at angles of 60° to the main one, and on adjacent bands the sub-bands are at 120° to each other. Figure 2.2 shows this effect in a crystal containing 21 at.% Tl. The development of the bands is associated with the severe strain at the fcc/fct interface. To relieve the strain field set up by passage of the transition interface, twins whose strain is alternately positive and negative are formed in the martensitic phase. Bowles et al. have found that the bands occur parallel to $\{110\}$ planes of the cubic material.

Two possible mechanisms are considered by Bowles et al. The first assumes that there is a simple expansion along one axis of the original cube and a contraction along another. The high internal stresses would then be relieved by twinning and the banded structure would result. The other mechanism they consider is that of a double shear. If one shear were to occur on a $\{110\}$ plane followed by a second on another $\{110\}$ at 60° to the first then a tetragonal configuration would ensue.

Figure 2.2(a) Transformation twins in an In-21 at.% Tl alloy. The main bands can be seen separated by the dark lines. Sub-bands are visible within them.

Figure 2.2(b) A region of an In-21 at.% Tl alloy in which main bands on three different $\{110\}$ planes can be seen. Slight interpenetration of bands is occurring.

Magnification on both photographs is $\simeq$ length $\times 50$.

The work of Mr. G. Aggett is gratefully acknowledged for preparation of the In-21 at.% Tl alloy and of these photographs.

This process is illustrated schematically in figure 2.3. Bowles et al. performed careful X-ray work to determine which mechanism was nearest to reality. Their determination depended on the slight rotation of axes ($\simeq 2^{\circ}$) which would accompany a double shear process, compared with no rotation for the more straightforward increase in atom separation along one axial direction. Their conclusion is that the double shear mechanism is the one responsible: a shear on (110) in the direction $[1\bar{1}0]$, followed by a second on (011) along $[0\bar{1}1]$. Additional confirmation comes from the way in which the bands tilt the surface, for each mechanism predicts a different result in this respect. A more detailed analysis by Burkart and Read (1953) shows that if the habit plane is an irrational one within about 1° of $\{110\}$ then an exact tetragonal structure could result, instead of what is, strictly, a triclinic one from the model proposed by Bowles, Barrett and Guttman. Burkart and Read were also able to calculate the orientation of the habit plane from the condition that the average strain at the cubic-tetragonal interface must be zero.

In their experiment to find the mechanism of the phase transition Bowles et al. (1950) also made observations on the form of the transformed material. They find that for a single crystal the bands in the martensite phase are at different orientations in different regions. This is just because the transformation is nucleated at several points with habit planes whose orientation varies from one region to another (there are six $\{110\}$ planes in a cubic crystal, and thus six possible habit planes.) The width of the main bands

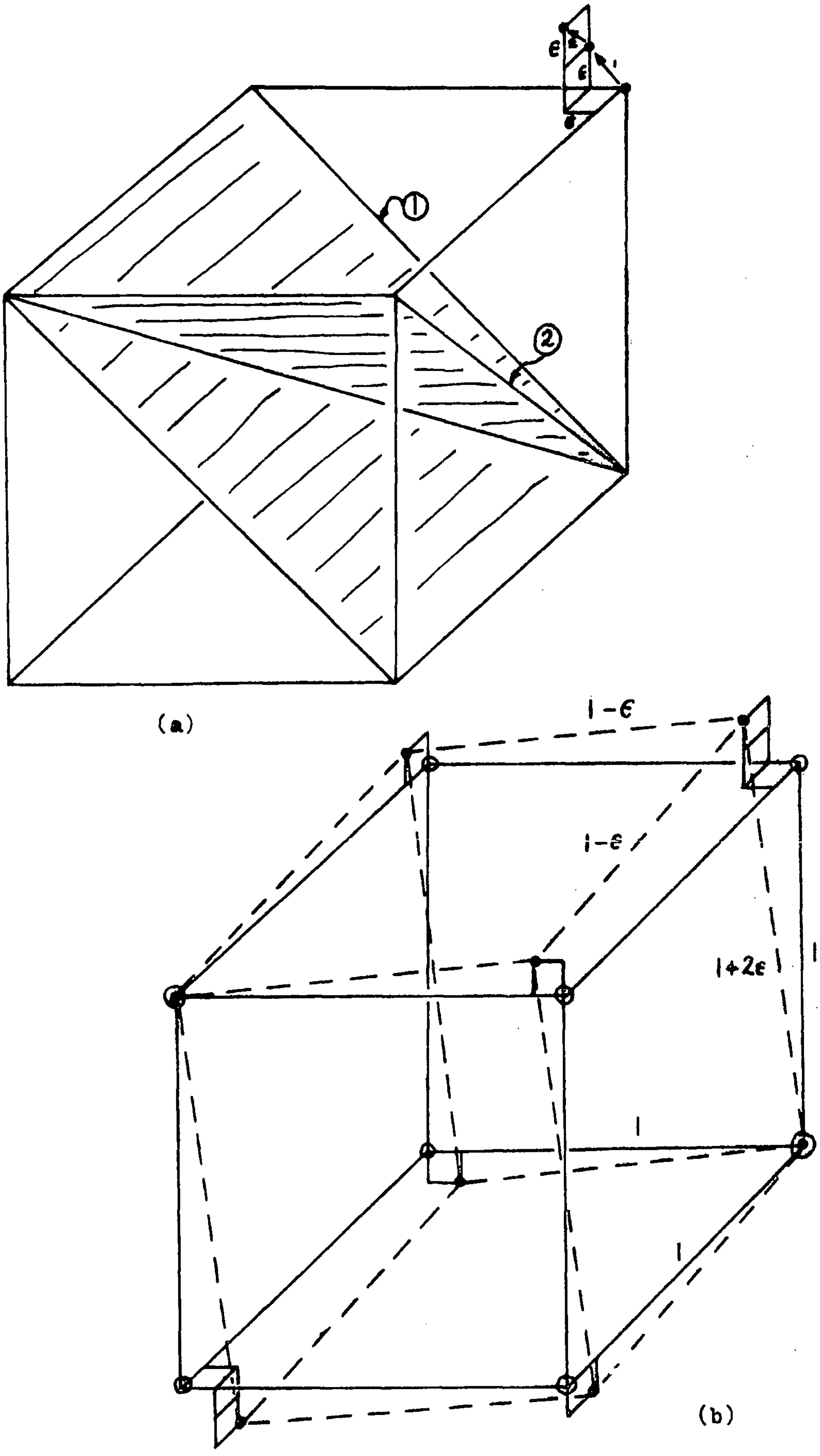

Figure 2.3

The cubic to tetragonal transition by the mechanism suggested by Bowles et al. (1950). The habit plane of the first shear is labelled 1, and of the second is marked 2.

also varies. When nucleating centres are close, and the two habit planes are at 60° to each other, Bowles et al. have found that it is possible to obtain interpenetration of the bands. When this happens the main bands in one region can extend into the other in the form of sub-bands. Another of their findings is that when the temperature is raised to reverse the transformation the cubic phase thus formed is once again single crystal. Subsequent cooling leads to a return to the twinned tetragonal form by the same interfaces as on the previous cooling.

From a practical viewpoint, the effect of the twinning on crystal growth is that a melt containing between 15.5 and 22.5 at.% Tl assumes the banded twin form on cooling to room temperature at atmospheric pressure. This limits the experimental determination of, for example, elastic constants.

Other cubic to tetragonal transitions are known. Those in Cr-Mn, Cu-Mn, Fe-Pt, Au-Cd and $BaTiO_3$ had been studied before In-Tl, and the lamellae seen in In-Tl are of similar form to those in Cu-Mn, Fe-Pt and $BaTiO_3$. (See Bowles et al. (1950) for a review).

2.2 Soft modes and phase transitions

2.2.1 General features

The soft mode concept is one which has been invoked to account for a number of displacive phase transitions; those studied have almost exclusively involved soft optic modes. A soft optic mode is a normal vibrational mode of the crystal lattice whose frequency tends to zero as the temperature tends to the transition temperature T_c. The effect of a soft optic mode can often be seen in acoustic properties of the crystal, such as sound velocity and attenuation, through optic phonon-acoustic phonon coupling which can cause a softening of one of the acoustic modes. However, it is also possible to have a soft acoustic mode in its own right: since all acoustic modes have zero frequency at zero wavevector (neglecting zero-point energy) the definition must be modified to include as soft modes only those whose slope $\partial\omega/\partial\underline{Q}$ tends to zero as ω tends to zero. Such modes have been discussed by Pytte (1971) and Shirane (1971) in connection with the structural phase changes observed in V_3Si and Nb_3Sn.

Cochran (1960) first proposed the soft optic mode as being responsible for the ferro-electric transition in $BaTiO_3$ at 393K, as well as for the cubic to tetragonal structural transition seen at 105K in $SrTiO_3$. Since then other perovskite materials have received considerable attention, including $NaNbO_3$ (Glazer and Megaw, 1972). Several general characteristics can be given for soft modes, both optic and acoustic, although the two types will differ in detail. When a lattice mode softens and finally collapses the forces between the atoms in the direction of the eigenvector of the mode become reduced, and finally vanish at T_c. The atoms can then move into new positions and a new structure is formed below T_c. In optic mode transitions it is one set of atoms which takes up a new position relative to another set, as in $SrTiO_3$ in which the tetrahedral array of oxygen atoms rotates with respect to the strontium and titanium atoms. For an acoustic mode transition we envisage the atoms as able to move, again according to the eigenvector of the soft mode, into new positions relative to their original ones. Thus in either case the structure of the new phase is determined by the eigenvector of the soft mode and the structure of the old phase. Dealing primarily with soft optic modes, Pytte (1971) describes the mechanism of a soft mode transition as an instability of one or more normal mode displacements for a lattice in which only harmonic forces are acting. At sufficiently high temperatures thermal fluctuations stabilise the lattice through the anharmonic interactions which are, in practice, always present. The transition temperature is that temperature at which thermal fluctuations are insufficient to produce stability, and the mode in question collapses. Pytte's analysis also holds when only acoustic modes are present. When an acoustic mode softens it is possible in principle to detect this experimentally from a measurement of sound velocity, since the drastic reduction in certain of the restoring forces between atoms means that an appropriately polarised wave will have a very small velocity of propagation.

2.2.2 The fcc to fct transition in In-Tl and soft modes

It has been suggested that the martensitic transformation in indium-thallium alloys proceeds by a soft acoustic phonon mode. The first definite evidence came from Pace and Saunders (1972,1972a), although tentative suggestions had been made earlier. Anderson and Blount (1965), as a result of a discussion of the order of cubic to tetragonal phase transitions in general, considered that, in the case of In-Tl, if a distorted tetragonal cell was formed then the instability of a phonon mode polarised in the [100] direction could be the cause of the transition. But this postulate was based on a too simplified model of the crystallography of the transition. Dynes (1970) also admitted the possibility of a phonon instability, an idea based on his determination of phonon density of states functions for In-Tl alloys by electron tunnelling in the superconducting region. Such an instability did not show up in his results, although he observed a slight decrease in the average phonon energy, when plotted against alloy composition, at about 31 at.% Tl. This was the composition at which the fcc to fct transformation occurred at the temperatures at which he was working, and also that at which a maximum was seen in the superconducting transition temperature. This result was by no means conclusive, but it was not inconsistent with the idea of an unstable mode.

The evidence produced for softening of the transverse mode polarised $[1\bar{1}0]$ propagating in the [110] direction by Pace and Saunders (1972) was based on elastic constant determinations for various indium-thallium alloys. Pace and Saunders combined their results with those of Novotny and Smith (1965) and were able to show quite clearly that the modulus $\frac{1}{2}(C_{11}-C_{12})$, determined from the sound velocity of the [110], $[1\bar{1}0]$ polarised mode decreased towards zero when the alloy composition for the 300K transition was approached from either the cubic or the tetragonal side. Such a result strongly indicated that at the transition the modulus would be zero, as would be the associated sound velocity.

The order of the phase transition is closely linked to the nature of the transformation process, as well as to the thermal properties of the alloys. Both first and second order processes have been postulated (Burkart and Read (1953); Guttman (1950)), but we defer a discussion of this point until chapter 8.

2.3 Ultrasonic and elastic data for indium-thallium alloys

The six independent elastic constants of indium were the subject of work by Winder and Smith (1958), who used an ultrasonic pulse-echo method for their determination. Chandresekhar and Rayne (1961) remeasured these constants over the temperature range 4 to 300K and Pace (1970) has made a small correction to the value of C_{13} determined by these later workers. The elastic constants of cubic alloys in the composition range In-28 at.% Tl to In-39 at.% Tl have been measured by Novotny and Smith (1965) over the temperature range 200 to 360K. More recently Pace and Saunders (1972) have given data for tetragonal alloys containing 10, 16.5, 18 and 21 at.% Tl, and for the cubic composition of 25 at.% Tl. The 10 at.% Tl alloy does not suffer a martensitic transformation, and Pace and Saunders were able to obtain the temperature variation of all six of its elastic moduli between 80 and 300K. (The pulse-echo method was used for all the work described above.) Such a complete determination was not possible for the other three tetragonal crystals on account of their banded twin structure; the results were given by Pace and Saunders for the quasitetragonal moduli obtained from the three velocities of wave propagation along the '[110]' direction in these twinned materials. The temperature range for the measurements in these cases was 290 to 390K, which included the transition temperatures of the 18 and 21 at.% Tl alloys, at 367 and 320K, respectively. But because of the limitations imposed by the twinned structures more detailed information concerning the tetragonal phase elastic constants could not be obtained.

The object of the present elastic constant determinations has been to extend the known data in two ways. Firstly, two alloys which are cubic at room temperature (25 and 27 at.% Tl) have been prepared, and the elastic constants C_{11}, C_{12} and C_{44} have been measured as each alloy was cooled from 300K towards and through its transition temperature. In the case of 25 at.% the transformation fcc to fct occurred at about 195K, while the 27 at.% one transformed at about 125K. As a result it was planned to check directly the idea that the modulus $\frac{1}{2}(C_{11}-C_{12})$ falls to zero at the phase transition, but without the problems encountered by Pace and Saunders over twinning. However, below the transition temperature in each case a twinned structure results , so that meaningful results would only be obtained above T_c. Even so, results of measurements approaching the phase transition from the cubic side with temperature as the variable represent an advance on previous work. The only way in which a study can be made of single crystal tetragonal alloys as the phase transition is approached is to investigate a composition which is very close to the fcc-fct boundary at the melting point, but which is still in the tetragonal form a fraction below the melting point. Such a composition is always tetragonal and does not transform to the cubic structure. It is thus free of twins, and can be produced in single crystal form, yet measurements made as the temperature is increased towards the melting point T_m represent also an approach to the phase boundary, as required.

The second way in which the known elastic data was extended was to investigate the behaviour of three tetragonal alloys, including a composition chosen to accord with the considerations expressed at the close of the preceding paragraph. The three single crystals produced contained 10, 11.5 and 15 at.% Tl; the phase diagram given by Pollock and King (1968), and shown in figure 2.1(b), shows the phase division line meeting the solidus at about 15.5 at.% Tl, so that the crystal containing 15 at.% Tl was the one whose properties close to T_m were of particular interest. The 11.5 at.% alloy served as a source of additional data to detect trends occurring in measured properties, while the 10 at.% alloy was only used to extend some of Pace and Saunders' data on this composition to 4K.

Ultrasonic attenuation in indium-thallium alloys has received very little attention. Pace and Saunders (1972) and Pace (1970) report a sharp peak in the ultrasound absorption in the vicinity of the phase transition, but no extensive study of the temperature or frequency dependence of attenuation has been made previously. The data available on indium itself appears to be almost entirely centred around the normal to superconducting transition region, although Bliss and Rayne (1969) extend their measurements up to 80K. In this work the temperature dependence is examined; the widest range covered was 4 to 423K, although the range varied from one sample and direction to another.

2.4 A general survey of previous work on In-Tl alloys

Most of the work on indium-thallium alloys has been performed at low temperatures, and has been centred on the superconducting properties. The variation of superconducting transition temperature with alloy composition has been studied by Stout and Guttman (1952), Merriam, Hagen and Luo (1967) and Gubser, Mapother and Connelly (1970). Connected with such effects, Stout and Guttman (1950) studied the Meissner effect, while Connell (1963) has observed the penetration of magnetic fields in superconducting alloys. Other work in the superconducting region includes that of Wraight (1968), Fischer et al. (1967,1968) and Tilley et al. (1966). Sladek (1953,1954) and Phillips (1955) have examined low temperature thermal conductivity in samples containing up to 50 at.% Tl, and found a maximum in thermal resistivity in alloys containing more than 15 at.% Tl at the destruction of superconductivity by a magnetic field.

Concerning the mechanical properties of indium-rich alloys, the shape-memory effect has been reported by Nagasawa (1971), while the rubber-like behaviour has also been described by Burkart and Read (1953). Khayutin and Spichinetskii (1967) have studied their plastic deformation, and conclude that indium deforms by slip, whereas the alloys do so by twinning.

Postnikov et al. (1969) and de Morton (1969) have reported results of internal friction measurements. Electrical resistivity measurements are given by Stout and Guttman (1952a), and by Predel and Sandig (1970). Yonemitsu et al. (1965) give transport properties of alloys of indium with various metals, including thallium, and Shiozaki and Sato (1967) report the temperature dependence of the Hall coefficient.

Eckert and Drickamer (1952) have studied the diffusion of thallium tracers in indium, and have found that near the melting point there is a rise in the diffusion coefficient, and that grain boundary melting occurs.

We turn now to some studies of more direct relevance to the present work. The thermal expansion of alloys of various compositions in the range 19 to 35 at.% Tl has been measured dilatometrically by Pahlman and Smith (1969). Hill (1970) has studied the pressure variation of the modulus $\frac{1}{2}(C_{11}-C_{12})$ at room temperature, and finds it to be large and negative: $(C_{11}-C_{12})$ tends to zero at a pressure induced fcc to fct transition. Schwartz (1970) has reported the heat capacity of three alloys (18.8, 28.9 and 34.6 at.% Tl) between 5 and 300K. One of the alloys — 28.9 at.% Tl — transformed in this range and he found a slight deviation of about 1% in the heat capacity versus temperature curve in the vicinity of the transition. Other heat capacity measurements have been reported by Bucher (unpublished) at low temperatures.

The results of previous workers have demonstrated that the indium-thallium system, and particularly that part involving the martensitic phase transformation, is only beginning to be understood. It is hoped that the work to be described on lattice properties of a selection of the alloys will go some way towards improving this understanding.

CHAPTER 3

SOME APPLICATIONS OF ANISOTROPIC ELASTICITY THEORY

Introduction

A large part of the experimental work to be described concerns the determination of the elastic constants of indium-thallium alloy single crystals in both the cubic and tetragonal modifications. This chapter sets out to show how the propagation of stress waves in a cubic or tetragonal material is governed by the elastic constants, and how the latter may be determined from a knowledge of the wave velocities along certain crystallographic directions. It also gives two applications of elasticity theory which will be of relevance to work described in chapter 6: the restrictions on elastic constants arising from crystal stability considerations, and the construction of some invariants.

3.1 Stress, strain and Hooke's law

The elastic constants relate the stress and strain through Hooke's law, which states that for an elastic body the strain within it is proportional to the stress producing that strain, and so

$$\epsilon_{ij} = S_{ijkl}\sigma_{kl} . \qquad (3.1)$$

Stress ($\hat{\sigma}$) and strain ($\hat{\epsilon}$) are both second rank tensors, so that $\hat{S}$, the elastic compliance tensor, is of fourth rank. The summation convention is implied in equation 3.1, which is a more compact representation of 81 equations. The stiffness tensor, $\hat{C}$, is just the inverse of $\hat{S}$, and hence

$$\sigma_{ij} = C_{ijkl}\epsilon_{kl} . \qquad (3.2)$$

Equations 3.1 and 3.2 represent an harmonic, or second order, approximation and $\hat{S}$ and $\hat{C}$ have as their components the second order elastic constants. Higher order constants can be defined, but we shall not concern ourselves with them here.

Before proceeding further, the formal definitions of the stress and strain tensors used in equations 3.1 and 3.2 must be given.

<u>Stress</u> The component of the stress tensor σ_{ij} is the force per unit area in the x_i direction acting on an elemental area on the plane normal to the x_j direction.

<u>Strain</u> Let a point at (x_1,x_2,x_3) in a body move to the position $(x_1+u_1,x_2+u_2,x_3+u_3)$ as a result of deformation of the body. The quantities u_1, u_2, u_3 are components of the displacement vector $\underline{u}$ of the point. Any general homogeneous deformation can be considered as made up of a strain and a rotation (e.g. Nye 1957). The strain tensor $\hat{\epsilon}$ is the symmetrical part of the tensor $\hat{e}$ describing the deformation; the antisymmetrical part gives the rotation. Thus

$$\epsilon_{ij} = \tfrac{1}{2}(e_{ij} + e_{ji}) \tag{3.3}$$

$$\text{where} \quad e_{ij} = \frac{\partial u_i}{\partial x_j} \quad , \quad i = 1,2,3 \ .$$

A component ϵ_{ij} represents the fractional change in length along the x_i direction, if $i = j$, and half the change in the angle defined originally by the x_i and x_j directions, if $i \neq j$.

The elasticity tensors have 81 components. However, there are certain relationships between some of these components which follow immediately from the symmetry of the stress and strain tensors, and we can write $C_{ijkl} = C_{ijlk} = C_{jikl}$.

The number of independent components is thus reduced to 36. An additional property of the tensor, namely that $C_{ijkl} = C_{klij}$, follows from the strain energy being a function of state. The effect of this is to further reduce the number of independent components to 21. Reduction to less than 21 can also occur, but the details depend on the crystal symmetry under consideration. A triclinic system requires all 21 components to describe its elastic behaviour.

Because of the reduction to 21 constants a convenient representaion is to use a symmetric 6× 6 matrix, and to denote the stiffness components as C_{ij} , i,j = 1,6. This in no way constitutes a reduction in the rank of the tensor. The tensor components are related to the matrix ones by the following relations between subscripts.

Tensor	11	22	33	32,23	13,31	12,21
Matrix	1	2	3	4	5	6

Thus $C_{1232} \rightarrow C_{64}$, $C_{1111} \rightarrow C_{11}$, and so on. The compliance tensor components can be treated in a similar way, except that factors of 2 or 4 are introduced (Nye 1957).

$$\begin{aligned} S_{mn} &= S_{ijkl} && \text{if m and n are 1, 2 or 3;} \\ &= 2S_{ijkl} && \text{when m or n are 4, 5 or 6;} \\ &= 4S_{ijkl} && \text{when m and n are 4, 5 or 6.} \end{aligned}$$

Elasticity tensors can be written in a way which shows a mixture of covariant and contravariant components: a notation which takes account of this is to write a stiffness component, say, as C_{ik}^{jl} . Such a distinction does not affect the analysis of sections 3.2 to 3.4, and will not be made until 3.5 where invariants are discussed.

3.2 Equation of motion of an elastic body

Consider the motion of a small rectangular volume element of an elastic medium. The components of the net force acting on this element can be equated to the acceleration components by Newton's second law, and for a medium of density ρ we obtain

$$\frac{\partial \sigma_{ij}}{\partial x_j} = \rho \ddot{s}_i \qquad i = 1,2,3 \qquad (3.4)$$

where $\underline{s}$ and $\underline{x}$ are the displacement and position vectors, respectively. Using equations 3.2 and 3.3 we can write

$$\frac{\partial \sigma_{ij}}{\partial x_j} = C_{ijkl}\frac{\partial \epsilon_{kl}}{\partial x_j} = \tfrac{1}{2}\left[\frac{\partial^2 s_l}{\partial x_k \partial x_j} + \frac{\partial^2 s_k}{\partial x_l \partial x_j}\right] C_{ijkl}$$

and hence

$$C_{ijkl}\, s_{l,kj} = \rho \ddot{s}_i \qquad i = 1,2,3 \qquad (3.5)$$

in which the comma notation denotes differentiation with respect to x, and where the fact that $C_{ijkl} = C_{ijlk}$ has been used. Equation 3.5 is the equation of motion: we look for solutions in the form of plane travelling waves. If the wave-vector along the direction of propagation, or normal to planes of constant phase, is $\underline{k}$, then the solution for one of the components of a plane wave is

$$s_l = s_{0l} e^{i(\omega t - \underline{k}.\underline{r})}, \quad l = 1,2,3 .$$

The particle displacement vector $\underline{s}$ is not, in general, parallel to $\underline{k}$. Let $\underline{n}$ (n_1, n_2, n_3) be a unit vector in the direction of $\underline{k}$. Then $\underline{k} = \frac{2\pi}{\lambda}\underline{n} = \frac{\omega}{v}\underline{n}$, where v is the propagation velocity, and

$$s_{l,kj} = -n_k n_j s_{0l} \frac{\omega^2}{v^2} e^{i(\omega t - \underline{k}.\underline{r})}$$

so that the equation of motion (3.5) becomes

$$C_{ijkl} s_{0l} n_k n_j = \rho v^2 s_{0i} , \quad i = 1,2,3 . \qquad (3.6)$$

When equation 3.6 is written more fully as a set of three equations in s_{01}, s_{02} and s_{03} the set is known as Christoffel's equations; if the displacement coefficients s_{0i} are to be determined, then the form of equation 3.6 means that the determinant of the coefficients of the s_{0i} must be zero, for if not, only the trivial solution $s_{01} = s_{02} = s_{03} \neq 0$ is possible. The condition can be written as

$$\begin{vmatrix} L_{11}-\rho v^2 & L_{12} & L_{13} \\ L_{12} & L_{22}-\rho v^2 & L_{23} \\ L_{13} & L_{23} & L_{33}-\rho v^2 \end{vmatrix} = 0 \qquad (3.7)$$

where the L's are linear combinations of two direction cosines and an elastic constant, and are known as Christoffel's coefficients. Equation 3.7 is a cubic in ρv^2. For a given propagation direction there are thus three velocities. The particle displacement vectors appropriate to each one can be found from a substitution of the three values for ρv^2 back into equation 3.6. The three displacement vectors are mutually perpendicular: in the special case when they are all either parallel or perpendicular to the propagation vector that direction is known as a pure mode direction, and a pure longitudinal and two pure transverse modes result. Quasi-pure and impure directions are those in which only one or none of the displacement vectors, respectively, is perpendicular to $\underline{k}$. Pure mode directions are to be preferred in ultrasonic work because a standard X or Y cut transducer can be used to excite one mode only; specially cut transducers would be required to propagate any one of the modes in a quasi-pure or an impure direction. In the next section we examine the propagation along low-index directions in cubic and tetragonal systems, and find that all of the propagation directions needed to determine their elastic constants are pure, except for one in the tetragonal case.

3.3 Solutions of the Christoffel equations for cubic and tetragonal (TI) symmetries

We wish to obtain expressions for the propagation velocities along low-index directions in terms of the elastic constants for cubic and tetragonal crystals. The distinction between the tetragonal Laue groups TI and TII must be made at the outset, because in the TI group, unlike the TII, the elastic constant C_{16} is zero for a normal axial set and the elastic constant equations are much simpler in form. The tetragonal indium-thallium alloys have TI symmetry: a material such as $CaWO_4$, in which the +z and -z directions are not equivalent, is in the TII group. A detailed description of wave propagation in TII crystals is given by Farley and Saunders (1972).

The form of the stiffness matrix for cubic and tetragonal TI symmetries is given below.

Cubic

$$\begin{pmatrix} C_{11} & C_{12} & C_{12} & 0 & 0 & 0 \\ C_{12} & C_{11} & C_{12} & 0 & 0 & 0 \\ C_{12} & C_{12} & C_{11} & 0 & 0 & 0 \\ 0 & 0 & 0 & C_{44} & 0 & 0 \\ 0 & 0 & 0 & 0 & C_{44} & 0 \\ 0 & 0 & 0 & 0 & 0 & C_{44} \end{pmatrix}$$

(3 independent constants)

Tetragonal (TI)

$$\begin{pmatrix} C_{11} & C_{12} & C_{13} & 0 & 0 & 0 \\ C_{12} & C_{11} & C_{13} & 0 & 0 & 0 \\ C_{13} & C_{13} & C_{33} & 0 & 0 & 0 \\ 0 & 0 & 0 & C_{44} & 0 & 0 \\ 0 & 0 & 0 & 0 & C_{44} & 0 \\ 0 & 0 & 0 & 0 & 0 & C_{66} \end{pmatrix}$$

(6 independent constants)

For the cubic system Christoffel's coefficients are

$$
\begin{aligned}
L_{11} &= n_1^2 C_{11} + (n_2^2 + n_3^2) C_{44} \\
L_{12} &= n_1 n_2 (C_{12} + C_{44}) \\
L_{13} &= n_1 n_3 (C_{12} + C_{44}) \\
L_{22} &= (n_1^2 + n_3^2) C_{44} + n_2^2 C_{11} \\
L_{23} &= n_2 n_3 (C_{12} + C_{44}) \\
L_{33} &= (n_1^2 + n_2^2) C_{44} + n_3^2 C_{11} \; .
\end{aligned}
\tag{3.8}
$$

If propagation in the $[\bar{1}10]$ direction is considered, then the velocities depend on the elastic constants in such a way that all of the independent elastic constants can be determined. A useful experimental check is to compare values of C_{11} and C_{44} thus obtained with those determined from propagation in $[100]$ direction. The polarisations involved, and the elastic constant equations are given in Table 3.1 (a).

The Christoffel coefficients for a tetragonal system are

$$
\begin{aligned}
L_{11} &= n_1^2 C_{11} + n_2^2 C_{66} + n_3^2 C_{44} \\
L_{12} &= n_1 n_2 (C_{12} + C_{66}) \\
L_{13} &= n_1 n_3 (C_{13} + C_{44}) \\
L_{22} &= n_1^2 C_{66} + n_2^2 C_{11} + n_3^2 C_{44} \\
L_{23} &= n_2 n_3 (C_{13} + C_{44}) \\
L33 &= (n_1^2 + n_2^2) C_{44} + n_3^2 C_{33}
\end{aligned}
\tag{3.9}
$$

Solutions are given in Table 3.1 (b) for propagation in $[100]$, $[001]$, $[110]$ and $[011]$ directions. It can be seen that all constants except C_{13} may be determined from propagation along the first three of these directions; all the modes are pure in these directions. From equations 3. 9 it follows that C_{13} can be obtained by propagation in any direction in which the direction cosines n_3 and either n_1 or n_2 are not zero. Convenient

TABLE 3.1

Relations between elastic stiffness constants and sound velocities

a) Cubic crystals

Propagation direction	Polarisation direction	Elastic constant equation
100	100	$\rho v_1^2 = C_{11}$
100	x-y plane	$\rho v_2^2 = C_{44}$
110	110	$\rho v_3^2 = \frac{1}{2}(C_{11} + C_{12} + 2C_{44})$
110	$1\bar{1}0$	$\rho v_4^2 = \frac{1}{2}(C_{11} - C_{12})$
110	001	$\rho v_5^2 = C_{44}$

b) Tetragonal crystals

Propagation direction	Polarisation direction	Elastic constant equation
100	100	$\rho v_1^2 = C_{11}$
100	010	$\rho v_2^2 = C_{66}$
100	001	$\rho v_3^2 = C_{44}$
001	001	$\rho v_4^2 = C_{33}$
001	x-y plane	$\rho v_5^2 = C_{44}$
110	110	$\rho v_6^2 = \frac{1}{2}(C_{11} + C_{12} + C_{66})$
110	$1\bar{1}0$	$\rho v_7^2 = \frac{1}{2}(C_{11} - C_{12})$
110	001	$\rho v_8^2 = C_{44}$
011	100	$\rho v_9^2 = \frac{1}{2}(C_{44} + C_{66})$
011	ϕ	$\rho v_{10}^2 = \frac{1}{2}(A + \sqrt{A^2 - B + C^2})$
011	$\phi + \pi/2$	$\rho v_{11}^2 = \frac{1}{2}(A - \sqrt{A^2 - B + C^2})$

ϕ is an angle which is determined by the elastic constants.

$A = C_{44} + \frac{1}{2}(C_{11} + C_{33})$

$B = (C_{11} + C_{44})(C_{33} + C_{44})$

$C = C_{13} + C_{44}$

directions would be those in the $(1\bar{1}0)$ plane at any angle to $[110]$ except 0° and 90°, and those in the (100) plane except 0° and 90° to $[010]$. Pace (1970) has considered their relative merits from an experimental viewpoint, and has shown that propagation in the (100) plane is to be preferred, on account of the modes being quasi-pure instead of impure as in the case of $(1\bar{1}0)$. He gives equations for finding a direction in the (100) plane which is, in fact, pure and which depends on the elastic constant values of the material in question. Such a direction is known as an accidental pure mode direction. In the case of indium-thallium alloys, with a c/a ratio of nearly 1.0, this accidental pure mode direction turns out to be at about 43° to the z-axis, so that the use of a $[011]$ propagation direction (at 45° to the z-axis) is acceptable, and excitation of the quasi-pure transverse and longitudinal modes gave no difficulty in practice. Furthermore, the equations relating sound velocity to elastic constants take on a simpler form, and become those given in Table 3.1(b). All the quantities in the expressions for v_{10} (and v_{11}) are known except C^2. Two values result from this for C_{13}, one positive and one negative, whose moduli differ by $2C_{44}$. Farley (private communication) has shown that only one of these solutions leads to the observed polarisations for tetragonal materials. In the particular case of indium-thallium it also happens that the negative value of C_{13} violates one of the Born stability criteria, and is physically unreal. We consider the various stability conditions in the next section.

3.4 Crystal stability

3.4.1 Strain energy density

The work done by the stress components σ_i when a crystal is subjected to a small change in its state of strain can be shown to be (e.g. Nye 1957)

$$dW = \sigma_i d\epsilon_i \qquad i = 1,2,3 \quad , \tag{3.10}$$

when the strain components change from ϵ_i to $\epsilon_i + d\epsilon_i$. By Hooke's law we may write

$$dW = C_{ij}\epsilon_j d\epsilon_i \ . \tag{3.11}$$

If the process is an isothermal one then dW gives the change in free energy of the system, and the C_{ij} are the isothermal elastic constants. For an adiabatic change the internal energy changes and the expression for dW involves the adiabatic constants. At the frequencies of the distortions caused by ultrasonic waves the changes can be considered to be adiabatic; the difference between the elastic constants defined in the two ways is very small (Hearmon 1961).

Let the change in internal energy be dU.

Thus
$$dU = C_{ij}\epsilon_j d\epsilon_i \tag{3.12}$$

On writing out equation 3.12 in full and integrating, we find an expression for the strain energy per unit volume.

$$U = \tfrac{1}{2}C_{ij}\epsilon_i\epsilon_j \tag{3.13}$$

where we have noted that $C_{ij} = C_{ji}$. Equation 3.13 can also be written

$$U = \tfrac{1}{2}S_{ij}\sigma_i\sigma_j \tag{3.14}$$

or, alternatively,

$$U = \tfrac{1}{2}\epsilon_i\sigma_i \quad . \tag{3.15}$$

3.4.2 The Born stability criteria

The strain energy U must be a positive definite quantity for a stable crystal lattice. That is to say, equations 3.13 or 3.14 can only be zero when ϵ and σ are zero: it is not possible to have a combination of C_{ij} or S_{ij} values which gives a zero energy density when either σ or ϵ is not zero. Now from equation 3.14 U is a homogeneous quadratic function in σ in which the S_{ij} are the coefficients. Salmon (1912) has shown that for such a function to be positive definite there are certain restrictions on the coefficients. These come from the requirement that the determinants of the principal minors of the matrix of coefficients must each be greater than zero. That matrix is given below, and the principal minors are shown by dashed lines.

$$\begin{vmatrix} S_{11} & S_{12} & S_{13} & S_{14} & S_{15} & S_{16} \\ S_{12} & S_{22} & S_{23} & S_{24} & S_{25} & S_{26} \\ S_{13} & S_{23} & S_{33} & S_{34} & S_{35} & S_{36} \\ S_{14} & S_{24} & S_{34} & S_{44} & S_{45} & S_{46} \\ S_{15} & S_{25} & S_{35} & S_{45} & S_{55} & S_{56} \\ S_{16} & S_{26} & S_{36} & S_{46} & S_{56} & S_{66} \end{vmatrix}$$

As a result we find several inequalities. It is simpler at this point to consider an actual example concerning a particular symmetry. We take tetragonal TI, whose matrix of compliances has the same form as the stiffnesses given in section 3.3, and the following inequalities result: $S_{11}>0$; $S_{33}>0$; $S_{44}>0$; $S_{66}>0$; $S_{11}>|S_{12}|$; $S_{33}(S_{11}+S_{12})>2S_{13}^2$. The minors could have been taken starting at the bottom right-hand corner; this would result in another inequality, consistent with the first set, of $S_{11}S_{33}>S_{13}^2$.

For a general axial set the simplification of the matrix, as in section 3.3, is not possible, and all components may be non-zero. But some of the inequalities still have a simple form: $S_{11}', S_{22}', S_{33}', S_{44}', S_{55}', S_{66}' > 0$; $S_{11}' S_{22}' > S_{12}'^2$. The dash indicates a compliance referred to the transformed axes, and whose value is given by the tensor transformation law:

$$S_{ijkl}' = a_{lm}a_{jn}a_{kp}a_{lq}S_{mnpq} \qquad (3.16)$$

in which the a's are the direction cosines for the transformation.

3.5 Invariants

One invariant has already been encountered, namely the strain energy density. An invariant is any quantity whose value does not depend on the set of co-ordinates used to describe it. There are several invariants which can be extracted from a tensor, and Brillouin (1938) gives a method of finding these in terms of the components. Examples for the compliance tensor are: $S_{11} + S_{22} + S_{33} + S_{44} + S_{55} + S_{66}$ and $S_{11} + S_{22} + S_{33}$.

In chapter 6 we shall be interested in the volume compressibility, β, which is defined as the fractional change in volume when a material is subjected to unit hydrostatic pressure. Or

$$\beta = -\frac{1}{V}\left.\frac{\partial V}{\partial P}\right|_T \quad . \qquad (3.17)$$

Hydrostatic pressure results in stress components σ_{11}, σ_{22} and

σ_{33} only, each of which is equal to the pressure p. The resulting strains are negative, and so

$$\epsilon_{ij} = -S_{ijkk}p .$$

The change in volume of a unit cube when the strains along the three axes are ϵ_{11}, ϵ_{22} and ϵ_{33} is the dilation Δ, and

$$\begin{aligned}\Delta &= (1+\epsilon_{11})(1+\epsilon_{22})(1+\epsilon_{33}) - 1\\ &= \epsilon_{ii}\\ &= -S_{iikk}p\end{aligned}$$

and consequently $\beta = -\frac{\Delta}{p} = S_{iikk}$. (3.18)

Written in full the explicit expression for volume compressibility is $\beta = S_{11} + S_{22} + S_{33} + 2(S_{12} + S_{13} + S_{23})$. (3.19)

To show that this is invariant we used the mixed components of both the stress and strain tensors σ^{l}_{k} and ϵ^{j}_{i} . Thus the compliance tensor is S^{jl}_{ik} . Let this be referred to the axial set x^1, x^2, x^3. We now transform to the set y^1, y^2, y^3, and write the result as T^{pq}_{mn} . Combining the transformation rules for covariant and contravariant components, we have:

$$S^{jl}_{ik} = T^{pq}_{mn} \frac{\partial y^j}{\partial x^p} \frac{\partial y^l}{\partial x^q} \frac{\partial x^m}{\partial y^i} \frac{\partial x^n}{\partial y^k} \qquad (3.19)$$

Setting i = j and k = l equation 3.19 becomes

$$\begin{aligned}S^{ik}_{ik} &= T^{pq}_{mn} \frac{\partial y^i}{\partial x^p} \frac{\partial y^k}{\partial x^q} \frac{\partial x^m}{\partial y^i} \frac{\partial x^n}{\partial y^k}\\ &= T^{pq}_{mn} \delta^m_p \delta^n_q\\ &= T^{mn}_{mn} \qquad (3.20)\end{aligned}$$

which establishes the invariance.

In an orthogonal axial system the metric tensor is unity, so that the contravariant and covariant components of the various tensors involved are equal. It is thus acceptable to write S^{ik}_{ik} as S_{iikk}.

CHAPTER 4

EXPERIMENTAL METHODS

Introduction

The experimental work on the indium-thallium alloys started with the preparation and growth of single crystals of several alloy compositions from the elements. The compositions chosen included two which had fcc structures at room temperature, and which became fct below this, and three which were fct at all temperatures up to the melting point. The single crystals were examined and oriented before being cut to give samples of the appropriate orientations for measurements to be performed.

The measurements which were made consisted of:

1) The elastic constants for each alloy composition over a wide temperature range, including the transition temperatures of the fcc alloys.

2) The ultrasonic attenuation as a function of temperature, for various frequencies and orientations.

3) The components of the thermal expansion tensor.

4) An estimation of the lattice parameters at room temperature for selected alloys.

In addition the density of each sample was obtained by Archimedes' method.

This chapter gives details of the apparatus and techniques used to prepare the crystals and to produce the data presented in chapter 5.

4.1 Sample preparation

Crystals of indium-thallium alloys have been grown from the melt using the horizontal zone method. Starting materials were 99.9999% indium ingots and 99.999% thallium rod, both obtained from Koch-Light Ltd. A pyrex glass boat of about 4 cc capacity served to contain the melt, and its pointed ends were sufficient to initiate the crystal growth without having to use a separate seed.

The two metals were cleaned in dilute nitric acid and washed thoroughly with distilled water to remove traces of nitrate. Subsequent handling of the indium gave no difficulty, as that element does not react very quickly when in contact with air. Thallium, however, reacts much more rapidly, and a bright, cleaned surface becomes dulled after about 15 seconds exposure to the atmosphere; the reactivity of thallium is even greater when heated. A special technique was evolved to cope with these problems during the weighing and melting of the alloy constituents, and this is now described.

The approximate weights of indium and of thallium which would almost fill the boat were determined for the alloy composition required. After washing both metals as described, the required mass of indium, less about one gram, was put into the boat and was melted under a reduced pressure of nitrogen; the boat and indium was then weighed. The thallium was dried on tissue, and an amount approximately equal to the calculated weight needed was weighed out as quickly as possible. Re-immersion in distilled water dissolved the small amount of oxide formed during the weighing. The pieces of thallium were then put on top of the indium in the boat, with the latter positioned near the mouth of a long glass tube through which flowed a stream of nitrogen gas. The tube was sealed and evacuated, and heat was applied with a flame to the outside of the tube to melt the metals in the boat. The problem of the extreme reactivity of thallium with any residual oxygen was not then encountered, because when the indium melted at 156°C the pieces of thallium sank beneath its surface before melting. Further heating ensured that all of the thallium had alloyed. When the metal had solidified a further weighing of boat plus contents led to an accurate determination of the mass of thallium present. The exact amount of indium still required to obtain an alloy of the desired composition could now be calculated, and this quantity was weighed out accurately and melted in under a nitrogen atmosphere. Mixing of the alloy to achieve homogeneity was achieved in the first instance by maintaining it molten under nitrogen for about 50 hours with a vertical temperature gradient of 20°C cm^{-1}.

Weighing could be done to an accuracy of 0.3 mg, leading to a 0.1% uncertainty in the composition. Five alloys of composition 10, 11.5, 15, 25 and 27 at.% thallium were prepared in this way.

4.2 Crystal Growth

4.2.1 Boats

The shape and dimensions of the boats used are shown in figure 4.1 . The important design features were a point at

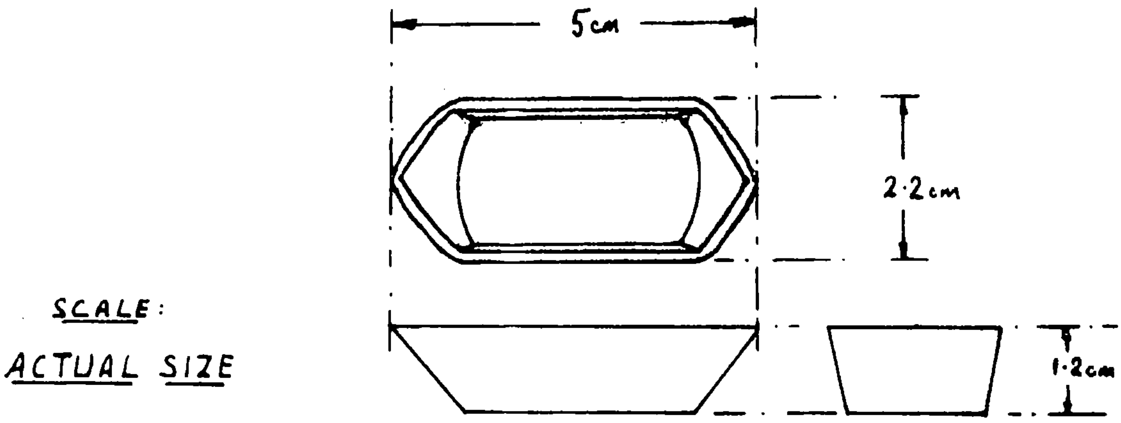

Figure 4.1 The pyrex glass boat in which crystals of indium-thallium alloys were grown.

each end, for seeding, and a smooth inside surface to reduce nucleation centres. At first the boats were made from extruded square section pyrex tubing, but later ones were formed by allowing hot glass to flow over a stainless steel mould. Either method produced boats of satisfactory quality.

4.2.2 Furnace

The horizontal furnace is illustrated in figure 4.2 . Constantan wire covered with heat-resistant electrical insulation was wound toroidally to form the heater, and was arranged as shown in figure 4.3 ; water passing through copper coils at each end increased the temperature gradient at the solid - liquid interface. The heater assembly was mounted on an aluminium block through which passed two guide rods. A third, screwed, rod also passed through the block, and when rotated by an electric motor it caused the heater to move along the guide rods. A reversing switch in the motor circuit set the sense of rotation of the screwed rod, and thus set the direction of movement of the heater; two microswitches limited the length of travel.

4.2.3 Procedure

Indium-thallium alloys in the composition range 0 to 40 at. thallium melt, to within a few degrees, at 155°C. A current of 1.46 amp through the heater winding produced the temperature profile shown in figure 4.4, with a maximum temperature of 160°C, and a gradient of 15°C cm^{-1} at the growth interface. The zone speed was 2.4 mm hr^{-1}. The boat and

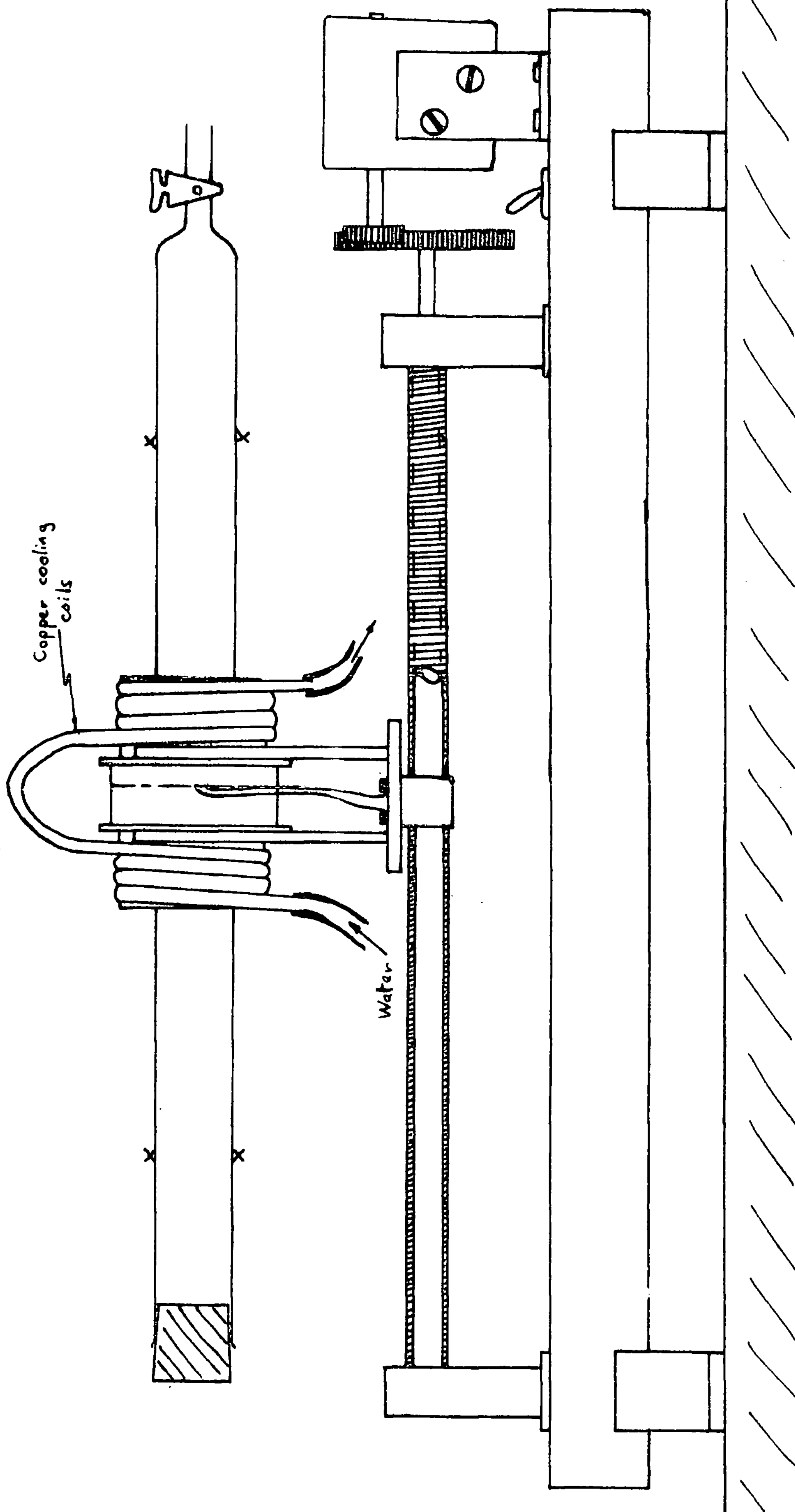

xx : clamps

Figure 4.2 The horizontal zone furnace.

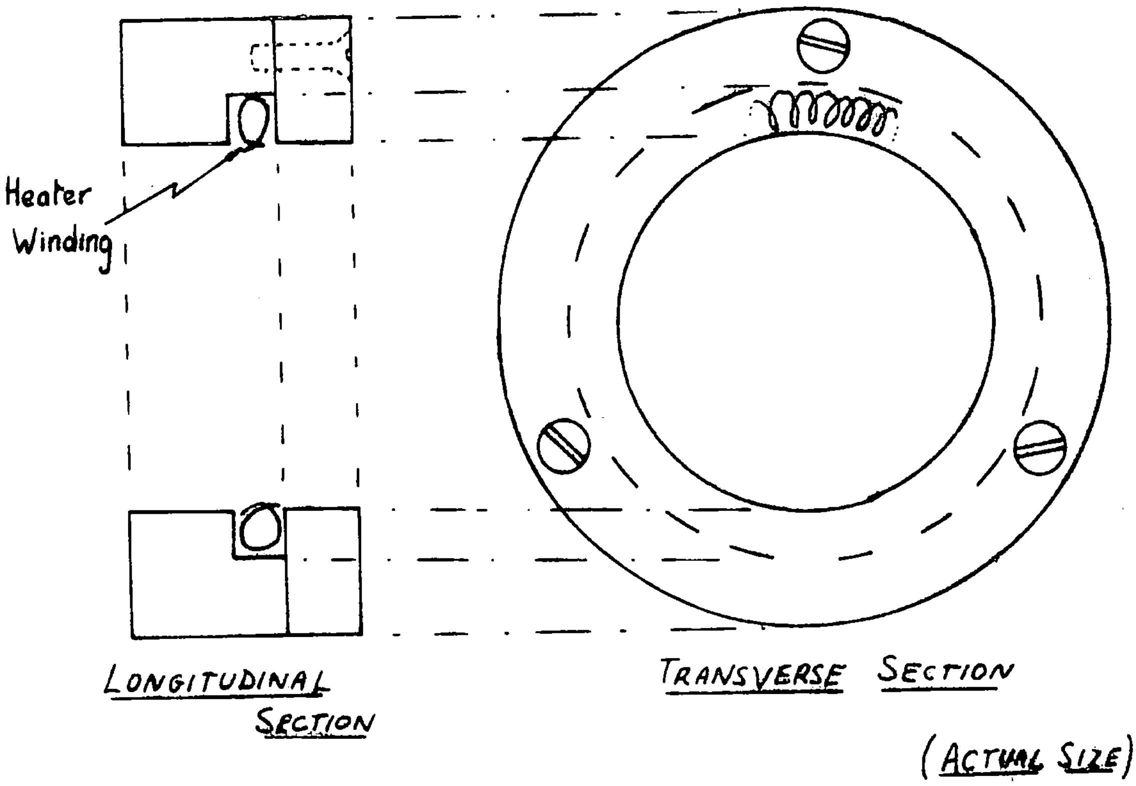

Figure 4.3 Details of the heater assembly.

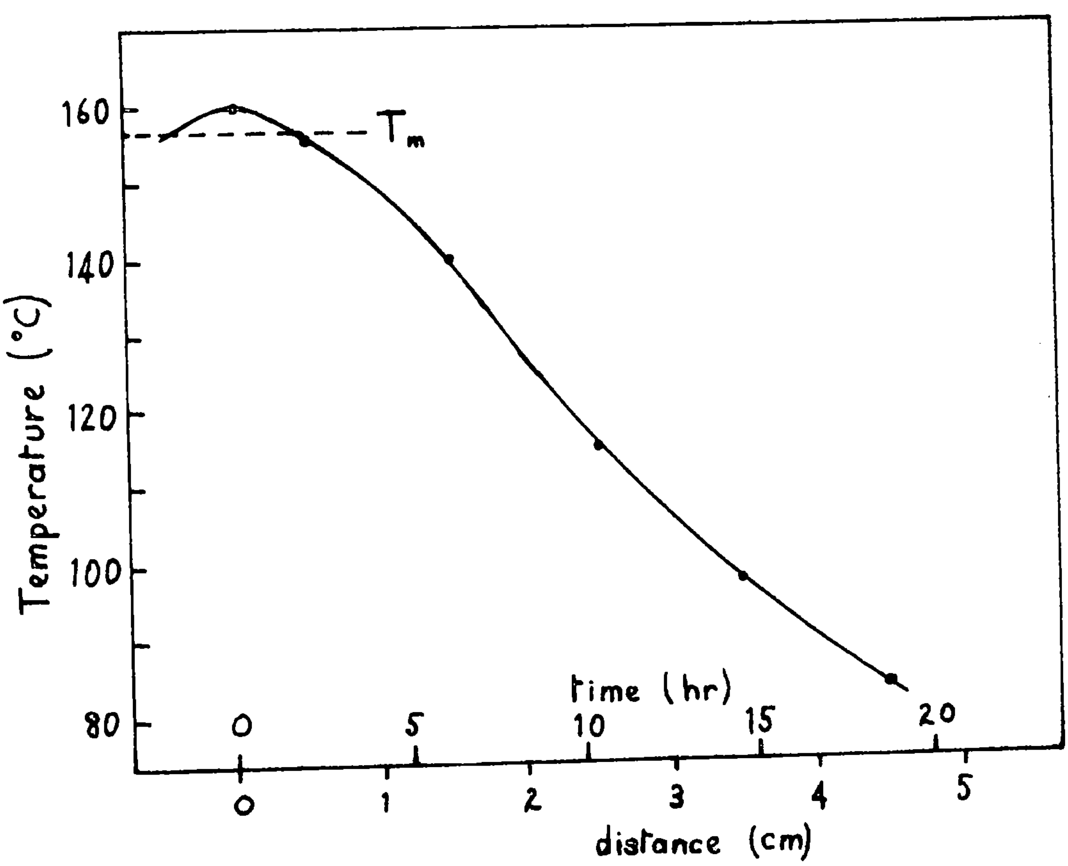

Figure 4.4 Temperature profile of the growth furnace (measured along the axis of the furnace before introduction of the boat and alloy).

contents were supported on a glass slide within a long pyrex tube having a tap at one end and closed by a rubber bung at the other. Growth occurred under a reduced pressure of nitrogen.

The success rate for crystals which were single, or which had about 90% of their volume single, seemed to depend on whether a fcc or a fct structure alloy was involved. For fcc about 5 passes were needed to achieve this; for fct the figure was nearer 10. For each of the first few passes the number of grains in the material, as revealed by etching in dilute nitric acid, decreased with each pass, as did the amount of oxide accumulating on the surface. Presumably the grain size increased as the number of nucleation centres, such as particles of dust or oxide, decreased as a result of the etching of the surface after each pass. It was to enable etching to be done between passes that growth in an open boat rather than in a sealed tube was chosen.

4.3 Examination of single crystals

4.3.1 Assessment of crystal quality

Each as-grown boule was in the form of a block about 3.5 by 1.6 by 0.8 cm. One such boule is illustrated in figure 4.5 . There was little or no tendency for the metal to adhere to the glass, so removal from the boat presented no problems. The boule was etched in nitric acid (1:1 w/w) for one or two minutes to clean the surface. Any grain boundaries could then be seen very easily; the boule was repeatedly passed through the

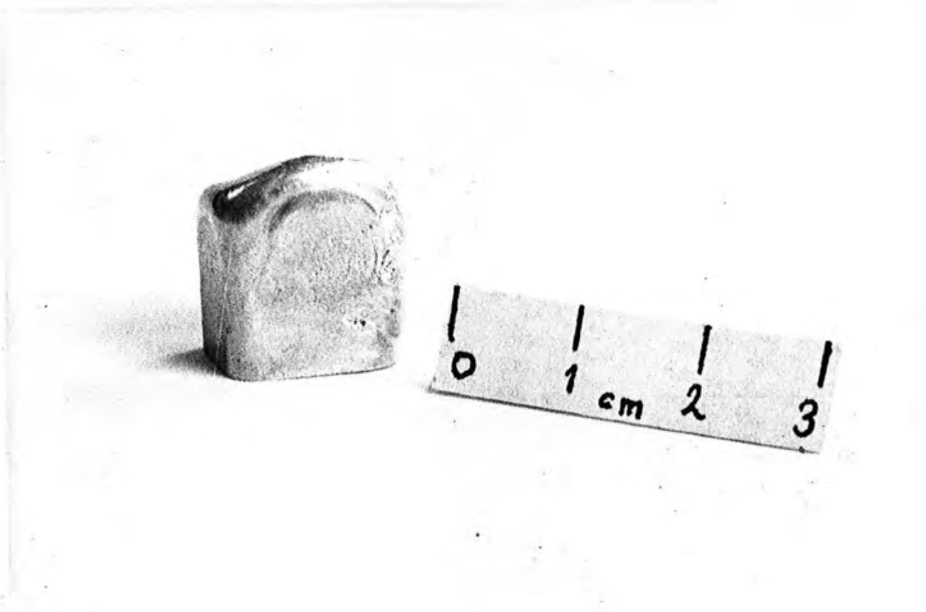

Figure 4.5 As-grown boule of an indium-thallium alloy. (Part of the boule (approx. $\frac{1}{3}$) has been cut away.)

furnace until any grains present were of such a size and position in the boule as to leave most of the volume as single crystal. Of the crystals grown, three (10, 15 and 27 at.% Tl) had no grains visible, while the other two (11.5 and 25 at.% Tl) had small grains along one side. In subsequent cutting of ultrasonic samples care was taken to avoid these defective parts. Slip bands were visible after etching the fct samples, especially in the 15 at.% Tl alloy. They were observed on $\{110\}$ or $\{011\}$ planes only, and each band was about $\frac{1}{2}$ mm wide. No more than half of any one boule was so affected.

Back-reflection Laue photographs were taken with the X-ray beam incident on the etched as-grown surface: well-defined, unsplit spots were usually obtained, indicating little surface strain and no twinning (Figure 4.6). Of particular interest in this respect was the lack of twinning in the 15 at.% Tl crystal. Doubt has surrounded the form of the phase diagram in the region where the fcc - fct phase boundary meets the solidus; the phase diagram given by Hansen (1958) shows a small temperature range in which the 15 at.% alloy is cubic, whereas that of Pollock and King (1968) suggests that it is always tetragonal. The work described here favours the second form.

4.3.2 Orientation

Orientation of a cubic crystal by the Laue back-reflection method presents little difficulty, but the procedure is more complicated for tetragonal materials. The orientation is all but complete once the $[100]$ direction has been distinguished from the $[110]$, since a Laue photograph with the X-ray beam

Figure 4.6 Laue back-reflection photograph of In-15 at.% Tl alloy. X-ray beam is directed along 4-fold axis.

perpendicular to either of these planes will result in a spot pattern of mm symmetry. Now the plane defined by [001] and [110] contains [111], an axis of pseudo-3-fold symmetry, while that defined by [001] and [100] contains [011], of m symmetry. Hence the ambiguity is removed once the pseudo-3-fold and m symmetry directions, together with the 4-fold axis, have been found. Figure 4.7a illustrates this point. A knowledge of the angle between the [011] direction and the z-axis leads to a determination of the axial ratio for the structure (Figure 4.7b). The tetragonal alloys studied had c/a very near to 1, and a calculation was made, using the method of Appendix I, of the angles between the pseudo-3-fold and the supposed x- and z-axes to check the assignment of these last two.

4.3.3 Lattice parameter and density determination

Debye-Scherrer powder photographs were produced for the 11.5, 15 and 27 at.% Tl alloys, and were indexed using a Bunn chart. The resulting photographs are shown in figures 4.8 - 10, together with the indexing. Values for the c/a ratio were determined approximately from the Bunn chart; a Nelson-Riley extrapolation produced values for 'c' and 'a'. The measured values are given in Table 4.1 and are compared with other lattice parameter measurements in figure 4.11. The agreement is quite acceptable.

Densities were measured by Archimedes' method involving flotation in both distilled water and alcohol. The results are shown in figure 4.12, together with remeasurements of the density of some of the alloys prepared by N. G. Pace.

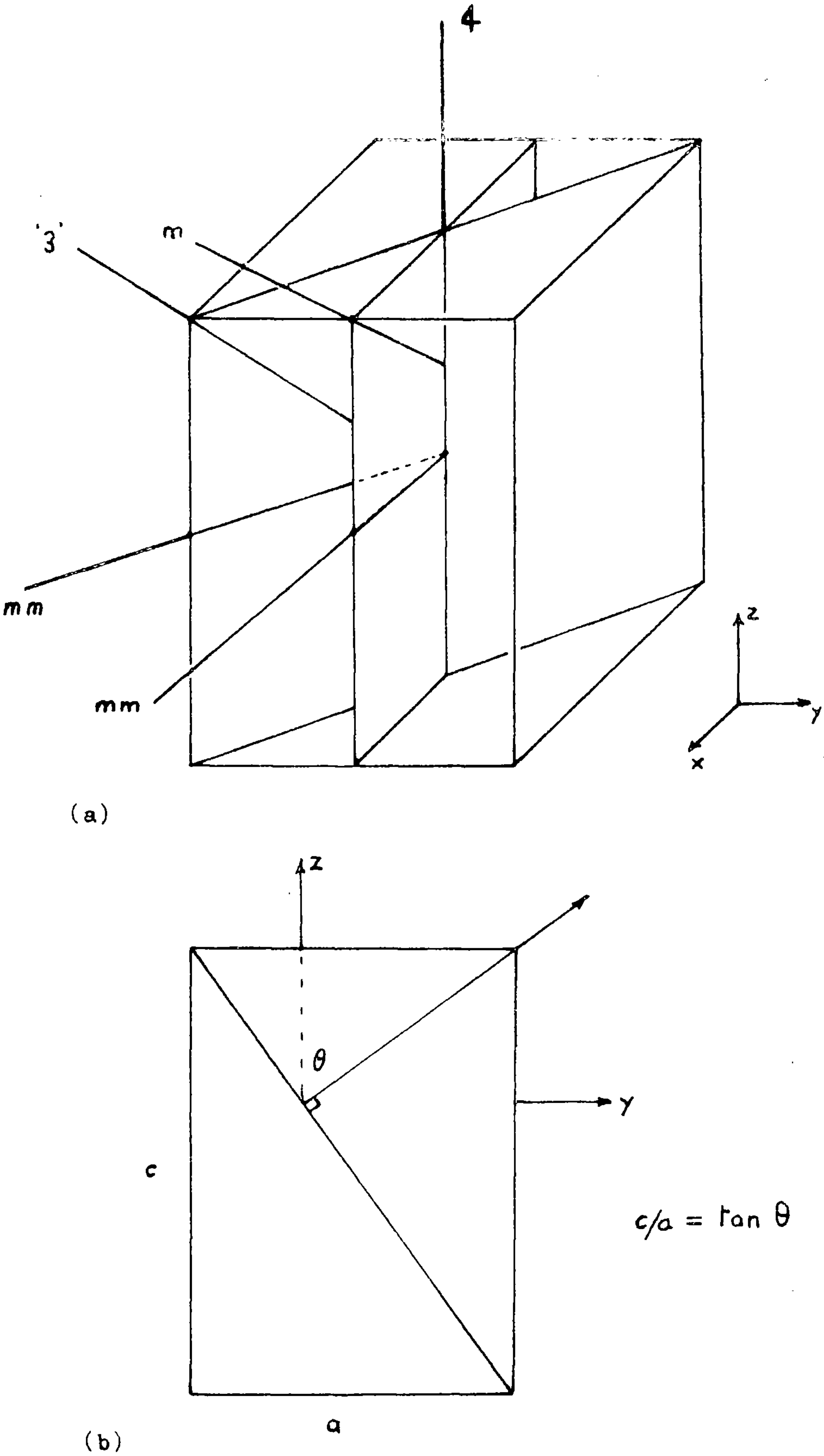

(b)

Figure 4.7 (a) Symmetry directions in a tetragonal structure.
(b) Determination of c/a ratio from a knowledge of symmetry directions.

Fig. 4.8
In-11.5% Tl

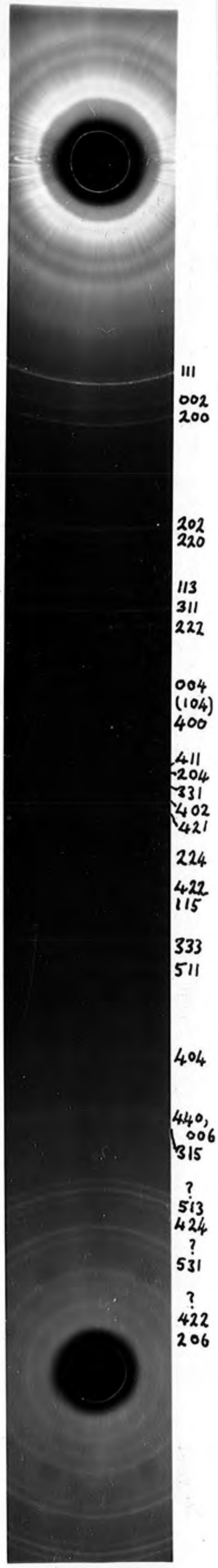

Fig. 4.9
In-15% Tl

Fig 4.10
In-27% Tl

Debye-Scherrer powder photographs of three In-Tl alloys

TABLE 4.1

Measured lattice parameters of indium-thallium alloys

at.% Tl	a (Å)	c (Å)	c/a	θ^{++}	$\tan\theta = c/a$
11.5	4.67±0.02	4.92±0.02	1.05	$47^{\circ}\pm\frac{1}{2}^{\circ}$	1.072±0.018
15	4.72±0.05	4.91±0.02	1.04	$46\pm\frac{1}{2}^{\circ}$	1.036±0.018
27	4.757±0.01		1.0		

++ θ is defined in figure 4.7 (b)

The results are compared with those of Guttman (1950) and of Matsuo and Kogachi (1971) in figure 4.11.

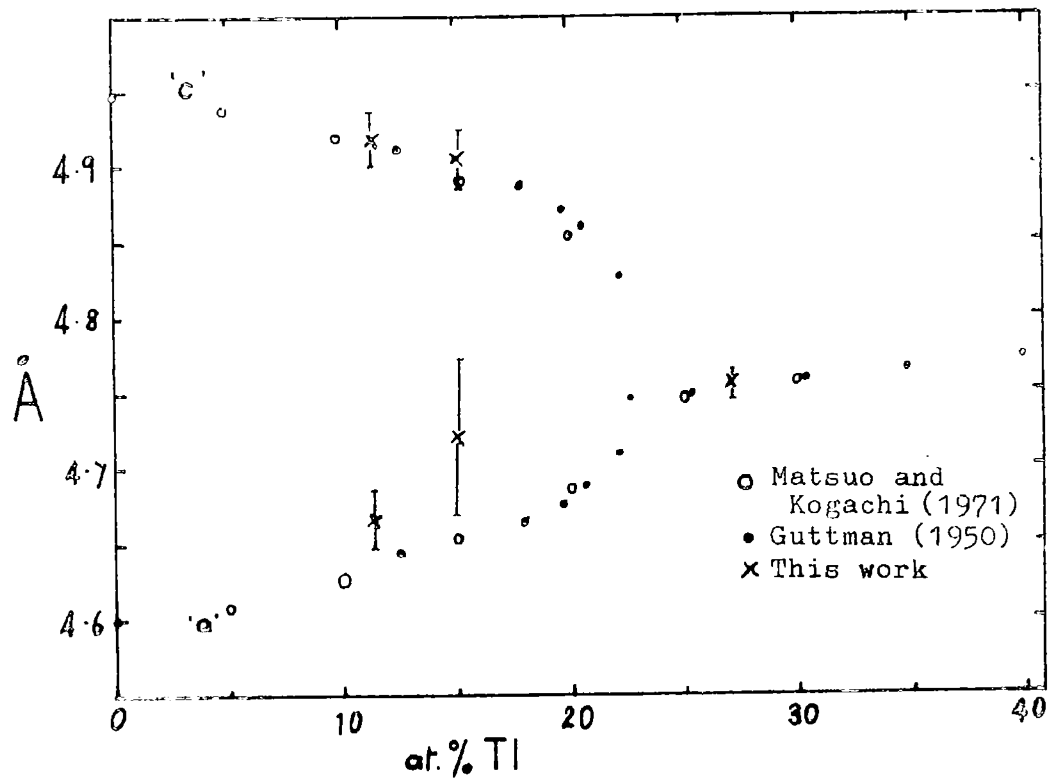

Figure 4.11 Lattice parameters of indium-thallium alloys.

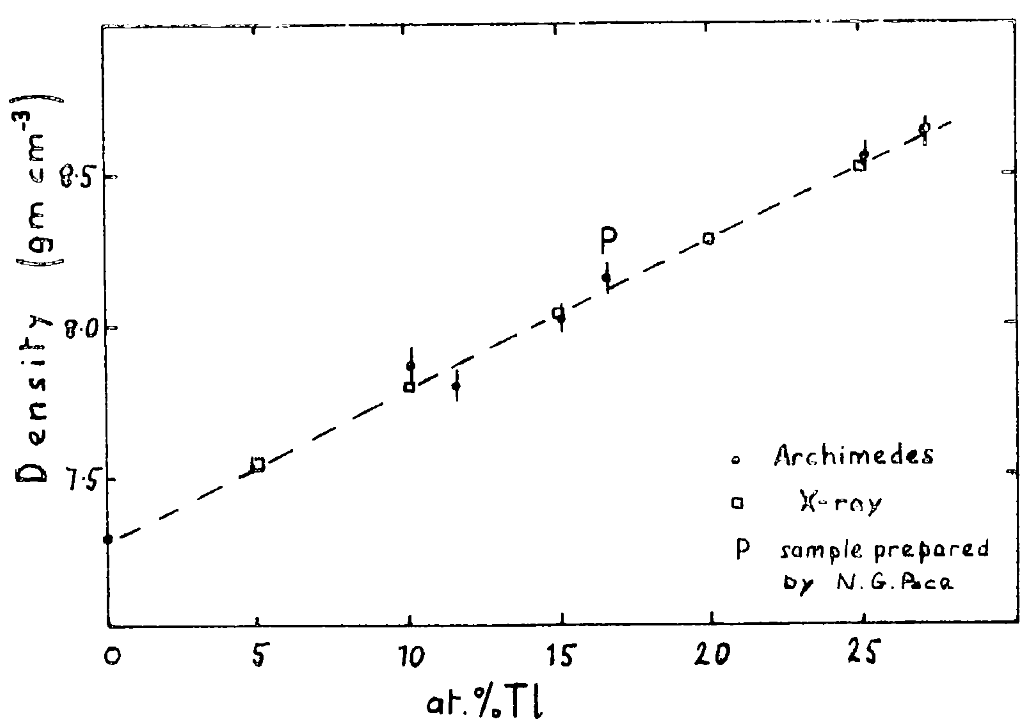

Figure 4.12 Densities of indium-thallium alloys.

Only a slight deviation from Vegard's law is seen.

4.4 Preparation of ultrasonic samples

4.4.1 Cutting the oriented crystals

Two differently oriented samples were needed for measurement of the three independent elastic constants of the cubic modification of indium-thallium crystals, and four samples needed to obtain the six independent constants in the tetragonal form. Once a particular orientation had been set up on the goniometer using back-reflection methods, the crystal and goniometer were transferred to the cutting platform of a 'Servomet' spark erosion machine. A copper plate of about $\frac{1}{2}$ mm thickness served as the cutting tool, and was positioned so as to cut the crystal in the correct direction. Sparking took place under paraffin. The Servomet had provision for limiting the maximum current passed during cutting: for indium-thallium alloys the optimum setting was 0.2 amp (range 6 on the machine). A larger current resulted in excessive pitting of the surface. Samples were produced from each boule so as to give as large a surface area as possible consistent with a reasonable thickness. The thickness was usually about 3 to 5 mm. All samples were at least 8 mm across, and most about 10 mm, so that 5 mm diameter quartz transducers could be used.

The orientation of the cut face was checked using the apparatus shown in figure 4.13, which was constructed to fit on to an X-ray generator: after a short etch to remove the deposit of carbon from the surface of the sample it was

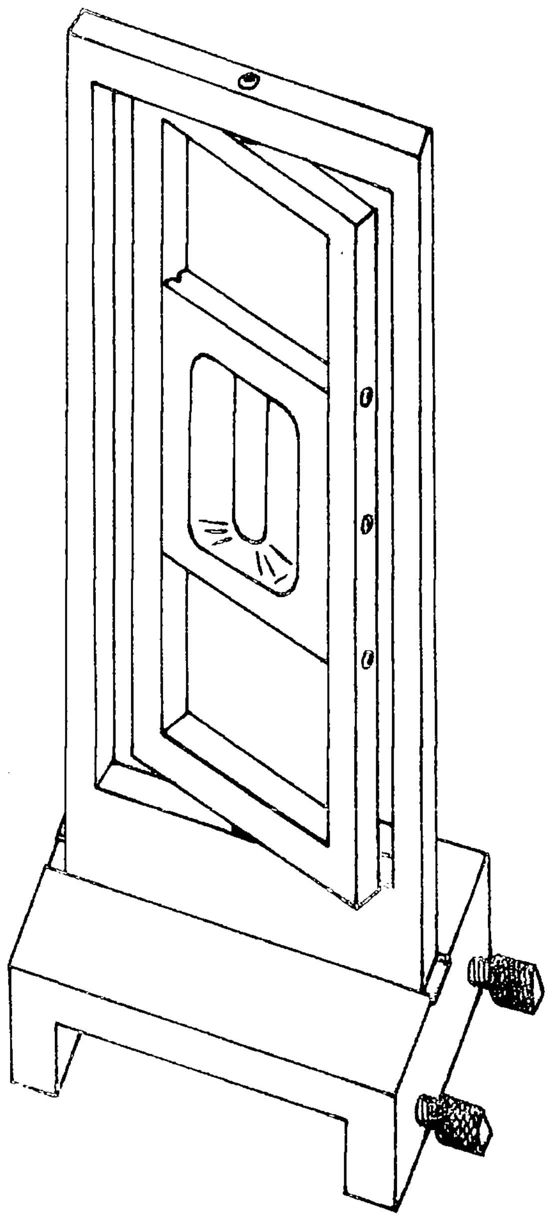

Figure 4.13 An apparatus for checking the orientation of planed faces of ultrasonic samples.

attached with glue onto the central flat plate with the cut surface in contact with the plate. When the three moveable sections were adjusted to be coplanar the design of the apparatus ensured that the X-ray beam was incident normally onto the cut face. Any slight misalignment could be estimated by the movement of the appropriate section of the apparatus which was needed to obtain the correct back-reflection spot pattern; such misalignment could be remedied in the planing process.

4.4.2 Planing

For good ultrasonic work using the pulse-echo method, samples must have flat and parallel faces. Indium-thallium alloys are very soft, and conventional polishing techniques are not suitable, so the method of spark planing was used to prepare the surfaces.

A brass disc about one inch thick and eight inches in diameter was supported in roller bearings and attached to the Servomet so that it could rotate in a horizontal plane above the cutting table. The lower surface of the disc was turned in a lathe to make it reasonably flat; there were six radial grooves milled into this face to assist circulation of the paraffin, and to remove swarf. Before planing the sample, the disc was used to plane a small circular table which was fixed to the main platform. This process had the dual effect of reducing the surface irregularities in the disc and table which resulted from machining, and of producing two surfaces which were themselves parallel to a very small tolerance (about 10^{-5} rad.). The disc could be raised by a servomotor to allow a cut and cleaned alloy crystal to be attached to the table by glue. (Care was taken to prevent glue from getting beneath the sample and thus destroying the electrical contact and sample parallelism.) The first face was planed, and the crystal was turned over and the other face planed. In this way two parallel surfaces were formed: checks with a dial gauge showed that the parallelism obtained was better than 3×10^{-4} rad. If the smallest current range was used to complete the planing process the surface irregularity was about 2-3 micron. (Manufacturer's figure). In assessing the quality of the surfaces and the parallelism required, the attenuation of sound in these materials at the frequencies used had to be considered. The alloys had a relatively large attenuation, and the sample preparation methods described were adequate for the measurements performed. Where not, correction factors to allow for the apparent increase in attenuation due to non-parallelism could be applied. (Truell, Elbaum and Chick, 1969).

The methods of this and the preceeding section resulted in samples whose orientations were within $\pm \frac{1}{2}$ degree of that desired, and which were parallel to less than 3×10^{-4} radian.

4.5 Ultrasonic measuring techniques

The propagation constant for any travelling wave in a given medium is a complex quantity. The real part gives the velocity of propagation in the medium, while the imaginary part gives the attenuation: an ultrasonic system can be used to determine both parts for propagation of a stress wave in a solid.

4.5.1.1 Pulse-echo method

If vibrations are induced at the surface of a material, then a stress wave will propagate into the bulk of the solid, and will suffer reflections and phase changes at discontinuities in the medium, wherever they occur, and particularly at boundaries with air. If both the geometry of the sample and the method of introduction of the wave are carefully controlled, then it is possible to obtain information about the way in which the material and the wave interact. In the pulse-echo method a sample is used which has flat and parallel faces; the wave is introduced by means of a short pulse of radio-frequency (rf) oscillations applied to a piezo-electric transducer bonded acoustically to one of the two parallel surfaces (figure 4.14). The resulting sound pulse travels back and forth between the parallel faces and becomes smaller in amplitude as it does so. A suitable transmit-receive (TR) device and an amplifier can then be used to display on an oscilloscope the 'echoes' of the original pulse after their conversion into an electrical signal by the direct piezo-electric effect in the transducer. Repetition of the pulse of rf at suitable intervals can result in a continuous oscilloscope display. The time interval between successive echoes is then a measure of the (group) velocity of propagation once the sample thickness is known, and the time rate of decay of the pulse amplitude leads to the attenuation of the sound by the solid.

4.5.1.2 Instrumentation

A schematic diagram of the experimental arrangement

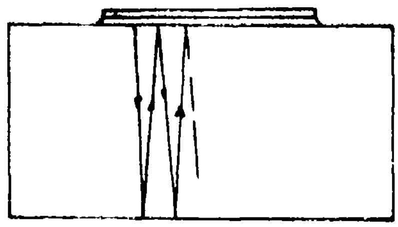

Figure 4.14(a) Ultrasonic sample and transducer showing (schematically) the path of the sound pulse.

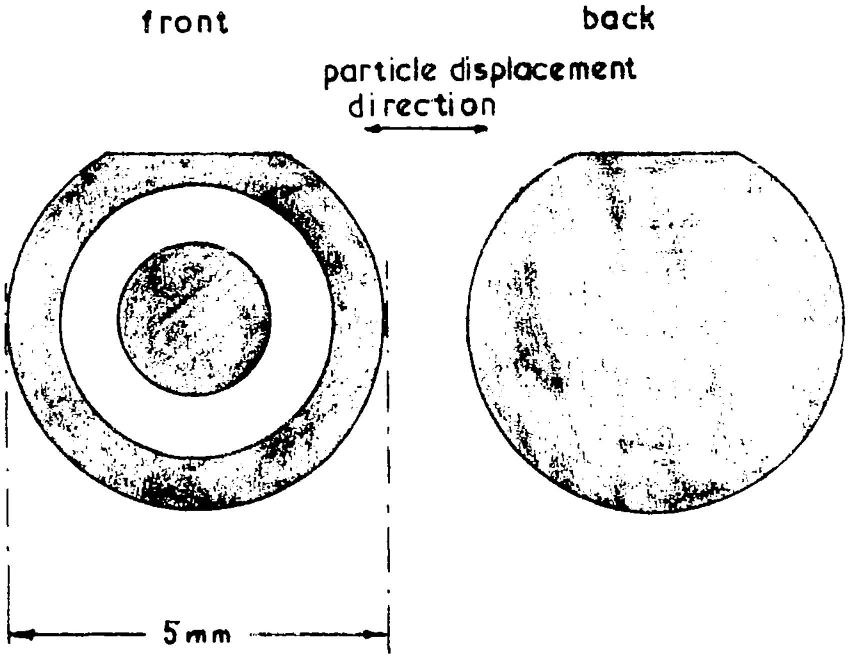

Figure 4.14(b) The dimensions and electrode configuration of the transducers used in this work. A shear transducer is shown; a longitudinal one needs no flat to indicate particle displacement direction, and is circular. The shading represents gold plating.

is shown in figure 4.15. A pulse of rf of about 1 microsecond duration was fed to the transducer on the sample every millisecond. The resulting set of echoes went to an oscilloscope through a mixer, where an adjustable exponential curve was added to enable attenuation measurements to be made. Equipment manufactured by Matec Inc. was used as the basis of the instrumentation. The Matec model 9000 included the rf pulse generator, amplifier, TR junction and calibrated attenuation comparator. Frequencies in the range 10 to 300 MHz were available, although the high attenuation in indium-thallium alloys effectively limited operation to 100 MHz. A second system was also used, consisting of the model 6600 pulse generator and amplifier as one unit, and the model 1204A attenuation comparator and master synchroniser as another. The second system had the advantage of producing signals at a higher power and a greater facility for pulse width control — both of which were used to good effect in highly attenuating samples. The attenuation comparator had a calibrated range of attenuation up to 4.2 dB/μsec in five switched steps. The exponential curve was produced by the discharge of a capacitor through a variable resistor. In order to be able to measure attenuation values greater than 4.2 dB/μsec, often encountered, the range was extended by the addition of an extra capacitor and a sixth switch position. A calibration curve was produced for this extra range.

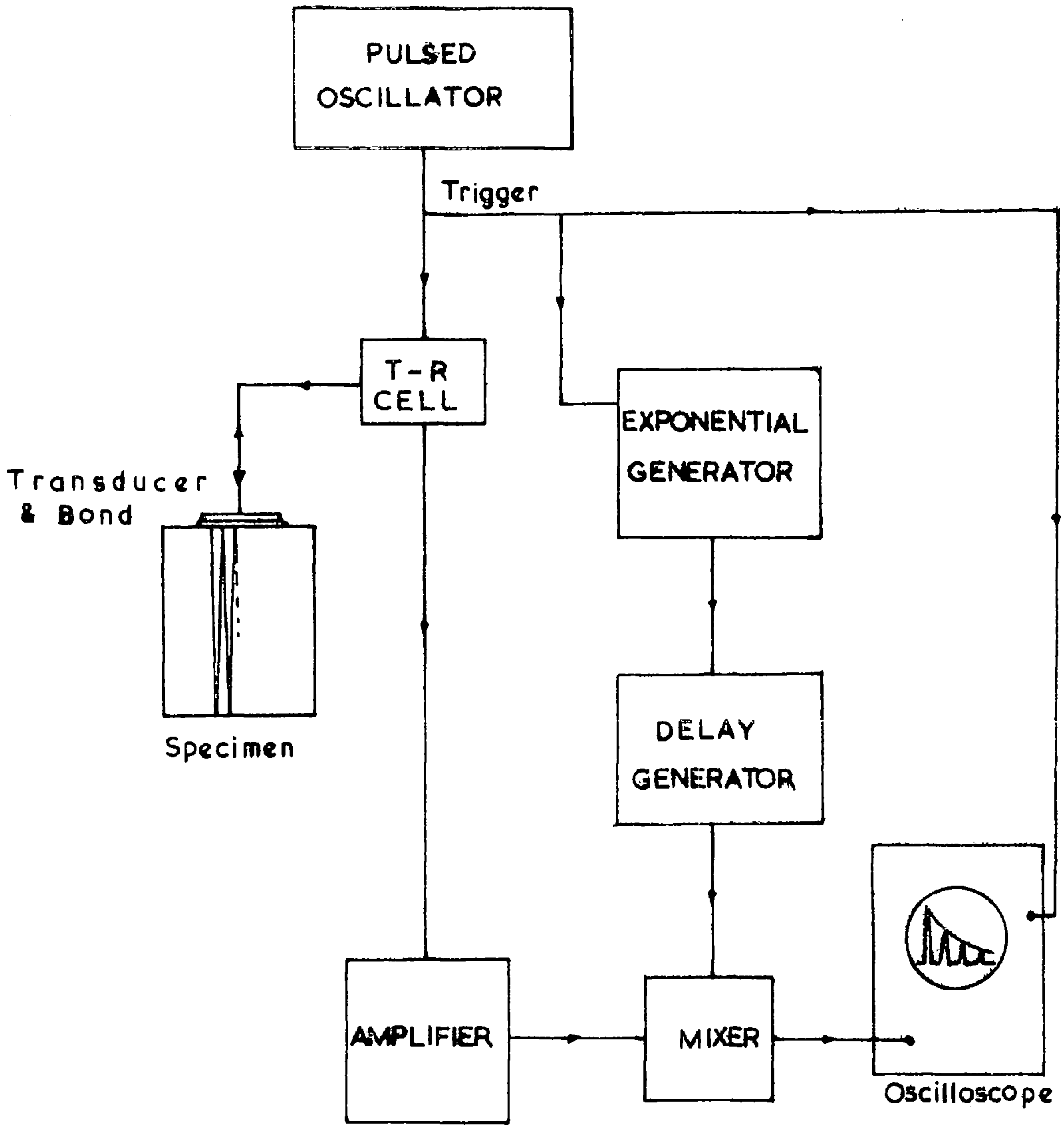

Figure 4.15 Block diagram of the instrumentation for the ultrasonic pulse-echo system.

4.5.2 The pulse superposition method

4.5.2.1 Introduction

The pulse superposition method was developed from the pulse-echo by McSkimin (1961), and is a system which can detect very small changes in sound velocity. Changes in transit time as small as 2 parts in 10^6 can be observed. The principle behind the method is that the frequency of the introduction of rf pulses to the transducer is increased until the time of transmission of one particular pulse coincides with the return to the transducer of the p-th echo of the previous one, where p is a small integer, usually 1, 2 or 3. If this condition is fulfilled, the echoes will add, and, superposing on each other, will produce a maximum in the received signal. When superposition is exact, the pulse repetition frequency (PRF) is given by

$$\mathrm{PRF} = \left[p\delta - \frac{p\gamma}{360f} + \frac{n}{f}\right]^{-1} \qquad (4.1)$$

in which δ is the transit time; f is the frequency of oscillation within the pulse; γ is the phase angle between the reflected and incident waves at the sample-transducer interface and n is an integer with positive or negative values giving the phase difference, in units of 2π, between the overlapping pulses. Figure 4.16 shows the effect of varying n.

The method of determining experimentally the pulse repetition frequency corresponding to this maximum condition, together with experimental difficulties and an estimation of the errors will be discussed below.

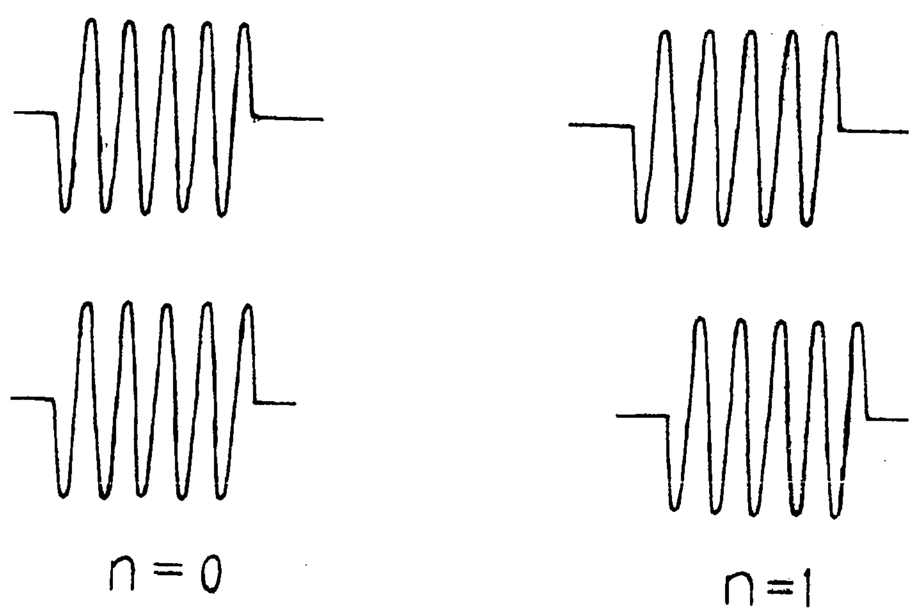

Figure 4.16 Superposition of r.f. pulses. Their phases differ by $2n\pi$ with respect to the start of the first pulse.

4.5.2.2 Experimental arrangement

The pulse superposition method relies for its precision on the stability of the frequency source used to trigger the rf pulse generator. A crystal controlled frequency synthesiser was employed: it had a short-term stability of 1 in 10^9 and long term of 1 in 10^7, with a sine wave output of maximum peak-to-peak amplitude 8 volt. Frequencies from 0.1 Hz to 2 MHz were available in steps of 0.1 Hz. A block diagram of the complete system is shown in figure 4.17. The particular set-up used was constructed by R. I. Cottam (Cottam 1973), J. M. Farley (Farley 1973) and C. A. Maynell (Maynell 1972), who all give fuller accounts of its operating characteristics.

4.5.2.3 Operation

When the PRF, as set by the frequency synthesiser, was 1 KHz, the system as described above was equivalent to either of the two Matec systems outlined in 4.5.1.2 , with the exception of the attenuation comparator. But much higher PRF's could be generated. A typical transit time for an ultrasonic pulse to travel once across a sample and back was 5 μsec. Thus, for coincidence between one rf pulse and the first echo (p=1) of the preceeding one, a PRF was required of 200 KHz, in this case. Overlap between one pulse and the 2nd, 3rd or 4th echoes of the previous one (p=2,3 or 4) would then require 100 KHz, 66.6 KHz and 50 KHz, respectively. The duty cycle of the rf oscillator used was such that it limited operation with 0.5 μsec pulses to 250 KHz; a p value was chosen so that this frequency was not exceeded.

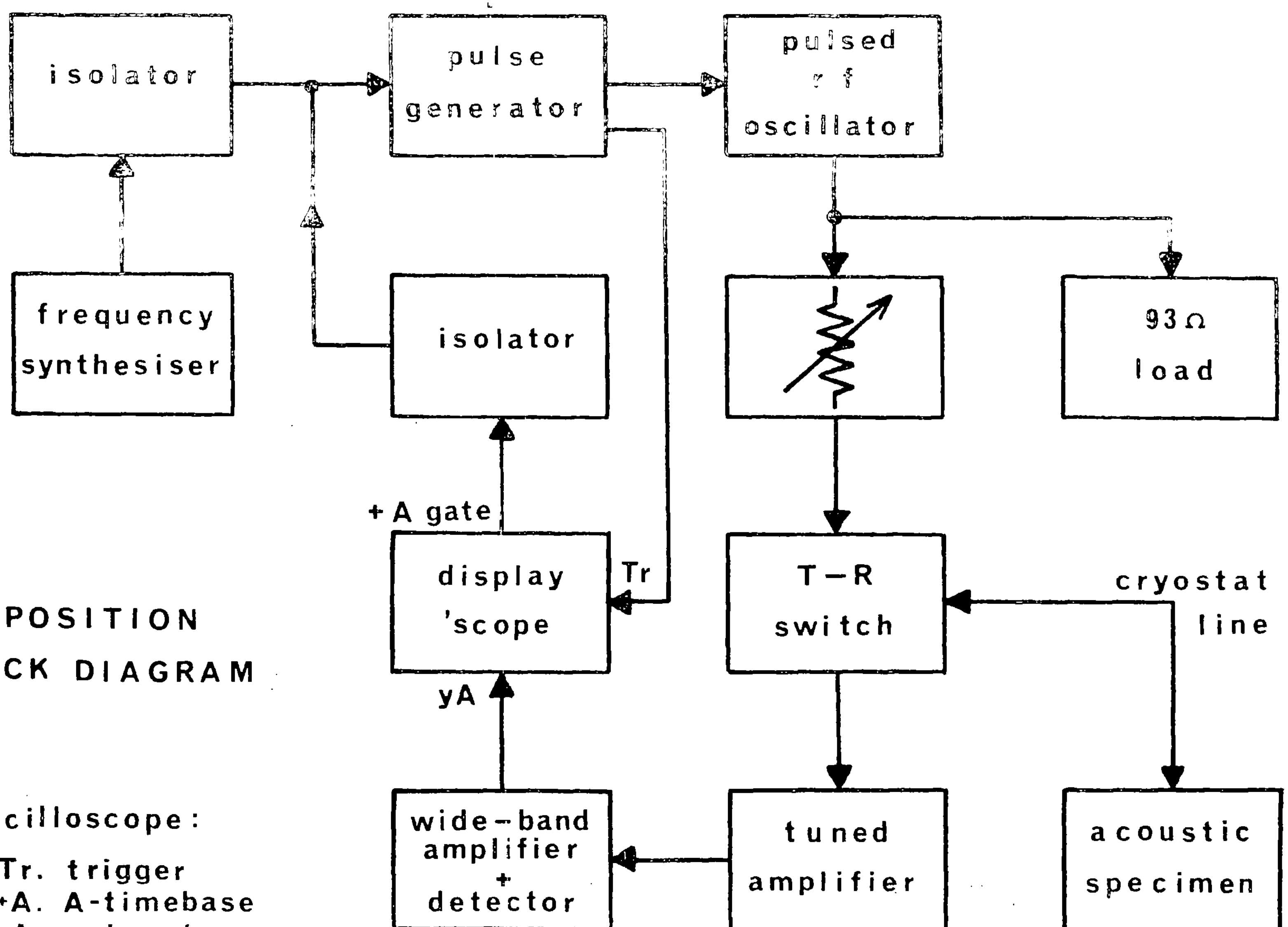

Figure 4.17

PULSE SUPERPOSITION SYSTEM BLOCK DIAGRAM

oscilloscope:

Tr. trigger
+A. A-timebase
yA. y-input

The first step in a determination of sound velocity by the pulse superposition method was to obtain an approximate value for the transit time of the sound pulse in the sample using the pulse echo method. Either a calibrated delay or a direct comparison of the echo train with the frequency synthesiser output was used to determine that time. Hence the approximate PRF needed for superposition could be found, taking account of the limitation on the rf oscillator mentioned above. With the rf generator tuned to the resonant frequency of the transducer and the repetition frequency set at the calculated value, the rectified amplifier output was displayed on a Tektronix 585A oscilloscope using the 'B' timebase. A few of the rf pulses were intensified on the screen by the 'A' time-base, and using the 'B intensified by A' mode of display. A gating pulse, which appeared for the duration of the intensified, or 'A' sweep, served to bias off the rf pulse generator; this resulted in there being no pulses applied to the transducer for that time. Consequently the ultrasound energy in the sample was able to decay away somewhat, and a more complete set of echoes was seen. Figure 4.18 shows the appearance of the display. The PRF could then be adjusted to obtain the maximum amplitude of these echoes, and thus to find the superposition condition. The 'A delayed by B' mode of operation on the oscilloscope eased this adjustment.

Once set up there was no need to change from this last display mode during the course of a set of measurements in which sound velocity was measured as a function of temperature. In practice there were several maxima in close proximity.

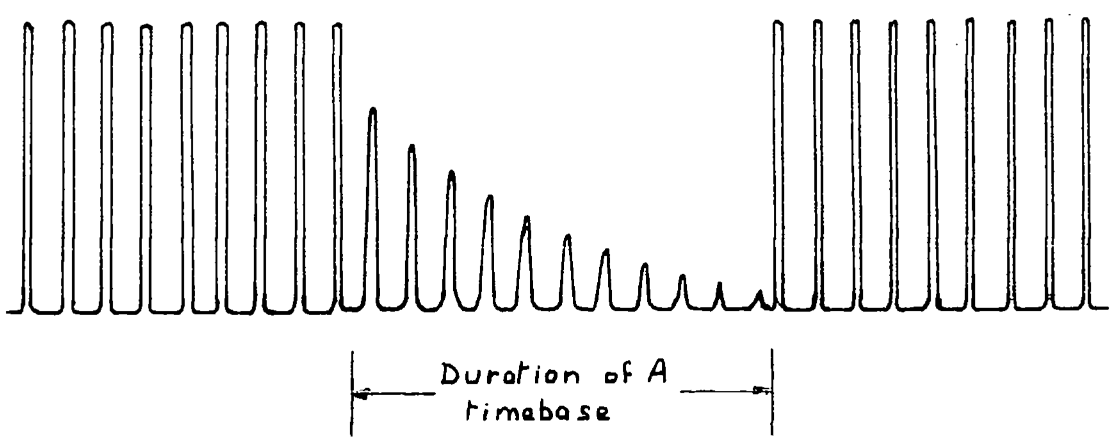

Figure 4.18 The appearance of the oscilloscope trace at or near superposition of echoes.

4.5.2.4 Determination of correct maximum

Each pulse transmitted to the transducer and sample consisted of a number of cycles of rf energy, and the reflected pulses within the sample had a similar form. To get the correct overlap the phases in the overlapping pulses had to correspond. However, it was possible to obtain overlap in which phases differed by a multiple of 2π with respect to the start of the pulse (figure 4.16). One of the main sources of difficulty lay in the determination of the correct overlap condition, that is, when $n = 0$. In this connection it is instructive to calculate the change in PRF corresponding to a change in n of 1, using typical figures for ultrasound frequency (f) and transit time (δ). Let the period of the pulses be T, where $T = 1/PRF$, and let a dashed symbol correspond to the value of a quantity when n is increased by 1. If p, δ, f and phase angle γ in equation 4.1 are unchanged, then $n' = n + 1$ and $T' = T + 1/f$. This leads to an expression for the fractional change in PRF

$$\frac{PRF - PRF'}{PRF} = 1 - \frac{f}{PRF + f} \quad . \qquad (4.2)$$

Take $f = 1.5\times10^7$ Hz and $PRF = 2\times10^5$ Hz. Then the fractional change in PRF is 2/152, or about 1.3% . Consequently, if the transit time could be measured initially using the pulse-echo method to an accuracy of 1% , the superposition maximum which corresponded to the correct transit time and, implicitly, to the $n = 0$ condition, could be identified. In practice the one required was usually quite easily distinguishable from the others by this method.

4.5.2.5 Errors in velocity measurement

Errors in the measurement of sound velocity by the pulse superposition method fall into three main categories; the error due to phase changes at the sample-bond interface, and affecting the measured PRF through γ in equation 4.2; the error arising from diffraction caused by beam divergence and an error arising from the uncertainty in ultrasound path length. Maynell (1972) has considered these various sources of error, and has shown that for the type of bonding materials, sample thicknesses and ultrasound frequencies used in this work the combined effect of the first two leads to an error of about 0.02% in the velocity, whereas the effect of the last, that is, of path length uncertainty, can be much greater. We therefore consider that error source in more detail.

The ultrasonic path length depends on the thickness of the sample, which is itself dependent on the temperature at which it is measured. Determination of sample thickness was made at room temperature using both a dial gauge and a micrometer; an average was taken of a number of measurements of thickness made at various positions over the area subsequently covered by the transducer. A typical result for a thickness was 0.3363 cm, standard deviation 0.0002 cm, or 0.06%. The systematic error arising from the calibration of the instruments was less than this when checked against a set of gauges. At other temperatures the change in dimensions owing to thermal expansion had to be considered. Where a correction has been made it is indicated on the appropriate graphs, but was approximately 0.25% per 100 degrees Kelvin from room temperature.

Thus the minimum error at room temperature was about 0.08%, but in order to achieve this accuracy there had to be a reasonable number (≥20) of well-formed echoes. If the attenuation was high enough to reduce the number available, then the initial transit time measurements could vary by up to about 2%, in the worst cases. Whatever the quality of the signal there was always the problem of determining the n=0 condition, as discussed in 4.5.2.4. Taking all this into account an overall accuracy of 0.5% could be put on the sound velocity results obtained.

The pulse superposition method was used in this investigation because of its ability to detect small changes in velocity, that is, its high precision. The precision obtained still depended on the quality of the echo train, but changes of 1 part in 10^5 could usually be detected, while those as small as 1 or 2 parts in 10^6 could be seen under good experimental conditions. Thermal expansion had a much more pronounced effect when the way in which a velocity changed with temperature was considered.

4.6 Ultrasonic transducers and the acoustic bond

The most convenient method of conversion of rf energy into ultrasound at megahertz frequencies is the use of a piezoelectric material. The main factors affecting the suitability of any particular piezoelectric substance are the magnitude of the electro-mechanical coupling coufficient, the mechanical strength of the material and the ease with which it can be prepared in a suitable form. Quartz has an electro-mechanical coupling coefficient of 1.2×10^{-12} coulomb newton^{-1}, which is not as large as that of, say, $LiNbO_3$ or $BaTiO_3$, but its superior mechanical strength makes it the most common material for transducers. Quartz transducers are usually either 'X-cut' or 'Y-cut', to propagate compressional or transverse waves, respectively. The X or Y indicates the axis of a quartz crystal perpendicular to which the transducer face lies. The shear transducers had a small 'flat' cut from their cicumference to indicate the particle displacement direction. The transducer dimensions and electrode configuration were as shown in figure 4.14; the diameter was limited by the size of the specimens.

A transducer is typified by its resonant frequency, which is determined by its thickness and its elastic properties. The transducers used in this work had fundamental frequencies of 10, 12 or 15 MHz. Odd harmonics of these frequencies could also be generated.

Very little energy transfer occurs at a solid-air interface, so an acoustic bonding material is needed to couple the transducer to the sample. For this purpose various viscous substances are used, such as greases, silicone oils and resins. Each type of material has its own characteristics, and for a particular sample and temperature range a process of trial-and-error is needed to select the best one to use. For bonding transducers on to indium-thallium alloys a stopcock grease 'Nonaq', distributed by the Fischer Scientific Company, was found to give the best results; its disadvantage was that it was hygroscopic. Nonaq gave a good bond in the temperature range 4 to 300K. Above 300K the decrease in its viscosity caused deterioration in the quality of the acoustic bond, and a silicone oil, of viscosity 60 000 cs, was used for such temperatures.

4.7 Sample holders and cryostats

4.7.1 Sample holders

A sample holder for ultrasonic work must be able to support the specimen, and provide an electrical contact on to the centre electrode of the transducer whilst earthing the outer one. The sample holders used in this work each consisted of a horizontal circular brass platform, which could slide along three vertical rods passing through holes 120° apart near the circumference, and on which was placed the sample. Adjustment of a screw enabled the platform and sample to be raised until contact was made between the centre electrode and a small spring-loaded copper plunger. Springs and collars supported the platform so that the screw could be tightened until sufficient pressure was applied to keep the sample in position. Such an arrangement is shown diagrammatically in figure 4.19.

4.7.2 Liquid nitrogen cryostat

4.7.2.1 Design

A cryostat made from stainless steel was designed and constructed with the object of being able to control sample temperatures in the range 77K to 300K; provision was made for reducing the pressure in the sample chamber with a rotary pump, while a diffusion pump was used to evacuate the interspace. The interspace pressure was indicated on a Pirani gauge. Figure 4.20 illustrates the sample holder and heater assembly:

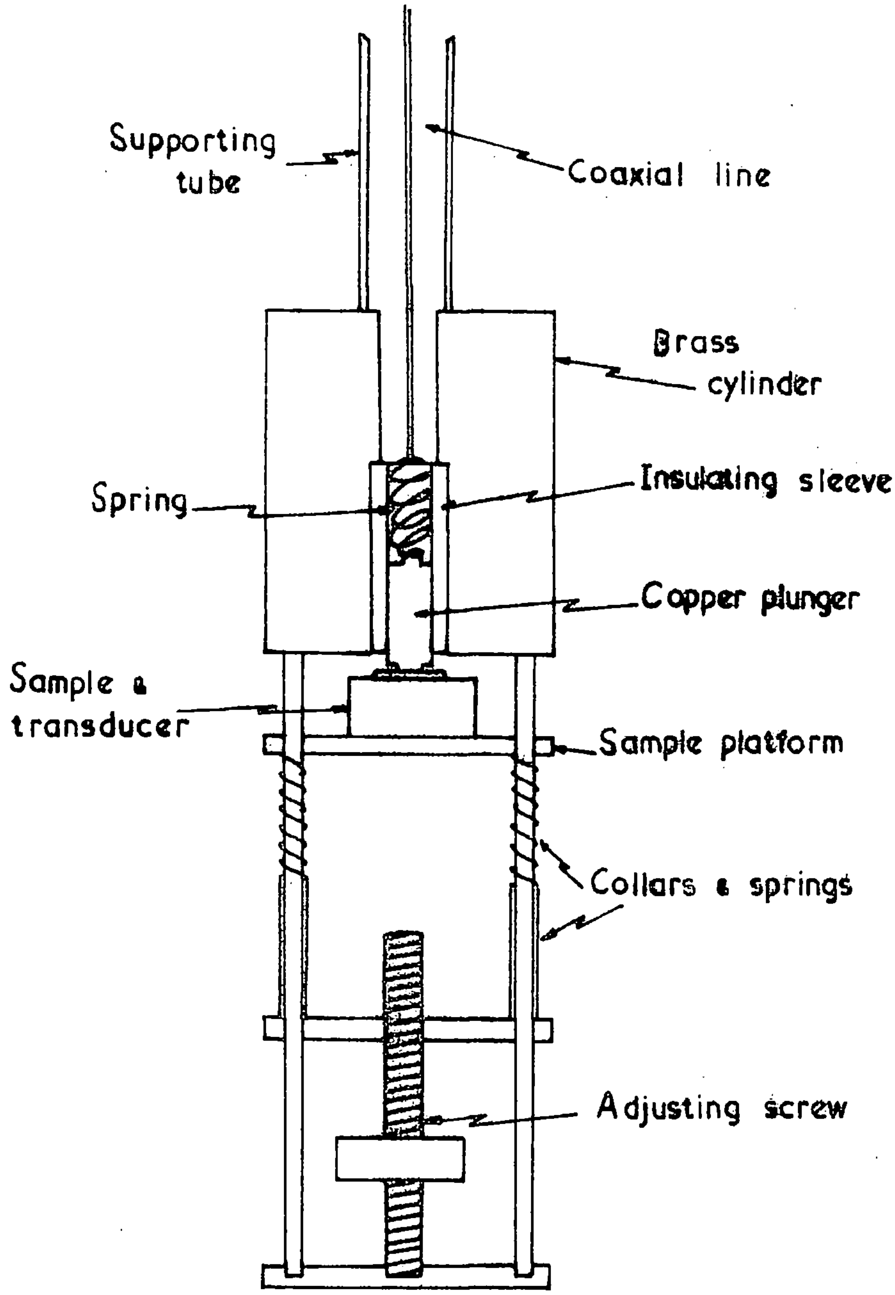

Figure 4.19 Schematic diagram of a sample holder for ultrasonic studies.

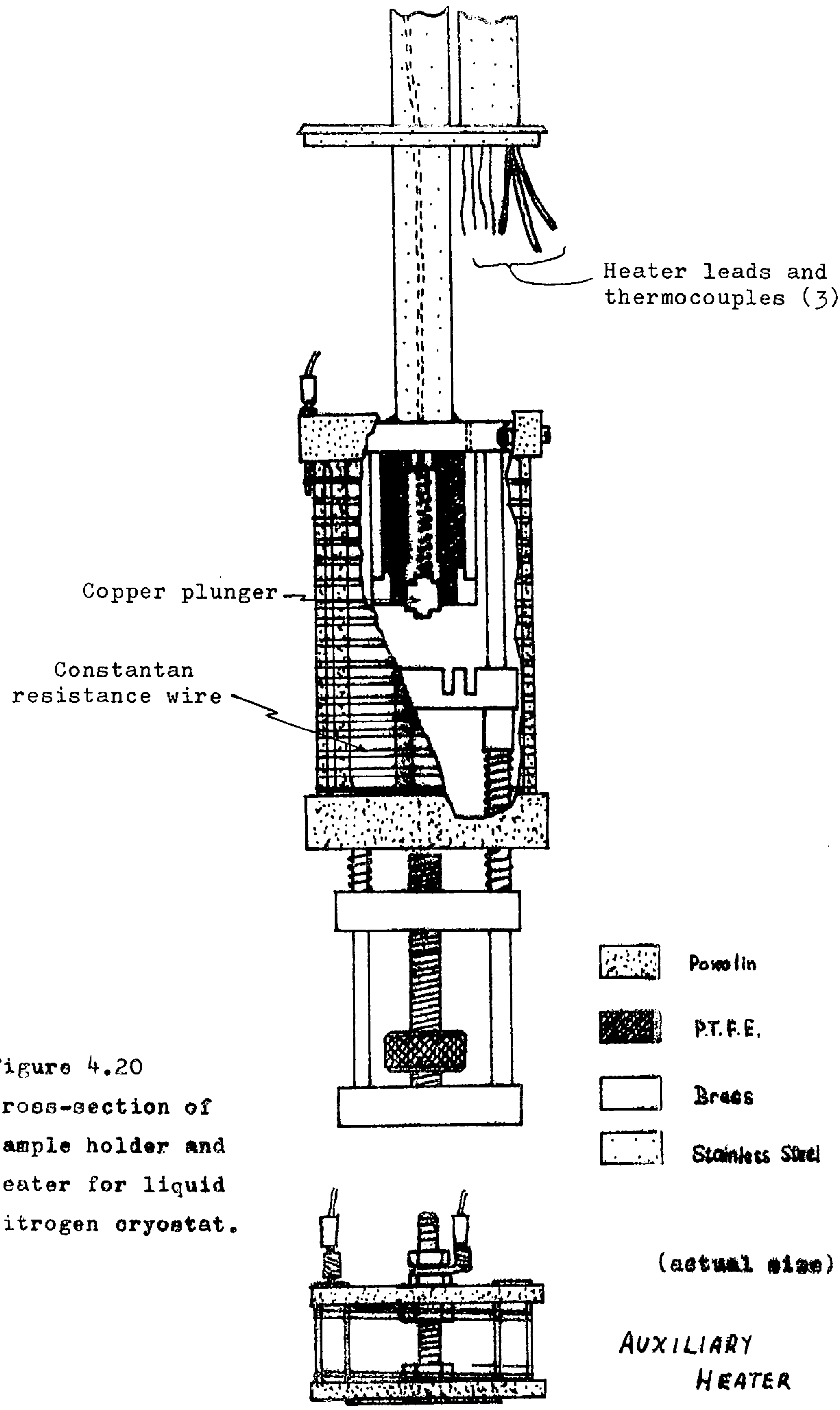

Figure 4.20
Cross-section of
sample holder and
heater for liquid
nitrogen cryostat.

The heater was wound non-inductively on a paxolin former, and three nylon grub screws held it in position so that the sample was at its centre. Constantan wire of such a length as to give a resistance of 300Ω was used, and electrical connections were made using two small plugs. An auxiliary heater, powered by a variable a.c. supply (maximum 15 volt) was available when necessary to increase the rate of evaporation of the liquid nitrogen from beneath the sample.

4.7.2.2 Temperature control

Heater current was provided by a Harwell temperature controller; control was achieved by comparing the e.m.f. of a thermocouple with a pre-set reference voltage. The current supplied to the heater depended on a combination of the difference between the thermocouple and reference e.m.f.'s and the time rate of change and the integral of the measured e.m.f. In this way overshoot of temperature could be avoided, and it was possible to maintain a temperature steady to $\pm$ 0.01K for a period of an hour or more. Various internal adjustments were made to the integrator and differentiator circuits in the controller to compensate for the thermal inertia of the cryostat and thus to prevent overshoot.

4.7.2.3 Operation

Three copper-constantan thermocouples were attached to the sample so that the presence of temperature gradients could be detected. A calibration curve was produced for each one (see 4.8.2). It was found that the 300Ω heater with a maximum heat output of 15W was not able to maintain a temperature difference between the sample and the outer shell of more than 150K. In order to achieve a rate of cooling of about 50 degree per hour, together with control possible at all temperatures the pressure in the interspace had to be carefully controlled with a needle valve.

Measurements could be made over the temperature range 300K to 90K by immersion of the outer shell in liquid nitrogen. For temperatures lower than 90K it was necessary to add liquid nitrogen to the sample chamber, and to lower the pressure within it to obtain a further reduction to 55K. Control of temperature using the heater was not possible below 77K.

4.7.3 Glass cryostat and pumping system

A glass dewar system was used for measurements to 4.2K and below. The sample holder was similar in design to that in figure 4.20, except that no heater was used, and the supporting tubes were thin-wall stainless steel to reduce heat leaks.

Two dewars were used; one fitted inside the other. The sample holder and specimen could be lowered into the inner one, and a sidetap on the inner one enabled a rotary pump to produce an interspace pressure of about 0.05 torr. The outer dewar was open to the atmosphere whereas the inner one was connected to a brass head by means of a vacuum tight rubber sleeve, and thus the pressure within the sample chamber could be reduced. The pumping system is illustrated in figure 4.21. Mercury and oil manometers measured the pressure in the sample

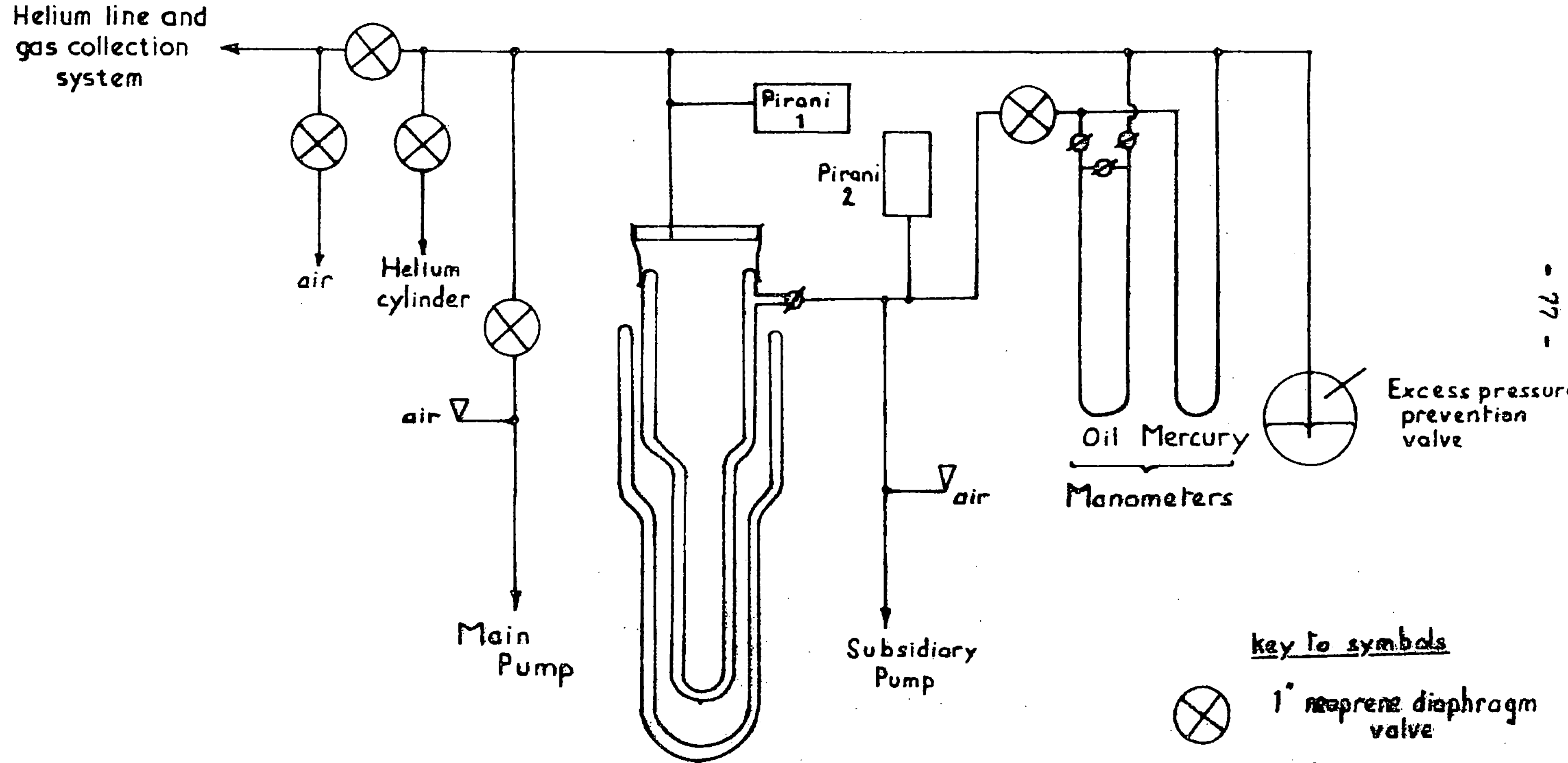

Figure 4.21 Pumping system for liquid helium cryostat.

chamber: when temperatures below 4.2K were produced by a reduction of pressure above the liquid helium, the temperature was found from a measurement of the vapour pressure.

4.8 Temperature measurement

4.8.1 Thermocouples

Copper-constantan thermocouples were used throughout, with junctions formed by electrically spot-welding the two wires (40 SWG) together. For the nitrogen cryostat with the temperature controller a reference junction at a higher temperature than the sample was needed, and an ice/water mixture was used. In the helium system a liquid nitrogen reference sufficed.

4.8.2 Calibration

Four calibration points were found for each thermocouple and a cubic equation of the form

$$V = AT^3 + BT^2 + CT + D \qquad (4.3)$$

was fitted, as suggested by White (1959). A least mean squares quadratic fit to the four points was also tried, and the results compared with the form of the curve obtained from the British Standards Thermocouple Tables (Copper-Constantan). It was found that in the cubic fit the coefficient of T^3 was small, so that either a cubic or a quadratic fit would have been acceptable. No standardised temperature measuring device was available to check the accuracy of calibration, although White gives the accuracy for a cubic fit as 0.1K between 73K and 273K.

The calibration points were:

1) 4.2K (liquid helium)

2) 77.3K (liquid nitrogen)

3) 196K (dry ice and acetone mixture)

4) 273.2K (ice and water mixture)

5) $\simeq$300K (water whose temperature was measured with an accurate mercury-in-glass thermometer).

Points (2) to (5) were used for thermocouples on the nitrogen cryostat sample holder, and points (1),(2),(4) and (5) with those for liquid helium use. In addition the voltage developed when both junctions were at the same temperature was measured and gave the coefficient D in equation 4.3. In all cases this e.m.f. was small ($< 5\mu V$).

4.8.3 Thermocouple leads and connections

If a thermocouple lead is not continuous to the potentiometer then there is always the possibility that an additional e.m.f. will be produced at the junction with another wire. Wherever possible the copper leads were taken directly to the measuring potentiometer terminals, and were always sheathed by PVC tubing to reduce the risk of their breaking. When a connection had to be made it took place outside the cryostat where the temperature gradients were small, and was done by putting both wires together under a screw terminal with no attempt at soldering. No ill effects were found using this method of connection on the nitrogen cryostat; the leads left the sample holder through a neoprene vacuum seal.

4.9 High temperature measurements

For measurements on indium-thallium alloys in the temperature range 300K to the melting point ($\simeq$425K) the sample holder and specimen were immersed in a bath of oil. A 1.5 KW main heater and a 60 W thermostatically controlled subsidiary one acted as heat sources. Fluctuations of temperature throughout the bath were reduced by a motor driven stirrer. Temperature measurement was by mercury-in-glass thermometers: up to 145^{o}C a conventional -30^{o}C to +200^{o}C type sufficed, but from 145^{o}C to just below the melting point of the alloys a Beckmann type of thermometer was used. The latter incorporated an adjustable electrode in the capillary above the mercury column; when the lower end of this electrode made contact with the mercury meniscus an electrical circuit was completed and a relay switched off the 60 W heater. Temperature control to $\pm \frac{1}{2}^{o}$C could be achieved in this way.

4.10 Measurement of thermal expansion

4.10.1 The strain gauge method

The thermal expansion of a cubic material is isotropic, while for tetragonal crystals the thermal expansion tensor has two components, α_{11} and α_{33}, which relate the strain along the x (or y) and z axes, respectively, to the temperature change producing that strain. Thus a single measurement is needed for crystals of cubic symmetry, whereas the expansion in two particular directions is required in the case of tetragonal crystals. A d.c. strain gauge method was used to measure the thermal expansion coefficients of indium-thallium alloys. The gauges were in the form of thin foil mounted on a thin plastic base. Two sizes were available: 2 by 1 mm and 2 by 8 mm, and the nominal gauge resistance of each was 120Ω. The gauges were attached to the alloy crystals by means of an epoxy resin adhesive. Pressure was needed while the glue was setting in order to obtain a uniformly thin film of adhesive beneath the gauge; failure to do so resulted in the glue cracking when cooled. On the tetragonal samples the gauges were oriented along the y and z directions of a (100) cut sample. The principle behind the strain gauge method is that a change in length of the gauge alters its electrical resistance, and such change is related to the change in length by the gauge factor. Thus a measurement of gauge resistance as a function of temperature enables the coefficient of thermal expansion appropriate to the orientation of the strain gauge to be found.

4.10.2 Bridge circuit

A resistance bridge was used to determine the change in gauge resistance, and the circuit was a modified form of that described by Chatterjee (1972). In essence it was a Wheatstone bridge with equal resistances in the ratio arms, and strain gauges in the other two. One gauge, attached to a piece of silica glass, served as a reference, while the other was attached to the sample. (In practice, the two gauges were close together on the sample holder to keep them at the same temperature.) Connected in parallel with the two gauges were two variable resistors of much larger value, and any small change in the resistance of a gauge caused by a strain led to an out of balance current in the bridge; balance was restored by adjustment of one of the parallel resistors. The circuit is shown in figure 4.22. Potentiometers P1 and P2 were ten-turn helipots each of total resistance 100KΩ. The potential divider D could be adjusted to compensate for any initial out-of-balance due to any slight difference in the gauge resistances. Potential divider T allowed for compensation to be made for the effects of thermal e.m.f. developing in the connections to the gauges; across T was connected a thermocouple with its junctions in water and liquid nitrogen. In this way a variable e.m.f. of up to about 6mV was available to back off the thermal voltage in the gauge leads. S1 and S2 were 2-pole 6-way switches ganged together to select different modes of operation, including reversal of the bridge current.

The potentiometer P1 and potential dividers T and D were duplicated on a separate mounting so that a second gauge on the sample could be used, allowing measurement of thermal expansion in two different crystallographic directions almost simultaneously. The second unit could plug in to the main one when required, and a 6-pole 2-way switch transferred the necessary connections. (It is not included in figure 4.22.) The functions of the six positions of S1/S2 were as follows.

Position	Function
1	Galvonometer shorted; no current applied to bridge.

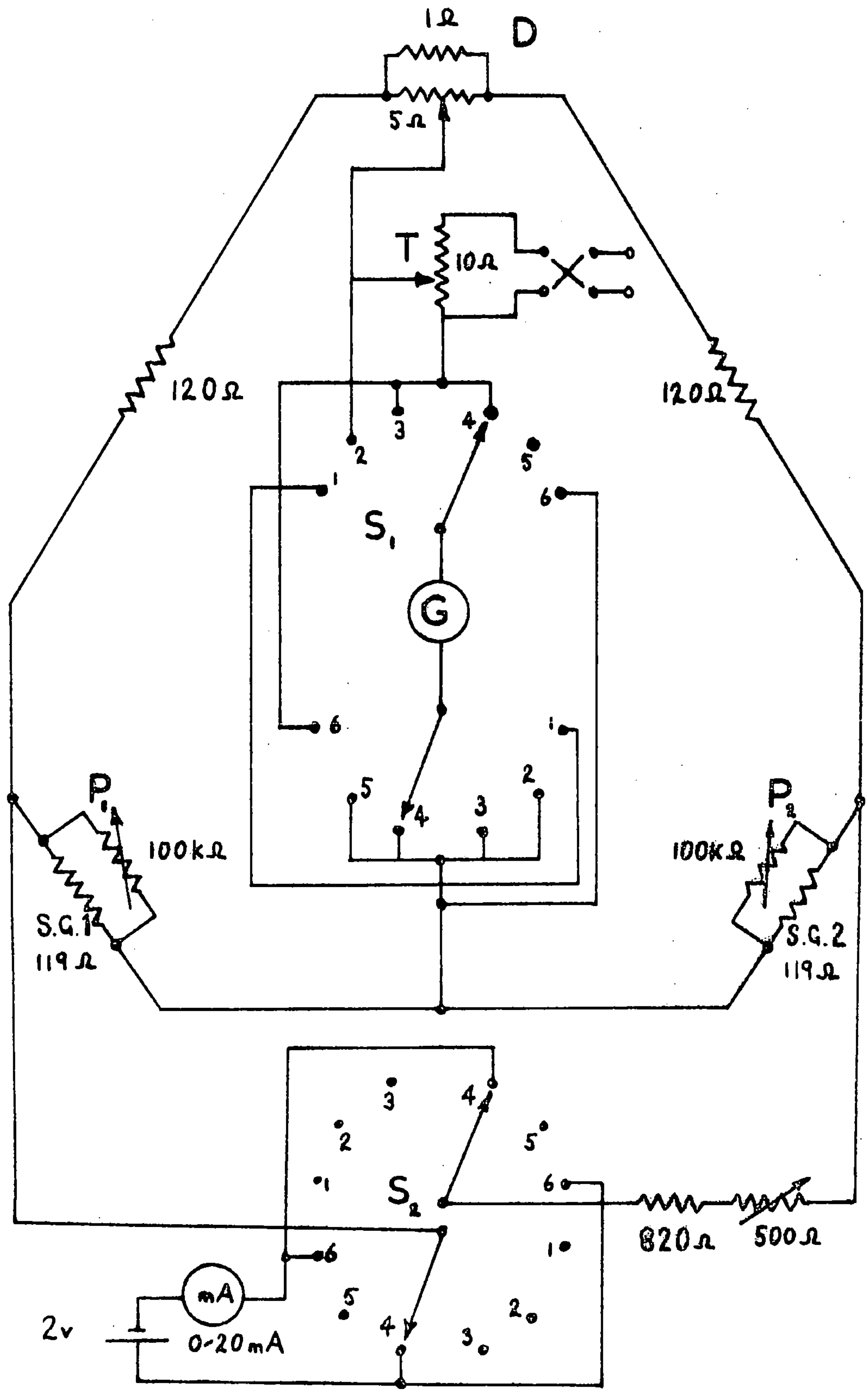

Figure 4.22 Strain gauge bridge used in measurement of thermal expansion.

Position	Function
2	Galvonometer in circuit; no current applied; any deflection due to thermal e.m.f.
3	No current applied; thermal e.m.f. back-off potentiometer in circuit.
4	As 3 but current supplied from a 2 volt accumulator.
5	Galvonometer open circuit.
6	As 4 but current through bridge reversed.

4.10.3 Sample holder

The sample holder was of simple construction, and consisted of a square copper platform of side one inch with a small terminal block along one edge. It was attached to a 3/16" diameter copper rod at one corner, which in turn led to a wooden post. The platform was horizontal and the rod and post were vertical, and the whole assembly could be lowered into the stainless steel cryostat. To prevent unnecessary strains the sample and silica reference rested on the platform and were only held in position by the leads of the strain gauges. Temperature measurement was by copper-constantan thermocouple.

4.10.4 Operation

Initial balancing of the bridge was performed with sample and reference at room temperature, and with P1 and P2 set at the same value, usually 90KΩ. D was then adjusted to give a balance, and thereafter no change was made to its setting. At any other temperature the procedure was as given below.

i)	Switch position	2	Observe any thermal e.m.f.
ii)	"	3	Adjust T until galvonometer deflection is zero, and thus back off thermal e.m.f.
iii)	"	4	Adjust P1 or P2 to obtain balance. The galvonometer zero could be checked using switch position 5.
iv)	"	6	Reverse current and check that deflection is the same as in (iii).

If the deflections in (iii) and (iv) were appreciably different it was usually owing to an unbalanced thermal e.m.f. and step (ii) was repeated.

The gauge factor is defined as the ratio of the strain to the resulting fractional change in resistance of the gauge:

$$K = \frac{\Delta l/l}{\Delta r/r}\ .$$

If ΔR is the change required in the appropriate parallel resistor to restore the balance, then solution of the bridge equation gives

$$\frac{\Delta r}{r} = \frac{r\Delta R}{R(R + \Delta R) - r\Delta R}$$

where R is the initial value of the parallel resistance. Since $R(R+\Delta R) \gg r\Delta R$, the strain is given by

$$\epsilon = \frac{\Delta l}{l} = \frac{r}{K}\frac{\Delta R}{R(R + \Delta R)} \qquad (4.4)$$

Thus a graph of strain against temperature could be constructed, and the coefficient of thermal expansion at some temperature was given by the gradient of the strain curve at that temperature, for

$$\alpha = \frac{\partial \epsilon}{\partial T}\ .$$

CHAPTER 5

EXPERIMENTAL RESULTS

Introduction

The results of experimental measurements on indium-thallium alloys are presented in three sections. Firstly, the thermal expansion behaviour is described; secondly, the sound velocity and elasticity measurements and thirdly the results of attenuation studies for the various alloy compositions considered. A discussion of the sources of error in the measurement of attenuation is included in the third section.

5.1 Measurements of thermal expansion in In-Tl alloys

Measurements of thermal expansion were made in both cubic and tetragonal alloys using a strain gauge technique, as described in section 4.10 . For the tetragonal compositions 11.5 and 15 at.% Tl the strain was measured in the [100] and [001] directions over the temperature range 150 to 425K, and the results are shown in figures 5.1 and 5.2 . A small amount of hysteresis was observed at temperatures near the melting point: the results shown for temperatures above 300K were obtained during heating. In the cubic alloy measured (25 at.% Tl) the strain gauges were attached so as to record the strain in the [100] and [110] directions. Measurements were made over the range 150 to 300K and the results are presented in figure 5.3 The extent of the hysteresis in thermal expansion near the martensitic transition can easily be seen. For a

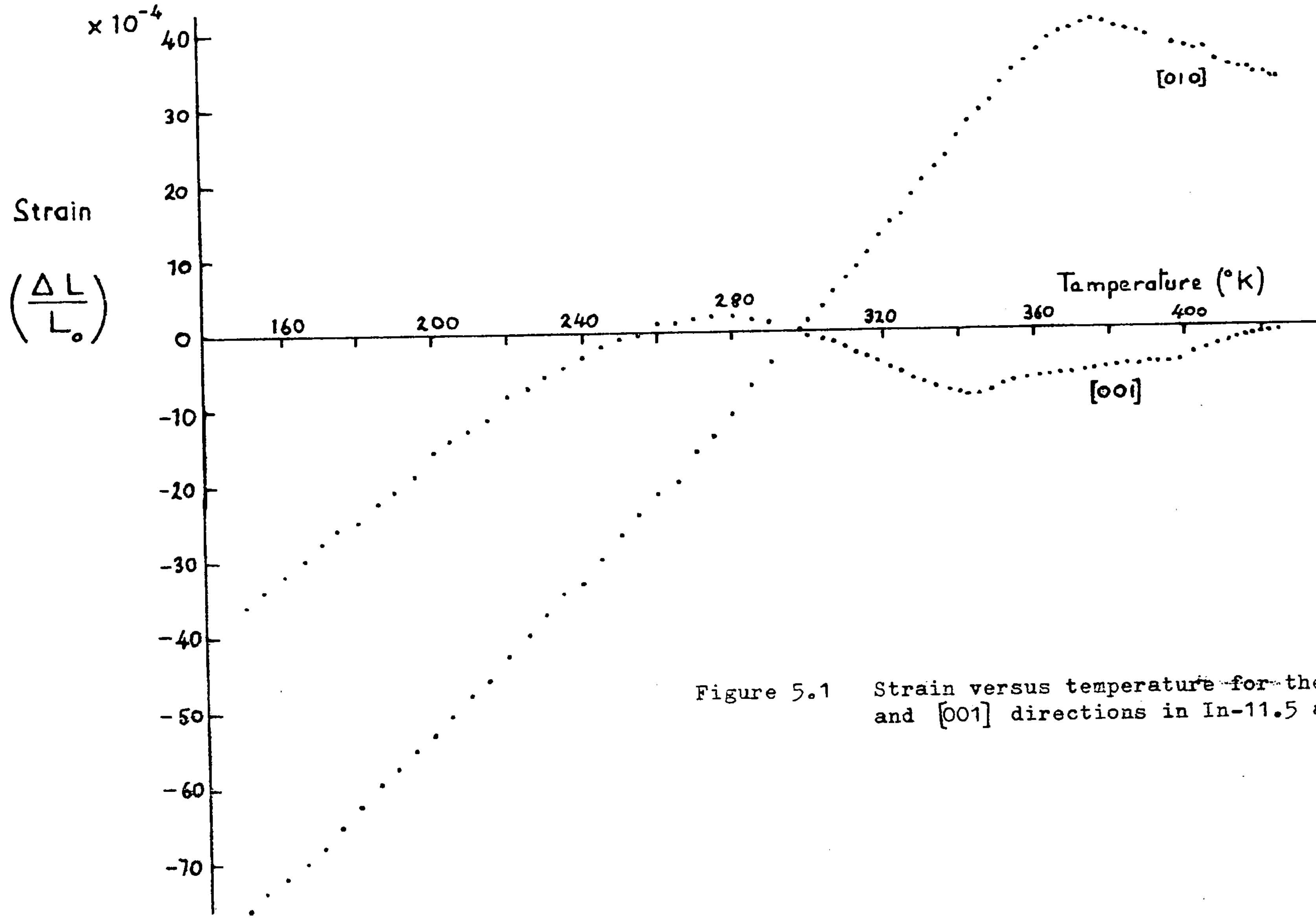

Figure 5.1 Strain versus temperature for the [010] and [001] directions in In-11.5 at.% Tl.

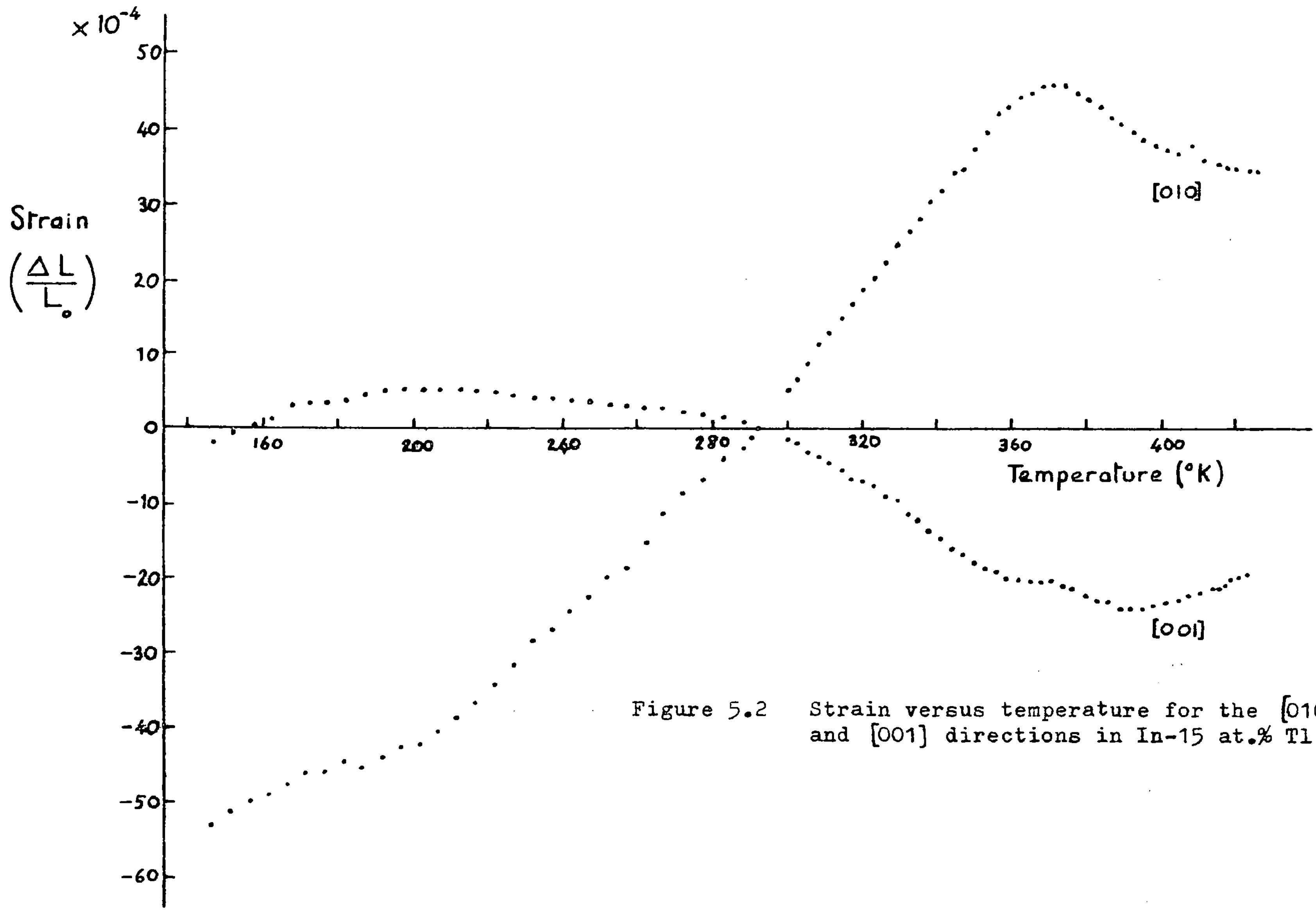

Figure 5.2 Strain versus temperature for the [010] and [001] directions in In-15 at.% Tl.

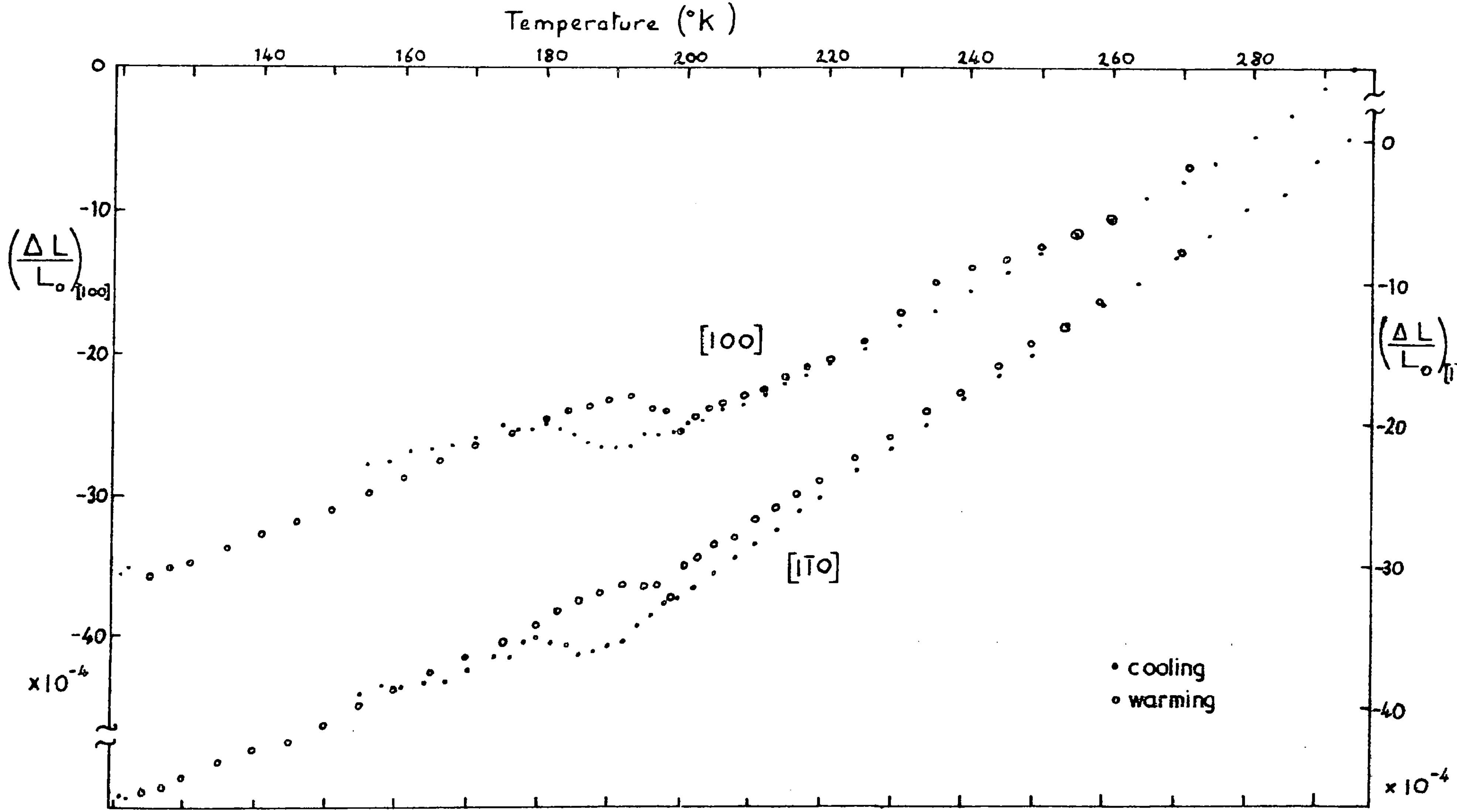

Figure 5.3 Strain versus temperature for the [100] and [$1\bar{1}0$] directions in In-25at.% Tl.

cubic material the thermal expansion is isotropic: the difference in the slopes of the [100] and [110] curves in the cubic region of figure 5.3 is a factor of 1.2, and this could be due to a difference in the gauge factors of the two gauges. (The manufacturers give a figure of 2.04 for the gauge factor.)

All these measurements were made with reference to the expansion of a gauge attached to a piece of silica glass. Scheel and Heaus (1914) give the expansion of silica as

$$L = L_o \left(1 + 0.362\ 10^{-6} T + 1.813\ 10^{-9} T^2 - 3.40\ 10^{-12} T^3 \right) .$$

This gives strains which are smaller than the measured ones for the alloys by a factor of 10^2; therefore, no correction has been made to the curves of figures 5.1 to 5.3. The thermal expansion coefficients α_{11} and α_{33} are shown for the three alloys in figure 5.4. The coefficients have been obtained from the derivative $\partial\epsilon/\partial T$, and the curves of figure 5.4 have been smoothed to reduce the errors which can easily occur when the derivative of an experimental curve is taken.

The accuracy of the strain gauge method is not high, and errors can be as large as 25% (Greenough, 1973, private communication). Several determinations of the strain as a function of temperature were made for each sample, and the measurements were found to vary by up to 15%, although the slopes of the linear regions were consistent to within less than 5%. However, the main use to which the measurements were put — correction of the measured ultrasonic sample thickness for changes due to temperature — meant that such a margin of uncertainty was quite acceptable.

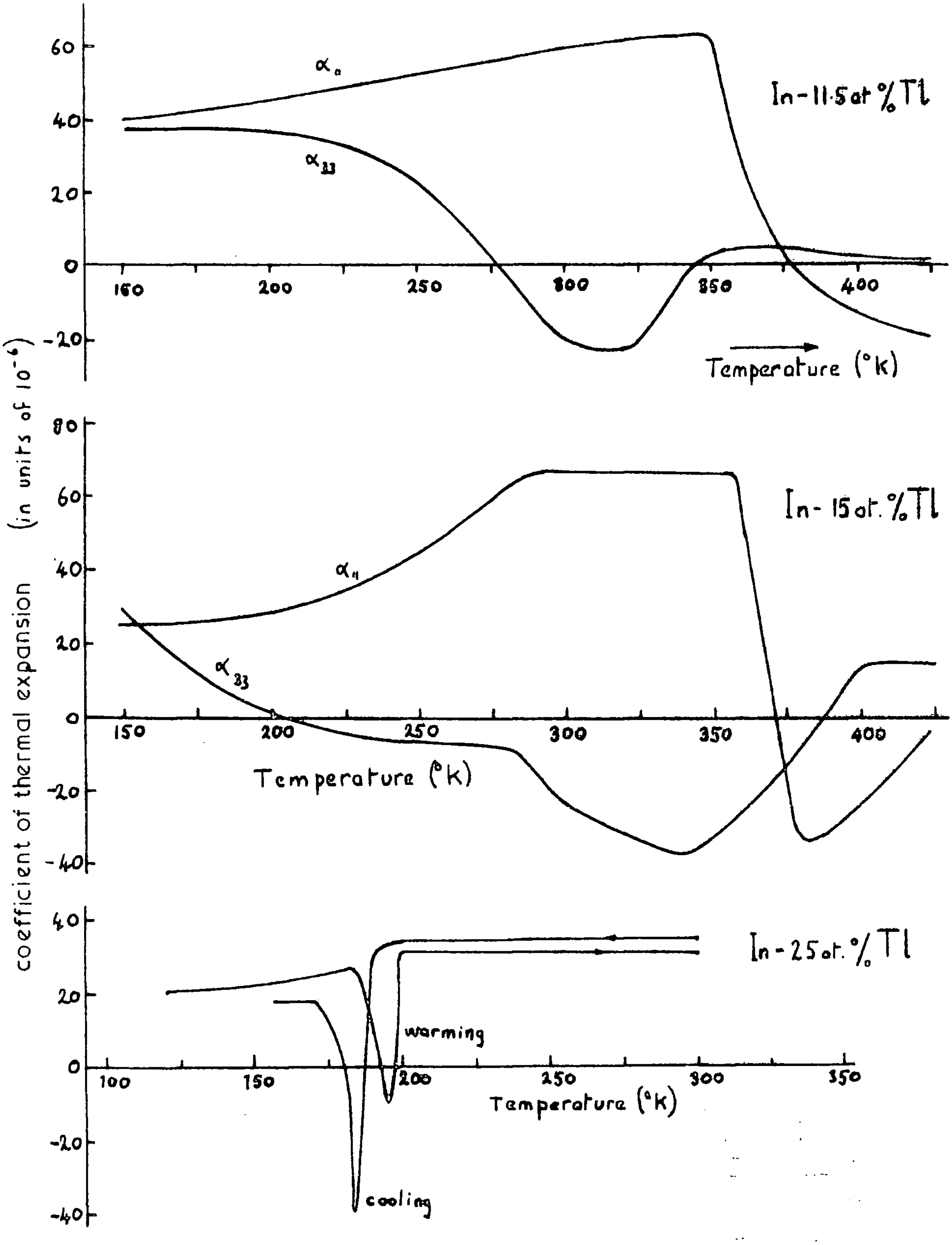

Figure 5.4 Thermal expansion coefficients of In-11.5, 15 and 25 at.% Tl alloys. (The result for 25 at.% is of a different form from that obtained by Pahlman and Smith (1968) and the dip seen here instead of the sharp rise as seen by these workers could be an anomaly associated with the different methods of measurement used.)

5.2 Elastic constants of In-Tl alloys

5.2.1 Cubic alloys

Three independent elastic constants C_{11}, C_{12}, C_{44} are required to determine fully the elastic behaviour of a cubic crystal. Measurements were made of the velocity of ultrasound waves (at about 15 MHz) in (110) and (100) cut samples of the 25 and 27 at.% Tl alloys as a function of temperature. The modulus C_{11} was obtained from the velocity of longitudinal waves in the [100] direction, while C_{44} was given by that of a transverse wave polarised [100] and propagating in the [110] direction. Finally, $(C_{11}+C_{12}+2C_{44})/2$ resulted from measurement of the velocity of a longitudinal wave in the same direction. The modulus $(C_{11}-C_{12})/2$ could also be found directly from a transverse wave polarised $[1\bar{1}0]$ along the [110] direction, although it was only possible to find a value for this modulus at room temperature on account of the high attenuation and low velocity of the mode. Even then its value had an uncertainty of about $\pm$ 10% because the velocity was so low that only two or three poorly defined echoes were available for measurement.

Turning first to the In-27 at.% Tl alloy, we present in figures 5.5 to 5.7 the results of the measured pulse repetition frequencies as the temperature was lowered from 300K to 80K for wave propagation in the [110] direction (longitudinal and [100]-polarised transverse modes) and in the [100] direction (longitudinal mode). The temperature range included the fcc to fct transition region. The precision of the measurements is indicated by the extent of the scatter on

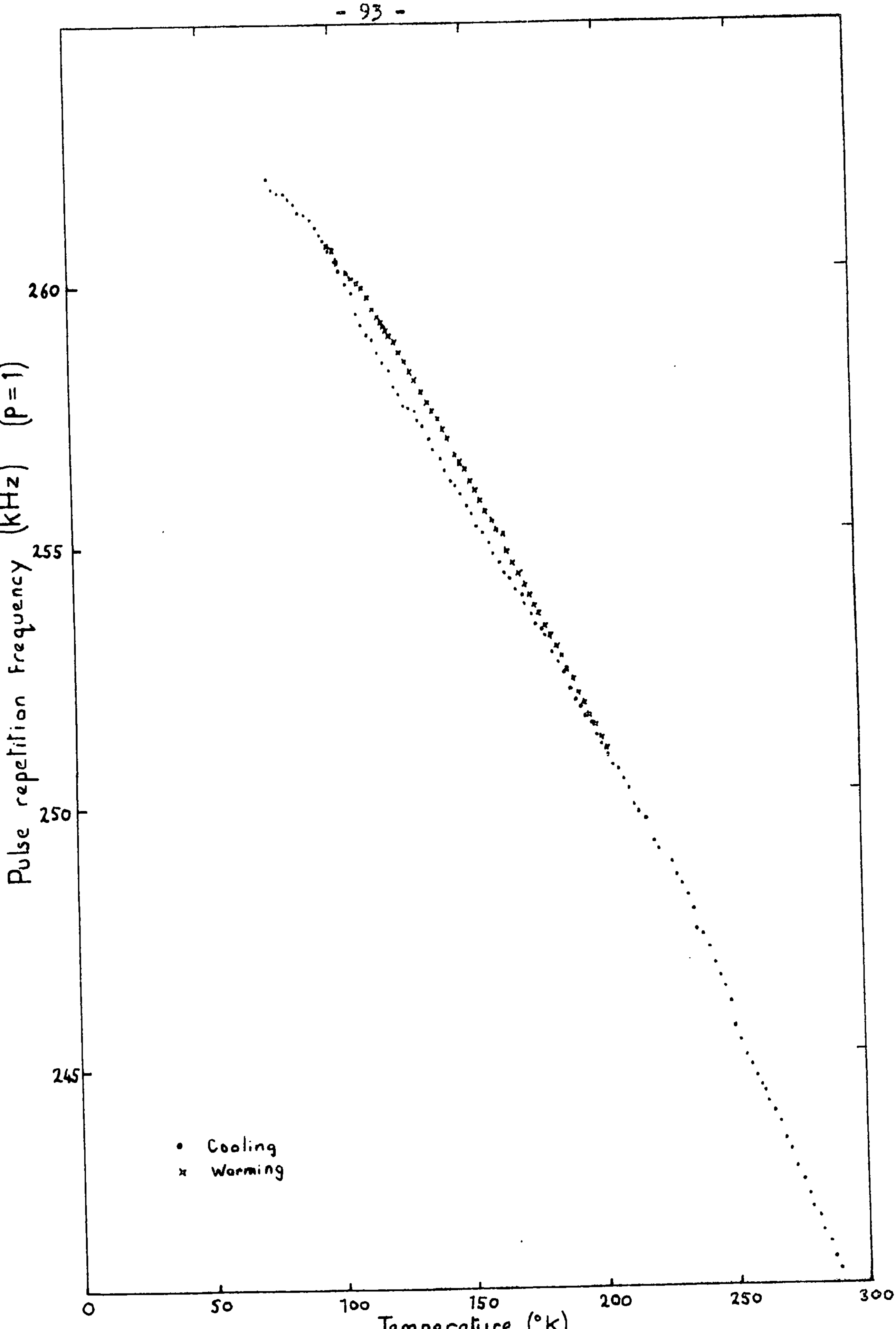

Figure 5.5 The measured PRF for propagation of [001] polarised shear waves in the [110] direction in In-27at.% Tl.

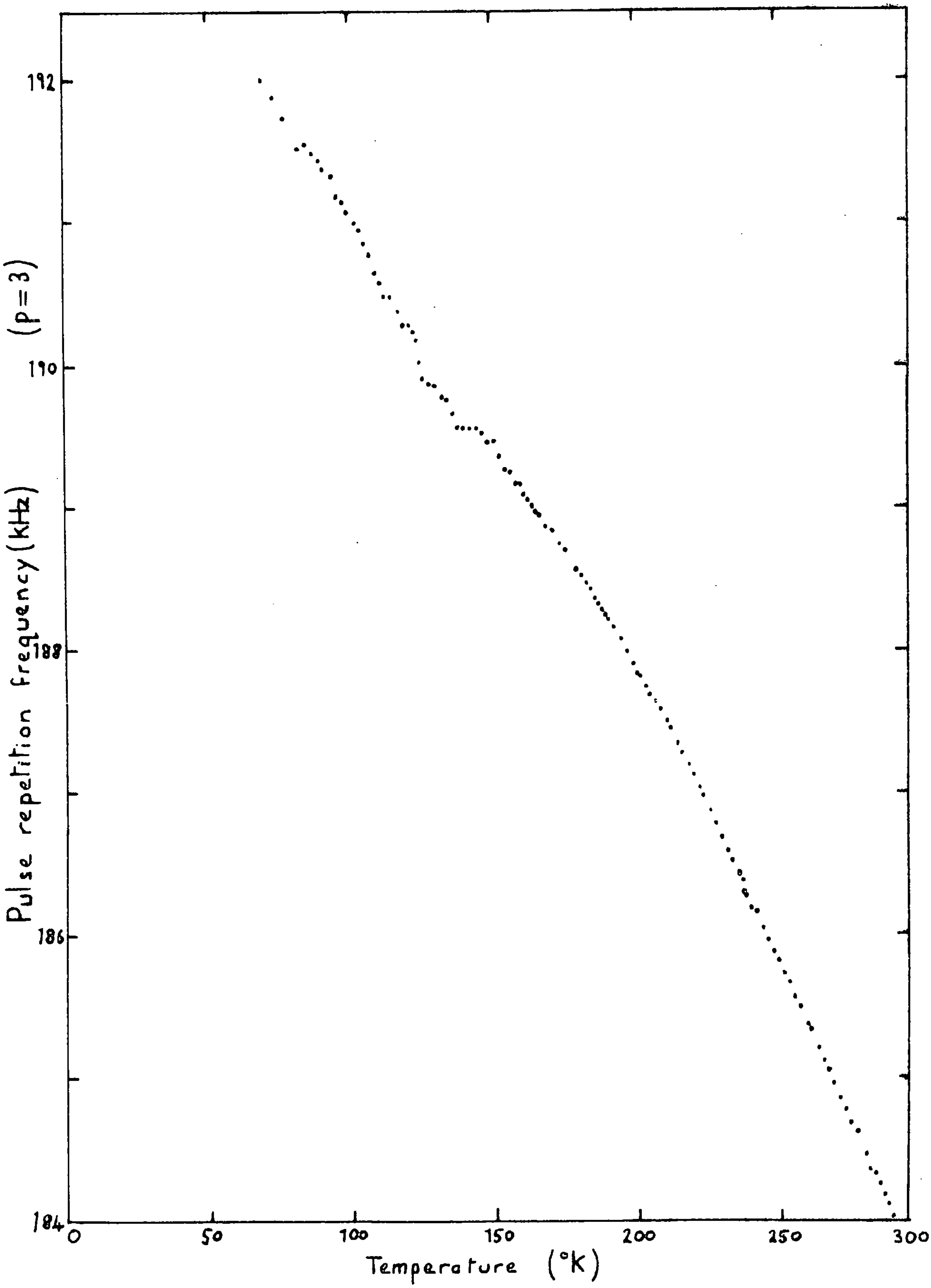

Figure 5.6 The measured PRF for propagation of longitudinal waves at 15MHz in the [110] direction in In-27at.% Tl

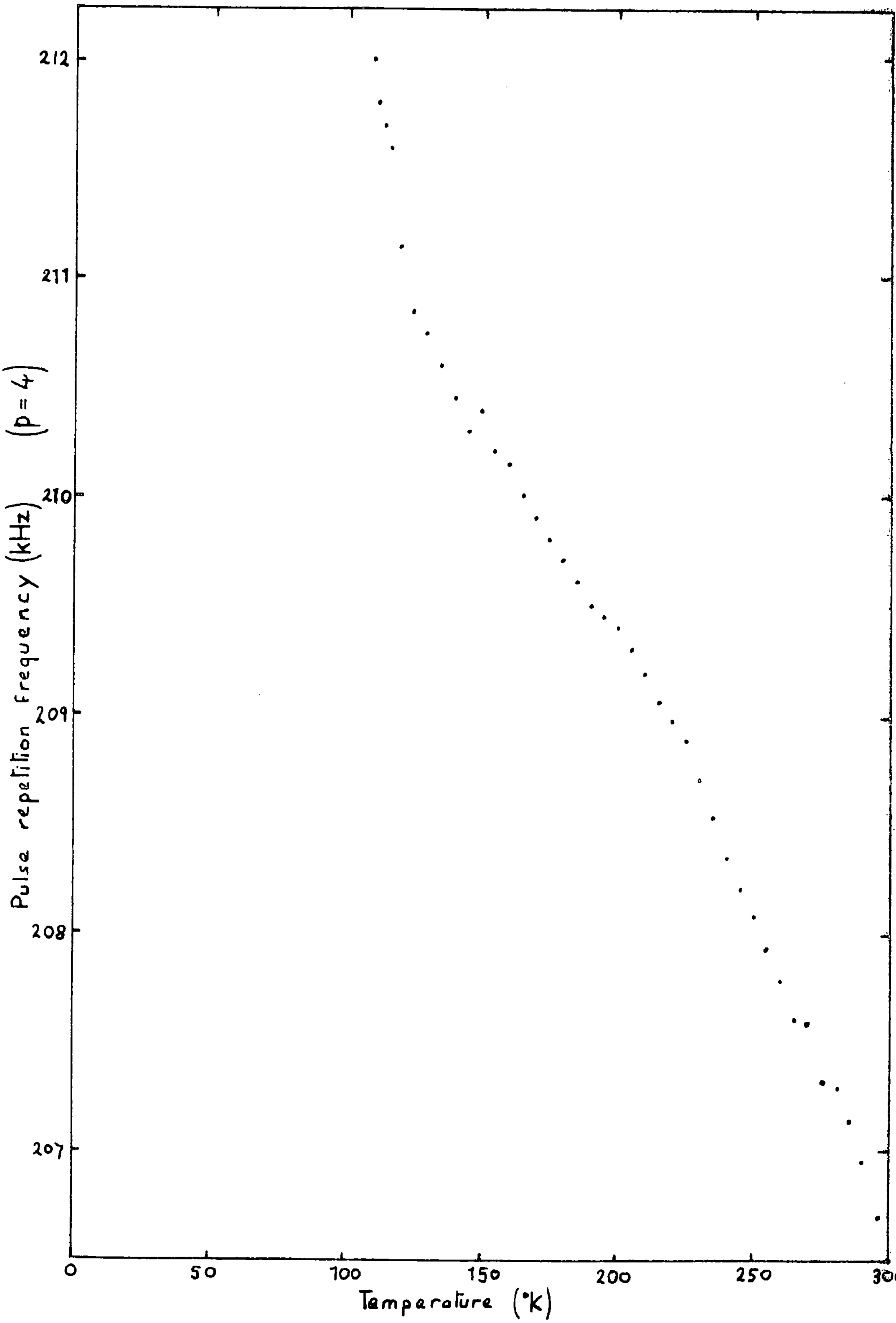

Figure 5.7 The measured PRF for propagation of longitudinal waves at 15MHz in the [100] direction in In-27at.% Tl.

the measured points; the method was sensitive enough to detect the slight depression which is shown in the curves of figures 5.5 and 5.6 and which occurred on cooling over a range of about 30 degrees near to the transition temperature of 125K. This effect was quite reproducible, and was seen on each of several sets of data obtained. At first these results were surprising in view of the large dip seen in the modulus C_{44} by Pace and Saunders (1972), but it was possible to make measurements every 0.5 degrees in the vicinity of the transition using the temperature controller, and it was ascertained that there was, in fact, no discontinuity in the velocity leading to C_{44}. Results for propagation in the [100] direction were not as precise near the transition because of the much higher attenuation encountered in that direction than in the [110]. In practice it was not possible to obtain any results at all until the (100) sample thickness had been reduced to about a millimetre (or about one third of the thickness of the (110) sample).

On the warming cycle there was a slight difference in the variation of measured pulse repetition frequency with temperature in that the slight depression did not appear.

The very nature of the transformation mechanism imposes certain restrictions on the experimental procedures which can be used to obtain sound velocity and attenuation results. The shears producing the tetragonal structure occur on [110] planes, and result in corrugation of the surface. Three (110) samples were examined, and in two cases the acoustic bond between sample and transducer was fractured near the transition temperature, resulting in the loss of the received signal, whereas in the third sample this did not happen. There are six possible habit planes of the $\{110\}$ type, and presumably in the last case the actual habit plane coincided with the cut surface, so that corrugations did not arise. For a (100) surface, which would always become distorted on transformation, a silicone oil bond proved satisfactory, for such a bonding material does not become brittle at low temperatures as Nonaq does, and so it could accommodate the movement of the surface beneath it. The third (110) sample was used throughout the series of experiments, and no problems were encountered with bond fracture. This fact is in line with an observation of Burkart and Read (1953) who remarked that the habit plane for transformations subsequent to the first was the same as for the first one. We were also able to verify another of their findings, in that on warming from below T_c a cubic crystal returned to the single crystal form; back-reflection photographs showed unsplit spots.

The three elastic stiffness moduli C_{11}, C_{12} and C_{44} are shown in figure 5.8 as a function of temperature. The measured sound velocities were corrected for thermal expansion using, for this alloy composition, the data of Pahlman and Smith (1968). In plotting these results the error on C_{12} from the measured value of $\rho v_3^2 = \frac{1}{2}(C_{11}+C_{12}+2C_{44})$ is about 3%, but the measured value of $\frac{1}{2}(C_{11}-C_{12})$ at 290K has been used to determine the value of C_{12} at that temperature (given the value of C_{11}), and the variation of the velocity v_3 was used to find its temperature dependence. The absolute error on C_{11} and C_{44} is

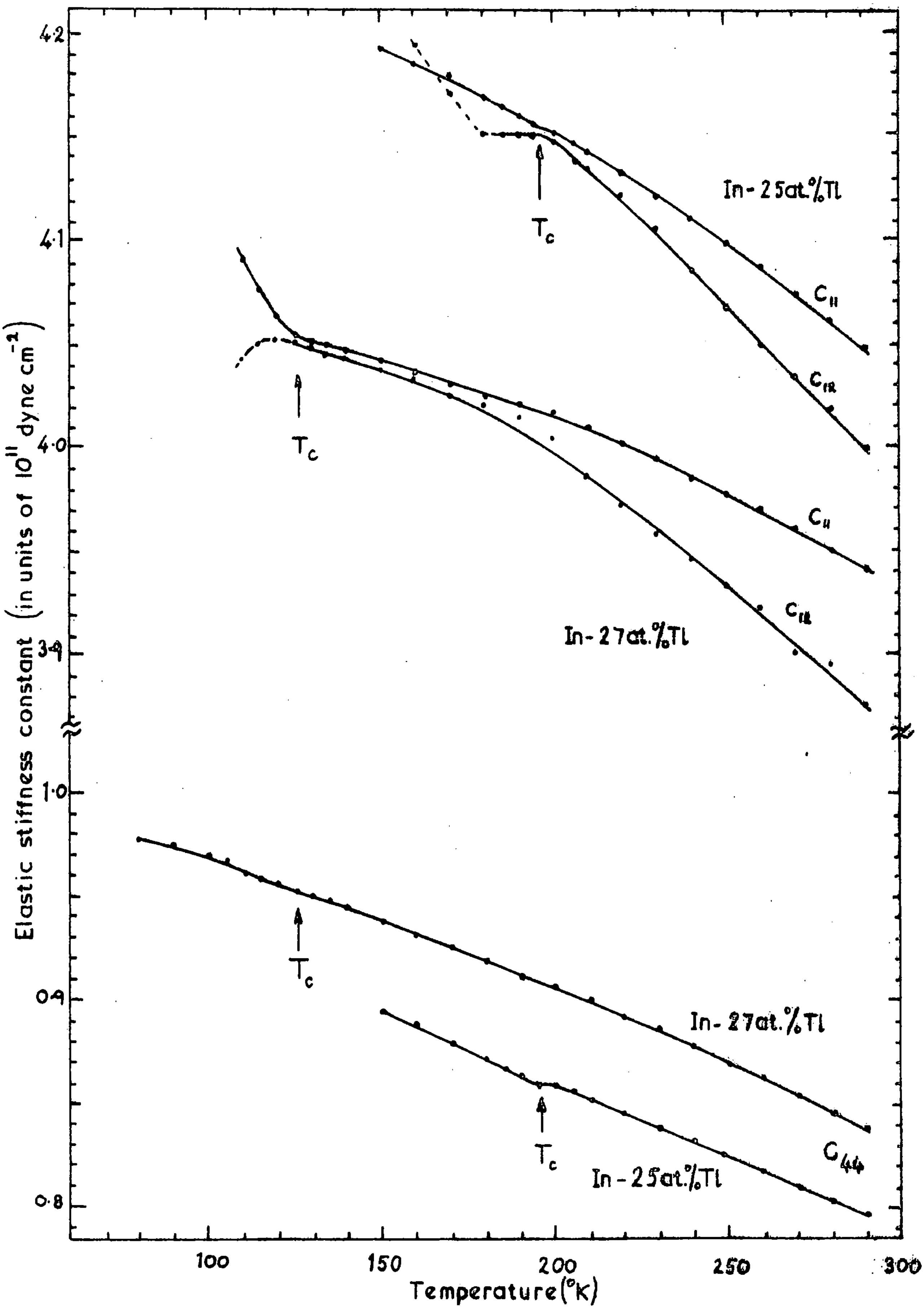

Figure 5.8 The elastic constants C_{11}, C_{12} and C_{44} for the cubic alloys In-25 and 27 at.% Tl over a temperature range which includes their transition temperatures.

about 1%, so that within the experimental limits $C_{11} = C_{12}$ at the phase transition.

The corresponding results for the In-25 at.% Tl alloy are shown in figures 5.9 to 5.11 for the observed pulse repetition rates, and in figure 5.8 for the elastic constants. Figure 5.8 enables a comparison between the results for the two compositions to be made. The transition in the 25 at.% alloy occurred near to 195K, and the attenuation of the sound pulses was not as high as in the other alloy with a lower T_c. This resulted in a smaller reduction in precision of the measurements at the phase transition. Comparing the curves of figure 5.8 we see that the depression in C_{44} is larger for the 25 at.% Tl alloy than for the other, and that C_{11} is approaching C_{12} near the transition temperature of both alloys. A general point must be made concerning the data obtained in the tetragonal phase of these two materials. When the structure becomes twinned the new tetragonal axes become tilted relative to the original cubic ones. As a result the elastic constant combinations which are related to the measured sound velocities take on an unknown form, and thus the curves shown in figure 5.8 only give the moduli C_{11}, C_{12} and C_{44} at temperatures above T_c. It is not surprising, therefore, that in figure 5.12, in which is shown the variation of $\frac{1}{2}(C_{11}-C_{12})$ for the two cubic alloys studied, the value of this modulus below 180K for the 25 at.% Tl alloy behaves in an anomalous way. It is clear, though, that there is no discontinuity in any of the moduli at the transition.

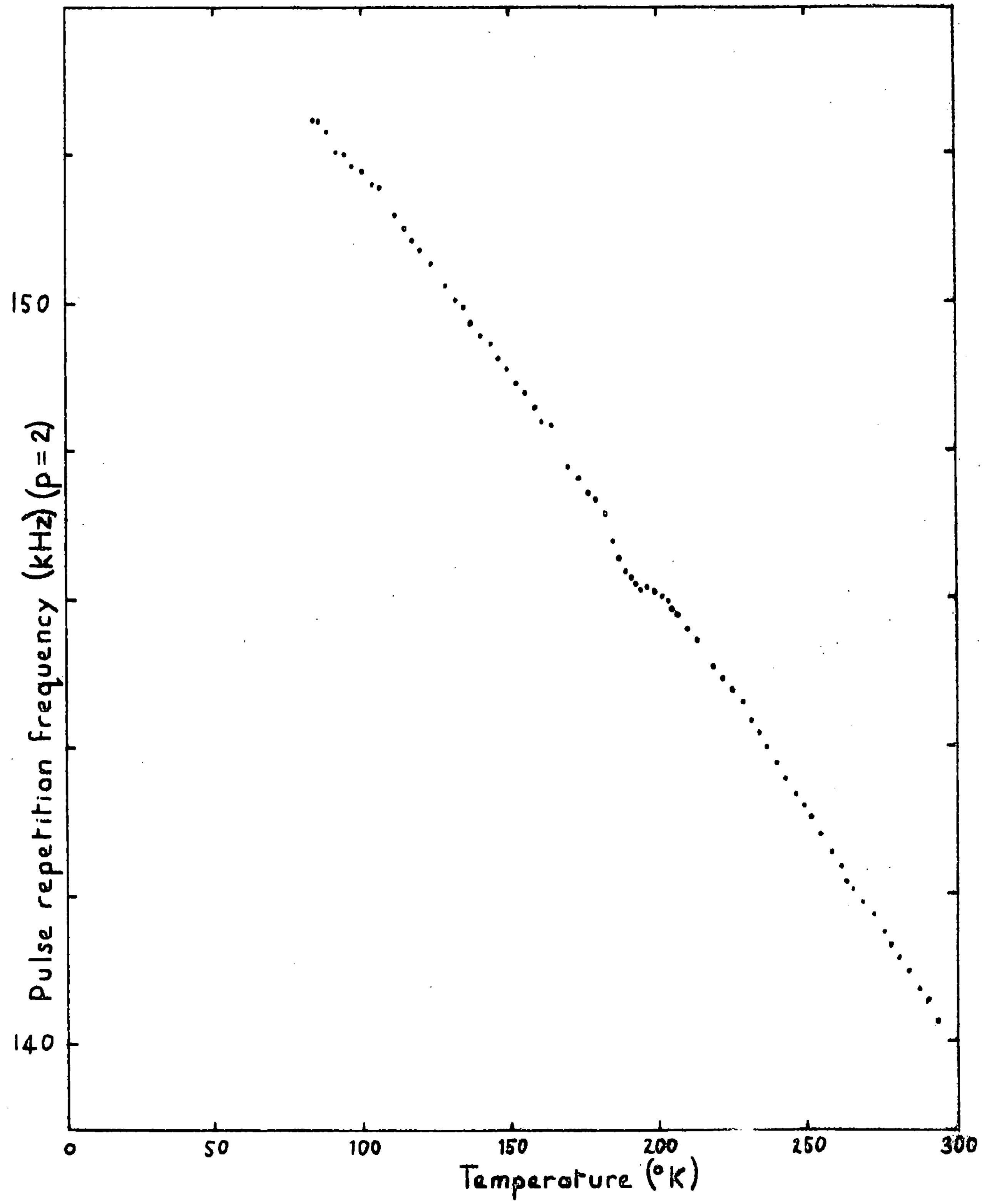

Figure 5.9 The measured PRF for wave propagation in the [110] direction of a shear wave polarised [001] at 15MHz in In-25 at.% Tl.

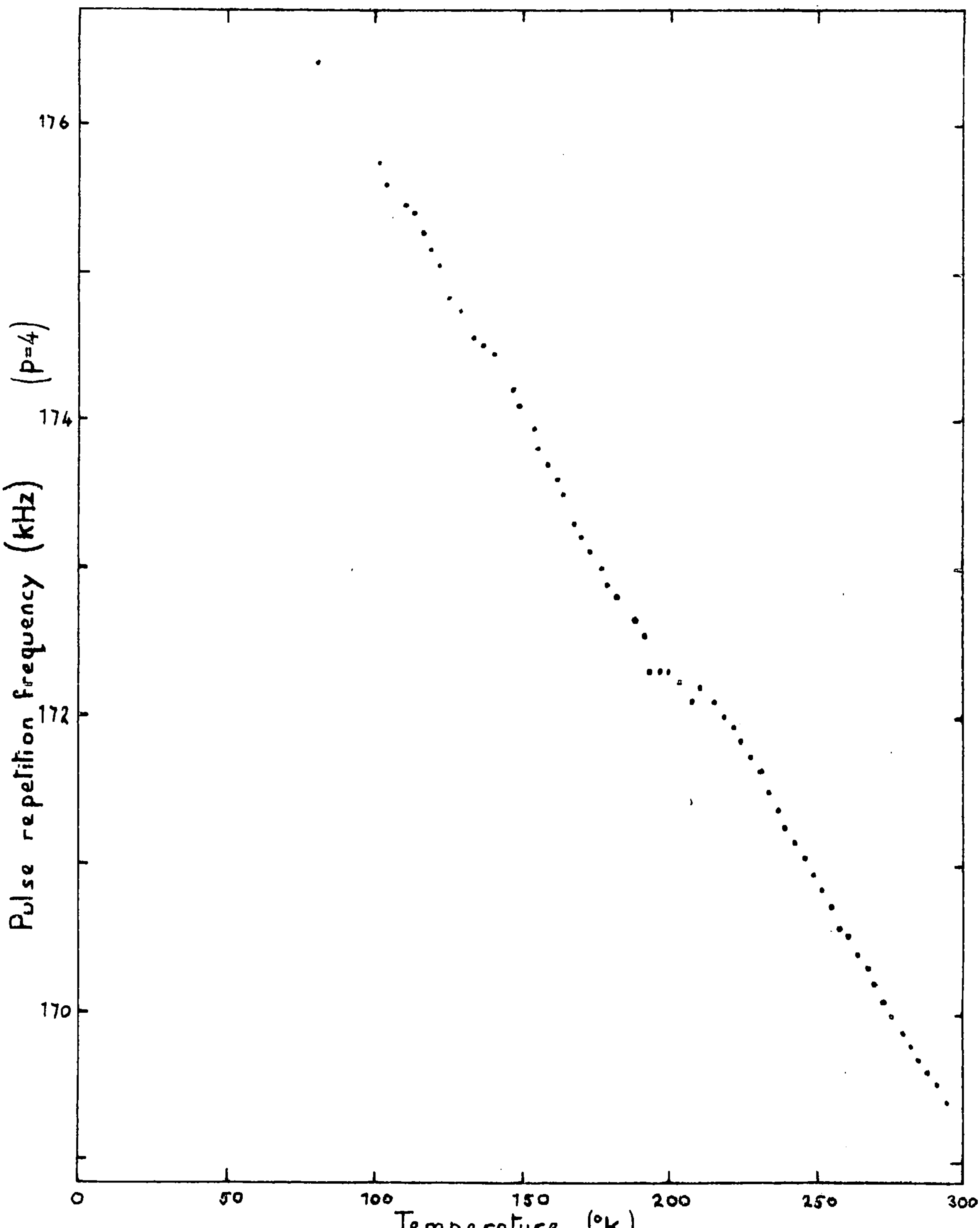

Figure 5.10 The measured PRF for wave propagation in the [110] direction of a longitudinal wave at 15MHz in In-25 at.% Tl.

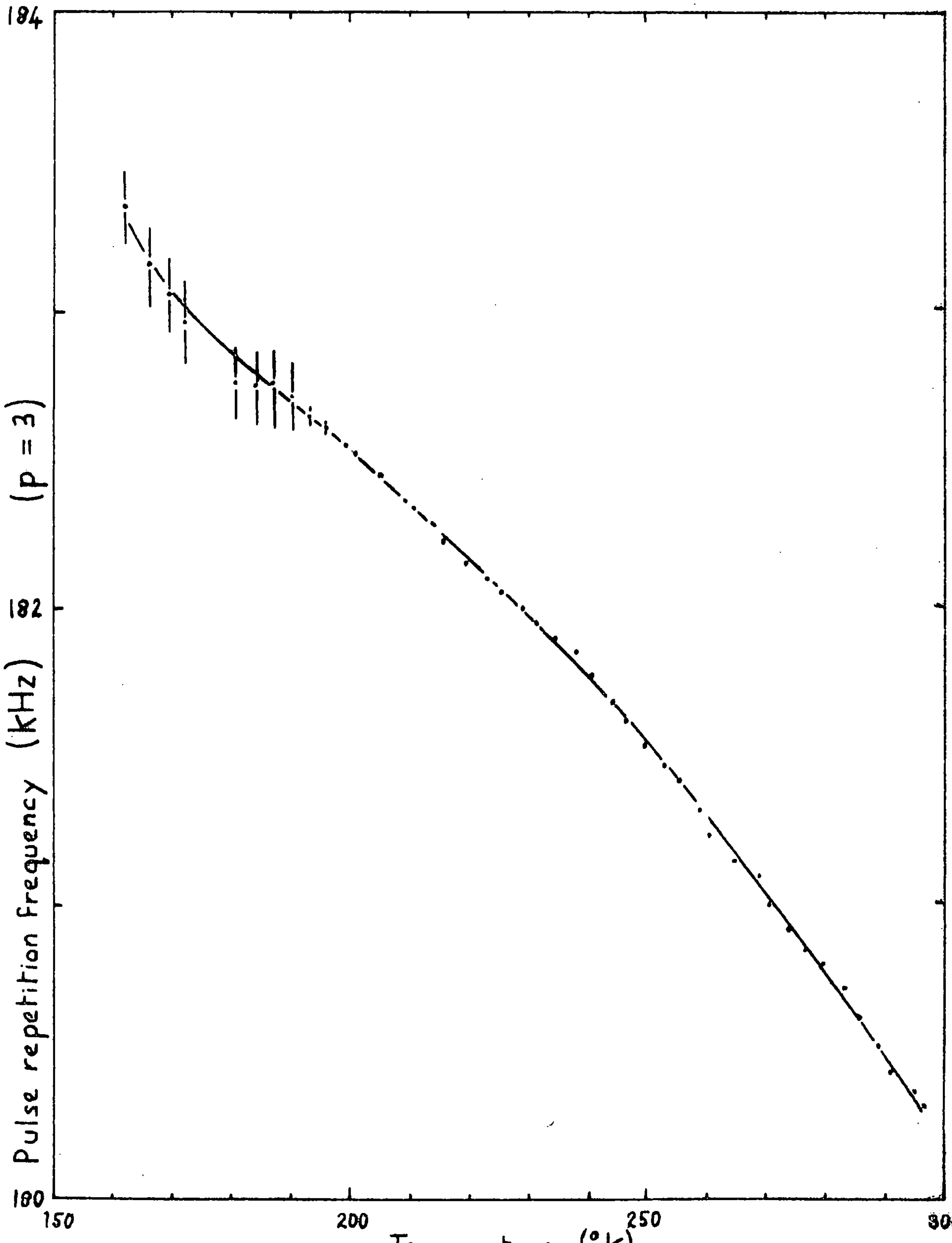

Figure 5.11 The measured PRF for wave propagation in the [100] direction of a longitudinal wave at 14MHz in In-25 at.% Tl.

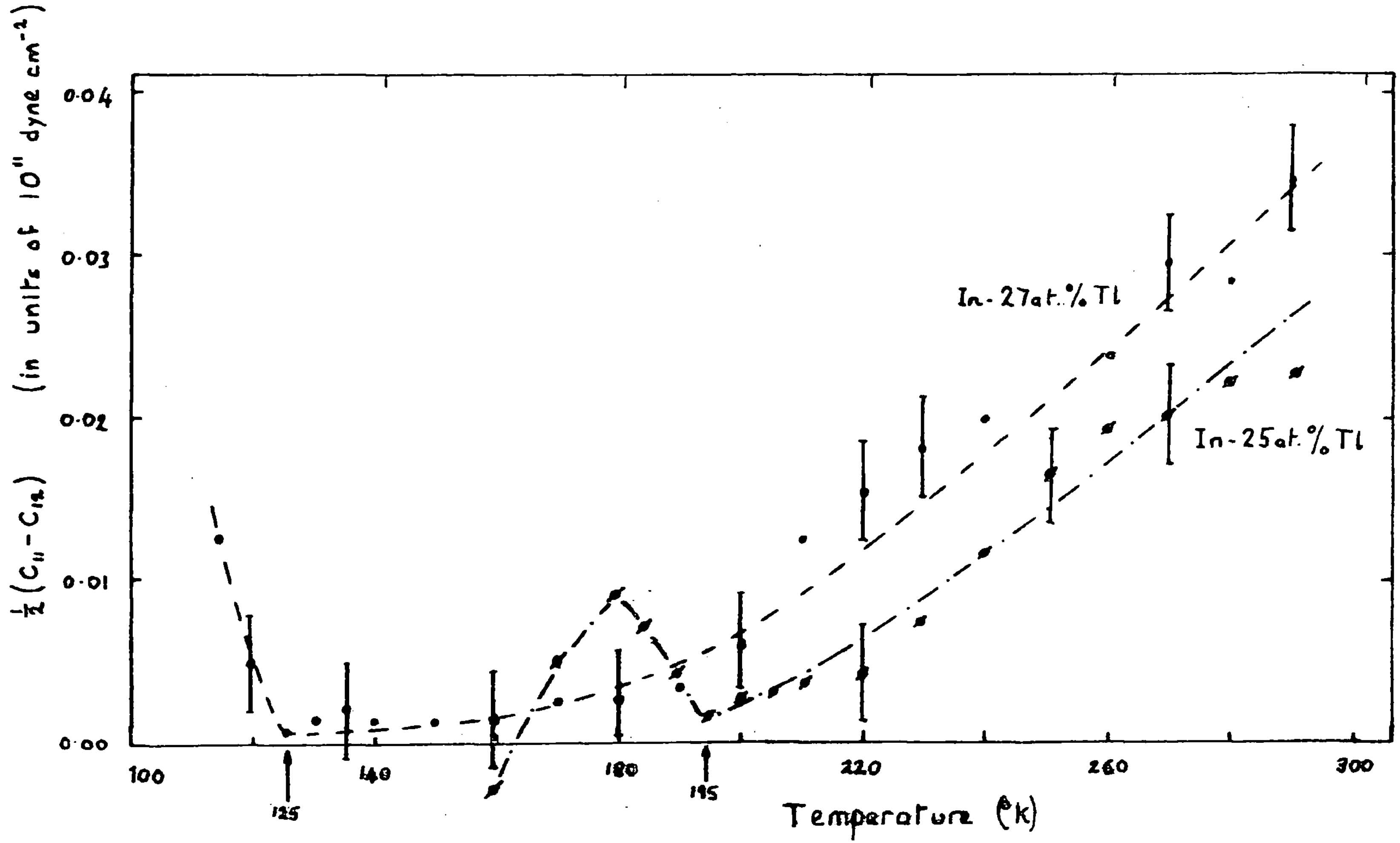

Figure 5.12 The variation of the modulus $\frac{1}{2}(C_{11}-C_{12})$ in the vicinity of the martensitic transition for In-25 and 27 at.% Tl alloys. The uncertainty limits on a selection of the points are given.

5.2.2 Tetragonal alloys

None of the tetragonal alloys studied suffered a martensitic transition, although at its melting point the In-15 at.% Tl alloy was very close to the fcc/fct boundary. Measurements have been made of the six independent elastic constants C_{11}, C_{12}, C_{13}, C_{33}, C_{44}, C_{66} over the temperature range 300 to 425K for the 15at.% composition, and over the range 150 to 425K for 11.5 at.% Tl. The velocities v_1 to v_{11} of Table 3.1 were measured by the pulse-echo method at room temperature, and the various cross-checks were made; a set of elastic constants at room temperature was determined for each alloy. The results are given in Table 5.1. The temperature variation of the stiffness constants C_{ij} was found by measuring v_1, v_2, v_4, v_7, v_8, v_{10} by the pulse superposition method. Figures 5.13 and 5.14 show the results of the elastic constant determination for In-11.5 at.% Tl and In-15 at.% Tl, respectively, after the velocities had been corrected for thermal expansion of the samples. It was possible to find directly a value for $\frac{1}{2}(C_{11}-C_{12})$ from a measurement of the velocity of the $[1\bar{1}0]$ polarised transverse mode in the $[110]$ direction. For the 11.5% alloy this was achieved up to 423K (melting point $\simeq$ 427K), but in the case of 15% a direct measurement was only possible to 390K. Results for these velocities are shown in figure 5.15.

Certain sound velocities have been measured to 4K. High values of attenuation meant that an extension to 4K was not possible with all the velocities examined, but those which have been thus obtained are shown, together with the

TABLE 5.1

Measured sound velocities and elastic constants for In-11.5 and 15 at.% Tl alloys at 290K

*	11.5% velocity (10^5 cm/sec)	11.5% ρv^2 (10^{11} dyne/cm^2)	15% velocity (10^5 cm/sec)	15% ρv^2 (10^{11} dyne/cm^2)
v_1	2.34	4.265	2.283	4.20
v_2	1.161	1.050	1.149	1.062
v_3	0.931	0.675	0.956	0.736
v_4	2.325	4.155	2.281	4.18
v_5	–	–	0.950	0.727
v_6	2.557	5.093	2.488	4.983
v_7	0.48	0.18	0.39	0.122
v_8	0.935	0.681	0.948	0.723
v_9	0.94	0.688	1.046	0.881
v_{10}	2.44	4.637	2.445	4.812
v_{11}	0.88	0.603	0.36	0.104

* Notation as in Table 3.1

	C_{11}	C_{12}	C_{13}	C_{33}	C_{44}	C_{66}
11.5%	4.27	3.92	3.93	4.21	0.678	1.05
15%	4.20	3.95	3.93	4.18	0.73	1.06
	S_{11}	S_{12}	S_{13}	S_{33}	S_{44}	S_{66}
11.5%	2.01	-0.85	-1.08	2.24	1.47	0.952
15%	2.70	-1.31	-1.32	2.73	1.37	0.943

Units

Stiffnesses (C_{ij})
10^{11} dyne cm^{-2}

Compliances (S_{ij})
10^{-11} cm^2 dyne^{-1}

Cross-checks on elastic constants

Elastic constant combination		calculated value	observed value	% error
$\frac{1}{2}(C_{11}+C_{12}+C_{66})$	11.5%	5.145	$\rho v_6^2 = 5.093$	1.1
	15%	5.135	$= 4.983$	3.0
$\frac{1}{2}(C_{44}+C_{66})$	11.5%	0.864	$\rho v_9^2 = 0.688$	20.4
	15%	0.895	$= 0.881$	1.6

Velocities giving C_{44}:

	ρv_3^2	ρv_5^2	ρv_8^2
11.5%	0.675	–	0.681
15%	0.736	0.727	0.723

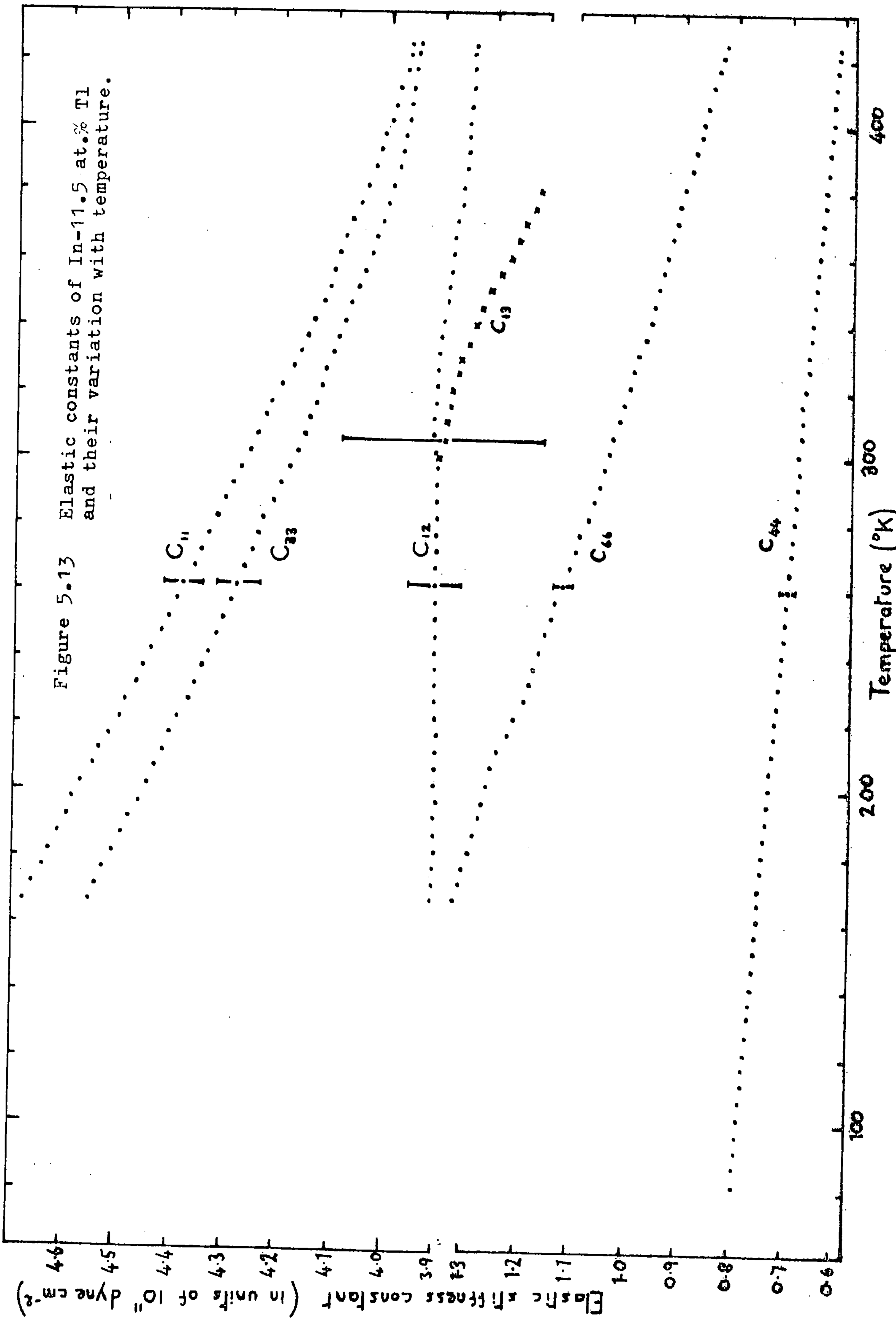

Figure 5.13 Elastic constants of In-11.5 at.% Tl and their variation with temperature.

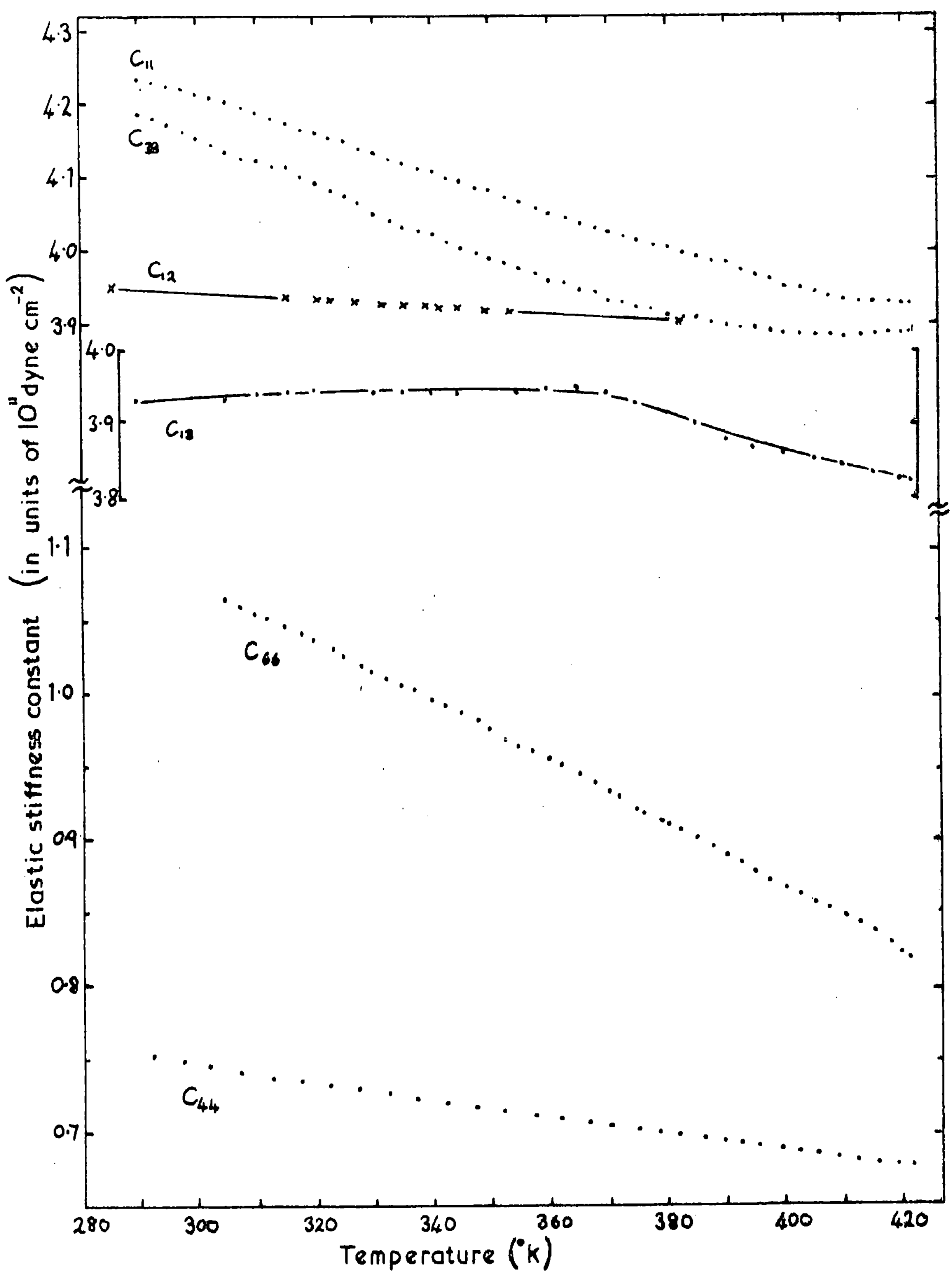

Figure 5.14 The elastic constants of In-15 at.% Tl and their variation with temperature.

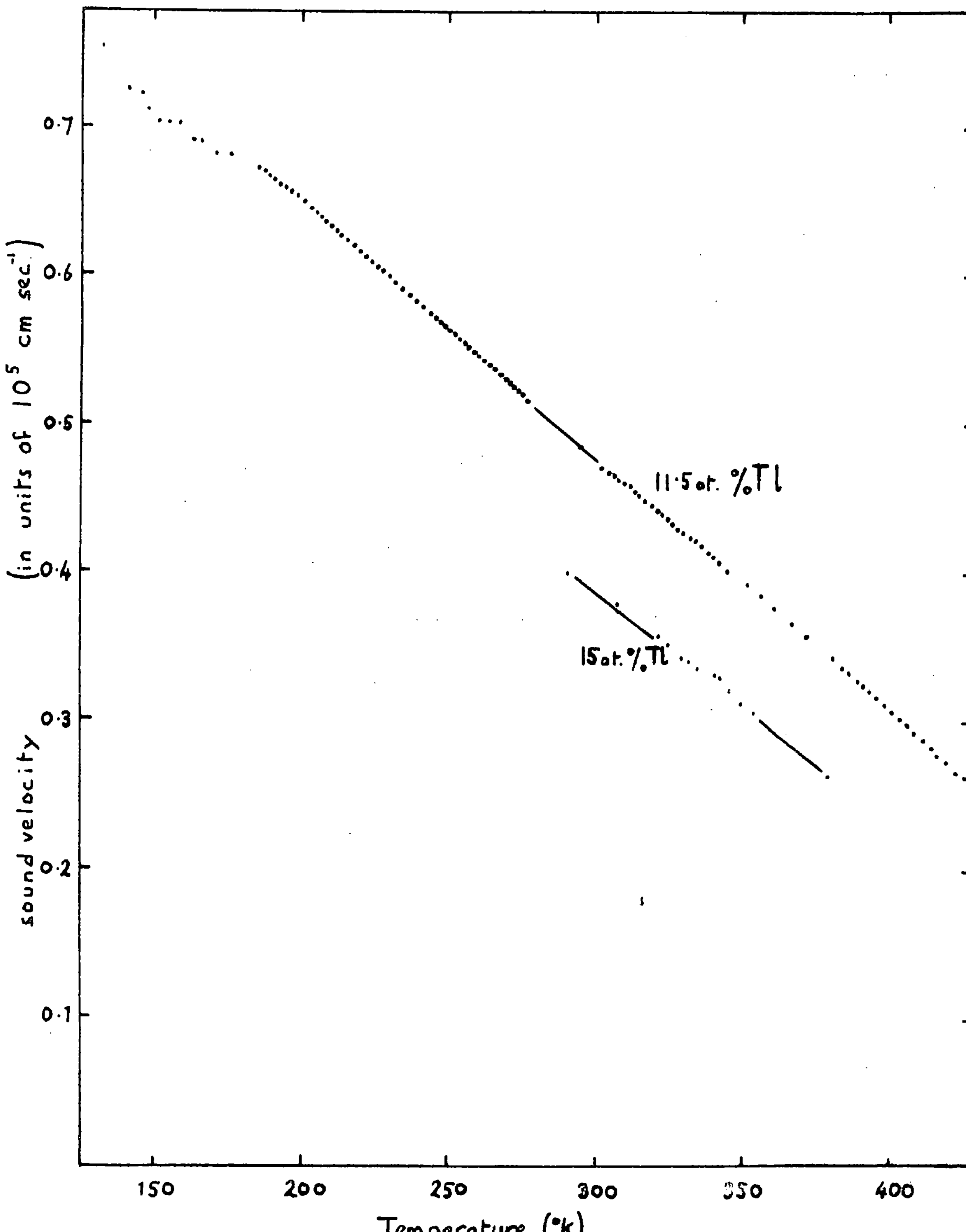

Figure 5.15 The temperature variation of the slow shear mode propagating in the [110] direction and polarised [1$\bar{1}$0] for In-11.5 and 15 at.% Tl.

polarisations involved, in figures 5.16 and 5.17. No thermal expansion correction has been applied to the results because of lack of data below 150K.

5.3 Attenuation measurements

All the attenuation measurements were made by fitting a variable exponential curve to the echo train produced by a pulse-echo method, and as described in section 4.5.1 . This gave an attenuation expressed in dB/μsec: a conversion to the unit of dB/cm was achieved by division by the speed of sound $\times 10^6$.

The dominating feature of all the measurements made in indium and in indium-thallium alloys was a rising background attenuation as the temperature was reduced. The rise commenced at between 200 and 220K for most of the samples; other effects, when they occurred, were seen superimposed on this background. The results will be given first for the cubic alloys, and then for the tetragonal ones.

5.3.1 Ultrasonic attenuation in In-25 and 27 at.% Tl alloys

Attenuation measurements have been made in the temperature range 80 to 300K for these alloys. Results are shown in figures 5.18 and 5.19 for attenuation at 14 and 42 MHz. Both show a frequency independent absorption peak at the fcc/fct transition: the peak was found for both longitudinal and transverse waves, and its width was greater in the alloy with the lower transition temperature. The peak position differed on the warming and cooling cycles, as might be expected if it

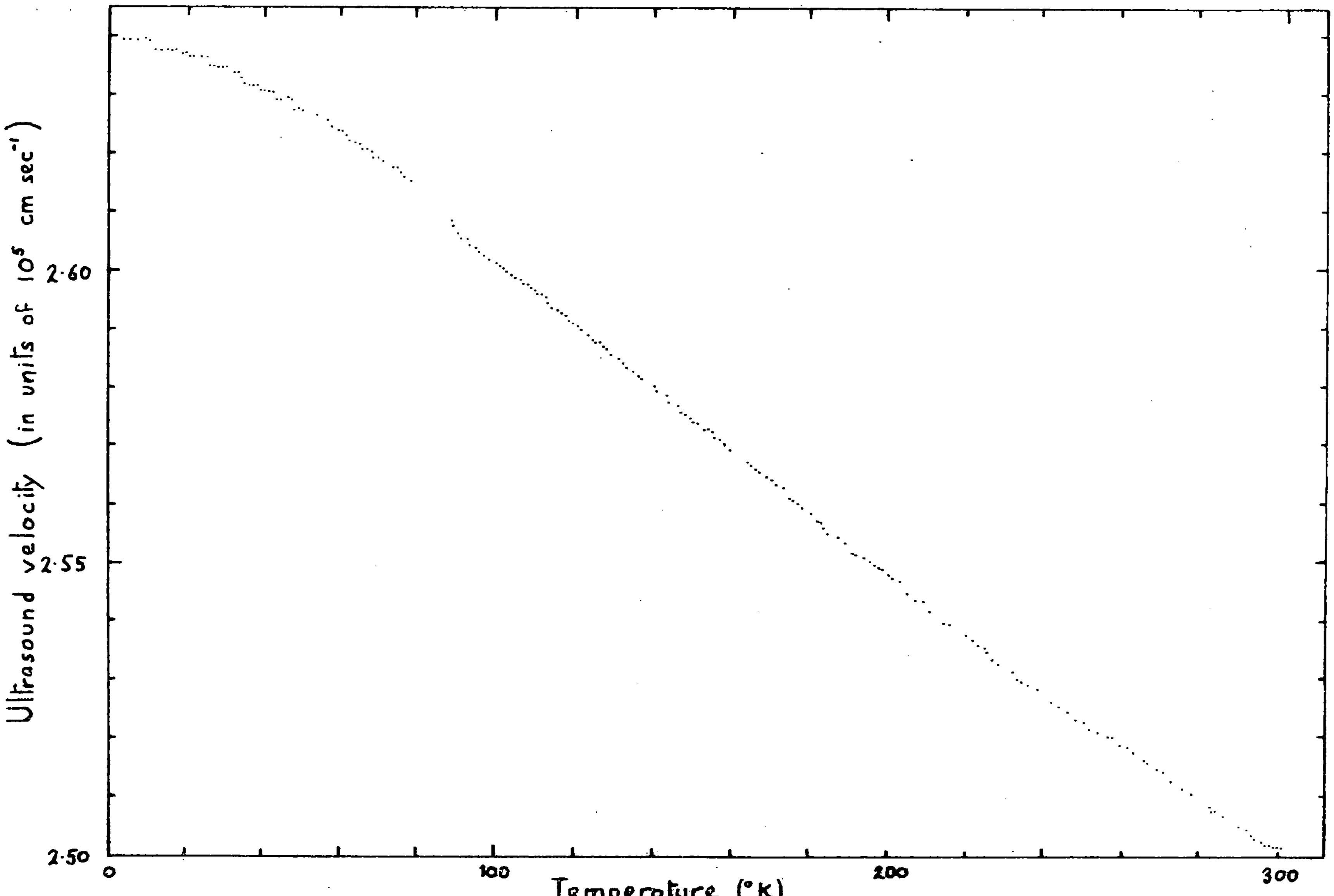

Figure 5.16 Temperature dependence of the velocity of a longitudinal wave propagating in the [110] direction in In-10 at.% Tl alloy.

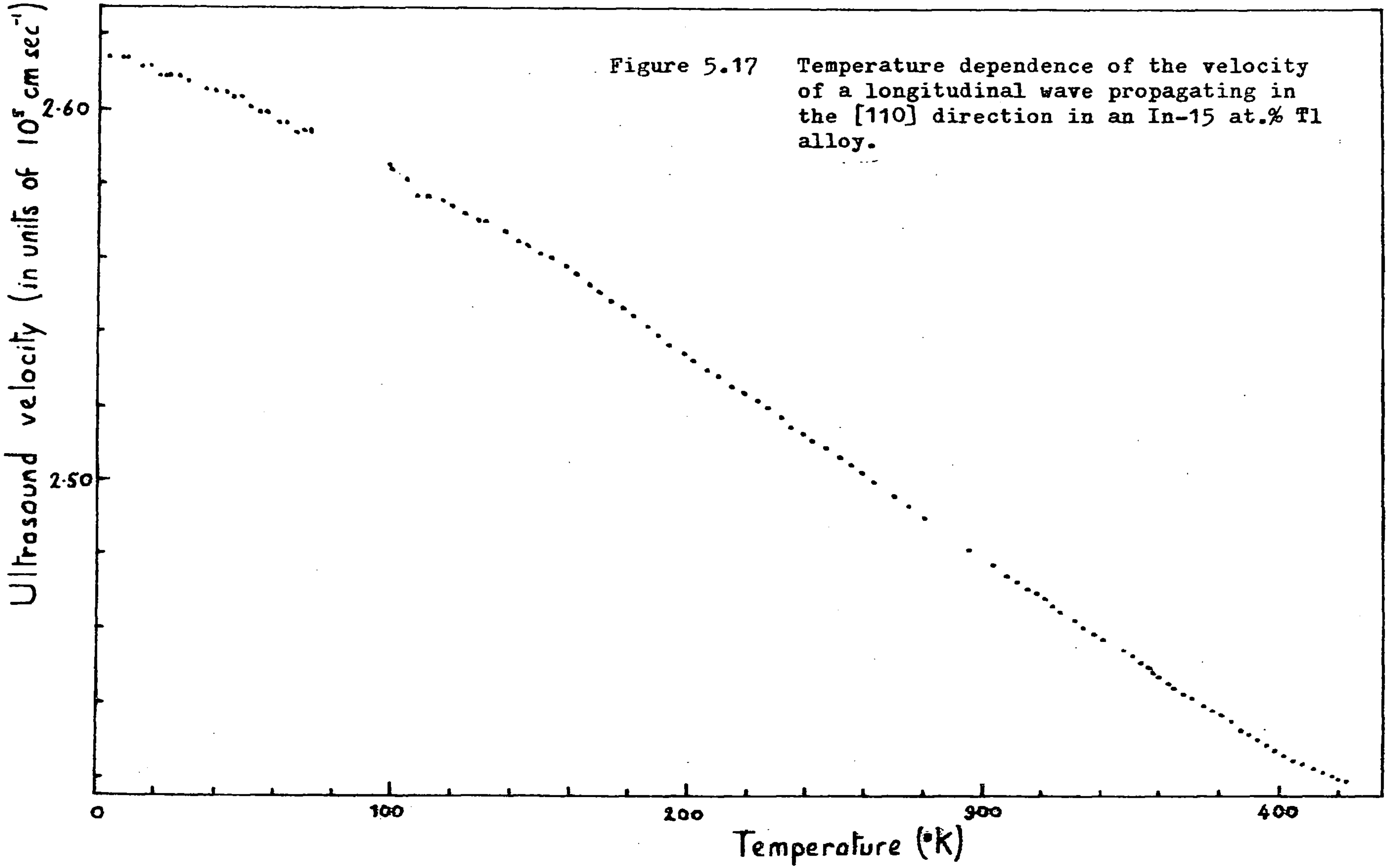

Figure 5.17 Temperature dependence of the velocity of a longitudinal wave propagating in the [110] direction in an In-15 at.% Tl alloy.

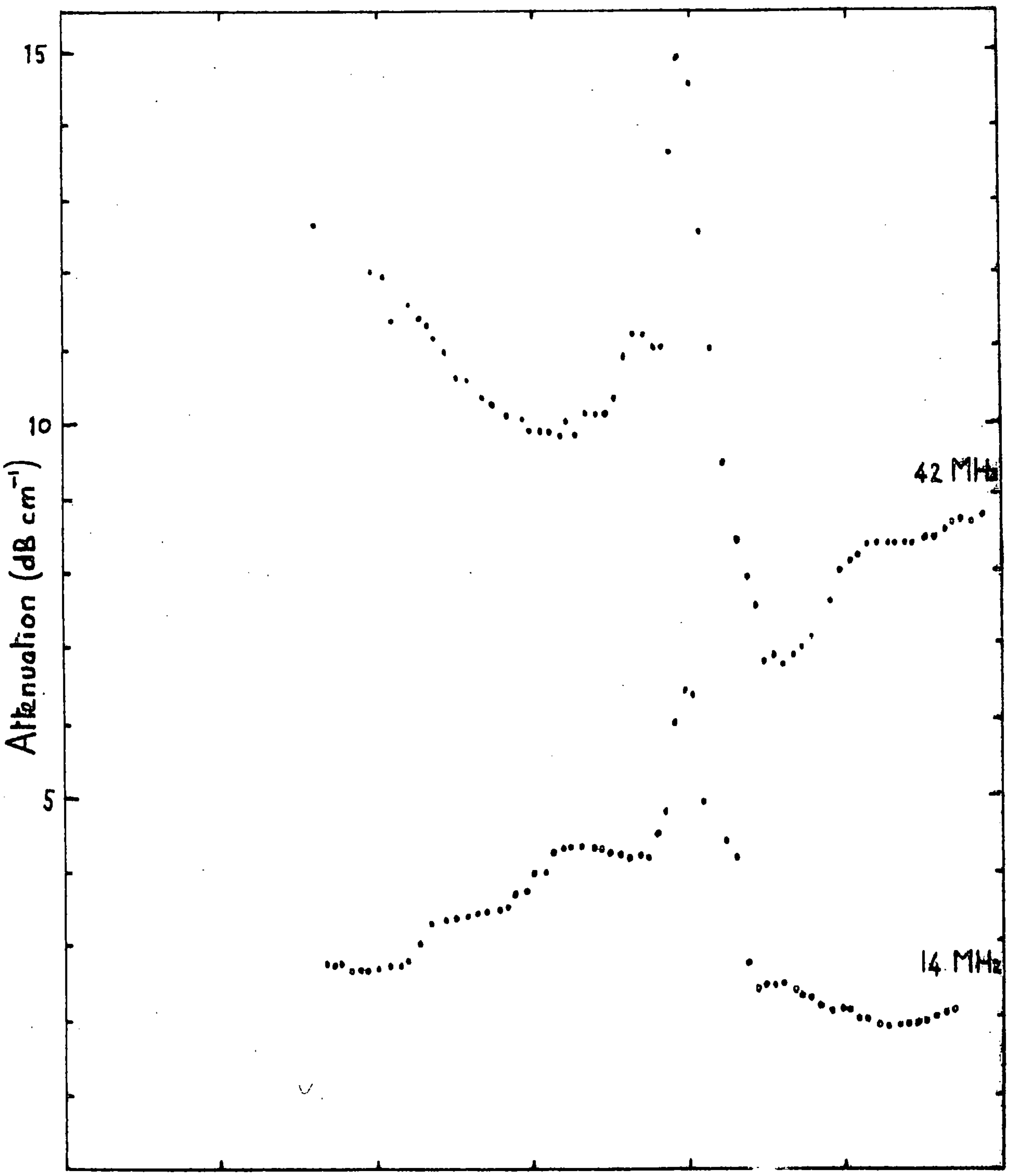

Figure 5.18 Attenuation of ultrasound in In-25 at.% Tl as a function of temperature. The measurements are for a longitudinal wave propagating [110], and were obtained on cooling.

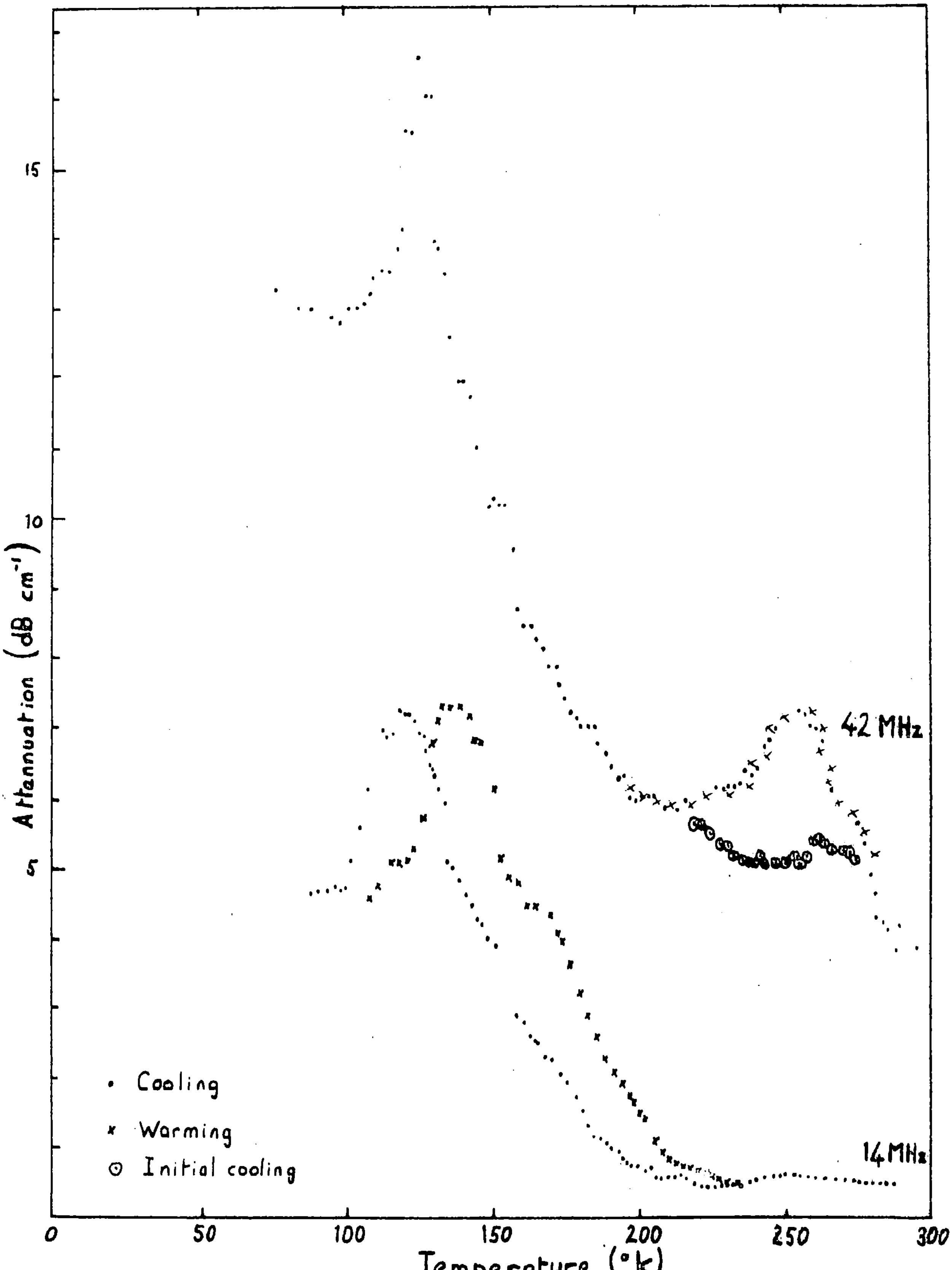

Figure 5.19 Attenuation of ultrasound in In-27 at.% Tl as a function of temperature. The 14MHz curve was for longitudinal waves, and the 42MHz one for shear waves polarised [001], both propagating in [110].

were associated with a martensitic transition with its attendant temperature hysteresis. The results of figures 5.18 and 5.19 are for propagation in the [110] direction.

Introduction of a Bordoni peak in In-27 at.% Tl

An additional feature in the attenuation variation of ultrasound propagation in the [110] direction of the 27at.% alloy was a peak whose position on the temperature axis varied with ultrasound frequency. The peak occurred on both warming and cooling, except for the first few (about 5) cycles following the cutting and planing of the (110) sample, when the peak was only seen on warming. (Each cycle consisted of cooling below T_c and warming again to room temperature.) The peak can be seen in figure 5.19 in the 42 MHz curve —— the circles on that figure indicate the form of the attenuation behaviour during the initial cooling experiments. The results for several frequencies are collected in figure 5.20. It was also observed that after the peak had become established for both warming and cooling its amplitude gradually decreased with time, until after about eight or nine months it had gone almost completely.

An absorption peak whose temperature of occurrence is frequency dependent is characteristic of a relaxation type of phenomenon. In such a case the relaxation time τ can be related to an activation energy E and temperature T by an Arrhenius type of expression $\tau = \tau_o \exp(E/kT)$, where k is Boltzmann's constant. If the attenuation depends on $\omega\tau$, and is a maximum when $\omega\tau = 1$, then the frequency dependence of the absorption peak is $\omega = \omega_o \exp(-E/kT)$, in which ω_o is an attempt

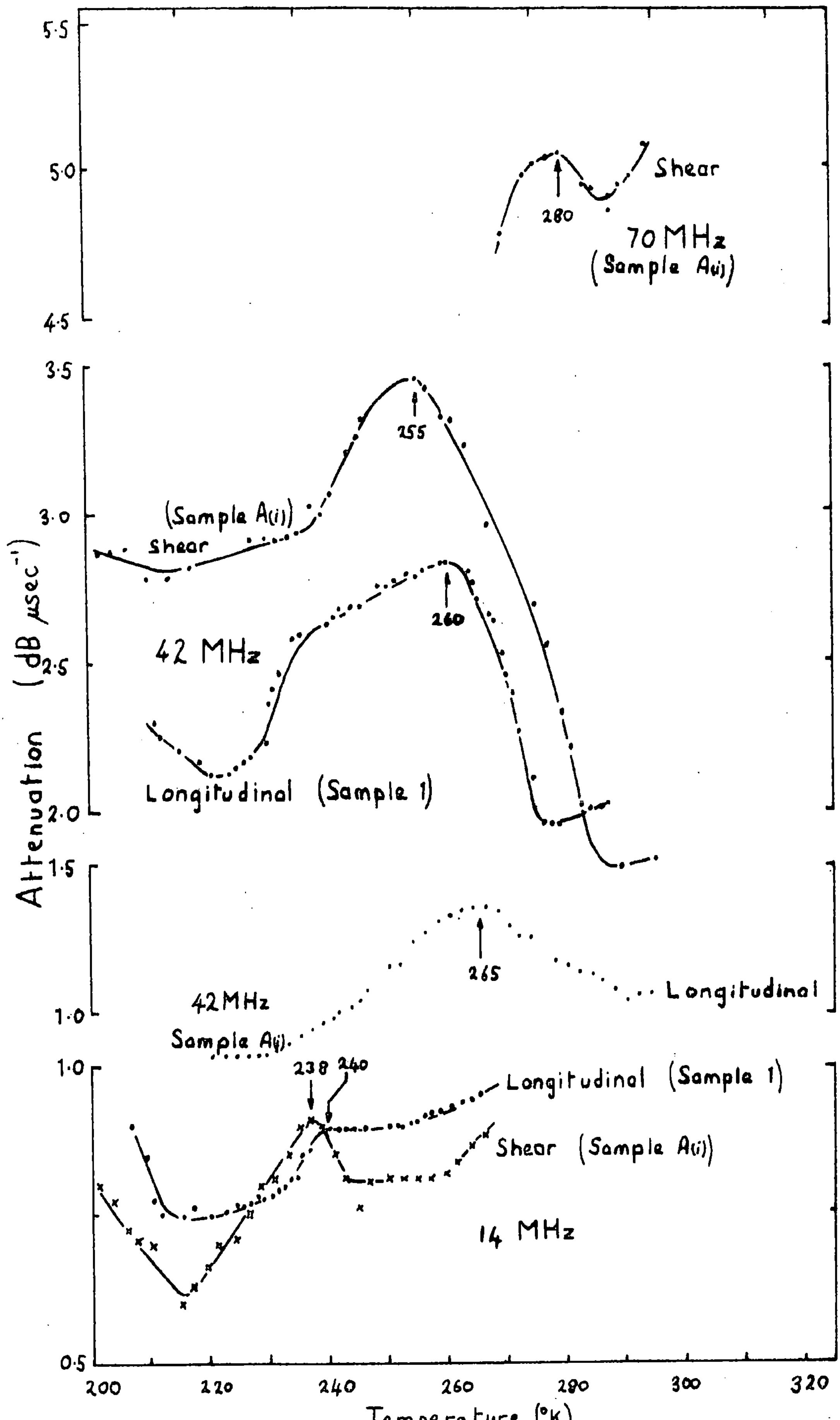

Figure 5.20 Collected data (for various samples and polarisations) of the Bordoni peak found for wave propagation in [110] in In-27 at.% Tl.

frequency. Values of E and ω_o can be obtained from a graph of $\ln\omega$ against T^{-1}. Several determinations were made of the peak position, and for a given frequency it was found to vary slightly between similarly oriented samples cut from the same boule, and between the polarisations of the sound wave. Figure 5.21 is the Arrhenius plot, and a straight line fit seems reasonable. It is interesting to note that there is no significant difference, within the limits of experimental error, between activation energies for the longitudinal and transverse modes. Such a difference could, in principle, occur because of the different nature of atom motion involved in the two polarisations.

Bordoni peaks in face-centred cubic metals, and theories to account for them, have been reviewed by Niblett (1966). The various theories of the mechanism all involve motion of dislocations, or of kinks in dislocations, by interaction with the stress wave. The theory developed by Seeger, Donth and Pfaff (1957) assumes that pairs of kinks are formed in dislocation lines in a metal, and do so at a temperature dependent frequency ν. When the frequency of the stress wave ω is approximately equal to ν then absorption of energy can occur, whereas at other frequencies the extent of the interaction is greatly reduced.

If a mechanism based on dislocations is assumed for the In-27 at.% Tl alloy then not only is the change in peak temperature accounted for, but also the observation that it was only seen initially on warming, for at the phase transition we suppose that large numbers of dislocations are introduced.

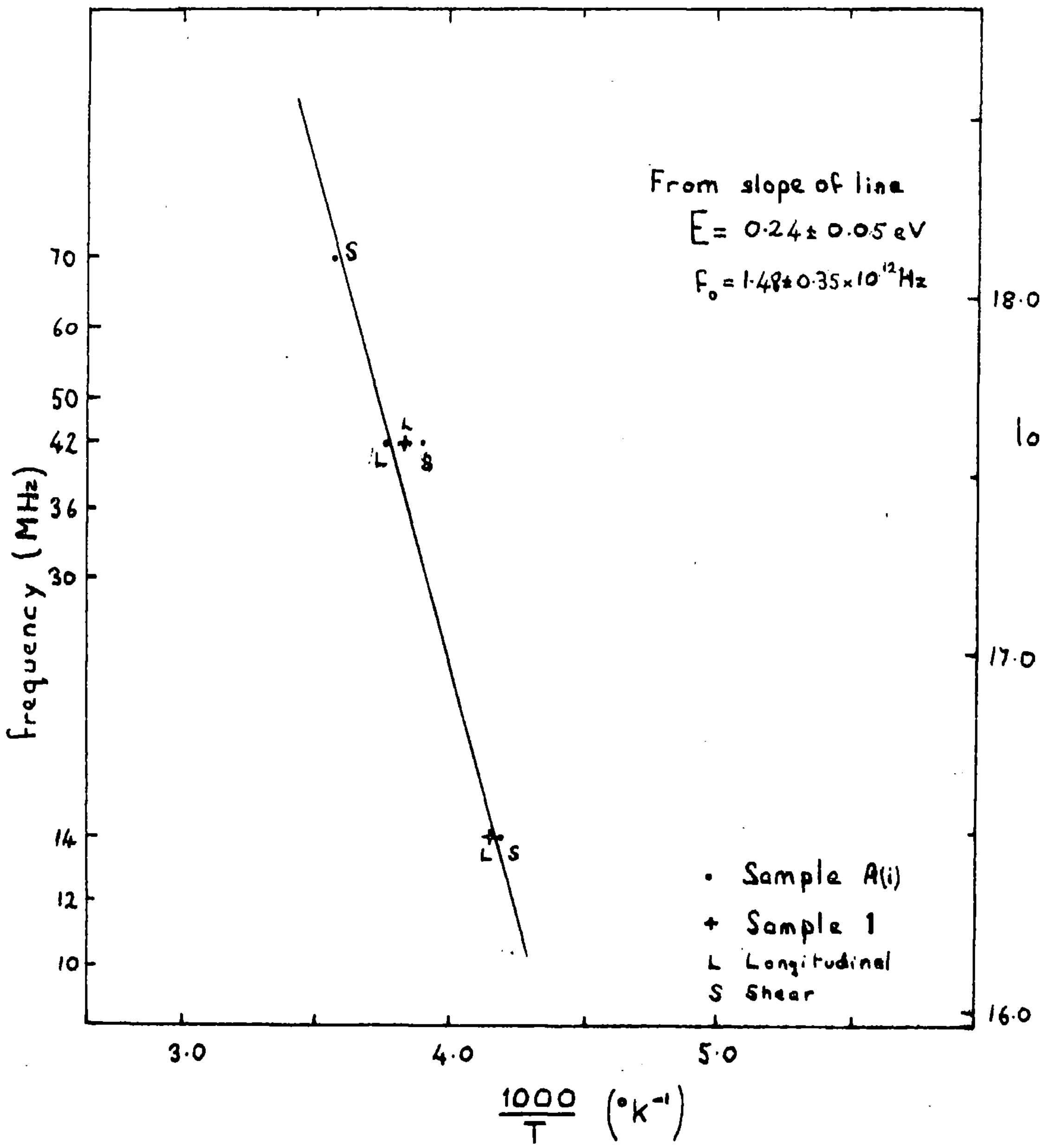

Figure 5.21 Arrhenius plot to determine activation energy and attempt frequency of Bordoni peak.

These interact with the sound wave as the temperature is raised, and then anneal out when the sample is left at room temperature for a few hours (300K is $\simeq$ 0.7 of T_m). Subsequent cooling does not, therefore, result in re-appearance of the peak. But if, after several cycles the dislocations become pinned sufficiently for annealing for a comparatively short time to be ineffective in removing them, then the peak would appear on both parts of the cycle.

The slope of the graph of figure 5.21 gives an activation energy of 0.24$\pm$0.05 eV, and an attempt frequency of 1.48$\pm$0.35$\times 10^{12}$Hz. This compares with values for copper of E=0.122eV, f_o=3.8$\times 10^{11}$Hz (Niblett, 1966); silver – (0.124eV, 4$\times 10^{12}$Hz); gold – (0.158eV, 7$\times 10^{10}$Hz); palladium – (0.192eV, 6$\times 10^{9}$Hz) (Bordoni et al., 1960).

5.3.2 Ultrasonic attenuation in tetragonal alloys

The ultrasonic attenuation measurements made in the temperature range 4 to 425K are presented in figures 5.22 to 5.26 for various propagation directions in the alloys, and also for the [110] direction in indium. Irrespective of direction or composition there was an increase in attenuation starting at about 220K, and then rising more or less rapidly as the temperature was reduced until a flattening out occurred, followed by a slight reduction towards 4K. No obvious change was seen in the region of the superconducting transition temperature, and no further fall from the 4K value occurred in the 11.5% alloy [001] for a reduction to 2.4K. The temperature variation of attenuation in the [110] direction in indium was

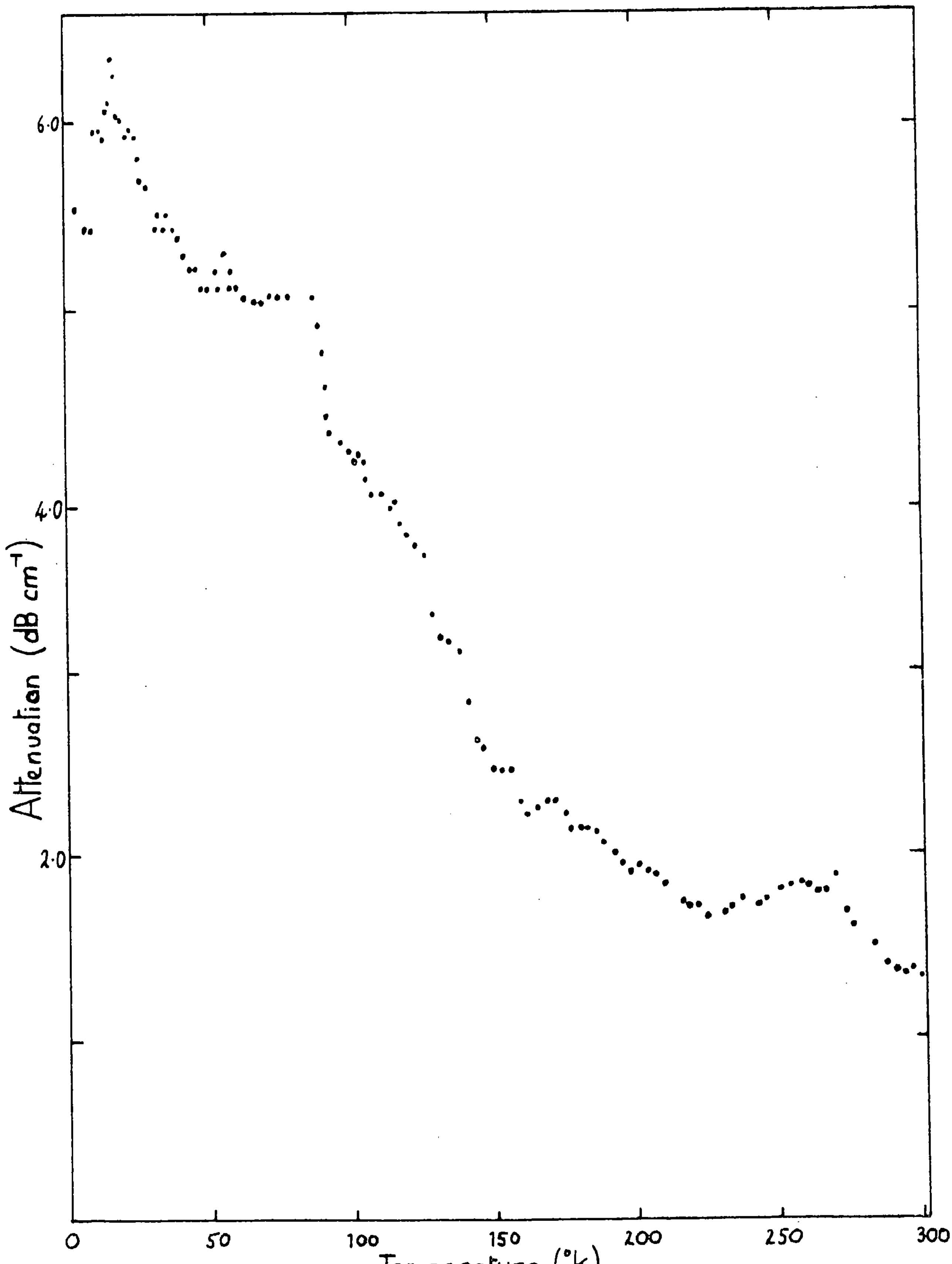

Figure 5.22 Ultrasonic attenuation at 15MHz in [110] in In-10 at.% Tl alloy (longitudinal waves).

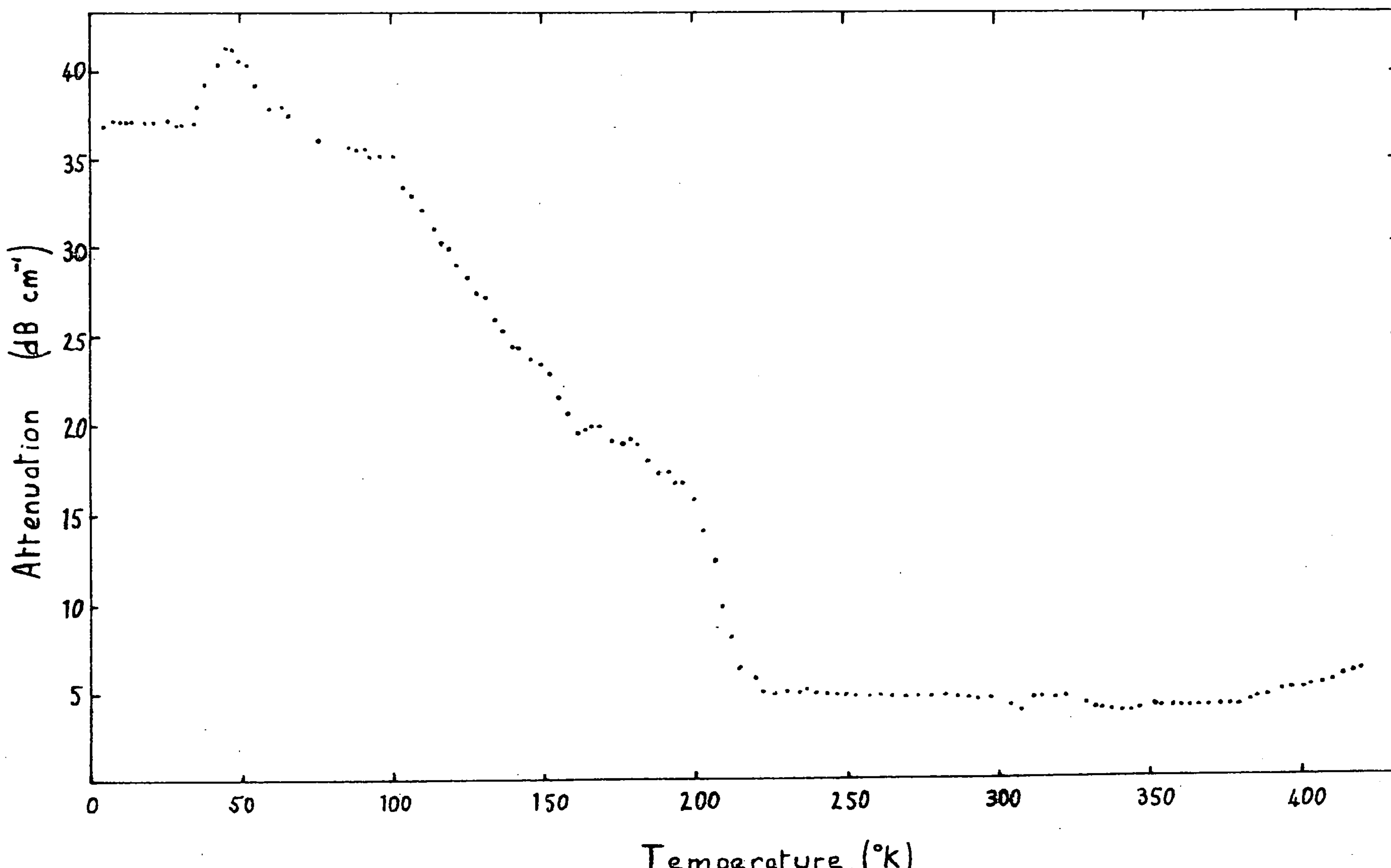

Figure 5.23 Ultrasonic attenuation at 14MHz for longitudinal waves propagating along [001] in In-11.5 at.% Tl.

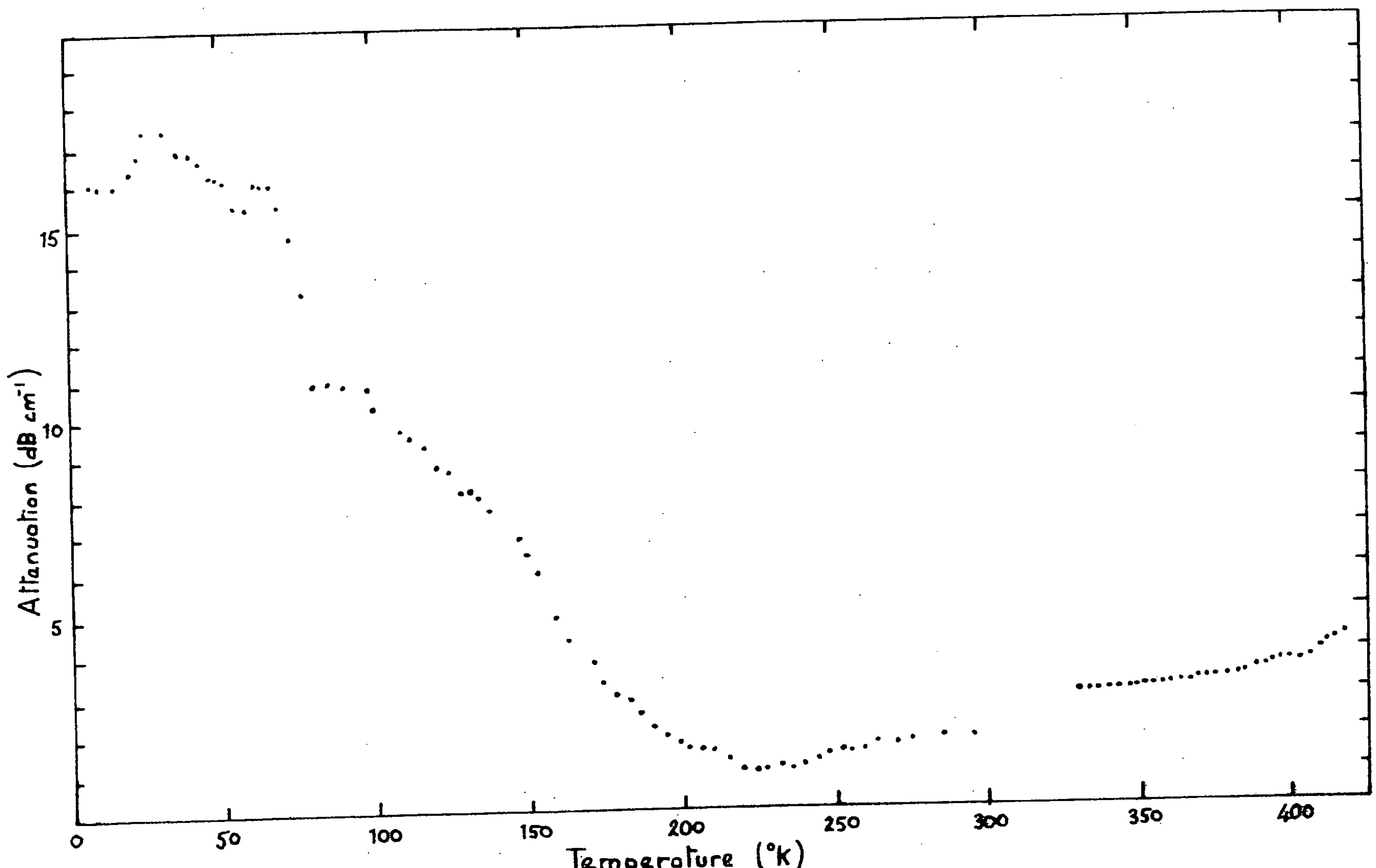

Figure 5.24 Ultrasonic attenuation at 14MHz for longitudinal waves propagating along [011] in In-15 at.% Tl.

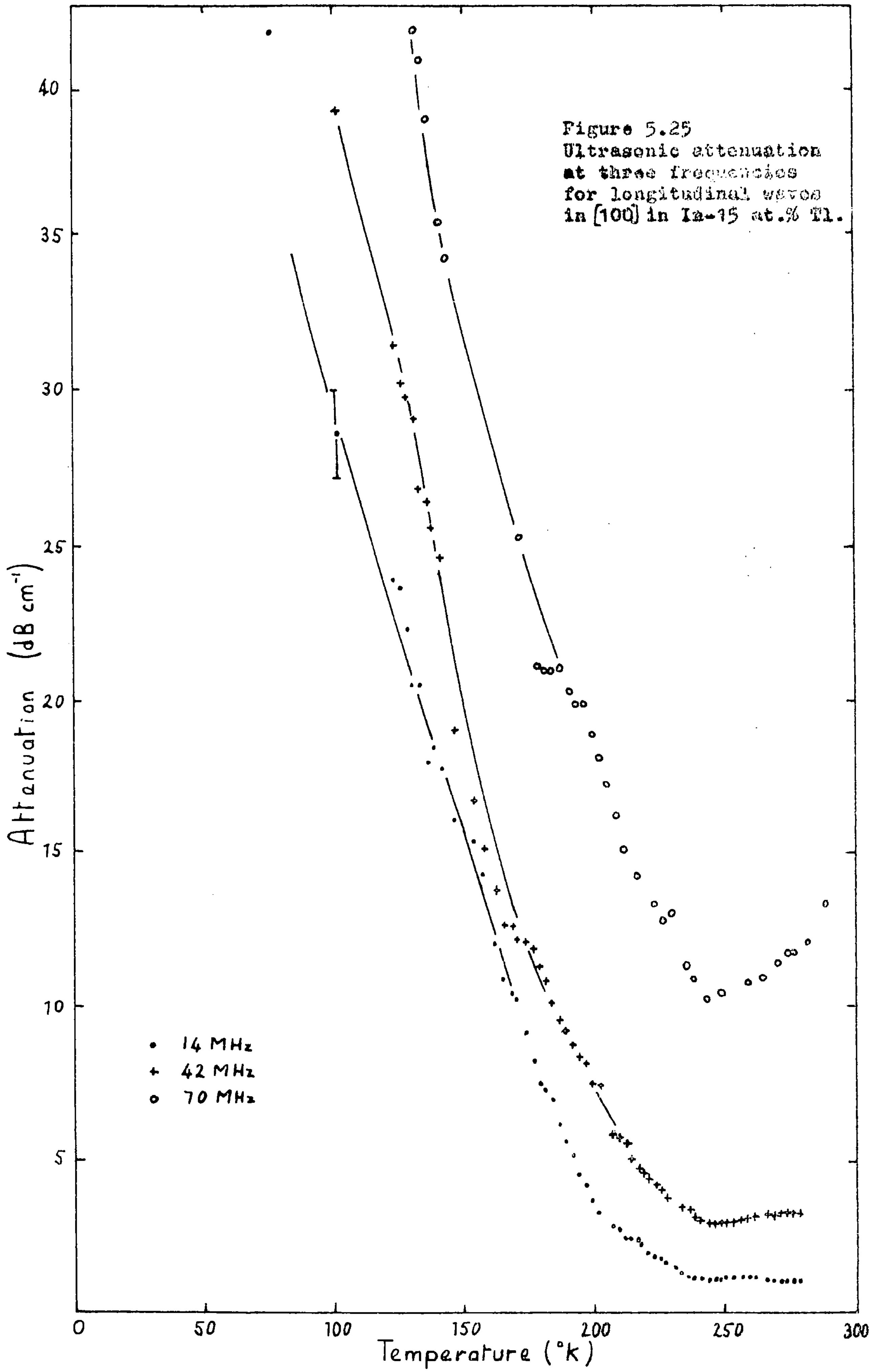

Figure 5.25
Ultrasonic attenuation at three frequencies for longitudinal waves in [100] in La-15 at.% Tl.

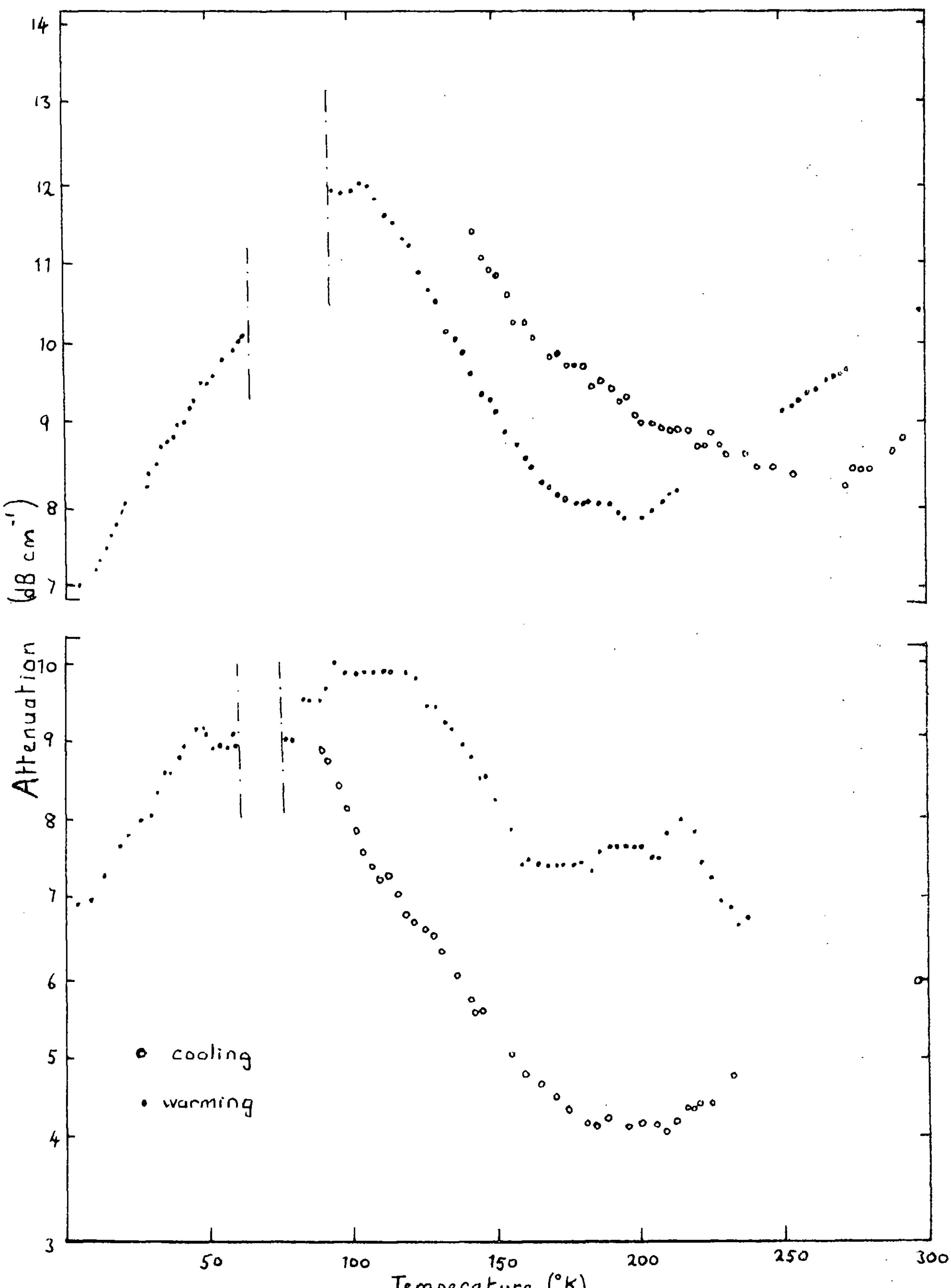

Figure 5.26 Ultrasonic attenuation at 14MHz in [110] in indium. The dot-dash lines show the temperature regions in which the anomalous attenuation peak occurred.

investigated, but the results were not very reproducible as far as magnitude of attenuation was concerned. However, the measured values for two cooling and warming cycles have been included as figure 5.26 for they both show a maximum in the attenuation at beteeen 50 and 60K. Its position was difficult to locate more precisely because of the occurrence of a very large rise in attenuation on warming at around the temperature corresponding to the triple point of nitrogen (63.5K). Such a peak has been observed in GaAs by Cottam (1973) and he suggests that it is due to the solidification of nitrogen on the sample which results in a change in the reflection conditions for the sound pulse at the solid/air boundary.

The attenuation behaviour on approaching the melting point has also been measured. The results show a small rise near the melting point starting at about 20 to 30 degrees from it: figure 5.27 collects the results obtained for the 11.5 and 15 at.% Tl alloys.

5.3.3 Errors in attenuation measurement

In addition to attenuation mechanisms which derive from inherent physical properties of the sample being studied, there are contributions to the measured attenuation from the geometrical properties of the sample. These must be identified and subtracted off from the measured values to obtain the true attenuation being studied. The two main sources of error arise from diffraction of the ultrasonic beam and from non-parallelism of the sample. The first results from the fact that a real transducer deviates from a true piston source and

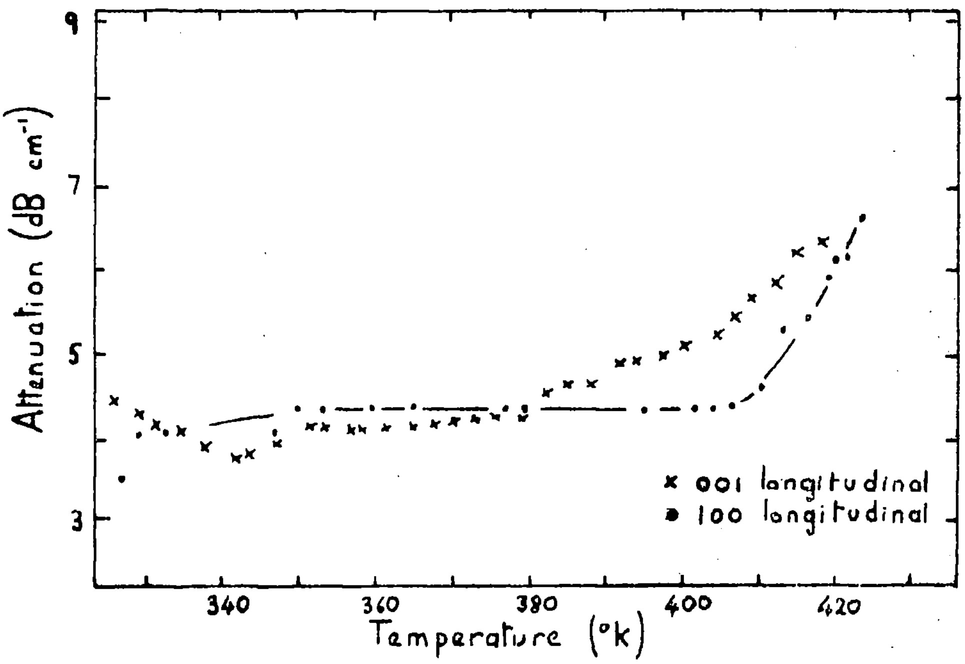

Figure 5.27(a) Ultrasonic attenuation at 14MHz in In-11.5 at.% Tl near to T_m.

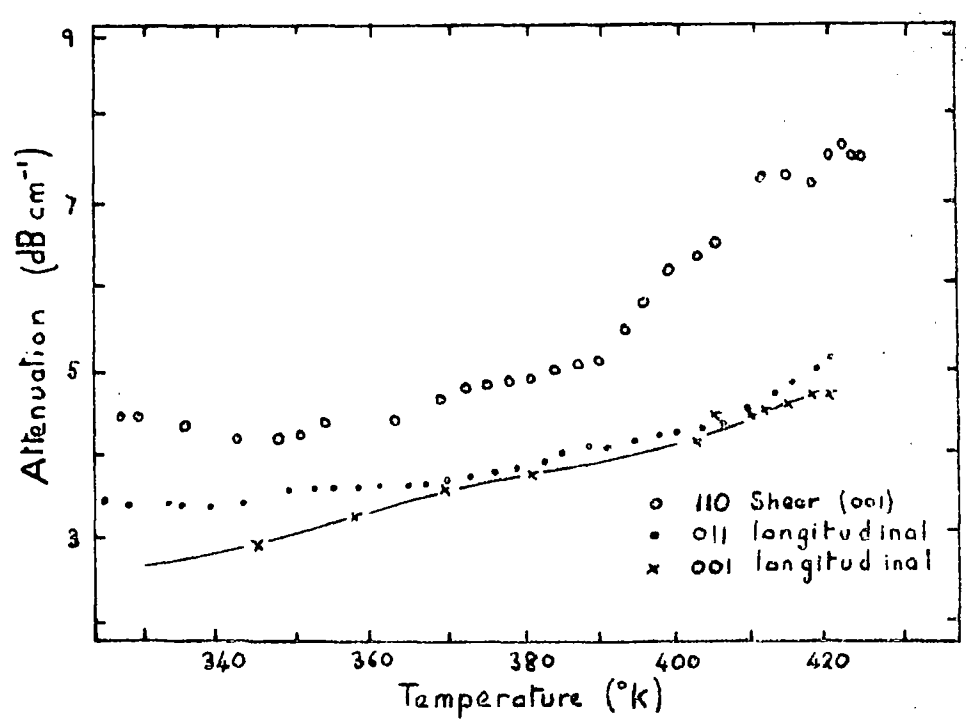

Figure 5.27(b) Ultrasonic attenuation at 14MHz in In-15 at.% Tl near to T_m.

produces wavefronts which are not planar. The ultrasound beam thus diverges and can strike the sidewalls of the specimen, a process which leads to an interference between parts of the beam which have travelled different distances in the sample. This shows up as a non-exponential echo train. Truell, Elbaum and Chick (1969) give an analysis of the problem and show that maxima in the envelope of the received pulses can be expected at $0.73\,a^2/\lambda$, $1.05\,a^2/\lambda$, $2.4\,a^2/\lambda$ and beyond. Here, a is the radius of the circular source and λ is the wavelength of the sound wave. When there is a diffraction effect present the attenuation can be measured by matching the calibrated exponential to the start of the echo train and to the top of one of the maxima. If the measured value thus obtained is α_m, then the correction to be subtracted is given by (Truell et al., 1969)

$$\alpha_d = \alpha_m \left[\mu(a^2/\lambda)\right]^{-1} \text{dB/cm},$$

where $\mu = 0.78$, 1.05 or 2.4 according to the maximum used to determine α_m. The correction is thus frequency dependent, and is smaller at higher frequencies.

Truell et al. (1969) also derive an expression for the effect of non-parallelism on the envelope of the echo train, and show that it is modulated by a Bessel function. The apparent increase in attenuation is less when the wedge angle Θ is smaller, and when the frequency is reduced, in contrast to diffraction effects which have the opposite frequency dependence. If the frequency of the wave is ν, then the attenuation due to non-parallelism is given by (Truell et al., 1969)

$$\alpha_{np} = 8.7\ 10^{-5} \nu\, a\, \Theta \quad \text{dB/echo}.$$

An apparent wedging effect can occur in non-uniform samples in which the variation of elastic properties can result in a variation of transit times in different regions. The analysis is then in terms of an effective wedge angle θ_e, which can be determined by the form of the echo train.

The work described here was carried out largely at a single frequency, with the qualitative frequency dependence of attenuation being of interest. Further, the changes seen on variation of temperature were greatly in excess of any error in the measurements from either of the above sources. Thus no correction need be, or has been, applied to any of the graphs of attenuation versus temperature presented. A specimen calculation of errors now follows in which typical values are used for the parameters involved.

i) Diffraction loss. Measure to 3rd maximum, occurring at $2.4\ a^2/\lambda$. Take $\nu = 15\times10^6$ Hz, $v = 2.0\times10^5$ cm sec^{-1}. Hence $\lambda = 0.0133$cm, and if $a = 0.2$ cm then $a^2/\lambda = 3.0$cm. The correction is thus $\alpha_m/2.4\times3.0 = 0.139\alpha_m$, or about 14%.

ii) Non-parallelism. Let a and ν be as before, and take $\theta = 5\times10^{-4}$ rad. Then $\alpha_{np} = 8.7\times10^{-5}\times15\times10^{-6}\times0.2\times5\times10^{-4}$ dB/echo

$$= 0.131 \text{ dB/echo}.$$

If the sample thickness is 0.3cm, then $\alpha_{np} = 0.217$ dB/cm at 15MHz. This last value is small compared with measured values of up to 20dB/cm, with a typical small value of 2 or 3 dB/cm.

Another source of error arises from the change in bond characteristics with temperature. This is more difficult to evaluate, but when certain sets of measurements were repeated using a different bonding material there was no apparent discrepancy in the results over a wide temperature range.

CHAPTER 6

POISSON'S RATIO IN INDIUM - THALLIUM ALLOYS

6.1 Introduction to Poisson's ratio

Interest in Poisson's ratio has stemmed from early work on elasticity. Poisson (1829) described a molecular theory of solids, and deduced a value for the ratio of lateral compression to longitudinal expansion, as a result of a longitudinal stress, to be $\frac{1}{4}$ for a central force polycrystal. In practice, deviations from $\frac{1}{4}$ were found for many solids. Wertheim (1848) performed experiments on glass and brass, and as a result suggested, with no theoretical foundation, that the ratio should be $\frac{1}{3}$. At the time of these workers there was discussion on the validity of the rari-constant and multi-constant theories of elasticity. The former implied that there were 15 independent elastic constants for a triclinic crystal, while the latter required 21. From the central force, rari-constant, theory come the Cauchy relations, which are a set of six equalities between six pairs of elastic constants. A Poisson's ratio of $\frac{1}{4}$ follows from rari-constant considerations, and interest in this ratio centred on attempts to test experimentally the two theories.

From a mechanical engineering point of view it is of interest to measure Poisson's ratio in constructional materials, and values have been obtained for a wide range of solids. Table 6.1 gives a representative selection. The usual method of determining Poisson's ratio for isotropic solids is by measurement of the shear modulus G and the Young's modulus E by extensional and torsional experiments.
Then Poisson's ratio ν is given by

$$\nu = \frac{E}{2G} - 1 \qquad (6.1)$$

TABLE 6.1

Poisson's ratio for various materials in an isotropic form *

Aluminium	0.345
Bismuth	0.330
Chromium	0.210
Gold	0.44
Iron (cast)	0.27
Lead	0.44
Platinum	0.377
Zinc	0.249
Steel (mild)	0.291
" (tool)	0.287

* Taken from Kaye and Laby (1966).

Very little work has been done on anisotropic media. In an elegant experiment on the vibration of quartz plates Wright and Stuart (1931) derived expressions, applicable to quartz, of the variation of Poisson's ratio for directions of applied stress in the xy plane; they gave the results for three such directions. For cubic crystals Turley and Sines (1971) have produced equations by which the Young's modulus, shear modulus and Poisson's ratio can be calculated for arbitrary axial sets, but in the case of Poisson's ratio they give no example of an actual computation. The methods devised by Turley and Sines and by Wright and Stuart have been aimed at simplifying the computational procedures so that calculations can be done by hand in a reasonable time. In calculations to be more fully described below a method is used for performing a computer-assisted evaluation of Poisson's ratio in the plane perpendicular to an arbitrary direction of applied stress. A direct use of the tensor transformation law of equation 3.16 is made and thus there is no need to invoke the special procedures developed for particular symmetries, mentioned above. An application of this method to arsenic, antimony and bismuth has already been made (Gunton and Saunders, 1972).

Crystal stability conditions impose limits on Poisson's ratio. Those which apply to isotropic media are well-known: any experimental value must lie between -1 and $+\frac{1}{2}$. (See, for example, Southwell 1941). In practice, no material is known which has a negative value of ν (which would mean that a longitudinal expansion was accompanied by a lateral expansion) when it is in a polycrystalline form. Ledbetter (1973) has discussed the meaning of the limits for central-force crystals.

No previous work has been published concerning the limiting values of Poisson's ratio for anisotropic media. A method for deriving these limits for single crystals will be described, based on the stability criteria of Born. This in itself is of interest in the study of the elastic behaviour of solids in general, but the prime object of this work has been to investigate the way in which the Poisson's ratio of indium-thallium alloy single crystals varies in the vicinity of the phase transition, and to compare the actual values for this ratio with calculated limiting ones to gain insight into the nature of the elastic instability that exists at the phase transition.

6.2 Evaluation of Poisson's ratio for single crystals

The generalised form of Hooke's law is

$$\epsilon_{ij} = S_{ijkl}\,\sigma_{kl} \qquad (6.2)$$

where $\hat{\epsilon}$ and $\hat{\sigma}$ are the strain and stress tensors respectively. For tetragonal crystals belonging to the Laue group TI, which includes the point group of interest here, the elastic compliance tensor components S_{ijkl} can be written in matrix notation as

$$\begin{pmatrix} S_{11} & S_{12} & S_{13} & 0 & 0 & 0 \\ S_{12} & S_{11} & S_{13} & 0 & 0 & 0 \\ S_{13} & S_{13} & S_{33} & 0 & 0 & 0 \\ 0 & 0 & 0 & S_{44} & 0 & 0 \\ 0 & 0 & 0 & 0 & S_{44} & 0 \\ 0 & 0 & 0 & 0 & 0 & S_{66} \end{pmatrix} \qquad (6.3)$$

Poisson's ratio relates lateral strain to longitudinal strain as a result of a longitudinal stress. This ratio is thus $\epsilon_{jj}/\epsilon_{ii}$, and from equation 6.2 we can write

$$\epsilon_{jj}/\epsilon_{ii} = S_{jjii}\sigma_{ii} / S_{iiii}\sigma_{ii} = S_{jjii}/S_{iiii} . \tag{6.4}$$

Since a positive longitudinal strain is always accompanied by a negative lateral strain for isotropic materials, Poisson's ratio is defined as $- S_{jjii}/S_{iiii}$ so as to give practical values which are positive for such materials. However, in single crystals the ratio has values which depend on the directions of the strains, and both positive and negative values can be found. For an arbitrary set of axes x', y', z', Poisson's ratio (ν'_{ij}) can be written as $- S'_{iijj}/S'_{iiii}$, using the fact that $S_{ijkl} = S_{klij}$. To calculate ν'_{ij}, the tensor transformation law must be used to obtain the primed compliances from the unprimed ones. Equation 3.16 is rewritten here:

$$S'_{ijkl} = a_{im}a_{jn}a_{kp}a_{lq}S_{mnpq} . \tag{3.16}$$

Let the transformed axes be defined as follows. Let the x' axis be in the direction of applied stress to produce the longitudinal strain. Then y' and z' will be in the plane perpendicular to Ox'. If ν'_{12} is considered, it is then necessary to evaluate $- S'_{12}/S'_{11}$ (using the contracted subscript notation) for various orientations of y' in its plane. Note that S'_{11} has a constant value for a given direction of applied stress. The method outlined by Turley and Sines (1971) has been used to calculate the direction cosines, relative to the conventional crystal axes, of the y' axis as a function of the angle it makes with the meridional tangent for the plane. From the angles as defined in figure 6.1 the direction cosines are

$$\left[a_{ij}\right] = \begin{bmatrix} A & B & C \\ D\cos\delta - E\sin\delta & F\cos\delta - G\sin\delta & H\cos\delta \\ D\sin\delta + E\cos\delta & F\sin\delta + G\cos\delta & H\sin\delta \end{bmatrix} \qquad (6.5)$$

where
$A = \cos\alpha\cos\beta$ $\quad E = -\sin\alpha$
$B = \sin\alpha\cos\beta$ $\quad F = -\sin\alpha\sin\beta$
$C = \sin\beta$ $\quad G = \cos\alpha$
$D = -\cos\alpha\sin\beta$ $\quad H = \cos\beta$

Substitution of values obtained from equation 6.5 into 3.16 leads to the desired result. Equations for S'_{11} and S'_{12} for tetragonal symmetry are given; cubic symmetry results follow as a special case of those for tetragonal.

$$S'_{11} = (a_{11}^4 + a_{12}^4)S_{11} + 2a_{11}^2 a_{12}^2 S_{12} + 2a_{13}^2(1 - a_{13}^2)S_{13} + a_{13}^4 S_{33} + a_{13}^2(1 - a_{13}^2)S_{44} + a_{11}^2 a_{12}^2 S_{66} \qquad (6.6a)$$

$$S'_{12} = (a_{11}^2 a_{21}^2 + a_{12}^2 a_{22}^2)S_{11} + (a_{21}^2 a_{12}^2 + a_{11}^2 a_{22}^2)S_{12} + \left[a_{23}^2(a_{11}^2 + a_{12}^2) + a_{13}^2(a_{21}^2 + a_{22}^2)\right]S_{13} + a_{23}^2 a_{13}^2 S_{33} + \left[a_{13}a_{23}(a_{12}a_{22} + a_{11}a_{21})\right]S_{44} + a_{21}a_{22}a_{11}a_{12}S_{66} \qquad (6.6b)$$

The form of equations 6.6 allows certain other primed compliances to be calculated. For example, S'_{22} can be found by substituting a_{21}, a_{22}, a_{23} for a_{11}, a_{12}, a_{13} in equation 6.6a, and so on.

A computer programme has been prepared (Appendix III) to perform these calculations as the angle δ is varied from 0 to 180°. (The range 180° to 360° is identical to 0 to 180° because of crystal symmetry.) The programme required for input data the unprimed elastic compliance constants and the direction

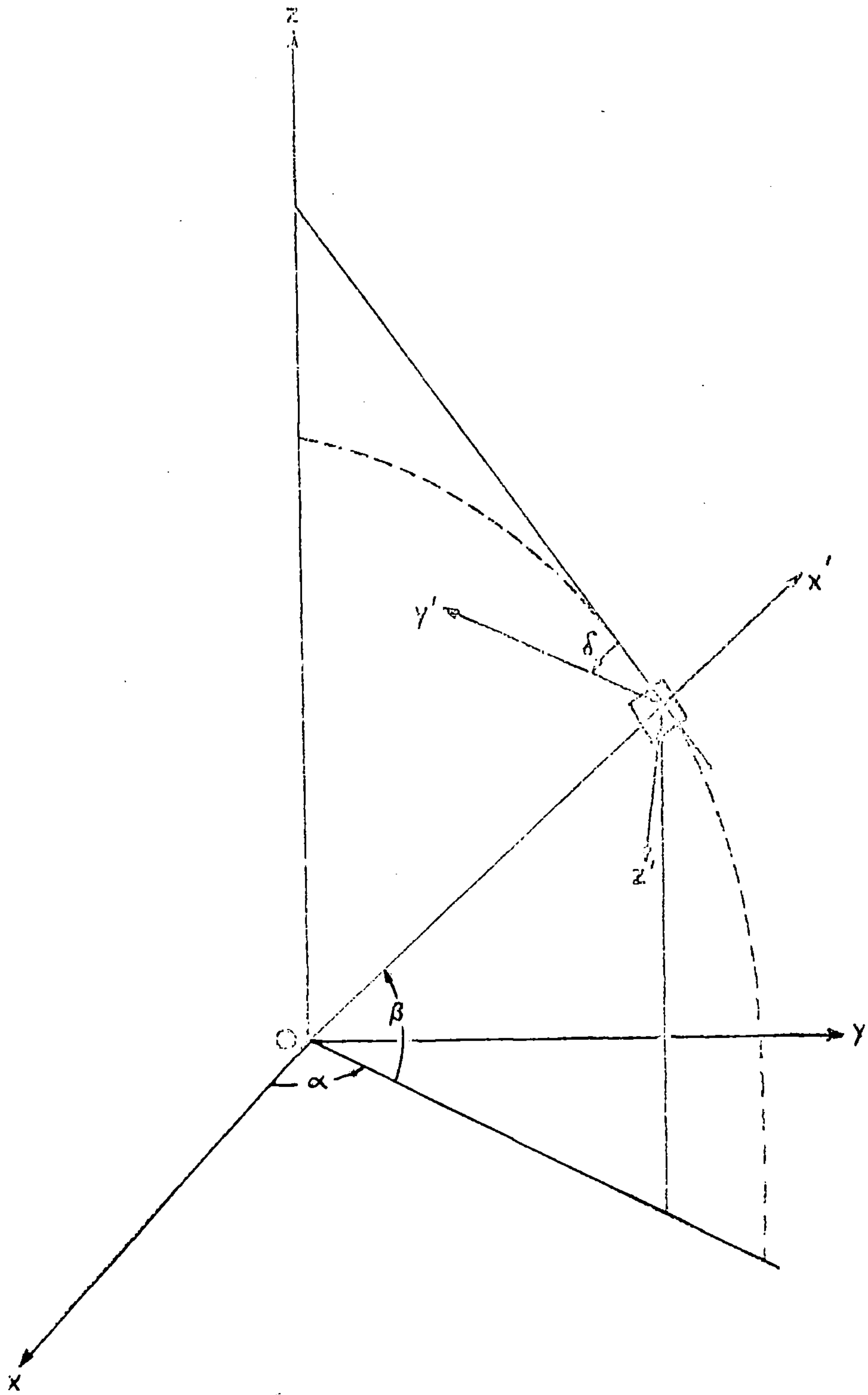

Figure 6.1 Transformation of axes.
The direction of x' is defined by the angles α and β. The axis y' is perpendicular to x' and is at an angle δ to a line, also perpendicular to x', which lies in the plane containing x' and z.

cosines of the line perpendicular to the plane in which the variation of Poisson's ratio was sought.

6.3 Representation of results

Unlike Young's modulus, the Poisson's ratio cannot be represented by a three-dimensional surface, because two directions are needed to specify its value. A convenient representation is to plot the angular dependence of the ratio for a given plane superimposed on a standard projection onto a suitable crystallographic plane. The centre of the plot coincides with the point on the standard projection which represents the plane perpendicular. In figure 6.2 is given, by way of illustration, the result for bismuth (Gunton and Saunders, 1972) in which a projection onto the (001) plane has been used. Bismuth has trigonal RI symmetry, with the [001] direction being one of three-fold rotational symmetry. Consequently figure 6.2 is three-fold symmetric about the point representing [001]. It is interesting to note that negative values are found. A 120° sector would be sufficient in this case to represent completely the Poisson's ratio behviour; a 180° sector has been used to show up more clearly the difference between the +y and -y axes. For tetragonal symmetries only a 45° sector is required, while an even smaller section of the stereographic projection is needed for a cubic system. But in the diagrams given for indium-thallium alloys a 45° sector has been used throughout to ease comparison by inspection.

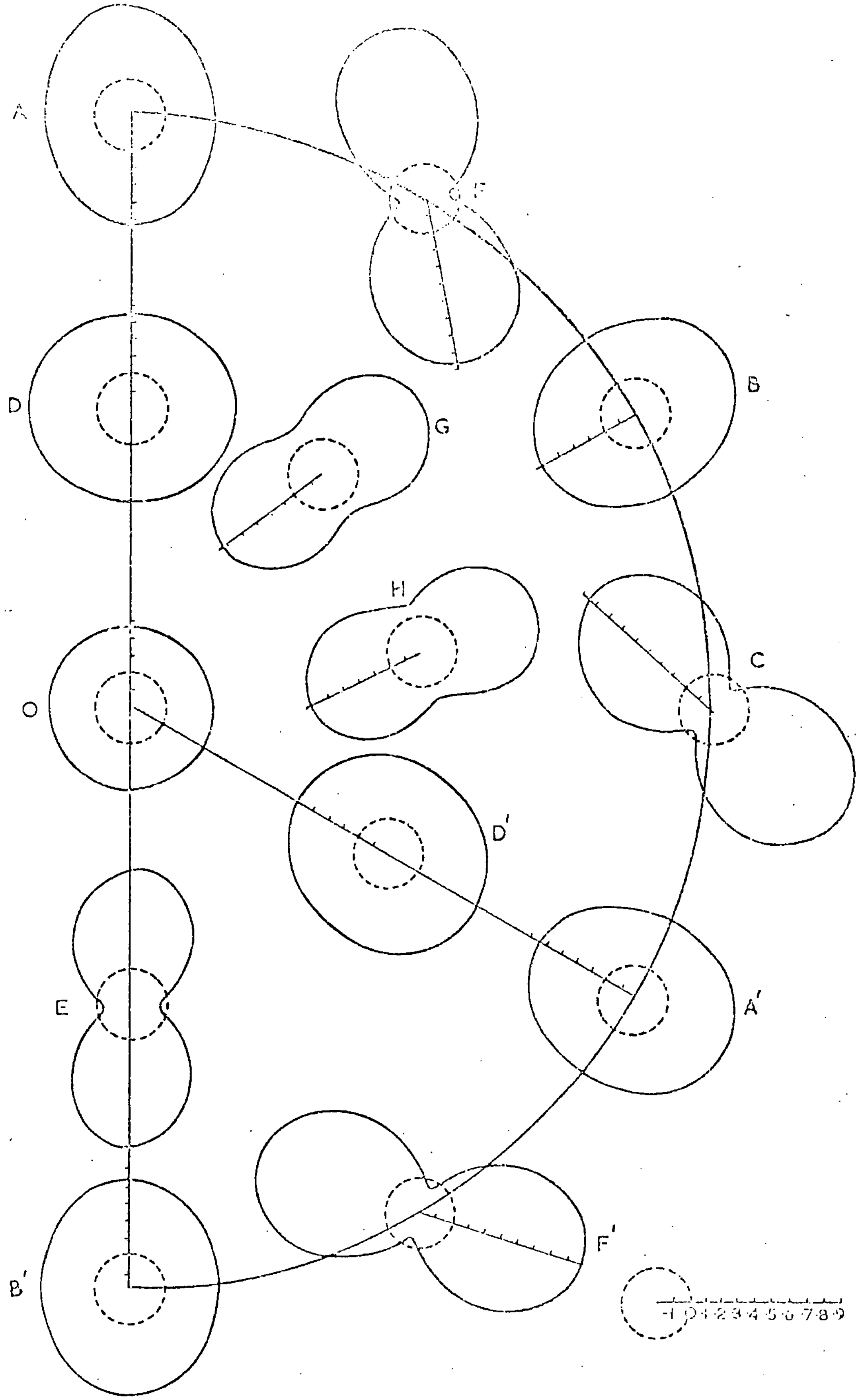

Figure 6.2 Poisson's ratio variation in bismuth shown on a stereographic projection onto the (001) plane. The x, y and z axes are represented by the points at the centre of diagrams C, A and O, respectively. B' represents -y.

6.4 Application to the indium-thallium alloys

The variation of Poisson's ratio has been investigated in planes perpendicular to a number of directions in indium-thallium alloys of both the cubic and tetragonal forms. The directions chosen were fairly evenly distributed over the quadrant of the stereographic projection onto the xy plane bounded by the x and y axes; they included the three crystallographic axes and directions midway between them. The calculations were performed using room-temperature values of the elastic compliance data of indium and of the tetragonal alloys containing 11.5 and 15 at.% thallium. In this way the Poisson's ratio variation could be studied as the phase boundary was approached from the tetragonal side, using composition as the variable. In addition, the behaviour of Poisson's ratio of a cubic alloy of composition In-27 at.% Tl was determined at 290K and at 200K and 125K, so as to enable an approach to the phase boundary from the cubic side to be studied. Elastic compliance data were taken from Table 5.1 and figure 5.8 for the alloys, and from Chandresekhar and Rayne (1961) for indium. The results of the calculations are shown in figures 6.3 to 6.6.

Several trends can be seen when the curves are compared. Addition of thallium to indium results in a reduction of the axial ratio, and an overall decrease in the anisotropy of the elastic constants, as the cubic phase is approached. Thus $(C_{11} - C_{33})$ and $(S_{11} - S_{33})$ both decrease towards zero, as do $(C_{12} - C_{13})$ and $(S_{12} - S_{13})$. Consequently, the diagrams for the tetragonal alloys reflect this trend, and the curves

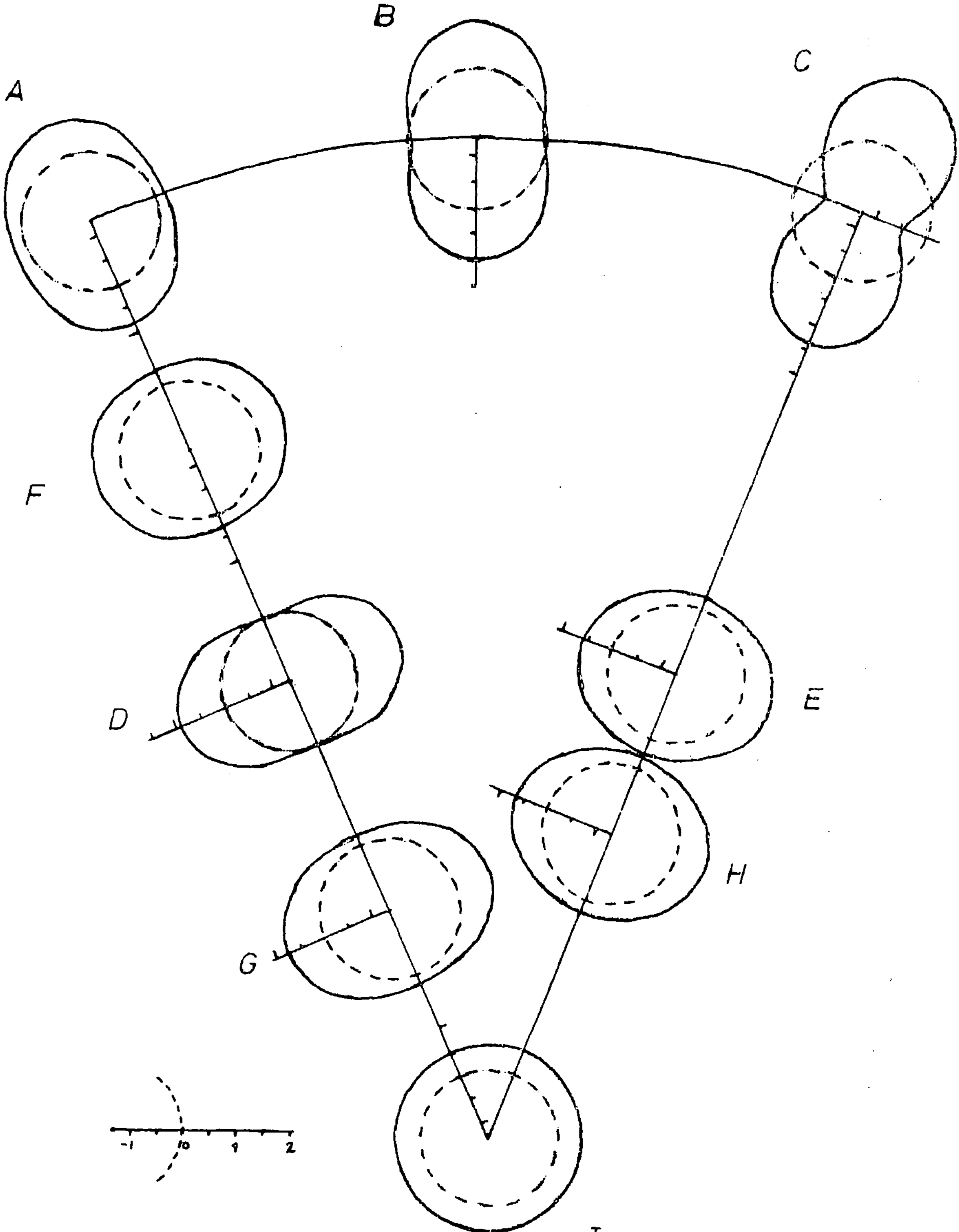

Figure 6.3 Poisson's ratio variation in indium. The diagrams are shown superimposed on a standard projection onto the (001) plane. Direction cosines for the diagrams shown are: A (0,1,0); B (0.382,0.925,0); C (0.707,0.707,0); D (0,0.707, 0.707); E (0.5,0.5,0.707); F (0,0.925,0.382); G (0,0.382,0.925); H (0.354,0.354,0.866); J (0,0,1).

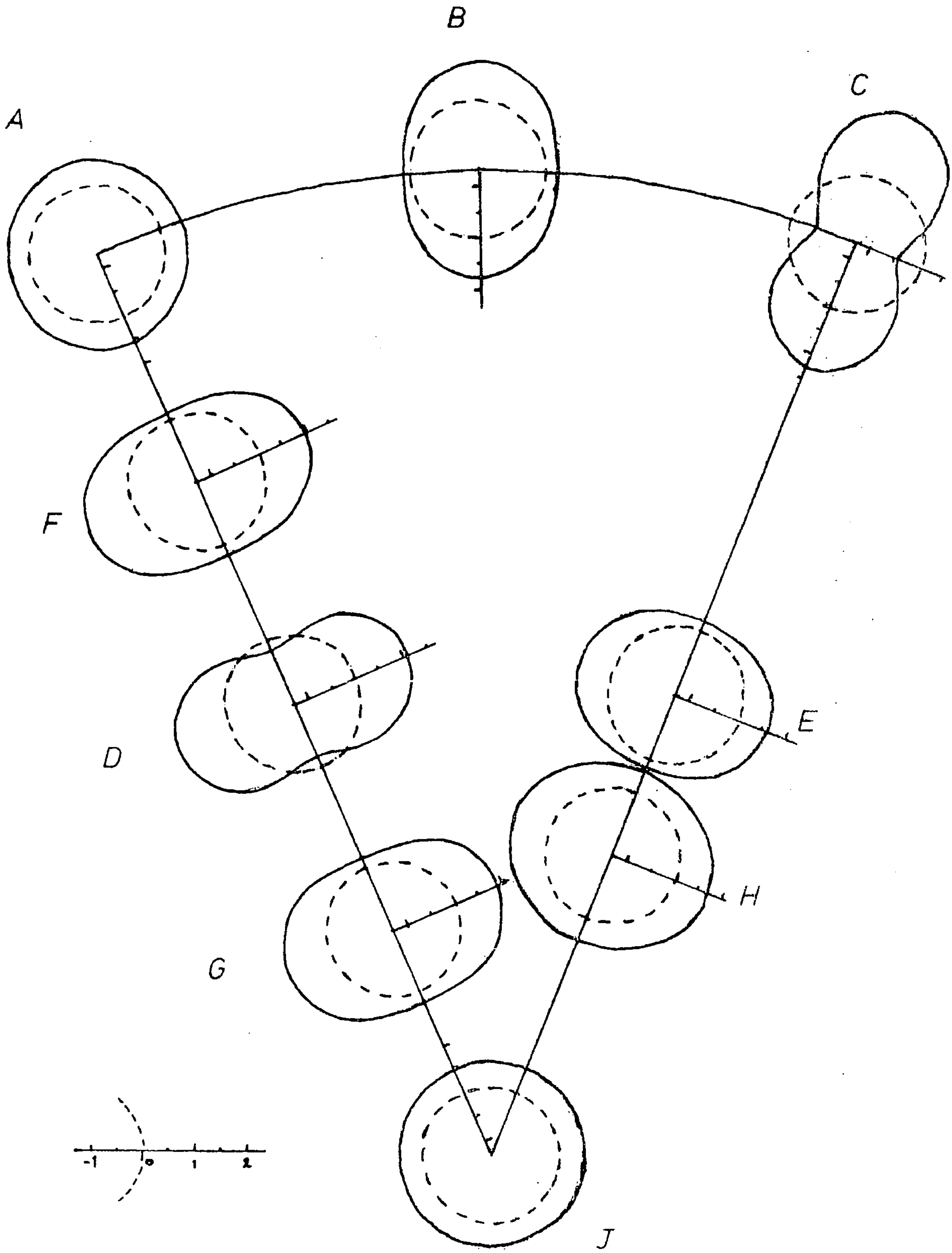

Figure 6.4 Poisson's ratio variation in In-11.5 at.% Tl. The direction cosines for the various diagrams are as given in figure 6.3

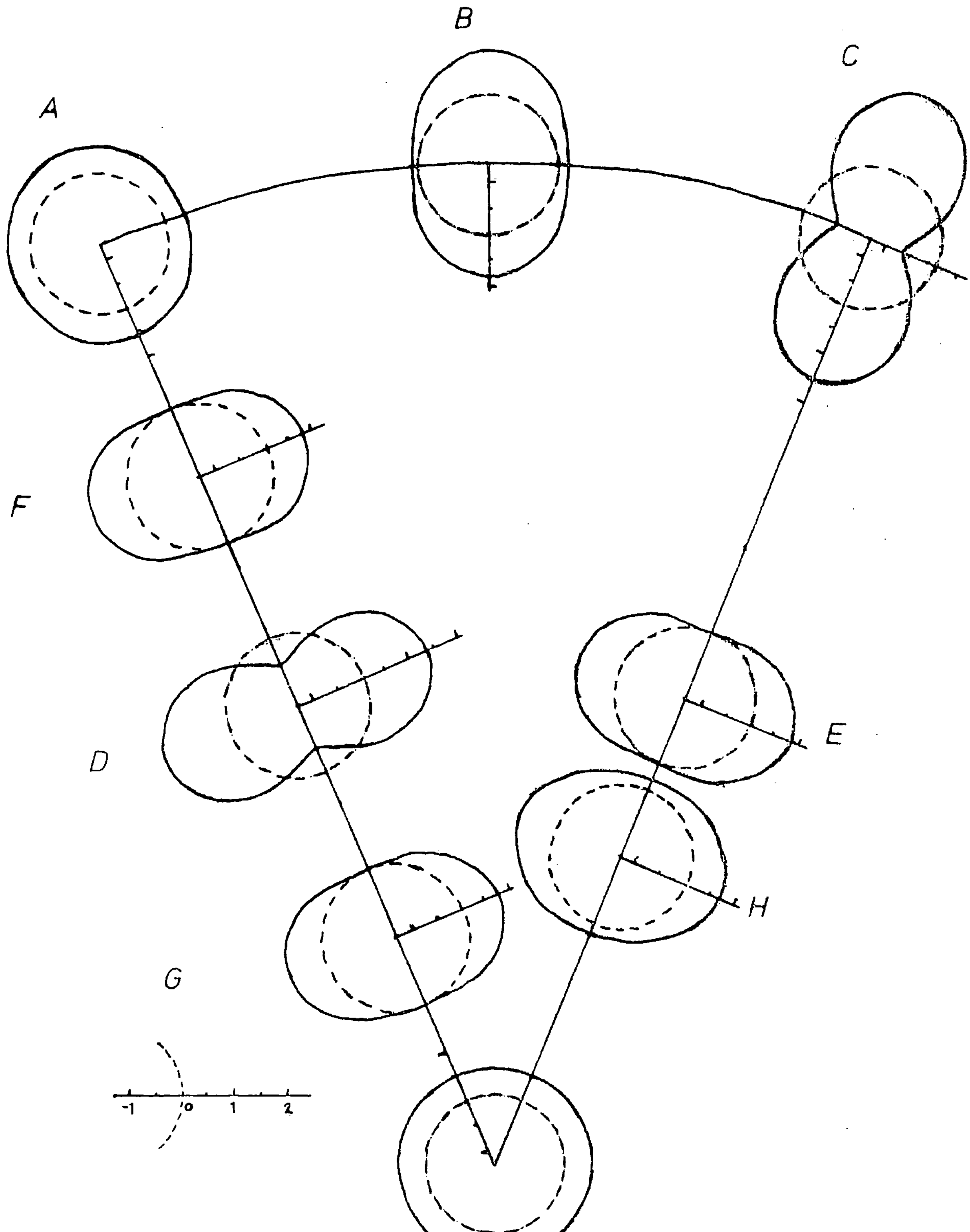

Figure 6.5 Poisson's ratio variation in In-15 at.% Tl. The direction cosines for the various diagrams are as given in figure 6.3

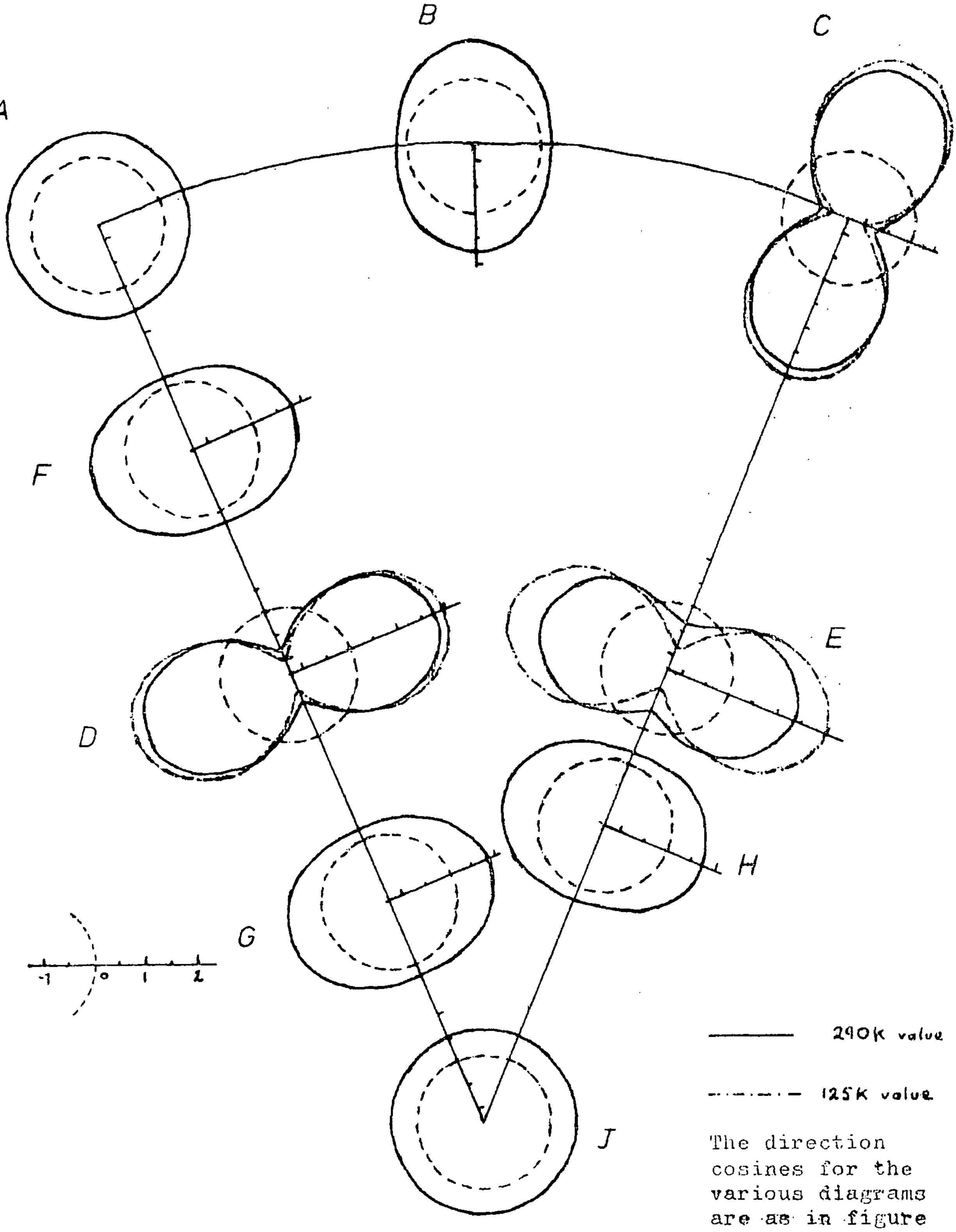

The direction cosines for the various diagrams are as in figure 6.3

Figure 6.6 Poisson's ratio variation for In-27 at.% Tl at 290K and at 125K. Where only the solid curve is shown it is because the values for 125K are indistinguishable on this scale from those for 290K.

centred on the [100] and [010] positions become more nearly circular until, in the case of the cubic In-27at.% Tl alloy, they are truly circular, and are identical to the curve centred on [001], by symmetry of the point group. A similar decrease in anisotropy can be seen in the curves labelled B on each figure. But there are some curves in which another effect can be seen. In curves C, D and E there is a marked increase in anisotropy, particularly in C, which is centred on the [110] position. The effect can be seen both as a function of composition, in figures 6.3 to 6.5, and of temperature, as in figure 6.6 . In both cases the increase accompanies the approach to the phase boundary. Now it is in the {110} planes that the two shears occur which can be considered to be the basis of the mechanism of the transition (Bowles et al., 1950; Burkart and Read, 1953), and it is in just these planes that the largest anisotropy of Poisson's ratio is found. However, this fact is not of primary importance when relating the Poisson's ratio behaviour to the mechanism of the phase transition, for a similar form of anisotropy is found in arsenic (Gunton and Saunders, 1972). Figure 6.7 shows the stereographic projection onto the xy plane for that element with the Poisson's ratio curves superimposed on it. The form of the variation for all directions of longitudinal strain in the xy plane is similar to that for the [110] direction in indium-thallium alloys, although the slip and cleavage properties of arsenic (slip and cleavage plane (001), no preferred slip direction) are very different from the alloys, in which no cleavage occurs and slip takes place on {110} planes. Consequently, before the variation of Poisson's ratio

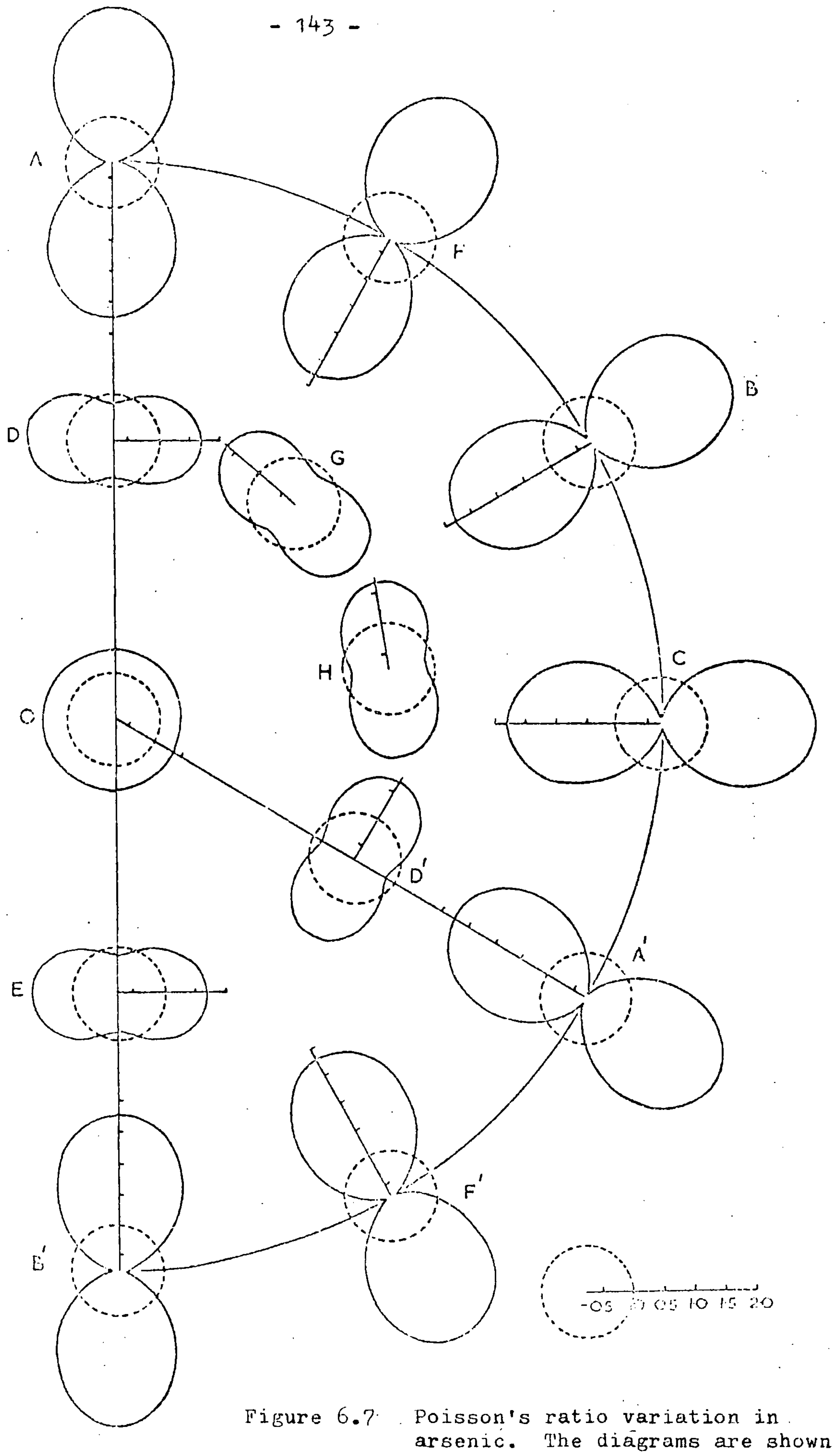

Figure 6.7 Poisson's ratio variation in arsenic. The diagrams are shown superimposed on the standard projection onto the (001) plane. C, A and O are centred on the x, y and z axes respectively.

with orientation, alloy composition and temperature can be satisfactorily related to the mechanism of the phase transition, it is necessary to consider the limits on that ratio set by crystal stability conditions; the next section is devoted to an analysis of those limits. In section 6.6 the results of the present section will be compared with the limiting values.

6.5 Stability limits on Poisson's ratio

The requirement that the strain energy density be positive definite for lattice stability implies that the bulk modulus K and the shear modulus G must be positive quantities. For an isotropic material, K and G are related to Young's modulus E and Poisson's ratio ν by

$$K = \frac{E}{3(1 - 2\nu)} \tag{6.7a}$$

and

$$G = \frac{E}{2(1 + \nu)} \tag{6.7b}$$

Thus the stability conditions that K and G are both greater than zero set the two well-known limits of 0.5 and -1.0 on Poisson's ratio. Treating now the isotropic material as a special case of an anisotropic medium, we can derive the upper limit by substituting the appropriate equalities between the elastic compliance constants ($S_{11}=S_{22}=S_{33}$; $S_{12}=S_{13}=S_{23}$) for an isotropic medium in the general expression for compressibility (equation 3.19).

$$\beta = \frac{1}{K} = S_{11} + S_{22} + S_{33} + 2(S_{12} + S_{13} + S_{23}) > 0$$

$$\therefore \; S_{11} + 2S_{12} > 0 \;, \quad \text{or } \nu = -S_{12}/S_{11} < \tfrac{1}{2} \,.$$

Also, for an isotropic solid S_{44} equals $2(S_{11}-S_{12})$, so that

$$\frac{1}{S_{44}} = G = \frac{1}{2(S_{11}-S_{12})} > 0$$

$$\text{i.e.} \quad \nu > -1$$

A value of Poisson's ratio of $\frac{1}{2}$ would be found in an incompressible fluid ($\beta = 0$), as may be seen quite easily by considering a cylindrical element of fluid of length l and radius r. Its volume V is equal to $\pi r^2 l$. If the length and radius become l+dl and r+dr, respectively, then for conservation of volume $dV = 2\pi rl\,dr + \pi r^2\,dl = 0$. Whence $-(dr/r)/(dl/l) = \frac{1}{2}$, as required. A fluid cannot support shear. The other limit of - 1 occurs when the shear modulus G is infinite, as can be seen from equation 6.7(b).

To extend the derivation of the stability limits to an anisotropic medium, such as a single crystal, the volume compressibility condition can be used as a starting point, but not the shear modulus one directly, since the latter does not in general involve S_{11} or S_{12}, and we turn instead to the Born stability criteria discussed in section 3.4.2. It will be shown that a positive definite shear modulus for isotropic materials follows as a special case of the more general expression derived for anisotropic media.

For a homogeneous deformation the energy density can be written in matrix notation as $\frac{1}{2}\sum S_{ij}\sigma_i\sigma_j$ and is positive definite if the determinants of the principal minors of the matrix of compliances S_{ij} are all positive. Several criteria for stability result, including the condition that $S_{11}S_{22} > S_{12}^2$, the one of relevance here. The stability criteria have the same form whatever axial set is used; therefore, for components referred to the set x', y', z' we have

$$S_{11}' S_{22}' > S_{12}'^2 , \qquad (6.8)$$

and, since the bulk modulus is invariant under a general transformation of axes,

$$S_{11}' + S_{22}' + S_{33}' + 2(S_{12}' + S_{23}' + S_{13}') > 0 \qquad (6.9)$$

Before the limits on the ratio $-S_{12}'/S_{11}'$ can be calculated it is necessary to rewrite the conditions 6.8 and 6.9 in a form which enables this ratio to be varied (or, equivalently, for S_{12}' to be varied, keeping S_{11}' fixed) independently of the other compliances until the limits of the inequality are reached. (As the equations stand at present this may not be possible because the six terms involved are not necessarily independent of each other, and a change in one of them may well imply a change in another.) A suitable form for equations 6.8 and 6.9 is one in which all the compliances involved are independent; in the most general transformation 21 compliance constants can be non-zero, but the number of independent components — as determined by the Laue group — remains unaltered. For example, in the fct indium-thallium alloys there are always six independent S_{ij}', but these need not have the same subscripts as those which apply when the normal crystallographic set Ox_i is used. Subject to certain restrictions for special cases of the axial transformations, we are free to choose any six components as the independent ones. But when a stress is applied along a symmetry direction a special case arises and all six compliances S_{ij}' in condition 6.9 are not independent.

The method used to find the relationship between any particular dependent component and the six chosen independent ones is given, together with considerations governing the choice of independent components for special cases, in Appendix II. It is sufficient to note here that a set which is suitable under some conditions is S_{11}', S_{12}', S_{23}', S_{33}', S_{44}' and S_{55}'. (That which follows will be written in terms of this set, but the method can be readily applied to any other set.) In equation 6.9 there are now two dependent terms (S_{13}' and S_{22}') whose dependence on the set of six must be found. We write

$$\begin{aligned} S_{13}' &= f_1S_{11}' + f_2S_{12}' + f_3S_{23}' + f_4S_{33}' + f_5S_{44}' + f_6S_{55}' \\ S_{22}' &= g_1S_{11}' + g_2S_{12}' + g_3S_{23}' + g_4S_{33}' + g_5S_{44}' + g_6S_{55}' \end{aligned} \qquad (6.10)$$

where f_i and g_i are coefficients determined by the methods of the Appendix. The inequality 6.9 then becomes

$$\begin{aligned} &(1+g_1+2f_1)S_{11}' + (2+g_2+2f_2)S_{12}' + (2+g_3+2f_3)S_{23}' \\ &\quad +(1+g_4+2f_4)S_{33}' + (g_5+2f_5)S_{44}' + (g_6+2f_6)S_{55}' > 0 \end{aligned} \qquad (6.11)$$

Since these compliances are independent, and noting that $S_{11}' > 0$, we can transform the inequality by dividing by S_{11}' and rearranging, to give

$$\begin{aligned} \nu(2+g_2+2f_2) < (1+g_1+2f_1) + \frac{1}{S_{11}'}\Big[&(2+g_3+2f_3)S_{23}' + (1+g_4+2f_4)S_{33}' \\ &+ (g_5+2f_5)S_{44}' + (g_6+2f_6)S_{55}'\Big] \end{aligned} \qquad (6.12)$$

Equation 6.12 is of the form $\nu k_1 < k_2$ and hence $\nu < k_2/k_1$, if $k_1 > 0$ or $\nu > k_2/k_1$, if $k_1 < 0$.

In this way the condition that the bulk modulus must be positive definite leads to either an upper or a lower limit — depending on the sign of $(2+g_2+2f_2)$ — on the Poisson's ratio in a crystal of tetragonal TI symmetry.

The Born stability criterion 6.8 becomes

$$s_{11}'(g_1 s_{11}' + g_2 s_{12}' + g_3 s_{23}' + g_4 s_{33}' + g_5 s_{44}' + g_6 s_{55}') > s_{12}'^2$$

or, dividing by $s_{11}'^2$ and rearranging

$$-\nu^2 - g_2\nu + g_1 + \frac{1}{s_{44}'}(g_3 s_{23}' + g_4 s_{33}' + g_5 s_{44}' + g_6 s_{55}') > 0 \qquad (6.13)$$

Setting the LHS of 6.13 to zero and solving for ν we obtain two limits between which the inequality is true; the existence of the negative coefficient of ν^2 ensures that the solutions define a finite range.

Thus an upper and lower limit is set by the Born stability criteria, and either an upper or a lower limit by the requirement that the volume compressibility be positive definite. From these the two limits that obtain in practice may readily be found.

For the isotropic case $g_1 = 1$; $g_2=g_3=g_4=g_5=g_6=0$, and either $f_2=1$ or $f_3=1$ while the other f_i are zero. Then 6.13 becomes $-\nu^2 + 1 > 0$, which results in $-1<\nu<+1$, while 6.12 leads to $4\nu<2$ or $\nu<\frac{1}{2}$: the limits are thus $-1<\nu<\frac{1}{2}$ in practice.

One further consideration, which affects the applicabitity of equation 6.12 needs to be discussed. For a particular orthogonal axial system the numerical values of f_i and g_i depend upon the particular set of independent compliances chosen. But because β is an invariant the LHS of inequality 6.11 must remain unaltered by this choice. Consider the case in which S_{66}' replaces S_{55}' in the chosen independent set; f_i and g_i are replaced by f_i' and g_i', and 6.11 becomes

$$(1+g_1'+2f_1')S_{11}' + (2+g_2'+2f_2')S_{12}' + (2+g_3'+2f_3')S_{23}'$$
$$+ (1+g_4'+2f_4')S_{33}' + (g_5'+2f_5')S_{44}' + (g_6'+2f_6')S_{66}' > 0 \quad (6.14)$$

The limiting value of ν as determined by this inequality (with one set of independent compliances) will differ from that given by 6.11 (using another set) unless $(2+g_2+2f_2)$ is equal to $(2+g_2'+2f_2')$. Consequently the axial sets for which the limit is defined by this method are restricted to those in which any alteration in those compliances taken as independent does not affect the overall dependence of the terms in 6.9 on S_{12}'. For the cubic and tetragonal symmetries this means that the limits, as defined by this method, can be calculated along crystallographic axes and midway between them.

6.6 Limits for the indium-thallium alloys

The calculation of the limits requires a knowledge of the independent elastic constants for the axial set under consideration, and the way in which the other dependent ones that enter into the calculation do, in fact, depend on them. The independent constants for the various orientations considered in the cubic and tetragonal systems are given in Table 6.2. The relations between dependent and independent constants for the tetragonal system are of a simpler form than those for the cubic, and it was possible to find the relations by direct inspection, although the procedures given

Table 6.2

Relationships between elastic compliances for various axial configurations. (The directions of x' and y' are expressed relative to the conventional crystallographic axes.)

Tetragonal

Direction of x'	Direction of y'	Independent compliances	Dependent compliances *
[100]	[010]	$S_{11}, S_{12}, S_{13}, S_{33}, S_{44}, S_{66}$	$S_{22}=S_{11}$; $S_{23}=S_{13}$
	[011]	$S'_{11}, S'_{12}, S'_{23}, S'_{22}, S'_{44}, S'_{66}$	$S'_{33}=S'_{22}$; $S'_{13}=S'_{12}$
	[001]	$S'_{11}, S'_{22}, S'_{13}, S'_{12}, S'_{44}, S'_{55}$	$S'_{33}=S'_{11}$; $S'_{23}=S'_{12}$
[110]	[001]	$S'_{11}, S'_{22}, S'_{12}, S'_{13}, S'_{44}, S'_{55}$	$S'_{33}=S'_{11}$; $S'_{23}=S'_{12}$
	[1$\bar{1}$0]	$S'_{11}, S'_{12}, S'_{13}, S'_{33}, S'_{44}, S'_{66}$	$S'_{22}=S'_{11}$; $S'_{23}=S'_{12}$
	45° to [001]	$S'_{11}, S'_{12}, S'_{23}, S'_{22}, S'_{44}, S'_{66}$	$S'_{33}=S'_{22}$; $S'_{13}=S'_{12}$
[001]	any	$S'_{11}, S'_{12}, S'_{23}, S'_{33}, S'_{44}, S'_{66}$	$S'_{22}=S'_{33}$; $S'_{13}=S'_{12}$

Cubic

Direction of x'	Direction of y'	Independent compliances	Dependent compliances *
[100]	[010] & [001]	$S'_{11}, S'_{12}, S'_{66}$	$S'_{13} = S'_{12}$; $S'_{23} = S'_{12}$ $S'_{33} = S'_{11}$; $S'_{22} = S'_{11}$
	[011]	$S'_{11}, S'_{12}, S'_{66}$	$S'_{13} = S'_{12}$; $S'_{22} = S'_{33}$ $S'_{33} = \frac{1}{2}(S'_{11}+S'_{12}) + \frac{1}{4}S'_{66}$ $S'_{23} = \frac{1}{2}(S'_{11}+S'_{12}) - \frac{1}{4}S'_{66}$
[110]	[001]	$S'_{11}, S'_{12}, S'_{44}$	$S'_{33} = S'_{11}$; $S'_{23} = S'_{12}$ $S'_{13} = S'_{11} - \frac{1}{2}S'_{44}$ $S'_{22} = 2S'_{11} - S'_{12} - \frac{1}{2}S'_{44}$
	45° to [001]	$S'_{11}, S'_{12}, S'_{44}$	$S'_{13} = S'_{12}$; $S'_{22} = S'_{33}$ $S'_{33} = 1\frac{1}{4}S'_{11} - \frac{1}{4}S'_{12} - \frac{1}{8}S'_{44}$ $S'_{23} = -\frac{1}{4}S'_{11} + 1\frac{1}{4}S'_{12} + \frac{1}{8}S'_{44}$
	[1$\bar{1}$0]	$S'_{11}, S'_{12}, S'_{66}$	$S'_{22} = S'_{11}$; $S'_{23} = S'_{13}$ $S'_{13} = \frac{1}{2}(S'_{11}+S'_{12}) - \frac{1}{4}S'_{66}$ $S'_{33} = \frac{1}{2}(S'_{11}+S'_{12}) + \frac{1}{4}S'_{66}$

* The dependent compliances given are those required by equation 6.9

in Appendix II have been used to check the results.

The results of the limits calculations are given in Table 6.3 for indium, for the 11.5 and 15 at.% Tl tetragonal alloys and for the 27 at.% Tl cubic one. Both the upper and lower limits, together with the value of Poisson's ratio calculated from the S_{ij} are listed for longitudinal strain directions in the (001), (100) and (110) planes.

Consider first the cubic alloy. Table 6.3(d) shows the variation of ν and of its limiting value as the phase transition is approached. In the plane normal to the [100] direction the upper limit of 0.5 applies to all directions in that plane, and it is an analytically determined one; that is, it does not depend on the values of the elastic constants. The lower limit in the (100) plane does depend on the elastic constants; for the present case it does not differ appreciably from -1.0 . In this plane the Poisson's ratio can be seen to be approaching the upper limit at 125K, that is, at a temperature very close to T_c. In a direction of 45° to the [001] in the (110) plane there is again an analytic upper limit of 0.5, whereas the lower one is approaching zero at the phase transition, and again the calculated value of ν is tending to its upper limit at 125K. A similar occurrence is seen in the [001] direction in the (110) plane, although here it is the lower limit of -1 which is an analytic one, while the upper limit is not and has a value of nearly 2.0. But in the [$1\bar{1}0$] direction in this plane both the upper and lower limits tend towards the same value (-1) with the observed value of ν sandwiched in between them. Thus at 125K we find -0.986,

Table 6.3

Comparison of the observed values of Poisson's ratio with the theoretical limits for indium and indium-thallium alloys

a) Indium (290K)

plane	direction	upper limit	observed value	lower limit
(110)	[001]	1.415	1.337	-1.659
	45° to [001]	0.519	0.441	-0.881
	[1$\bar{1}$0]	-0.298	-0.453	-1
(100)	[001]	0.716	0.673	-1.180
	[011]	0.510	0.470	-0.719
	[010]	0.343	0.264	-1
(001)	x-y plane	0.514	0.486	-0.848
	[110]	0.514	0.486	-0.603
	x-y plane	0.514	0.486	-0.848

b) Indium-11.5 at.% Thallium (290K)

plane	direction	upper limit	observed value	lower limit
(110)	[001]	1.324	1.321	-1.660
	45° to [001]	0.528	0.453	-0.855
	[1$\bar{1}$0]	-0.265	-0.416	-1
(100)	[001]	0.567	0.536	-1.058
	[011]	0.511	0.481	-0.621
	[010]	0.487	0.425	-1
(001)	x-y plane	0.507	0.480	-0.946
	[110]	0.507	0.430	-0.603
	x-y plane	0.507	0.480	-0.946

Table 6.3 (continued)

c) Indium-15 at.% thallium (290K)

plane	direction	upper limit	observed value	lower limit
(110)	[001]	1.481	1.417	-1.714
	45° to [001]	0.526	0.461	-0.803
	$[1\bar{1}0]$	-0.523	-0.494	-1
(100)	[001]	0.509	0.489	-1.006
	[011]	0.511	0.487	-0.799
	[010]	0.537	0.485	-1
(001)	x-y plane	0.505	0.482	-0.994
	[110]	0.504	0.482	-0.584
	x-y plane	0.505	0.482	-0.994

d) Indium-27 at.% thallium

temperature	plane	direction	upper limit	observed value	lower limit
290K	(110)	[001]	1.788	1.757	-1
		45° to [001]	0.5	0.485	-0.179
		$[1\bar{1}0]$	-0.767	-0.787	-0.928
	(100)	[001]	0.5	0.496	-1
		[011]	0.5	0.496	-1.02
		[010]	0.5	0.496	-1
200K	(110)	[001]	1.946	1.937	-1
		45° to [001]	0.5	0.496	-0.057
		$[1\bar{1}0]$	-0.934	-0.945	-0.982
	(100)	all	0.5	0.499	-1
125K	(110)	[001]	1.988	1.986	-1
		45° to [001]	0.5	0.499	-0.014
		$[1\bar{1}0]$	-0.986	-0.988	-0.996
	(100)	all	0.5	0.50	-1

-0.988 and -0.996 as the upper limit, calculated value and lower limit, respectively.

The tetragonal alloys show a similar, although less marked, trend in the approach of Poisson's ratio towards its limit as the thallium content increases and the phase boundary is approached. The proximity of the phase boundary is still not particularly close at room temperature, even for the 15 at.% Tl composition, and so the values calculated for ν are not very near to their limits. But because of the problems associated with the growth of a single crystal in the tetragonal form containing more than about 15 at.% Tl, it has not been possible to obtain information at room temperature any closer to the boundary.

The upper and lower limits on Poisson's ratio correspond to the value of the strain energy density U passing through zero; for stability U must be positive definite. There are two ways in which U can become negative. When the volume compressibility is zero, the bulk modulus is infinite. Now the bulk modulus K can be related directly to the strain energy density, through (see, for example, Kittel,1966)

$$U = \tfrac{1}{2} K \delta^2 \qquad (6.15)$$

in which $\tfrac{1}{3}\delta = \epsilon_{11} = \epsilon_{22} = \epsilon_{33}$ to give a uniform dilation. The compressibility β is just the inverse of K, so that if β passes through zero then K, and consequently U, changes from $+\infty$ to $-\infty$, and there is a singularity. This corresponds to violation of the upper limiting condition on ν. On the other hand, when the Born stability criteria are violated, U can change from positive to negative without the singularity, because U can tend to zero as, for example, $(S_{11}' S_{22}' - S_{12}'^2)$ tends to zero, whereas in the first case $U \to \infty$ as $K \to 0$. It can be seen, therefore, that in the direction in the alloys corresponding to the shear responsible for the phase transition, and only in this direction, does the observed Poisson's ratio approach the limiting value set by instability of the second kind. It is interesting to note that in this particular direction it is also very close to its upper limit, and consequently the range of ν for which stability exists is very small.

An analysis of instability associated with the martensitic transformations seen in Li, Na and βCuZn has recently been made by Clapp (1973) using a somewhat different method. He has calculated the surface in strain space for which the Born stability criteria are violated. This calculation uses the third order elastic constants. He finds that the strain required to produce instability has a minimum value (of $\simeq 3\%$) in the [111] direction for the three materials he considered: this is just the direction of shear required to cause the transformation fcc to bcc which is seen in those materials. Clapp then proceeds to identify this form of instability with a mechanism of nucleation of a martensitic transformation, and points out that if there are regions within a crystal in which there is a stress-free strain of the appropriate type then near-instability can occur and lattice vibrations will be of a much lower frequency and larger amplitude than in the bulk. He thus suggests a localised soft-mode theory for nucleation in these particular martensites.

6.7 Conclusion

It has been shown that as the martensitic transition in indium-thallium alloys is approached, the value of Poisson's ratio in various directions tends towards one of its limiting values. The value of this ratio in the shear plane, in the direction in which the shear occurs which is responsible for the transformation, tends to the lower limit, set by the Born stability criteria. This is consistent with a result obtained for other martensitic transformations using a different method. Both results are also consistent with a soft-mode mechanism for martensitic transitions.

CHAPTER 7

AN APPLICATION OF THE OPTIMISED MODEL POTENTIAL THEORY TO CALCULATION OF PHONON DISPERSION CURVES FOR INDIUM - THALLIUM ALLOYS

Introduction

Theories of metals have been in existence for a long time, from the early work of Drude (1900). The optimised model potential theory represents one of the latest in a series of developments based on pseudopotential theory (Phillips and Kleinman, 1959; Cohen and Heine, 1961; Austin et al., 1962), in which pseudo-wavefunctions were made up of a sum of valence and core electron states. The first model potential was introduced by Heine and Abarenkov (1964,1965): any potential which could be adjusted so as to reproduce the observed energy eigenstates could be considered as a possible model potential. Further work by Animalu and Heine (1965) and by Animalu (1965) extended the theory to a form in which it could be applied to a set of 33 'simple' elements (elements for which the small-core approximation is valid). Shaw and Harrison (1967) reformulated it, and Shaw (1968,1968a) optimised it to remove some of the arbitrariness in the setting up of a potential which had existed hitherto. It is Shaw's formulation which has been applied here to indium-thallium alloys.

Once a potential has been set up it is possible, in principle, to calculate any atomic or electronic property for a metal. Band structure calculations, both on metals and on semiconductors, have been performed, together with computations of electrical resistivity and of total energy (leading to a determination of stable crystal structures).

Elastic constants, too, can be calculated. One method is to find the second derivatives of the total energy with respect to strain, as Cousins (1970) has done for the hexagonal metals Be, Mg, Zn and Cd; an alternative approach is from the evaluation of phonon dispersion curves.

Very little work has been reported so far for applications of model potential methods to alloys. Inglesfield (1969), using the pseudopotential formalism, has described the evaluation of total energy for an alloy in terms of an alloying potential, and also (Inglesfield, 1972) has developed a method for solution of the Schroedinger equation for an impurity in a host lattice. The latter method he has applied to a calculation of the density of states for Mg in Li and Al in Li. Clark and Dawber (1972) give a method for an alloy which requires the density of states functions for the pure metals. Matsuo, Kogachi and Katada have variously applied the Animalu (1966) pseudopotential to alloys of In-Mg, Al-Mg (Kogachi and Matsuo, 1971) and In-Tl (Matsuo and Katada, 1973) to try to account for their observed structures. No previous work has been published for calculations of phonon dispersion relations for alloys by the model potential method.

In this chapter we extend the methods of Shaw (1968, 1968a) to computation of the optimised model potential and average energy-wavenumber characteristics for random indium-thallium alloys of up to 35 at.% Tl, and use the procedures outlined by Harrison (1966) to calculate the phonon dispersion curves for these materials. In section 7.1 is given a brief account of the theory underlying the setting up of a potential, together with an explanation of the necessary nomenclature, in order that the application to random alloys can be discussed in the following sections.

The object of the calculations has been to see whether a lattice softening, thought to be the mechanism of the martensitic transformation in these alloys, can be predicted from basic atomic and lattice parameters within the context of a harmonic model, (which is of limited applicability close to a soft mode instability). We shall also discuss briefly the stability problem encountered in indium by several workers, and which this study, too, has brought to light.

In view of the necessary intermixing of established ideas and new ones in this chapter, a short description of what is original to the present work and what is not might be useful. The optimised model potential theory for metallic elements is due to Shaw (1968,1968a). The application to alloys of the pseudopotential formalism has been given in outline by Inglesfield (1969); a similar method can be used for model potentials, but the details of the calculation of energy-wavenumber characteristics differ. The evaluation of alloy energy-wavenumber characteristics (whether screened or not) from optimised model potentials has not been reported elsewhere, nor has the calculation of phonon dispersion curves for alloys by this method. The simplification of the expression for band-structure energy change, described in section 7.4.2 is also not mentioned elsewhere, although Finnis (private communication, 1973) has independently derived a similar result.

7.1 Optimised Model Potential theory

7.1.1 Introduction

The object in any model potential theory is to overcome the problems associated with the deep potential well in the vicinity of the positive ion core of a metal atom. Because the well is deep and its form is not known exactly it is not possible to perform calculations of electronic and atomic properties of the metal using standard perturbation methods. The equation which would have to be solved is

$$(T + V + V_e)|\psi_k\rangle = E_k|\psi_k\rangle \tag{7.1}$$

which applies to an electron of wavevector $\underline{k}$ moving through a periodic lattice potential V. The electron wavefunction is $|\psi_k\rangle$ and the energy eigenvalue required is E_k. V_e is a self-consistent potential due to all the other electrons. In writing equation 7.1 certain simplifying assumptions are implied, which will be described in more detail below, but it is still not easy to solve on account of the strong potential V.

To overcome that problem the real potential V is replaced by a model potential W; real wavefunctions $|\psi_k\rangle$ become model wavefunctions $|\chi_k\rangle$, and equation 7.1 becomes

$$(T + W(E_k) + V_e)|\chi_k\rangle = E_k|\chi_k\rangle \quad . \tag{7.2}$$

Although the real and model wavefunctions are different, it is always possible to obtain W such that the real energy eigenvalues are preserved, and then $|\chi_k\rangle$ can be related to $|\psi_k\rangle$. The advantage of equation 7.2 is that W is a weak potential, so that it can be treated as a perturbation on the free electron potential, and calculations based on it can proceed. Figure 7.1(a) shows diagrammatically the relation between the real and model wavefunctions and potentials.

7.1.2 Approximations

i) The small-core approximation

The small-core approximation means that overlap of ion core potentials is neglected. From a practical viewpoint this limits the applicability of the theory to so-called 'simple' metals, such as the alkalis and simple polyvalent metals. The theory does not apply to transition metals as it is presented here; overlap of core d-states occurs in such metals, and other methods have been tried for calculations of transition metal properties. (See, for example, Heine (1969).)

ii) Self-consistent field approximation

The assumption is made that any electron moves in a field due both to the other electrons and to the positive ions. But the arrangement of the electrons is itself causing part of that field. Thus any calculation of the screening of a positive charge by the electrons must be carried out in a self-consistent manner to allow for this interdependence.

iii) Perturbation theory

The model potential is assumed to be weak so that a perturbation expansion will converge. Calculations are rarely carried beyond second order.

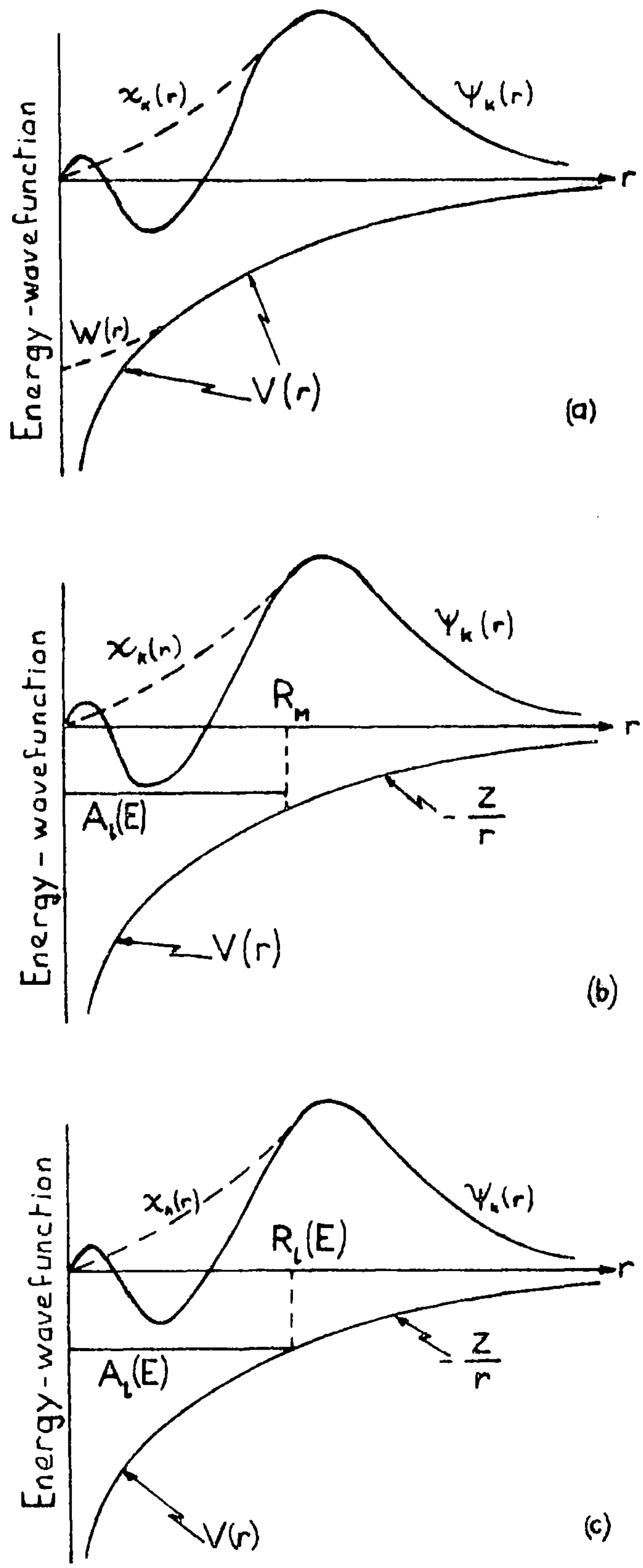

Figure 7.1 Schematic diagrams of various forms of model potential and model wavefunctions.

(a) A general form, showing the replacement of the deep potential V by a shallow one W.

(b) The form used by Heine and Abarenkov.

(c) The optimised form of Shaw.

7.1.3 Construction of a potential

Before discussing the optimised model potential of Shaw, which forms the basis of the work to be described, we turn to the earlier ideas of Heine and Abarenkov (1965), to be referred to as HA. HA used as their model a potential W which varied as $-Z/r$ beyond a model radius r_m from the ion centre, and which had a constant value of A_l for $r < r_m$. Z was the valency of the ion in question, and A_l could be adjusted to give the energy eigenvalues required. Each orbital angular momentum quantum number l required a different value of A, and in the HA model l values up to ∞ were thought to be necessary. The HA model can be written as

$$\begin{aligned} V &= -\sum_l A_l(E)\, P_l \qquad r < r_m \\ &= -\frac{Z}{r} \qquad\qquad\quad r > r_m \end{aligned} \tag{7.3}$$

which applies to a bare ion core of charge Z; the potential due to conduction electrons must be added to this. P_l is a projection operator which, when operating on the model wavefunction, picks out the component of the wavefunction corresponding to the l value in question. A_l is adjusted to give the spectroscopically observed energy levels; since it is the electrons near the fermi level which are excited, the values of A_l are evaluated at $E_k = E_{k_F}$.

When the model potential for a metal is rquired, as distinct from a bare ion, the Schroedinger equation to consider is

$$\left(T + \sum_i v_i + V_e \right)|\psi_k\rangle = E_k|\psi_k\rangle \tag{7.4}$$

for the real wavefunctions, in which v_i are the self-consistent ion potentials, and

$$(T + \sum_i w_i + V_e)|\chi_k\rangle = E_k|\chi_k\rangle \qquad (7.5)$$

for the model wavefunctions. In both cases V_e includes the interaction of all conduction electrons with the single electron described by equation 7.2. When many ions and electrons are brought together to form a metal there is a reduction in the energy, and a cohesive energy can be defined. Shaw (1968, 1968a) describes how the energy at which the model parameters must now be evaluated is the fermi energy relative to the free ion. Methods of calculating this energy will be given later.

Shaw (1968, 1968a) made two important modifications to the HA model. The first concerned the modelling of $A_l(E)$ for all l, from zero to infinity. The second had a bearing on the choice of model radius R_M.

For $l > 2$ HA set A_l equal to A_2, as there were essentially no spectroscopic term values for calculating these well depths. However, there is no need to include $l > 2$ at all, or, more correctly, for l greater than the value l_0 for which there are core states in the ion in question. For example, in indium $l_0 = 2$, whereas in aluminium $l_0 = 1$ and in sodium $l_0 = 0$. This is because the lowest eigenstate will have no nodes, and any others will have nodes outside the core. Hence the potential near the core due to these states will be weak already, and so one of the main reasons for needing a model, the strong potential near the core, will not apply in these cases.

The model radius of HA was a fixed distance: Shaw allowed this quantity to depend on energy, and also to vary for each l value required. Thus the new model radius could be written as $R_l(E)$, and the unscreened model potential for a single ion can now be written as

$$w_0 = v_b(r) - \sum_{l=0}^{l_0} \theta(R_l - r)\left[A_l(E) + v_b(r)\right]P_l \qquad (7.6)$$

$$\text{with } \theta(r) = \begin{cases} 1, & r > 0 \\ 0, & r < 0 \end{cases} .$$

If the values from l_0+1 to ∞ are considered, then the effect of these can be shown (Shaw (1968a)) to be at least 2 orders smaller than for those up to l_0. Hence the bare ion potential can be approximated, with an error which is known to be small, as

$$w_0 = -\frac{Z}{r} - \sum_{l=0}^{l_0} \theta(R_l - r)\left[A_l - \frac{Z}{r}\right]P_l . \qquad (7.7)$$

The criterion used for optimisation of the parameters is to look for the smoothest wavefunction possible which is nodeless within the core, as suggested by Cohen and Heine (1961). The extra parameter introduced, R_l, turns out to depend on A_l, so that no new variable is introduced by Shaw's modifications. The optimisation conditions are

$$\left. A_l(E)\right|_{R_l} = -v_b(R_l)$$
$$\left.\frac{\partial A_l}{\partial R_l}\right|_{R_l} = 0 \qquad (7.8)$$

Shaw has shown that these conditions are equivalent, so that if the assumption is made that $v_b(r)$ is equal to $-Z/r$ outside the core, the optimisation condition can be written as

$$\left. A_l(E)\right|_{R_l} = Z/R_l . \qquad (7.9)$$

The procedure for calculating optimised parameters for specific metals will be given in section 7.2 .

This completes our description, given in outline only, of the optimised model potential. There still remains much numerical work and computation to be done before functions based on it can be produced, and which enable calculation of observable physical properties of a metal to be performed.

An important application, of relevance here, is the calculation of phonon dispersion curves for a lattice. Such a calculation provides a good test for a model, and considerable effort has gone into the determination of lattice vibration spectra in recent years, both from a theoretical and a practical starting point. Pindor and Pynn (1969) have described a calculation for hexagonal crystals, and have applied it to magnesium, while Shaw and Pynn (1969) have modified the computation to include the effects of exchange and correlation. When such effects were included the experimentally determined phonon dispersion curves were reproduced quite well.

Harrison (1966) has simplified some of the convergence problems associated with the calculation, and it is his method that has been used in the work to be described. The remainder of this section is given to introducing and defining various topics and functions which will be needed in the calculation of phonon dispersion curves for the indium-thallium alloys.

7.1.4 Contributions to the total energy

Three interactions are considered: the ion-ion (or direct interaction), the electron-ion (or indirect interaction), the electron-electron interaction.

(i) The first, the ion-ion interaction depends only on the ion separation, and not on their arrangement. It is thus a volume-dependent term. The energy per ion can be written as

$$E_d = \frac{1}{2N} \sum_{i,j \; i \neq j} V_d(|r_i - r_j|) \qquad (7.10)$$

where $V_d(r)$ is the energy of interaction of a pair of ions with separation **r**.

(ii) The electron-ion interaction depends not only on the volume of the system but also on the arrangement of the ions. Harrison (1966) gives the energy of the state $\underline{k}$ as

$$E(\underline{k}) = \frac{\hbar^2 k^2}{2m} + \langle \underline{k}|W|\underline{k}\rangle + \sum_{q}' \frac{\langle \underline{k}+\underline{q}|W|\underline{k}\rangle\langle \underline{k}|W|\underline{k}+\underline{q}\rangle}{(\hbar^2/2m)(k^2 - |\underline{k}+\underline{q}|)^2} \qquad (7.11)$$

and the prime indicates that $\underline{q} = 0$ is ommitted. This expression follows from a perturbation theory calculation taken to second order. In the absence of the potential W equation 7.11 would reduce to the free-electron result, and a spherical fermi surface would ensue. The free-electron energy of the perturbed system is represented by the first two terms of 7.11; the last term gives a contribution known as the band structure energy, and it is this term which is affected by the ion arrangement.

(iii) Finally we come to the electron-electron interaction. The effect of conduction electrons in the vicinity of an ion core is to reduce its interaction with electrons further away: some of the positive charge is 'screened'. The result of the screening is to modify the band structure energy. A screened model potential is produced which takes into account the effect of conduction electrons, and this then takes the place of the unscreened potential in calculations performed for a metal.

These interactions combine to give three terms in the expression for total energy. The first is the free-electron energy, the second is the band structure energy and the third, known as the electrostatic energy, arises from a combination of the ion-ion interaction energy, part of the electron-electron energy and the second term of equation 7.11. The electrostatic energy can be considered as representing the effect of positive ions in a 'sea' of negative charge.

Thus we may write the total energy as

$$E_{tot} = E_{fe} + E_{bs} + E_{es} \quad . \tag{7.12}$$

The essence of a calculation of lattice vibration properties is in finding the way in which the total energy changes as the result of an applied distortion to the lattice.

7.1.5 Decomposition of the matrix elements

If the model potential for a metal W consists of the sum of potentials w centred on each of the N ion positions $\underline{r}_j$, then at $\underline{r}$ the potential is

$$W(\underline{r}) = \sum_{j=1}^{N} w(|\underline{r}-\underline{r}_j|) \quad . \tag{7.13}$$

We can now write in full the matrix element $\langle \underline{k}+\underline{q}| W(r)|\underline{k}\rangle$, using equation 7.13 together with the expressions of which the bra and ket vectors are abreviations.

$$\langle \underline{k}+\underline{q}|W(\underline{r})|\underline{k}\rangle = \Omega^{-1} \int e^{-i(\underline{k}+\underline{q})\cdot\underline{r}} \sum_j w(|\underline{r}-\underline{r}_j|)e^{i\underline{k}\cdot\underline{r}}\, d\tau$$

in which Ω is the volume of the metal and the integration is over all space. Multiplying and dividing the right hand side by $e^{-i\underline{q}\cdot\underline{r}_j}$ and rearranging, we have

$$\begin{aligned}\langle \underline{k}+\underline{q}|W(\underline{r})|\underline{k}\rangle &= \Omega^{-1} \sum_j e^{-i\underline{q}\cdot\underline{r}_j} \int e^{-i(\underline{k}+\underline{q})\cdot(\underline{r}-\underline{r}_j)} \\ &\qquad \times w(|\underline{r}-\underline{r}_j|)e^{i\underline{k}\cdot(\underline{r}-\underline{r}_j)}\, d\tau \\ &= \frac{1}{N}\sum_j e^{-i\underline{q}\cdot\underline{r}_j} \frac{1}{\Omega_o}\int e^{-i(\underline{k}-\underline{q})\cdot\underline{r}} w(r)e^{i\underline{k}\cdot\underline{r}}\, d\tau\end{aligned}$$

since $(\underline{r}-\underline{r}_j)$ has become a dummy variable. $\Omega_o = \frac{\Omega}{N}$, the volume per ion.

The last equation can be written as

$$\langle \underline{k}+\underline{q}|W|\underline{k}\rangle = S(\underline{q})\langle \underline{k}+\underline{q}|w|\underline{k}\rangle \tag{7.14}$$

in which

$$S(\underline{q}) = \frac{1}{N}\sum_{j} e^{-i\underline{q}\cdot\underline{r}_j} \tag{7.15}$$

and

$$\langle \underline{k}+\underline{q}|w|\underline{k}\rangle = \frac{1}{\Omega_0}\int e^{-i(\underline{k}+\underline{q})\cdot\underline{r}}\, w(\underline{r})e^{i\underline{k}\cdot\underline{r}}\, d\tau \tag{7.16}$$

The factorisation has produced two terms: one depends only on the arrangement of the ions, and the other only on the individual ion potential w. The former is called the STRUCTURE FACTOR, and the latter is the FORM FACTOR.

The above analysis has assumed one type of ion present. Let a binary alloy have constituents A and B, and let the fraction of ions from element A be c. Let those of type A be at positions $\underline{r}_{i(A)}$, and those of B at $\underline{r}_{i(B)}$. Then equation 7.13 becomes

$$W(\underline{r}) = \sum_{i(A)} w^A(|\underline{r}-\underline{r}_i|) + \sum_{i(B)} w^B(|\underline{r}-\underline{r}_i|) \tag{7.17}$$

Thus

$$\begin{aligned}\langle \underline{k}+\underline{q}|W|\underline{k}\rangle &= \frac{1}{N}\sum_{i(A)} e^{-i\underline{q}\cdot\underline{r}_i}\langle \underline{k}+\underline{q}|w^A|\underline{k}\rangle \\ &\quad + \frac{1}{N}\sum_{i(B)} e^{-i\underline{q}\cdot\underline{r}_i}\langle \underline{k}+\underline{q}|w^B|\underline{k}\rangle \\ &= \frac{1}{N}\sum_{i} e^{-i\underline{q}\cdot\underline{r}_i}\langle \underline{k}+\underline{q}|w^A|\underline{k}\rangle \\ &\quad + \frac{1}{N}\sum_{i(B)} e^{-i\underline{q}\cdot\underline{r}_i}\langle \underline{k}+\underline{q}|w^B-w^A|\underline{k}\rangle \end{aligned} \tag{7.18}$$

Equation 7.18 contains two sums; the first is over all ion positions, while the second is taken over all sites at which there is an ion of type B. The lattice over which the first sum is taken is called the average lattice, and that for the second sum is the difference lattice. There are thus two types of structure and form factors involved. When $\underline{q}$ is a wavenumber of the average lattice it is denoted by $\underline{q}_o$, and $e^{-i\underline{q}_o \cdot \underline{r}} = 1$ at each ion position. Hence $S(\underline{q}_o) = 1$, and equation 7.18 becomes, in this case,

$$\langle \underline{k}+\underline{q}_o|W|\underline{k}\rangle = c\langle \underline{k}+\underline{q}_o|w^A|\underline{k}\rangle + (1-c)\langle \underline{k}+\underline{q}_o|w^B|\underline{k}\rangle \; . \qquad (7.19)$$

If $\underline{q}$ is not on this lattice then $S(\underline{q}) = 0$ and

$$\langle \underline{k}+\underline{q}|W|\underline{k}\rangle \;=\; S'(\underline{q})\langle \underline{k}+\underline{q}|w^B - w^A|\underline{k}\rangle \; . \qquad (7.20)$$

For a random alloy the difference lattice is random, and Harrison (1966) has shown that for such a lattice

$$S'(\underline{q})^* \, S'(\underline{q}) \;=\; c(1-c)/N \; ; \qquad (7.21)$$

$S'(\underline{q})^* = S'(-\underline{q})$.

Because of its dependence on the type of ion(s) present only, the form factor need only be computed once for a metal or alloy. A calculation of any atomic property can then proceed using a structure factor appropriate to the ion arrangement under consideration.

7.1.6 The energy-wavenumber characteristic

An important function in any calculation of metallic properties is the energy-wavenumber characteristic. It gives the contribution to the band-structure energy of the wavevector $\underline{q}$. The band-structure contribution to the energy of an electron in state $|\underline{k}\rangle$ is, from equation 7.11,

$$E_{bs} \;=\; {\sum_{\underline{q}}}' \frac{\langle \underline{k}+\underline{q}|W|\underline{k}\rangle\langle \underline{k}|W|\underline{k}+\underline{q}\rangle}{(\hbar^2/2m)(k^2 - |\underline{k}+\underline{q}|)^2} \; . \qquad (7.22)$$

The two matrix elements in the numerator can be decomposed as described in section 7.1.5 to give an expression which consists of a structure-dependent part, and a structure-independent part.

Thus

$$E_{bs} = \sum_{q}{}' \frac{S^{*}(q)S(q)\langle \underline{k}|w|\underline{k}+\underline{q}\rangle\langle \underline{k}+\underline{q}|w|\underline{k}\rangle}{(\hbar^2/2m)(\underline{k}^2 - |\underline{k}+\underline{q}|)^2} \tag{7.23}$$

in which w is the unscreened bare ion model potential. This equation may be rewritten as

$$E_{bs} = \sum_{q}{}' S^{*}(\underline{q})S(\underline{q})F(q) \tag{7.24}$$

where F(q) is the energy-wavenumber characteristic; equation 7.24 is its defining relationship. Now the sum over $\underline{q}$ can be changed to an integral over $\underline{k}$ provided that a factor $2\Omega_o/8\pi^3$ is introduced. This represents the number of electrons which occupy states in a unit volume of wavenumber space. Hence the expression for F(q) becomes (for an element)

$$F(q) = \frac{2\Omega_o}{8\pi^3}\int d^3k \frac{\langle \underline{k}|w|\underline{k}+\underline{q}\rangle\langle \underline{k}+\underline{q}|w|\underline{k}\rangle}{(\hbar^2/2m)(k^2 - |\underline{k}+\underline{q}|)^2} \tag{7.25}$$

The energy-wavenumber characteristic is based on the form factor and, like that function, does not depend on the ion arrangement. The general form of the energy-wavenumber characteristic is shown in figure 7.2 ; of particular interest is the minimum occurring at a point near to $q = 2k_f$, called q_o, for at such a wavenumber there is little contribution to the binding energy from the band-structure part. It has been suggested (Heine and Weaire, 1966) that elements assume a crystal structure such that the principal reciprocal lattice vectors avoid q_o.

The form of equation 7.25 for alloys is similar, but it contains extra terms resulting from decomposition of the alloy matrix elements.

7.1.7 Effective valency

It is useful at this stage to consider the effect of

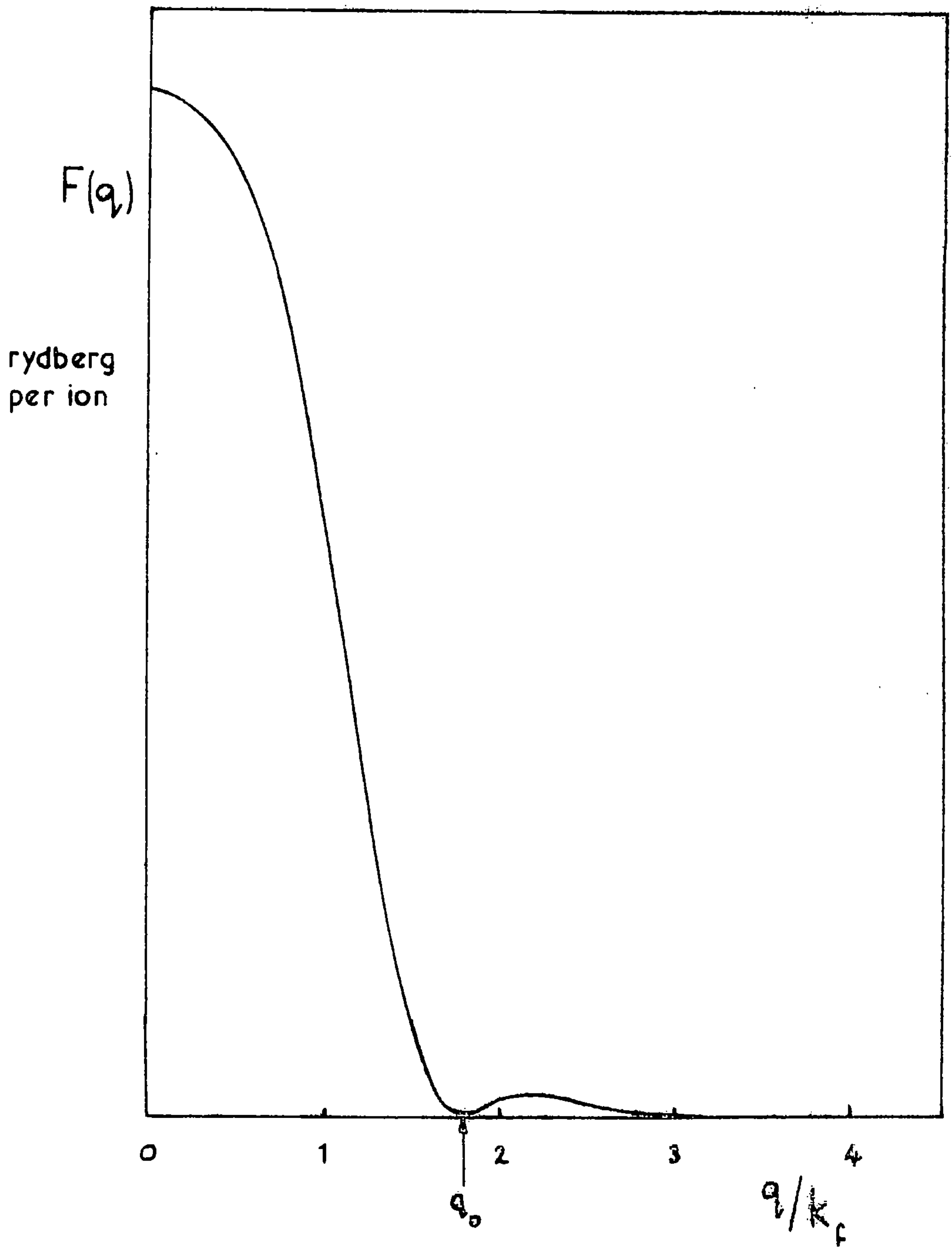

Figure 7.2 Schematic form of an energy-wavenumber characteristic.

using a model wavefunction instead of the real wavefunction in calculations involving the electron density. The electron density is given by

$$n(\underline{r}) = \sum_{k \leq k_f} \Psi^*_k(\underline{r}) \Psi_k(\underline{r}) \quad . \tag{7.26}$$

This will equal 3 electrons per atom for the case of indium. But in general the model wavefunction $\chi_k(r)$ will not lead to the same result; a correction term is needed ($\rho_k(\underline{r})$)

$$n(\underline{r}) = \sum_{k \leq k_f} \chi^*_k(\underline{r}) \chi_k(\underline{r}) + \rho_k(\underline{r}) \quad . \tag{7.27}$$

The last term, when summed over $\underline{k}$, gives rise to the depletion charge density $\rho(\underline{r})$. Consequently, in performing any calculation involving the valency, an effective valency must be used in order to be consistent with the model wavefunction employed. The effective valency is given the symbol Z^*, and

$$Z^* = Z(1 - \rho) \quad ; \tag{7.28}$$

ρ is usually positive, and is often called the depletion hole.

7.1.8 Screening the form factor

The screening calculation takes into account the effect of the electrons near to a positive ion reducing its influence on electrons further away. The result is expressed as a correction term to the form factor discussed in section 7.1.5 and we obtain the screened form factor.

The electron potential can be calculated from the electron density as given in equation 7.27 after substituting a perturbation expansion for χ_k .

Shaw (1968 a) gives the result for an elemental metal as

$$V_{eq} = \frac{4\pi}{q^2} \frac{4}{\Omega} \frac{\langle \underline{k}+\underline{q}|W|\underline{k}\rangle}{k^2 - |\underline{k}+\underline{q}|} + \frac{\rho}{\Omega_0} S(q) \qquad (7.29)$$

W in equation 7.29 includes the electron potential, so that

$$\langle \underline{k}+\underline{q}|W|\underline{k}\rangle = \langle \underline{k}+\underline{q}|W_o|\underline{k}\rangle + V_{eq} \qquad (7.30)$$

in which W_o is made up of bare ion potentials. Substitution of equation 7.30 into 7.29 allows a self-consistent determination of V_{eq} to be made; combining it with the unscreened matrix element as in 7.30 gives the screened matrix element. This can be decomposed as before to give a structure factor and a screened form factor.

When considering an alloy two types of form factor are involved, as in equations 7.19 and 7.20. Evaluation of the matrix element for the average lattice from equation 7.19 is quite straightforward, since it only involves the weighted mean of the screened form factors for atoms of type A and of type B, and the resulting form factor is correctly screened. The procedure is slightly more involved in the case of the difference form factor $\langle \underline{k}+q|w_o^B - w_o^A|\underline{k}\rangle$. A simplified approach is to decompose it into $\langle \underline{k}+q|w_o^B|\underline{k}\rangle - \langle \underline{k}+q|w_o^A|\underline{k}\rangle$, as Kogachi and Matsuo (1971) have done in the cases of In-Mg and Al-Mg alloys for which the components have different valencies, but this neglects altogether the screening difference introduced by alloying. The reason why there is a difference lies in the different form of the model wavefunctions for the two elements, a difference reflected in the effective valence Z^* through the depletion hole calculation.

To attempt to compensate for this difference, we may screen the difference form factor starting from an expression for the electron density of a binary alloy which is similar in form to equation 7.27 .

$$n(\underline{r}) = \sum_{k \leqslant k_f} \chi_k^*(\underline{r})\chi_k(\underline{r}) + (1-c) \sum_{i(B)} \rho(\underline{r}-\underline{r}_i) - c\sum_{i(A)} \rho(\underline{r}-\underline{r}_i) \tag{7.31}$$

The analysis follows that given for an element by Shaw (1968a) and the resulting screening correction is in terms of the effective valences and the weighted means of the atomic volumes and depletion holes of the two elements concerned.

This description of the screening of the difference form factor has been rather brief because, as will be shown below in section 7.4.2, there is no need to compute the difference form factor in the calculation of phonon dispersion curves. Its value would be required, though, if a total energy determination was to be carried out.

7.1.9 Summary

An account of the ideas behind the optimised model potential theory has been given, together with an explanation of various functions which can be derived from it. The extension of the appropriate sections to a binary alloy system has been discussed. The sections following will describe the determination of the optimised parameters for indium and thallium, and will give the results of normalised energy-wavenumber characteristics for indium and selected alloy compositions so that a determination of their phonon spectra can be made.

7.2 Determination of model parameters for indium and thallium

7.2.1 Model parameters for the Heine-Abarenkov model

The HA model required that the wavefunction for the region inside the model radius should match smoothly to that outside. This was equivalent to the requirement that the logarithmic derivatives of the internal and external solutions to the radial Schroedinger equation for the model wavefunction should match at R_M. Using this condition Abarenkov (1965) produced a set of tables in which the quantity A_l/Z^2 was given as a function of $Z/\sqrt{2E}$ for a number of values of ZR_M; he took l values of 0, 1 and 2. To find the well depths for a given metal, the column of the tables with the ZR_M appropriate to that metal was used to produce a graph of A_l/Z^2 against E/Z^2 for each l value up to 2. The curves had a number of singularities at which they went to infinity, but it was found that the points on the curves corresponding to the spectroscopic term values for the metal fell on a straight line. This was true for most metals, and the assumption was made that for any other energy intermediate between the term values an interpolation along the straight line would give A_l for that energy; the required well depths for the HA model potential were obtained by an interpolation at the fermi energy.

7.2.2 Model parameters for the optimised model potential

From the optimisation procedure described in section 7.2.3 we require that

$$A_l(E)\Big|_{R_l} = \frac{Z}{R_l} \qquad (7.32)$$

Shaw (1968) has interpolated Abarenkov's tables to find values of $A_1(E)$ which satisfy this equation, and as a result a set of curves giving A_1/Z^2 as a function of E/Z^2 has been produced. Interpolation between the well depths corresponding to spectroscopic term energies is again used to determine $A_1(E)$ for arbitrary E.

7.2.3 Term values for indium and thallium

For the present work term values from spectroscopic data have been taken from Bacher and Goudsmit (1932). For a given ionisation state of an element these workers list wave-numbers corresponding to the various electronic states; they are usually given relative to the lowest one, and are known as the term values for those states.

In model potential theory we are intersted in the term values of the free ion, that is, of In^{+++} and of Tl^{+++} in the present case. The ground state electronic configuration for these elements is

In: $1s^2\ 2s^2\ 2p^6\ 3s^2\ 3p^6\ 3d^{10}\ 4s^2\ 4p^6\ 4d^{10}\ 5s^2\ 5p$

Tl: $1s^2\ 2s^2\ 2p^6\ 3s^2\ 3p^6\ 3d^{10}\ 4s^2\ 4p^6\ 4d^{10}\ 4f^{14}\ 5s^2\ 5p^6\ 5d^{10}\ 6s^2\ 6p$

The highest core states in indium (4d) correspond to $l_o = 2$, whilst those in thallium (4f) have $l_o = 3$. However, the f states in thallium have not been modelled as their contibution is very small compared to that for $l = 0$ (Appapillai and Heine, 1972). Thus for both metals the values of the well depths A_0, A_1 and A_2 only have been sought.

The details of the calculation are given in Table 7.1 and the results are shown graphically in figure 7.3. Atomic

TABLE 7.1

Optimised model parameters for indium and thallium at spectroscopic term energies.

Indium (Z = 3)

l		Term value (cm^{-1})	E (a.u.)	E/Z^2	A_l/Z^2	A_l (a.u.)	$\partial A_l/\partial E$
0	5s	226133	1.0308	0.1145	0.1530	1.3768	
	6s	99255	0.4524	0.0502	0.1242	1.1176	-0.477
	7s	56706	0.2585	0.0287	0.1121	1.0090	
1	5p	168948	0.7701	0.0855	0.1674	1.5063	-0.208
	6p	81545	0.3717	0.0413	0.1582	1.4235	
2	5d	97675	0.4452	0.0494	0.1290	1.1613	0.0062
	6d	55602	0.2534	0.0281	0.1292	1.1625	
		a	b		c		

Thallium (Z = 3)

l		Term value (cm^{-1})	E (a.u.)	E/Z^2	A_l/Z^2	A_l (a.u.)	$\partial A_l/\partial E$
0	6s	240600	1.0973	0.1218	0.1656	1.4908	
	7s	101391	0.4622	0.0513	0.1298	1.1683	-0.508
	8s	57413	0.2620	0.0291	0.1168	1.0515	
1	6p	176443	0.8043	0.0893	0.1843	1.6587	-0.468
	7p	82748	0.3772	0.0419	0.1621	1.4591	
2	6d	95245	0.4341	0.0482	0.1178	1.0602	-0.128
	7d	54244	0.2472	0.0274	0.1151	1.0362	
		a	b		c		

Notes
- a Term values obtained from Bacher and Goudsmit (1932).
- b Energy corresponding to term value; $1 cm^{-1} \equiv 4.409 \times 10^{-6}$ au.
- c Values of A_l/Z^2 corresponding to each E/Z^2 obtained from tables given by Shaw (1968).

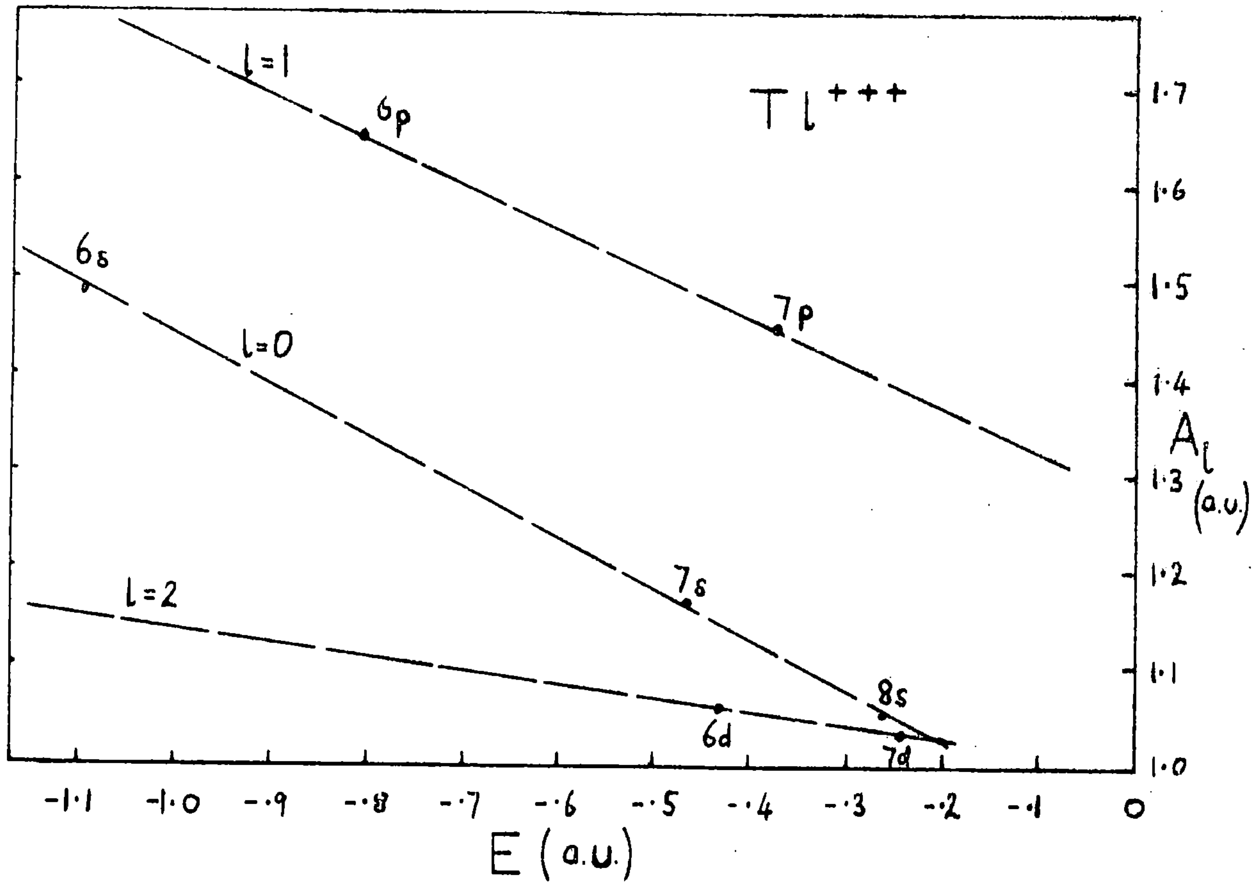

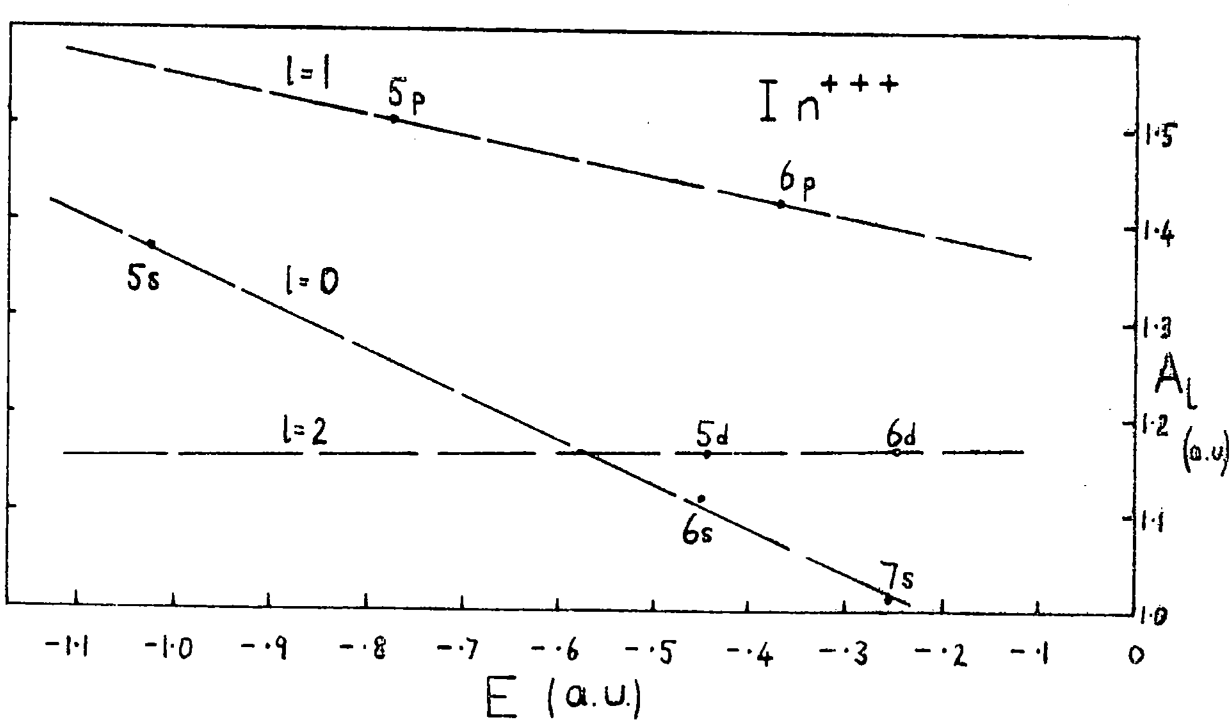

Figure 7.3 Graphs from which the optimised model parameters for indium and thallium were obtained. The points plotted were calculated as described in Table 7.1 .

units have been used throughout the numerical work ($e = \hbar = m = c = 1$; energies are in Hartrees (1 Hartree = 2 Rydbergs) = 27.2eV).

7.2.4 The fermi energy

The optimised model parameters must be evaluated at the fermi energy relative to the free ion E_f, as described in section 7.1.3. Following Animalu and Heine (1965) we see that this energy is made up of the fermi energy for an isolated ion ϵ_f and a contribution from the potential due to the rest of the ions and conuction electrons in the metal. Thus we have

$$E_f = \epsilon_f - (V + \Sigma)_{rest} \qquad (7.33)$$

where Σ_{rest} represents the exchange and correlation hole around the electron and V_{rest} is the potential due to the rest of the system. Seitz (1940) has outlined a way of relating the bottom of the conduction band to the cohesive energy, (that is, the energy required to form separated atoms). If E_o is the energy of the bottom of the band and E_f' is the fermi level relative to E_o, the E_f is just (E_o+E_f'). Seitz has shown that the cohesive energy per electron E_c can be written as

$$E_c = \frac{3}{5}\frac{\hbar^2 k^2}{2m} + E_i + E_o + E_x + E_c - E_{coul} \qquad (7.34)$$

where E_i is the ionisation energy, E_x and E_c are the energies due to exchange and correlation effects and E_{coul} is the electrostatic self-energy of the electron gas. Consequently (Animalu and Heine (1965)) we have an expression for ϵ_f as

$$\epsilon_f = - \text{M.I.E} + \text{B.W.E.} + \Sigma_{rest} + \frac{2}{5}\frac{\hbar^2 k^2}{2m} - E_x - E_c + E_{coul} \,. \qquad (7.35)$$

M.I.E. is the mean of the first 3 ionisation energies of the free atom and B.E.E. is the cohesive energy per electron. Seitz (1940) gives expressions for E_x and E_{coul} as

$$E_x = -0.916/r_s \quad ; \quad E_{coul} = 0.6Ze^2/R_a .$$

The radius of the sphere whose volume is equal to the volume per electron is r_s; R_a is the radius of a shere equal in volume to the atomic volume Ω_0. Animalu and Heine give the following expression for V_{rest}:

$$V_{rest} = \frac{Z}{R_a}\left[3 - \tfrac{3}{4}(R_M/R_a)^2\right] , \qquad (7.36)$$

in which R_M is the model radius. (All the energies in equations 7.34 to 7.36 are in rydbergs.) Table 7.2 shows details of the calculation of E_f for indium and thallium by means of equations 7.33 to 7.36, together with sources of the data.

This method of determining the value of E_f is not completely satisfactory, but is probably the best available at present. Published values for the cohesive energy for indium, and particularly for thallium, are subject to wide variation. Bichowsky and Rossini (1936) cite values as widely different as -28 and -45 Kcal mole^{-1} for thallium. The values for cohesive energy used in Table 7.2 are based on figures given by Kittel (1966). But the largest single term in the determination of E_f from equation 7.33 is V_{rest}, which is a radially dependent term. A weighted mean value taken over a sphere of radius R_M has been used by Animalu and Heine, using the fixed model radius; some mean of the various optimised model radii might now be more appropriate. Further, the weighting factor was rather arbitrary.

As a result of these considerations it would seem that any value for E_f determined by equation 7.33 is subject to

TABLE 7.2

Parameters required for the calculation of E_f relative to the free ion

	K_f	R_a	r_s	R_M	M.I.E	B.E.E.	V_{rest}	E_c	E_x	E_{coul}	E_f
In	0.7972	3.47	2.4	2.4	0.6874	-0.0674	2.282	-0.090	-0.3806	0.5186	-1.794(= -0.897 a u)
Tl	0.7713	3.58	2.4	2.4	0.7316	-0.0458	2.232	-0.090	-0.3816	0.5026	-1.798(=-0.899 a u)
					(a)	(b)		(c)			

Lengths are in a.u. Energies in rydbergs (except where specified)

(a) Bacher and Goudsmit (1932) (b) Kittel (1966) (c) Animalu and Heine (1965) some uncertainty.

7.2.5 Results

The model parameters A_0, A_1 and A_2 together with the their energy derivatives have been evaluated at the fermi energy relative to the free ion, as given in Table 7.2, by use of the curves of figure 7.3. These parameters represent a re-calculation in the case of indium, and are reported for the first time by this method for thallium. Table 7.3 gives the results and compares the figures for indium with those of Shaw (1968a). To give an idea of the effect on the well depths of a change in the value used for the fermi energy, parameters are given corresponding to E_f = -0.75a.u. for both indium and thallium. (That particular value has been chosen because it will be required later in the calculations.) Also, for comparison, the Animalu and Heine parameters for these metals are included in the table.

7.2.6 Other determinations of model parameters

The earlier work of Animalu and Heine has already been mentioned. Appapillai and Heine (1972,1973) have recently used the quantum defect method of Ham (1955) to determine well depths at the fermi energy for 33 elements; their results for indium and thallium are also shown in Table 7.3.

TABLE 7.3

Model parameters for indium and thallium

Indium

	A_0	A_1	A_2	$\partial A_0/\partial E$	$\partial A_1/\partial E$	$\partial A_2/\partial E$
This work:						
E_f = -0.9 a.u.	1.33	1.53	1.16	-0.465	-0.028	0.006
E_f = -0.75 a.u.	1.25	1.50	1.16	"	"	"
Shaw (1968 a)	1.34	1.49	1.09	-0.454	-0.224	0.094
Animalu and Heine (1965)	1.32	1.46	1.10			
Appapillai and Heine (1972)	1.34	1.52	1.09	-0.432	-0.270	0.094

Thallium

	A_0	A_1	A_2	$\partial A_0/\partial E$	$\partial A_1/\partial E$	$\partial A_2/\partial E$
This work:						
E_f = -0.9 a.u.	1.39	1.71	1.11	-0.508	-0.468	-0.128
E_f = -0.75 a.u.	1.32	1.63	1.10	"	"	"
Animalu and Heine (1965)	1.44	1.51	0.98			
Appapillai and Heine (1972)	1.42	1.54	0.88	-0.462	-0.250	0.310

7.3 Calculation of form factors and energy-wavenumber characteristics

7.3.1 Indium and thallium

The computation of form factors and energy-wavenumber characteristics for indium and thallium was performed using a slightly modified version of the PL1 computer programme given by Shaw (1968a). In addition to the two functions mentioned it produced a value for the effective valence Z^*. The programme used is listed in Appendix III under the name MODPOT. The input data required were the well depths A_l and their energy derivatives, together with the fermi wavevector k_f, the valency Z and the atomic volume Ω_0. All these quantities were expressed in atomic units. The output gave the form factor and the energy wavenumber characteristic for values of q/k_f from 0.1 to 5.0 in steps of 0.1, and from 5.4 to 7.0 in steps of 0.4. By $q/k_f = 7.0$ both functions had decreased to less than 10^{-5} of their value at $q/k_f = 0.1$. The energy wavenumber characteristic was normalised, so that it had a value of unity at $q = 0$. The normalised characteristic $F_N(q)$ was related to the unnormalised form by

$$F_N(q) = -\frac{q^2\Omega_0}{2\pi(Z^*)^2} F(q) . \qquad (7.37)$$

7.3.2 Indium-thallium alloys

There are two types of form factor for a binary alloy, as explained in section 7.1.5. In section 7.4.2 it will be shown that for phonon dispersion calculations there is no need to compute the difference form factor, but only the average one. From equation 7.19 the latter is just the mean of the form factors of the constituent elements, weighted according to the composition. In the case of the average energy-wavenumber characteristic such a simple treatment was not possible, for its value depended on the square of the form factor, as in equation 7.25, and a direct separation was not possible. Rewriting equation 7.25 with the average form factor for a binary alloy and including the effect of screening, we have

$$F_{av}(q) = \frac{2\Omega}{8\pi^3}\int d^3k \, \frac{2\left[c\,|w^A(\underline{k})| + (1-c)\,|w^B(\underline{k})|\right]^2}{k^2 - |\underline{k}+\underline{q}|^2} - \frac{\Omega q^2}{8\pi}\left[cV_{sc}^{A} + (1-c)V_{sc}^{B}\right]^2 \tag{7.38}$$

in atomic units, and in which $\Omega = c\,\Omega_o^A + (1-c)\,\Omega_o^B$ and V_{sc} is the screening contribution. The notation for the form factors has been abbreviated to $w^A(\underline{k})$ and $w^B(\underline{k})$. The integral decomposes to give the average energy-wavenumber characteristic for the alloy as

$$F_{av}(q) = c^2 F_A(q) + (1-c)^2 F_B(q) + 2c(1-c)\left\{\frac{2\Omega}{8\pi^3}\int d^3k \, \frac{2\left[w^A(\underline{k})w^B(\underline{k})\right]}{k^2 - |\underline{k}+\underline{q}|^2} - \frac{\Omega q^2}{8\pi}V_{sc}^{A}V_{sc}^{B}\right\} \tag{7.39}$$

where $F_A(q)$ and $F_B(q)$ are the energy-wavenumber characteristics of elements A and B. In the computation of actual values of $F_{av}(q)$ for the alloy the first two terms on the R.H.S. of this equation were obtained from MODPOT directly, with data calculated as described in section 7.2. Evaluation of the last term was quite straightforward and was parallel to that for an element, with the appropriate modifications to allow for the fact that it contained a product of two different form factors. These modifications meant that certain intermediate functions involved in the computation of F(q) for indium and thallium had to be extracted from the calculations performed by MODPOT, and then recombined in the appropriate way to give the required results for an alloy of a particular composition. A programme listed in Appendix III as COMBINE was written to carry out this task; it gave the energy-wavenumber characteristics in their normalised form. The results of these calculations are given in Table 7.4, and those for indium and thallium are shown in figure 7.4.

7.4 Application of optimised model potentials to calculation of the lattice vibration spectra of indium-thallium alloys

7.4.1 The vibration spectrum

At finite temperatures the atoms or ions which are bonded together to make up a solid are each vibrating about a mean position. The frequencies of these vibrations are quantised, and depend on the forces acting between the ions. The vibrations of the ions can be decomposed into a number of component sinusoidal oscillations. The introduction of a wave of frequency ω to the lattice, by, for example, either physically causing a disturbance at the surface as with an ultrasonic wave, or by transferring momentum to a nucleus through inelastic neutron scattering techniques, reinforces one or more of these components of the thermal vibration and a coherent wave will be propagated. That is the physical picture. In any calculations the thermal motion is ignored and the ions are considered as stationary unless a coherent wave is passing

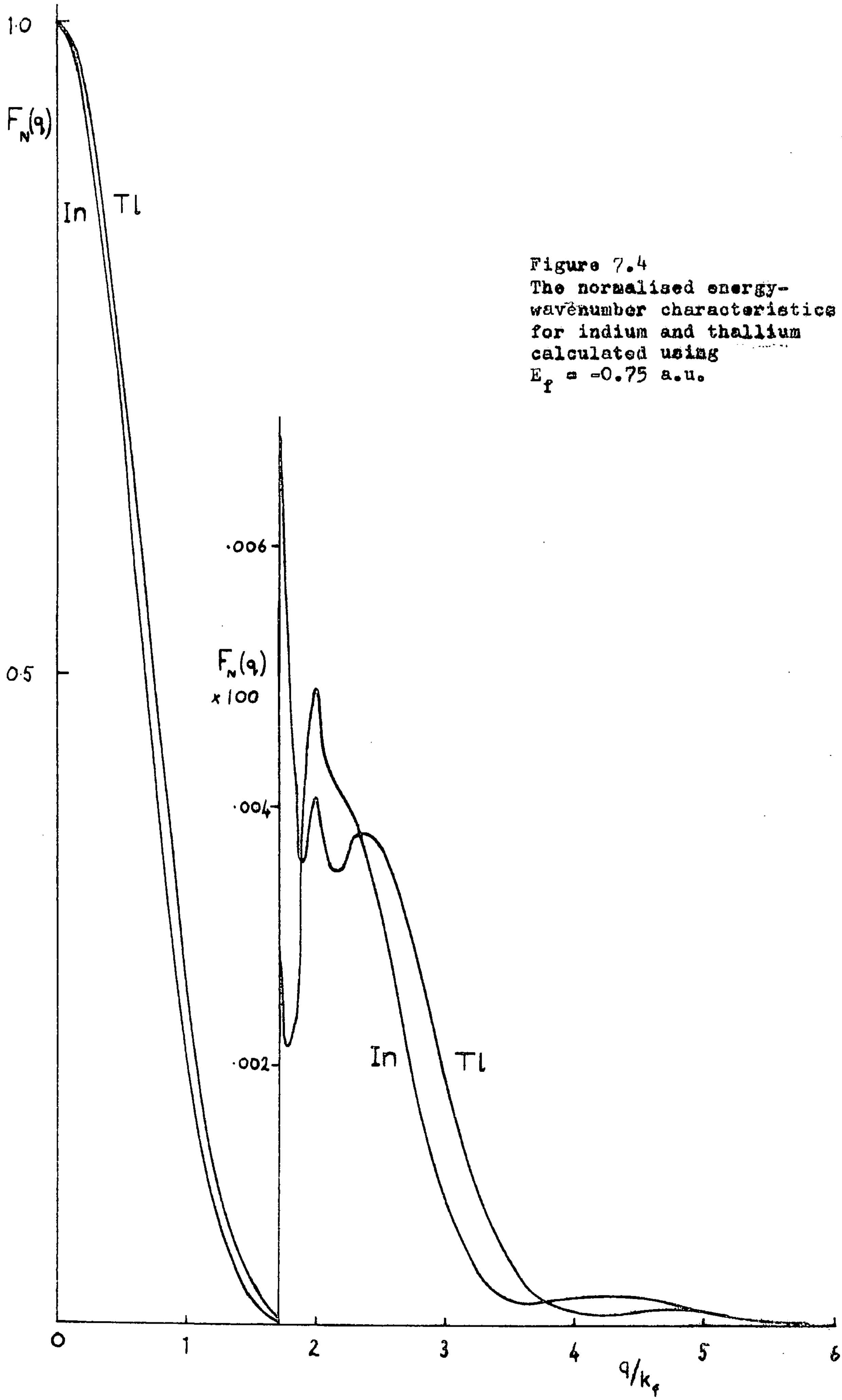

Figure 7.4
The normalised energy-wavenumber characteristics for indium and thallium calculated using E_f = -0.75 a.u.

TABLE [illegible] (CONTINUED)

ATOMIC PERCENT THALLIUM:

C/K	%	5%	[illegible]	[illegible]	2[illegible]	2[illegible]	[illegible]	35	[illegible]
2.7	.224	.24[illegible]	.2[illegible]	.[illegible]	.2[illegible]	.[illegible]	.2[illegible]	.[illegible]	.[illegible]
2.[illegible]	.177	.1[illegible]	.21[illegible]	.22[illegible]	.234	.2[illegible]	.2[illegible]	.23[illegible]	.2[illegible]
2.[illegible]	.135	.1[illegible]	.1[illegible]	.[illegible]	.1[illegible]	.1[illegible]	.1[illegible]	.1[illegible]	.23
3.[illegible]	.1[illegible]	.117	.13	.1[illegible]	.14[illegible]	.1[illegible]	.1[illegible]	.1[illegible]	.152
3.1	.72	.[illegible]	.[illegible]	.[illegible]	.113	.11[illegible]	.12	.12	.1[illegible]
3.2	.51	.[illegible]	.73	.[illegible]	.[illegible]	.[illegible]	.[illegible]	.[illegible]	.122
3.3	.35	.[illegible]	.[illegible]	.[illegible]	.[illegible]	.[illegible]	.7	.7[illegible]	.[illegible]
3.[illegible]	.26	.[illegible]	.42	.[illegible]	.[illegible]	.2	.[illegible]	.[illegible]	.[illegible]
3.[illegible]	.21	.2[illegible]	.33	.3[illegible]	.[illegible]	.[illegible]	.2	.2	.32
3.[illegible]	.19	.24	.2[illegible]	.31	.3	.3[illegible]	.3[illegible]	.3[illegible]	.37
3.7	.19	.23	.2[illegible]	.2[illegible]	.2[illegible]	.2[illegible]	.2[illegible]	.2[illegible]	.27
3.[illegible]	.2[illegible]	.23	.25	.2[illegible]	.27	.27	.2[illegible]	.2[illegible]	.1[illegible]
3.[illegible]	.21	.2[illegible]	.2[illegible]	.2[illegible]	.27	.2[illegible]	.2[illegible]	.2[illegible]	.15
4.[illegible]	.23	.2[illegible]	.2[illegible]	.26	.2[illegible]	.2[illegible]	.2[illegible]	.2[illegible]	.13
[illegible].1	.24	.25	.2[illegible]	.27	.27	.2[illegible]	.2[illegible]	.2[illegible]	.12
[illegible].2	.24	.2[illegible]	.26	.27	.26	.26	.2[illegible]	.2[illegible]	.12
4.3	.24	.25	.2[illegible]	.2[illegible]	.2[illegible]	.2[illegible]	.2[illegible]	.24	.13
4.[illegible]	.23	.24	.25	.25	.2[illegible]	.2[illegible]	.2[illegible]	.23	.14
4.[illegible]	.22	.23	.23	.24	.2[illegible]	.23	.2[illegible]	.22	.1[illegible]
4.[illegible]	.2[illegible]	.21	.21	.21	.21	.2[illegible]	.21	.2[illegible]	.1[illegible]
[illegible].7	.1[illegible]	.1[illegible]	.1[illegible]	.2[illegible]	.2[illegible]	.2[illegible]	.1[illegible]	.1[illegible]	.17
[illegible].8	.1[illegible]	.16	.17	.1[illegible]	.1[illegible]	.1[illegible]	.1[illegible]	.1[illegible]	.17
[illegible]	.13	.1[illegible]	.1[illegible]	.1[illegible]	.1[illegible]	.1[illegible]	.1[illegible]	.1[illegible]	.1[illegible]
[illegible]	.1	.1[illegible]	.12	.13	.13	.13	.13	.13	.15
[illegible]	.3	.4	.[illegible]	.5	.[illegible]	.[illegible]	.[illegible]	.[illegible]	.[illegible]
[illegible]	.	.1	.2	.2	.2	.2	.2	.2	.3
[illegible].2	.	.1	.1	.1	.1	.1	.1	.	.1
[illegible]	.	.1	.1	.1	.1	.1	.1	.	.
7.	.	.	.	.	.	.	.	.	.

TABLE 7.4

NORMALISED ENERGY-WAVENUMBER CHARACTERISTICS FOR IN-TL ALLOYS

ATOMIC PERCENT THALLIUM:

Q/K	3%	5%	10%	15%	20%	25%	30%	35%	10.%
0.1	0.98495	0.98632	0.98722	0.98771	0.98785	0.98777	0.98733	0.98677	0.98637
0.2	0.94121	0.94276	0.94364	0.94453	0.94488	0.94494	0.94478	0.94446	0.94609
0.3	0.87278	0.87458	0.87594	0.87662	0.87757	0.87796	0.87812	0.87812	0.88430
0.4	0.78553	0.78763	0.78932	0.79065	0.79166	0.79242	0.79297	0.79336	0.80421
0.5	0.68632	0.68873	0.69074	0.69242	0.69386	0.69474	0.69569	0.69665	0.71228
0.6	0.58276	0.58473	0.58774	0.58902	0.59073	0.59222	0.59352	0.59468	0.61452
0.7	0.47892	0.48179	0.48431	0.48653	0.48850	0.49025	0.49183	0.49328	0.51641
0.8	0.38187	0.38454	0.38749	0.38986	0.39195	0.39391	0.39566	0.39729	0.42243
0.9	0.29446	0.29744	0.30011	0.30252	0.30470	0.30668	0.30850	0.31027	0.33597
1.0	0.21881	0.22171	0.22431	0.22666	0.22878	0.23072	0.23250	0.23417	0.25923
1.1	0.15583	0.15856	0.16101	0.16321	0.16519	0.16695	0.16864	0.17015	0.19335
1.2	0.10645	0.10795	0.11019	0.11216	0.11393	0.11551	0.11695	0.11827	0.13864
1.3	0.06687	0.06910	0.07114	0.07278	0.07428	0.07561	0.07678	0.07784	0.09474
1.4	0.03857	0.04082	0.04249	0.04391	0.04512	0.04614	0.04704	0.04781	0.06059
1.5	0.01997	0.02132	0.0223[illegible]	0.02413	0.02505	0.02577	0.02634	0.02685	0.03669
1.6	0.00860	0.00998	0.01108	0.01193	0.01258	0.01304	0.01336	0.01355	0.01919
1.7	0.00319	0.00432	0.00519	0.00580	0.00621	0.00643	0.00651	0.00647	[illegible]
1.8	0.00214	0.00308	0.00374	0.00417	0.00440	0.00444	0.00435	0.00413	0.00428
1.9	0.00373	0.00451	0.00503	0.00534	0.00544	0.00538	0.00518	0.00487	0.00356
2.	0.00490	0.00552	0.00592	0.00614	0.00620	0.00611	0.00591	0.00562	0.00402
2.1	0.00429	0.00476	0.00509	0.00524	0.00528	0.00521	0.00505	0.00482	0.0035[illegible]
2.2	0.00413	0.00453	0.00479	0.00494	0.00498	0.00492	0.00479	0.00461	0.00382
2.3	0.00394	0.00425	0.00453	0.00467	0.00471	0.00469	0.00458	0.00443	0.00365
2.4	0.00363	0.00395	0.00414	0.00432	0.00435	0.00434	0.00427	0.00414	0.00338
2.5	0.00321	0.00350	0.00370	0.00383	0.00389	0.00391	0.00388	0.00379	0.00356
2.6	0.00273	0.00299	0.00318	0.00331	0.00338	0.00341	0.00339	0.00335	0.00336

through the lattice. The phonon dispersion curves give the variation of the vibrational frequency ω with the wavevector $\underline{Q}$. Because of the various degrees of freedom associated with the assembly of particles there are several discrete values of ω associated with each $\underline{Q}$. We can define a unit vibrational cell: if this contains n atoms, then there are 3n modes of vibration. Each of these is taking place at the same time, and the system is eqivalent to a set of 3n oscillators. In order to simplify calculations the amplitude of each component of vibration can be assigned a value $\underline{a}_{\underline{Q}}$; there are 3n such values and they are known as the normal coordinates. Solution in terms of normal coordinates is simpler because the oscillators can be considered as uncoupled: 3n normal modes result. The slope of a dispersion curve $\partial\omega/\partial\underline{Q}$ at some particular value of $\underline{Q}$ gives the velocity of propagation of a wave having the appropriate mode of vibration and with that value of $\underline{Q}$. Three of the 3n modes are known as acoustic modes, and for those modes ω tends to zero as $\underline{Q}$ tends to zero: the slope $\partial\omega/\partial\underline{Q}$ near to $\underline{Q} = 0$ gives the velocity of sound in the medium. In an acoustic mode adjacent ions are vibrating together. It is also possible to have the situation, when there are two or more ions in the unit cell, in which adjacent ions move out of phase with each other. Such a mode of vibration is called an optic mode: the frequencies are generally much higher than for acoustic modes, and do not necessarily approach zero towards $\underline{Q} = 0$. In general there are (3n-3) optic modes and 3n acoustic modes. For the case when n = 1 (that is, there is one ion per unit cell, as is found in indium, for example), there are no optic modes. Indium-thallium alloys have two types of ion in the lattice but there is no optic branch to the phonon spectrum. This is due to the alloy being random, and so the vibrational unit cell can be considered as being made up of ions on a face centred lattice (of either cubic or tetragonal form), and each ion having a mass given by the mean, weighted according to the composition, of the constituent ion masses, and thus there is still only one ion per unit cell.

Consider now the acoustic branch of the spectrum. The three normal coordinates $\underline{a}_{\underline{Q}}$ are all perpendicular; each $\underline{a}_{\underline{Q}}$ is a vector, with three components in some axial system. If one of these axes coincides with the direction of $\underline{Q}$, that is, with the propagation direction, and if two of the three components of $\underline{a}_{\underline{Q}}$ are zero, then a pure longitudinal or a pure transverse mode results. The former implies that the components of $\underline{a}_{\underline{Q}}$ perpendicular to $\underline{Q}$ are zero, while the latter means that the parallel component is zero. Suitable rotation of the other two axes will then set one of the perpendicular components to zero, also. For a general $\underline{Q}$, pure transverse and pure longitudinal modes do not always result, but we shall only consider such directions of $\underline{Q}$ in which the polarisations of the $\underline{a}_{\underline{Q}}$ can be thus simplified.

Two assumptions have been made in the calculations of phonon dispersion curves. The first is that the ion motion has been taken as harmonic. This is only a true description of the lattice behaviour at the absolute zero of temperature. At any finite temperature there are third and higher order terms in an expansion of total energy in terms of ion displacements. However, these higher order terms are usually small, but they are responsible for such such effects as thermal expansion and the variation of sound velocity with temperature. The second assumption is that when an ion moves the electron 'cloud' moves with it. Experimental results from neutron diffraction reflect the motion of the ions, whereas calculations based on energy-wavenumber characteristics give the motion of the electrons in the vicinity of the ions. This approximation is a good one because of the large difference in the relative masses of ions and electrons.

7.4.2 Method of calculation of phonon spectra

We wish to determine the change in total energy of the system when a distortion of wavevector $\underline{Q}$ is applied. Assuming harmonic motion we can then determine the frequencies, corresponding to that energy change, of a set of 3n oscillators. Only the simpler case of n = 1 need be treated here.

Contributions to the total energy were discussed in section 7.1.4, and equation 7.12 is rewritten here:

$$E_{tot} = E_{fe} + E_{bs} + E_{es} \qquad (7.12)$$

The total energy is made up of the sum of the free electron, band structure and electrostatic energies. Thus the change in total energy δE_{tot} is given by

$$\delta E_{tot} = \delta E_{fe} + \delta E_{bs} + \delta E_{es} \quad . \qquad (7.40)$$

Any change in the free electron energy arises from distortions to the fermi surface because of volume changes; we are restricting our treatment to constant volume, so that the first term on the R.H.S. of equation 7.40 can be neglected.

The evaluation of the last two terms is given here in outline only: for a fuller description of the procedures see Harrison (1966).

A displacement of the ions results in a change in the structure factor $S(\underline{q})$: if $\underline{q}_o$ is a lattice wavenumber, then for a periodic displacement of wavevector $\underline{Q}$ structure factors $S(\underline{q}_o \pm \underline{Q})$ at $\underline{q}_o \pm \underline{Q}$ can be defined. We have already seen that the band structure energy for an undistorted lattice (of an element) is given by equation 7.24:

$$E_{bs} = \sum_{\underline{q}}{}' S(\underline{q}_o)^* S(\underline{q}_o) F(q) \qquad (7.24)$$

We now consider an alloy and find the effect of a distortion on its band structure energy. The energy for an undistorted alloy is

$$\begin{aligned} E_{bs} &= \sum_{\underline{q}_o}{}' S^*(\underline{q}_o) S(\underline{q}_o) F_{av}(q) \\ &\quad + \sum_{\underline{q} \neq \underline{q}_o} S'^*(\underline{q}) S'(\underline{q}) F_{diff}(\underline{q}) \end{aligned} \qquad (7.41)$$

in which $F_{av}(q)$ and $F_{diff}(q)$ are the energy-wavenumber characteristics for the average and difference lattices. Harrison (1966) has shown that the structure factor $S'(\underline{q})$ for a random lattice is given by, for a binary alloy

$$S'^*(\underline{q}) S'(\underline{q}) = c(1-c)/N \qquad (7.42)$$

when there are cN ions of one type and (1-c)N of the other. But a distortion applied to a random lattice leaves it random and then its structure factor does not change. As a result the second term in equation 7.41 remains unchanged and so does not enter into the evaluation of δE_{bs}.

It now remains to compute the structure factor for the average lattice to second order in the vibration amplitudes $\underline{a}_{\underline{Q}}$. Consider the case of a lattice with one ion per unit cell and let the position of the ion in the j-th cell be $\underline{r}_j$. If the distortion takes it a distance $\delta\underline{r}_j$, its position is then $\underline{r}_j+\delta\underline{r}_j$ which in terms of the normal coordinates $\underline{a}_{\underline{Q}}$ is

$$\underline{r}_j+\delta\underline{r}_j = \underline{a}_{\underline{Q}}\, e^{i\underline{Q}\cdot\underline{r}_j} + \underline{a}_{\underline{Q}}^{*}\, e^{-i\underline{Q}\cdot\underline{r}_j} , \qquad (7.43)$$

where $\underline{a}_{\underline{Q}}^{*} = \underline{a}_{-\underline{Q}}$. From the definition of structure factor in equation 7.15 the structure factor for the distortion is

$$S(\underline{q}) = \frac{1}{N}\sum_j e^{-i\underline{q}\cdot(\underline{r}_j+\delta\underline{r}_j)} . \qquad (7.44)$$

By substituting equation 7.43 into 7.44 and expanding the exponential we can obtain an expression for $S(\underline{q})$ to any order required. Harrison (1966) has shown that for the harmonic approximation it is sufficient to calculate the zero and second order structure factors at $\underline{q}_o$ only, and the first order one at $\underline{q}_o \pm \underline{Q}$. The band structure energy follows from a substitution of these structure factors into equation 7.24 and evaluation to second order. The change in band structure energy is found by subtracting off the zero order term (corresponding to this energy for the undistorted lattice); Harrison (1966) gives the result for one ion per unit cell, and it is rewritten here for the case of a random alloy with propagation along a pure mode direction.

$$\delta E_{bs} = \sum_{\underline{q}_o}\Big[\big|(\underline{q}_o+\underline{Q})\cdot\underline{a}_{\underline{Q}}\big|^2 F_{av}(\underline{q}_o+\underline{Q}) + \big|(\underline{q}_o-\underline{Q})\cdot\underline{a}_{\underline{Q}}\big|^2 F_{av}(\underline{q}_o-\underline{Q}) - 2\big|\underline{q}_o\cdot\underline{a}_{\underline{Q}}\big|^2 F_{av}(\underline{q}_o)\Big] \qquad (7.45)$$

Harrison also gives the electrostatic energy change as

$$\delta E_{es} = \frac{2\pi Z^{*2}e^2}{\Omega_o} \lim_{\eta\to\infty} \sum_q{}' S^*(q)S(q) \frac{e^{-q^2/4\eta}}{q^2} \qquad (7.46)$$

which follows from an expression of Fuchs (1935). This is analogous in form to the expression for the change in the band structure energy, but with F(q) replaced by

$$\frac{2\pi Z^{*2}e^2}{\Omega_o q^2} \; e^{-q^2/4\eta} \quad .$$

(η is a parameter adjusted to optimise the convergence in Fuchs' expression). The squared structure factors in equation 7.46 take the form of those discussed above. After making a substitution for $S^*(q)S(q)$ in 7.46 Harrison (1966) obtains as the result for the change in electrostatic energy

$$\begin{aligned}\delta E_{es} = \frac{2\pi Z^{*2}e^2}{\Omega_o} \Bigg\{ 2|a_{\parallel}|^2 + \sum_{\underline{q}_o}{}' \Bigg(& \left[(q_o^{\parallel} + \underline{Q})^2 + q_o^{\perp 2}\right]^{-1} \\ & + \left[(q_o^{\parallel} - \underline{Q})^2 + q_o^{\perp 2}\right]^{-1} - 2(q_o^{\parallel 2} + q_o^{\perp 2})^{-1}\Bigg) \qquad (7.47) \\ & \times \left[\left|\underline{q}_o^{\perp} \cdot \underline{a}_{\perp}\right|^2 - q_o^{\perp 2}|a_{\parallel}|^2\right]\Bigg\} \; .\end{aligned}$$

Here $q_o^{\parallel}$ and $\underline{q}_o^{\perp}$ are the components of $\underline{q}_o$ parallel and perpendicular to $\underline{Q}$; $a_{\parallel}$ and $\underline{a}_{\perp}$ are similarly the components of $\underline{a}_{\underline{Q}}$. Equation 7.47 holds for $\underline{Q}$ lying in a symmetry direction in the crystal, with the vibration amplitude vectors parallel and perpendicular to $\underline{Q}$: for a more general direction this would not necessarily be the case. For the calculations performed, in ehich the directions investigated were [100], [001] and [110], the form of equations 7.45 and 7.47 was sufficient.

The expressions for δE_{bs} and δE_{es} can each be evaluated for the three displacement vectors corresponding to one longitudinal and two transverse waves. The results for

$\delta E_{bs} + \delta E_{es}$ can be represented as

$$\delta E_{bs} + \delta E_{es} = \sum_{i=1,3} E_i a_i^2 \qquad (7.48)$$

This equation gives the potential energy of the distortion per ion. The kinetic energy per ion is $M \sum_{i=1,3} \dot{a}_i^2$, where M is the mass of the vibrating ion for an element with one ion per unit cell, or is the weighted mean of the two ion masses for a binary alloy such as we have been considering. The sum of the potential and kinetic energies for a simple harmonic oscillator is a constant, and consequently the frequencies follow from

$$\omega_i^2 = E_i / M \quad . \qquad (7.49)$$

A computer programme was written in Fortran to perform the calculations of the lattice frequencies, based on an evaluation of equations 7.45 and 7.47-9. It is listed in Appendix III as DISPS, together with an account of the procedures used to evaluate the various functions required.

7.4.3 Summary of sections 7.1 to 7.4

The methods described have enabled the following calculations to be performed.

1) Starting with the valency, fermi wavevector, maximum angular momentum quantum number of the core states and the optimised model potential well depths and their energy derivatives, we have produced form factors and normalised energy-wavenumber characteristics, together with values for the effective valencies, of indium and of thallium.

2) The normalised energy-wavenumber characteristics

for alloys of indium and thallium (up to 35 at.% Tl) have been calculated from a combination of functions computed for the elements.

3) Phonon dispersion curves for indium and indium-thallium alloys have been obtained from a harmonic model, with the mean atomic weight, valency, effective valency, atomic volume and lattice parameters of the alloys as the input data.

The results of the calculations for the indium-thallium alloys are presented and discussed in the next section.

7.5 Results and discussion

7.5.1 The phonon dispersion curves

Before embarking on a calculation of the phonon dispersion curves of the indium-thallium alloys themselves, it was necessary to test the method used and the programme developed by reference to a well-known material. Therefore the dispersion curves of Aluminium were computed using the normalised energy-wavenumber characteristic given by Shaw (1968a) with a correction for exchange and correlation effects given by Pindor and Pynn (1969). The results are compared in figure 7.5 with those obtained by Yarnell et al. (1965).

There are at present no experimental measurements available for the dispersion curves of indium-thallium alloys, or of indium, although Rowell and Dynes (1971) have given density of states curves for both indium and thallium measured, in the case of indium, by electron tunnelling, and for thallium by neutron diffraction. Consequently the validity of the

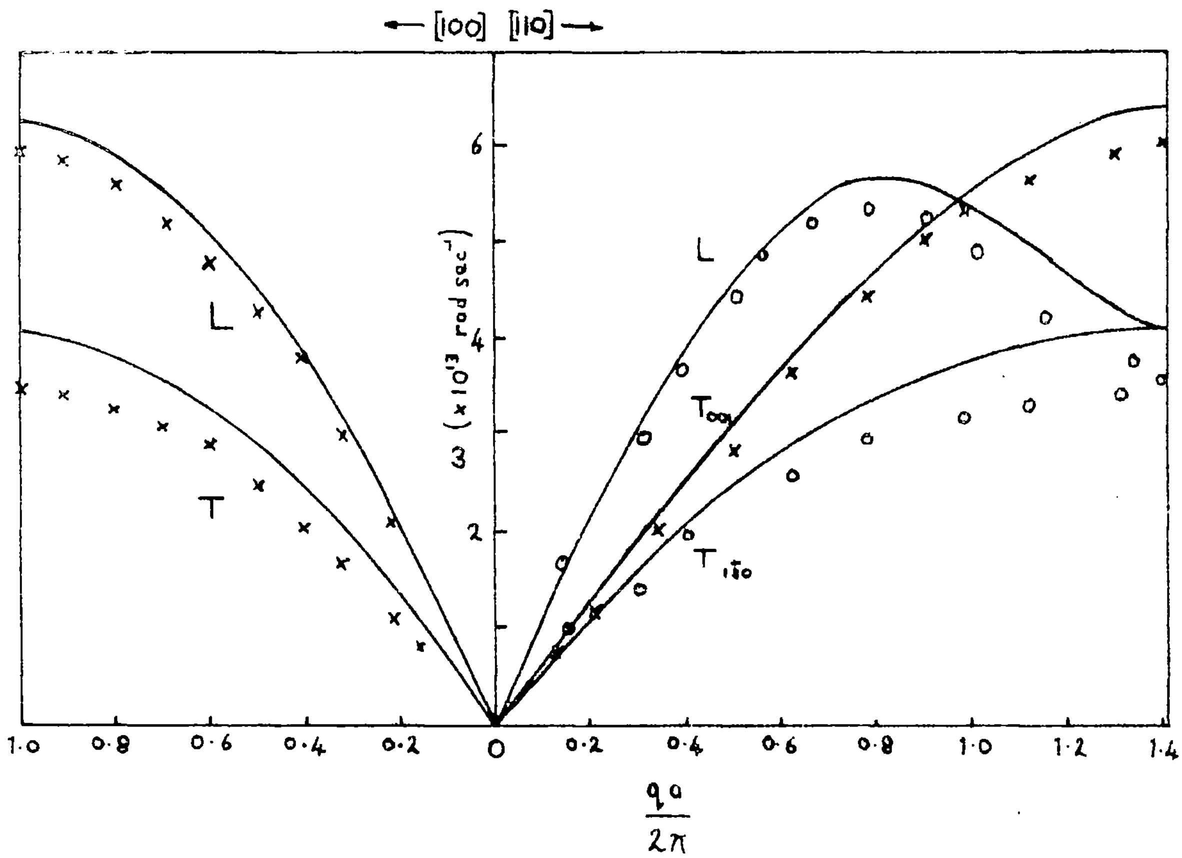

Figure 7.5 The phonon dispersion curves for aluminium calculated using the methods described in this chapter, and the measured points from neutron diffraction studies by Yarnell et al. (1965).

——— calculation

x, o } Yarnell et al.

theoretical curves can only be assessed at present by their ability to predict the observed sound velocities.

Initially the calculations were performed for indium and the alloys with normalised energy-wavenumber characteristics based on a fermi energy of -0.9 a.u., as in Table 7.2. It was found that the sum of changes in band structure and electrostatic energies (required by equation 7.48) was negative for values of $\underline{Q}a/2\pi$ less than about 0.2, for certain polarisations in certain directions. The mode most affected was that polarised $[1\bar{1}0]$ for propagation in the $[110]$ direction. Moreover, the sum $\delta E_{bs} + \delta E_{es}$ for that mode was very sensitive to changes in c/a ratio and in model parameters, much more so than any other mode. A negative total energy change implies imaginary frequencies, which would be physically unrealistic for acoustic modes. This problem could be overcome if the model parameters were evaluated at a slightly different value for the fermi energy from that used initially. Mention has been made in section 7.3.4 of the difficulties involved in a determination of the fermi energy relative to the free ion. In the light of that discussion it would appear to be quite acceptable to use a value for E_f differing somewhat from -0.9 a.u., and a value of -0.75 a.u. was found to lead to changes in the total energy which were positive for $\underline{Q}a/2\pi$ values at least as small as 0.005. The total energy change must, of course, be zero at $\underline{Q} = 0$ (the Brillouin zone centre).

In figures 7.6 to 7.9 are shown the phonon dispersion curves in three crystallographic directions, $[100]$, $[001]$, $[110]$, for indium and for alloys containing 15, 25 and 35 at.% thallium for which the energy-wavenumber characteristics used have been

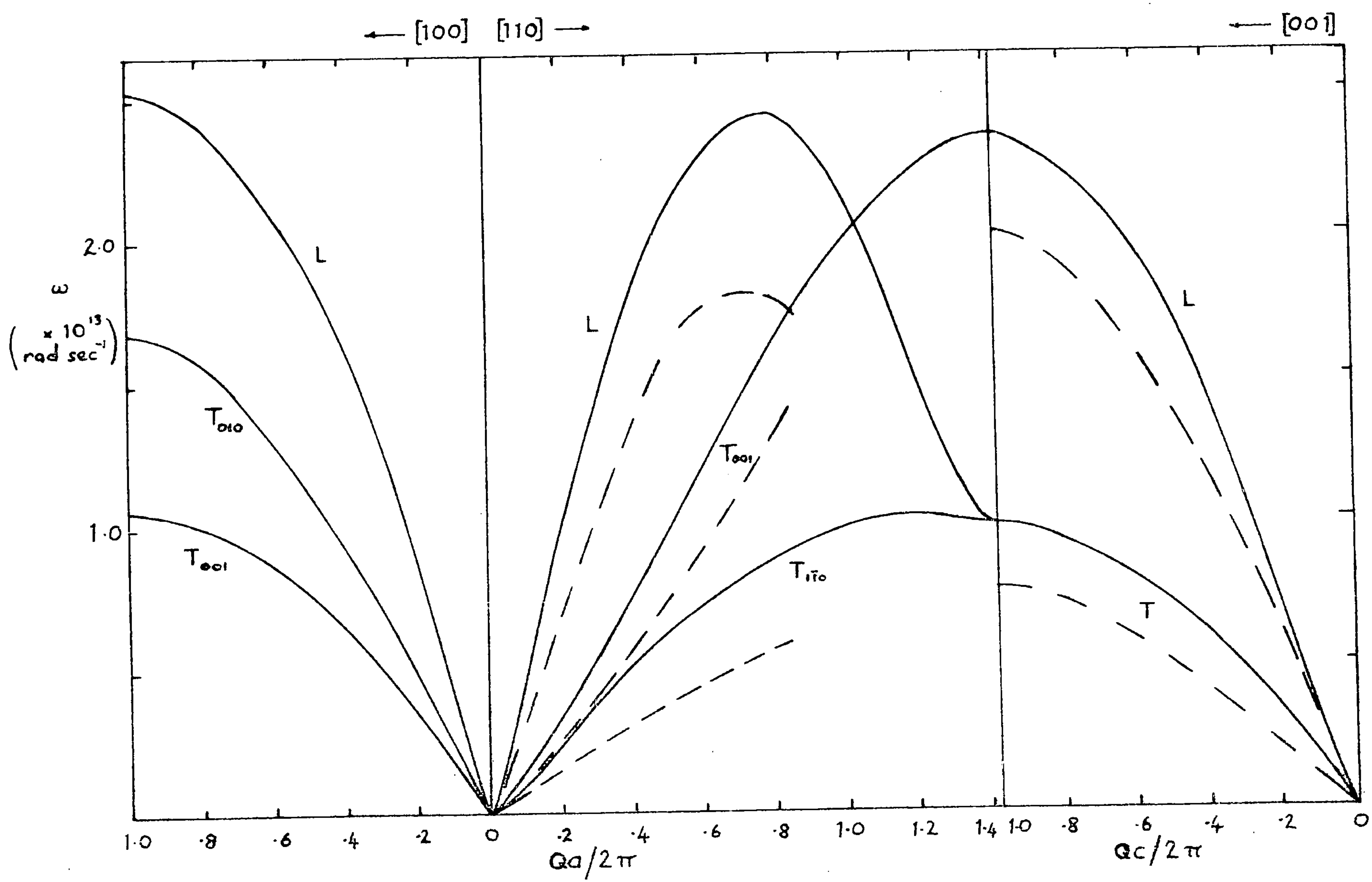

Figure 7.6 The calculated phonon dispersion curves for indium obtained from the optimised model potential (full lines), and also the results of the force-constant calculations of Kumar and Sharan (1972) (dashed lines).

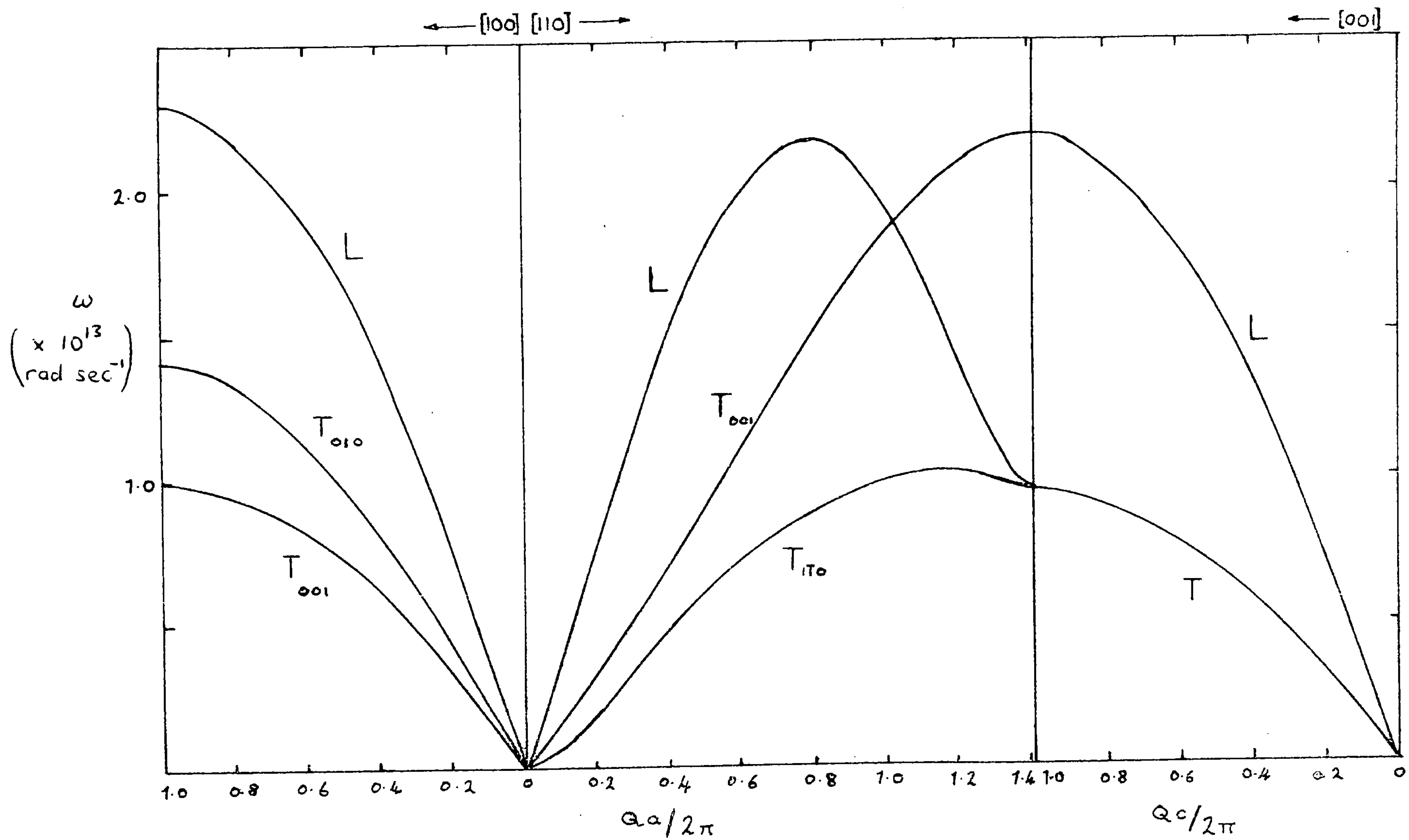

Figure 7.7 The calculated phonon dispersion curves for In-15 at.% Tl.

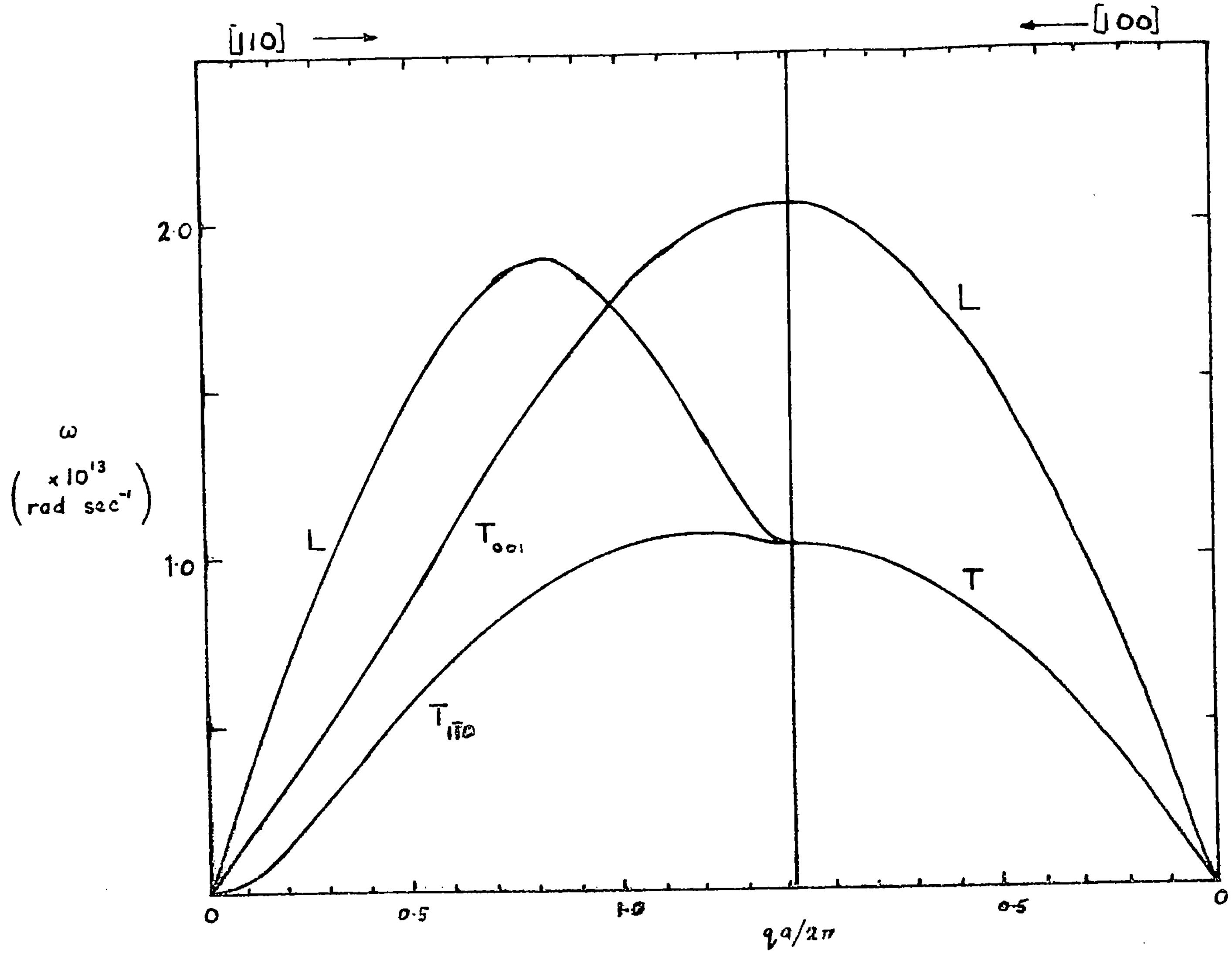

Figure 7.8 The calculated phonon dispersion curves for In-25 at.% Tl.

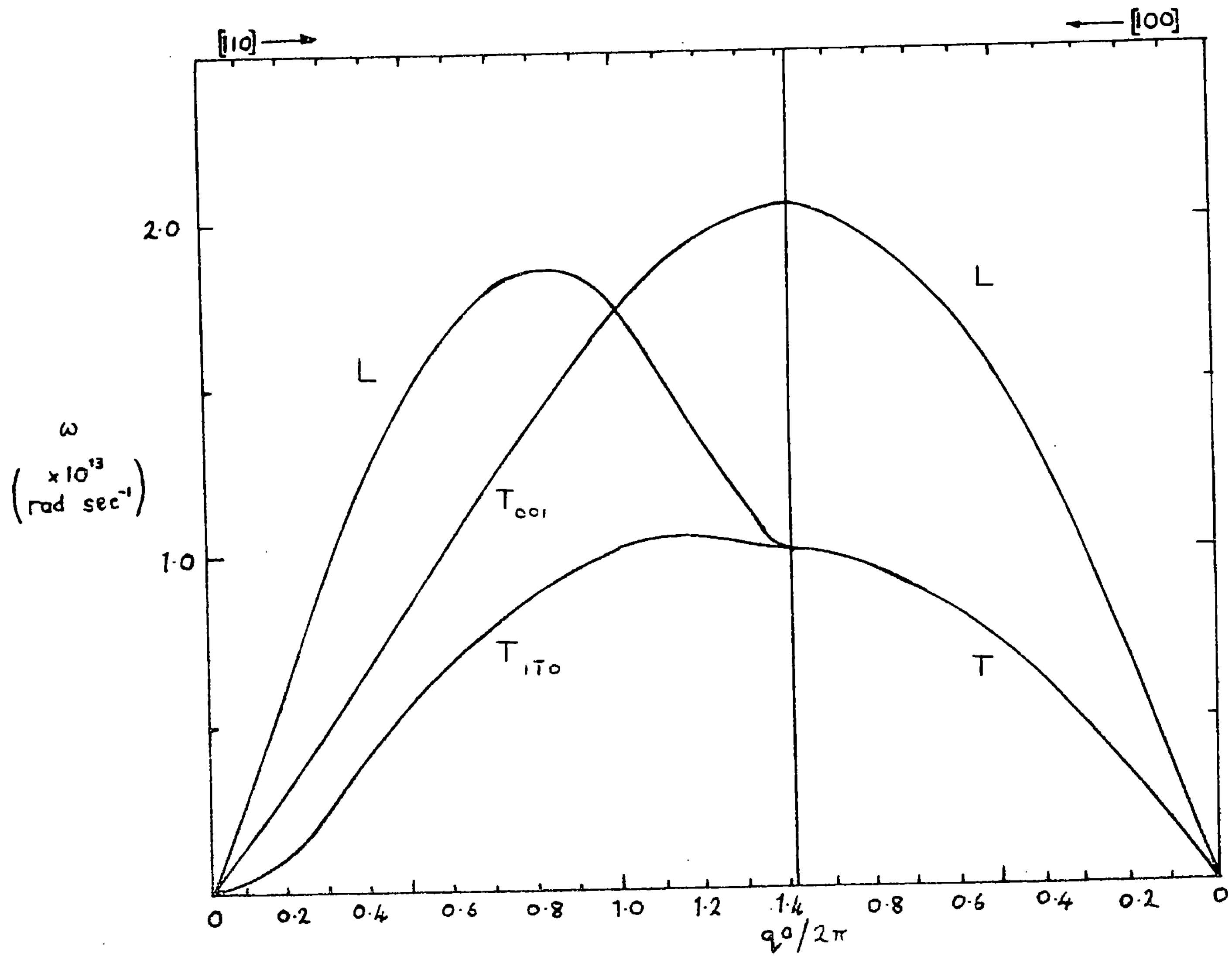

Figure 7.9 The calculated phonon dispersion curves for In-35 at.% Tl.

based on the model parameters resulting from $E_f = -0.75$ a.u. The model parameters are given in Table 7.3 and the $F_N(q)$ are in Table 7.4. It can be seen immediately from figures 7.5 to 7.8 that the differences between corresponding curves for the four compositions are not large, except for the slope near $\underline{Q} = 0$ of the transverse mode in the [110] direction, polarised [1$\bar{1}$0]. This particular mode is the one of main interest here and in figure 7.10 is shown the variation of the dispersion curve for that mode as thallium is added to indium in steps of 5 at.%. It can be seen that the reduction in $\partial\omega/\partial\underline{Q}$ near to $\underline{Q} = 0$ takes place by an increase in the concavity of the curve. As described in section 7.5.1, the velocity of propagation of an ultrasound wave can be found from the slope $\partial\omega/\partial\underline{Q}$ of the appropriate dispersion curve. This means that a direct comparison can be made with experiment to check the low $\underline{Q}$ region of the curves. In all of these calculations the c/a ratio used has been that observed in practice. Numerical values for the lattice parameters from which this ratio has been obtained are as given in figure 4.11.

The major objective of this study has been to investigate from a theoretical viewpoint the assertion that the phase transition is accompanied by the collapse of the [110], [1$\bar{1}$0] polarised transverse mode. (Dynes (1971), Taylor and Vashishta (1972), Pace and Saunders (1972).) Measurement of the velocity of sound in the [110] direction, with polarisation [1$\bar{1}$0] leads to a value of the elastic constant combination $\frac{1}{2}(C_{11}-C_{12})$, as described in table 3.1; the onset of collapse of the mode means that C_{11} approaches C_{12}. (One of the Born stability criteria restricts $C_{11}-C_{12}$ to positive values.)

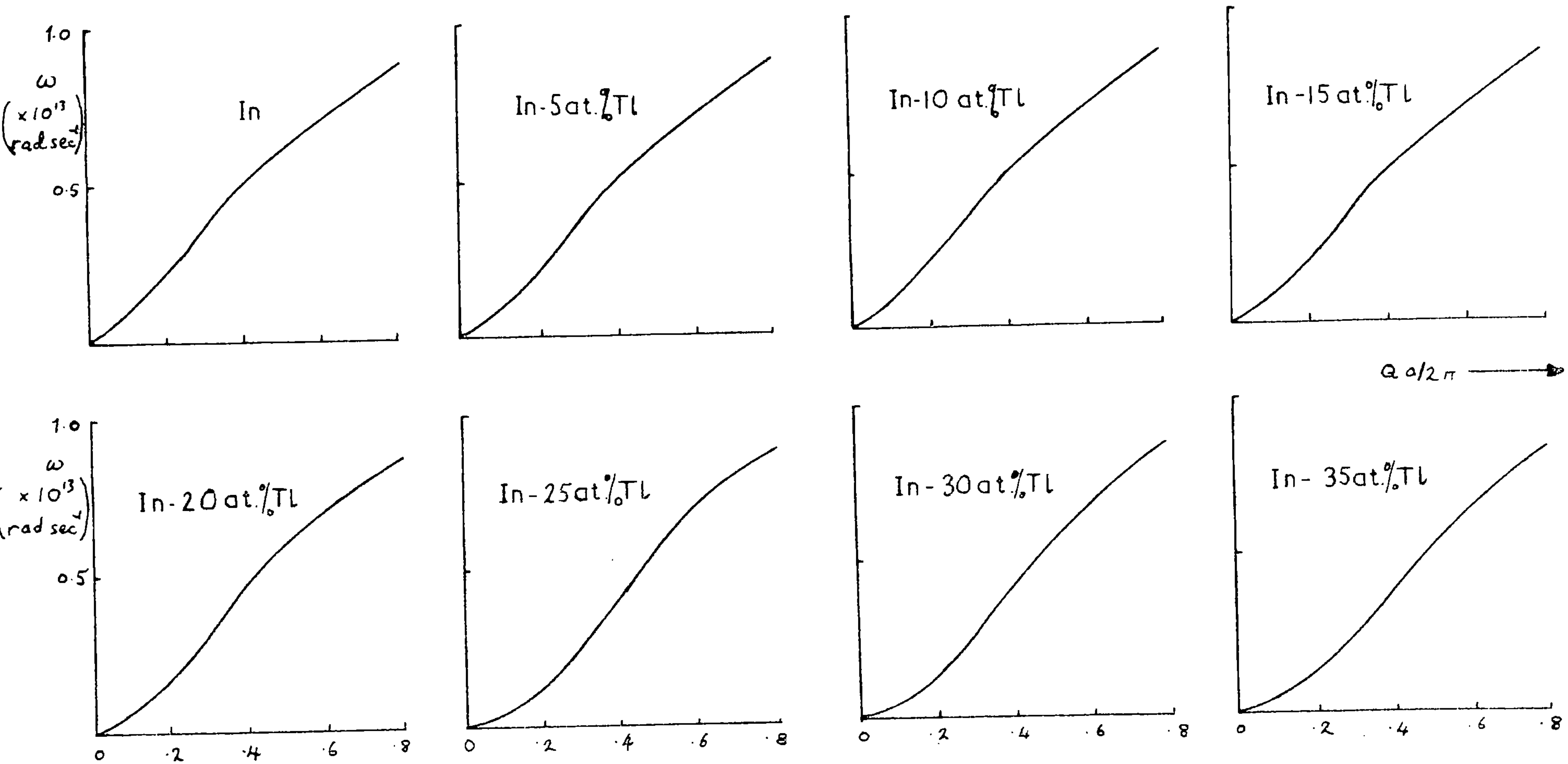

Figure 7.10 The variation of the dispersion curve for the slow shear mode in the [110] direction for several alloy compositions up to 35 at.% Tl.

Thus we present in figure 7.11 the variation of $\frac{1}{2}(C_{11}-C_{12})$ with alloy composition. Both the theoretical and experimental results are shown, and in view of the sensitivity of the calculations on the parameters involved the fit is surprisingly good. However, the positions of the calculated points depend, ultimately, on the model potential well depths used and on the value chosen for E_f. If a different value for the fermi energy E_f is used, the well depths re-evaluated and a new energy-wavenumber characteristic is calculated, then the effect of this modification on the theoretical curve of figure 7.11 is to raise or lower it relative to the position shown. But it still shows a minimum near to 22 at.% Tl, which is indicative of mode softening when the phase transition is approached from either side. Thus it can be seen that if a fermi energy value is chosen such that the calculated value of $\frac{1}{2}(C_{11}-C_{12})$ for indium agrees with the observed one (and such a choice of E_f can be made well within the uncertainty limits on that quantity), then the values of $\frac{1}{2}(C_{11}-C_{12})$ calculated for the addition of thallium to indium also agree quite well with those observed. Further, the approach of $\frac{1}{2}(C_{11}-C_{12})$ towards zero shows that the calculated form of the dispersion curve for the [110], [1$\bar{1}$0] polarised mode has a slope which, in the long wavelength limit, approaches zero at the phase transition. Such a result is consistent with the collapse of this mode.

We turn now to the sound velocities predicted by the computation for other modes. Table 7.5 lists these velocities, and compares them with the observed ones for indium and alloys containing 15 and 25 at.% Tl. As remarked by Cousins (1970),

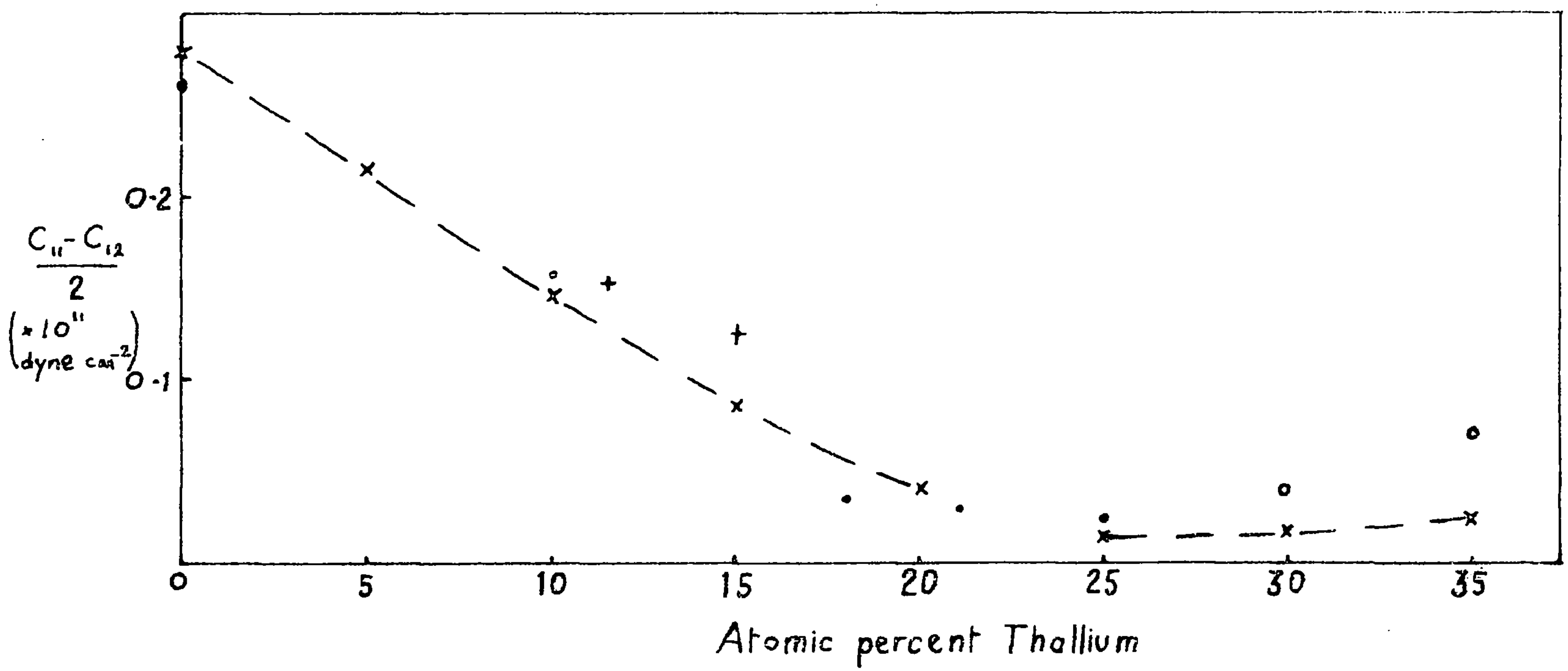

Figure 7.11 Observed and calculated values of the modulus $\frac{1}{2}(C_{11}-C_{12})$ at 290K.
+ this work, experimental; × this work, theoretical; o Novotny and Smith (1965); • Pace and Saunders (1972).

TABLE 7.5

A comparison between observed and calculated sound velocities and elastic moduli

	n^{**}	calculated v_n	calculated ρv_n^2	observed v_n	observed ρv_n^2	elastic constant given by ρv^2
Indium*	1	3.25	8.02	2.50	4.54	c_{11}
	2	1.89	2.71	1.29	1.21	c_{66}
	3	1.33	1.26	0.95	0.65	c_{44}
	4	2.61	4.97	2.49	4.52	c_{33}
	5	1.30	1.23	0.95	0.65	c_{44}
	6	3.78	10.04			$\frac{1}{2}(c_{11}+c_{12}+2c_{44})$
	7	0.56	0.23	0.60	0.26	$\frac{1}{2}(c_{11}-c_{12})$
	8	1.30	0.93	0.95	0.65	c_{44}
In-15at.% Tl	1	3.07	7.34	2.28	4.20	c_{11}
	2	1.42	1.57	1.15	1.06	c_{66}
	3	1.28	1.28	0.96	0.74	c_{44}
	4	3.23	8.38	2.28	4.18	c_{33}
	5	1.20	1.15	0.95	0.73	c_{44}
	6	3.33	8.85	2.49	4.98	$\frac{1}{2}(c_{11}+c_{12}+2c_{44})$
	7	0.34	0.09	0.39	0.12	$\frac{1}{2}(c_{11}-c_{12})$
	8	1.29	1.33	0.95	0.72	c_{44}
In-25at.% Tl	1	2.19	4.13	2.18	4.10	c_{11}
	2	1.21	1.26	0.97	0.81	c_{44}
	3	2.83	6.89	2.37	4.84	$\frac{1}{2}(c_{11}+c_{12}+2c_{44})$
	4	0.15	0.02	0.16	0.022	$\frac{1}{2}(c_{11}-c_{12})$
	5	1.25	1.34	0.97	0.81	c_{44}

* Chandresekhar and Rayne (1961) report the observed values.

** velocity subscripts as in Table 3.1.

the comparison of predicted longitudinal velocities with experimental ones is not very productive, since a longitudinal wave involves volume changes, whereas the calculation has assumed constant volume. Comparing the shear velocities in Table 7.5 we can see that the predicted velocities are predominantly larger than the observed ones by a factor of about 1.5. There may be several reasons for this. Indium has proved to be a difficult metal to understand theoretically (it has not yet been possible to calculate the correct crystal structure), and a potential which is adequate to describe all of its observed properties has yet to be constructed. The cause for the sound velocity discrepancies could, therefore, lie in the potential used. On the other hand, the assumption has also been made that the alloys behave in a harmonic fashion. This is never rigorously true for any solid at finite temperatures, but the validity of the approximation varies from one solid to another. In the indium-thallium system near the phase transition it is unreasonable to suppose that this approximation is a good one, and thus we should be surprised to find good agreement between results calculated in this way and those determined experimentally. We shall discuss the extent of the anharmonicity in the alloys in the concluding chapter. But the variation of elastic properties with alloy composition is seen to be qualitatively correct from Table 7.5. Kumar and Sharan (1972) have used a force constant model to produce phonon dispersion curves for indium. Their results are shown as dashed lines in figure 7.6. A force constant calculation uses the measured elastic data as its starting point, and hence the slopes $\partial\omega/\partial \underline{Q}$ near to $\underline{Q} = 0$ of the dispersion curves given by Kumar and Sharan will be consistent with the observed sound velocities. Consequently the regions on figure 7.6 near to $\underline{Q} = 0$ serve well to compare the results obtained from first principles with those derived from experiment. Kumar and Sharan note an 'abnormality' in the higher frequency transverse mode of the [110] direction, which they found to be slightly concave. This effect is seen, too, in the optimised model potential result for that mode; in addition the lower frequency transverse mode has a similar shape. The ramifications of such a form for one or more modes of the phonon dispersion curves are interesting. For phonon-phonon interactions there is a principle which, as given by Ziman (1960), states that the created phonon in a three-phonon interaction must lie in a higher branch than at least one of the destroyed phonons. When a shear branch contains a point of inflection, as is found here in indium, then there are certain values for $\underline{q}$, $\underline{q}'$ and $\underline{q}''$ such that the condition $\underline{q} + \underline{q}' = \underline{q}''$ can be satisfied by phonons whose wavevectors all lie on the same branch.

7.5.2 Limitations on the method: the structure of indium

There has been much work done in recent years in trying to establish a theoretical basis for the observed crystal structures of simple elements. Early work centred on the 'q_o effect', briefly mentioned in section 7.2.6, includes that of Heine and Weaire (1966) who discussed the structures of di- and tri-valent metallic elements. They found that in many cases the observed crystal structure was, out of the various possibilities considered, that one whose first few reciprocal lattice vectors were furthest from the value q_0 at which the first minimum of the energy-wavenumber characteristic occurred. Kogachi and Matsuo (1971) used a similar method in the analysis of the In-Mg and In-Cd systems: they were able to show how the changes in the position of q_0 as Mg or Cd was added to indium could account for the change in structure at the appropriate composition. They have also studied the In-Ga-Tl system in a similar way (Matsuo and Kogachi, 1971). In dealing with indium, though, the q_0 effect method has not been too successful. Heine and Weaire (1966) find that indium should be fcc, but postulate the splitting of the $\{200\}$ set of reciprocal lattice points to give the tetragonal structure, because of the proximity of q_0 to the $\langle 200 \rangle$ reciprocal lattice vector.

There have been later attempts to resolve the problem by the calculation of total energy of indium as a function of c/a ratio. Heine and Weaire (1970) describe a result which gives a minimum in the energy curve at $c/a = 1.0$ with another minimum at 0.95, although Finnis (private communication, 1973) has obtained a minimum at $c/a = 1.25$. This latter value is still far from the observed one of 1.08, but at least it is greater than 1.0. The energy curve based on the energy-wavenumber characteristic used for indium in the present work has a stable structure of fcc. The band structure part (calculated from equation 7.24) is shown in figure 7.12.

A possible solution to the problem has been suggested by Matsuo and Katada (1973) in connection with their study of In-Tl doped with Sn and/or Cd, who have evaluated the strain

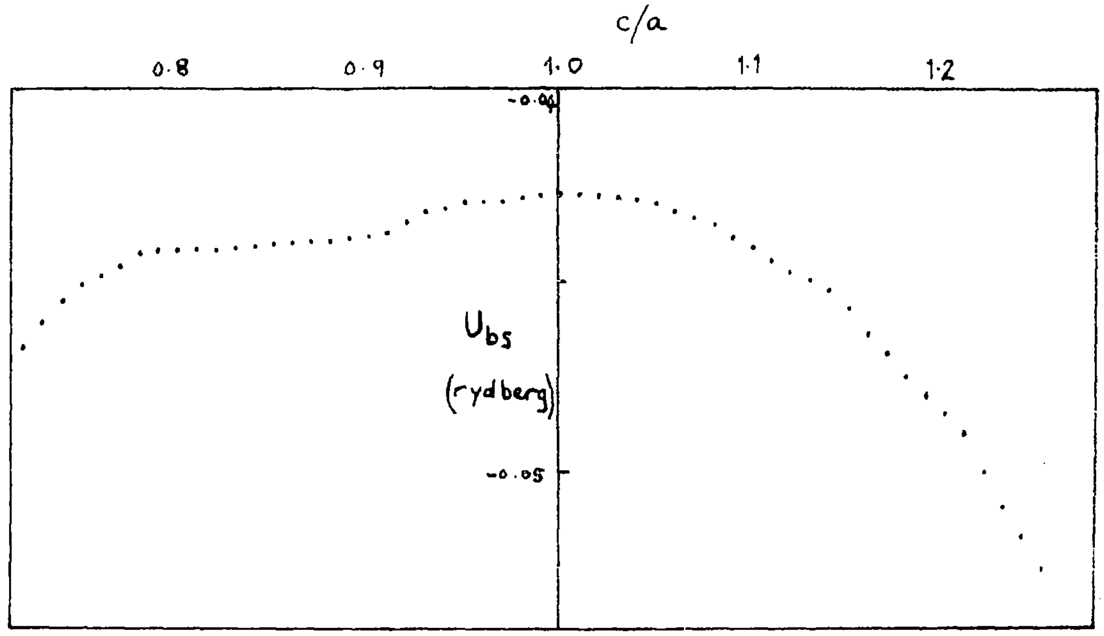

Figure 7.12(a) The variation of band-structure energy for indium calculated using the $F_N(q)$ of Table 7.4. A stable structure of fcc is predicted.

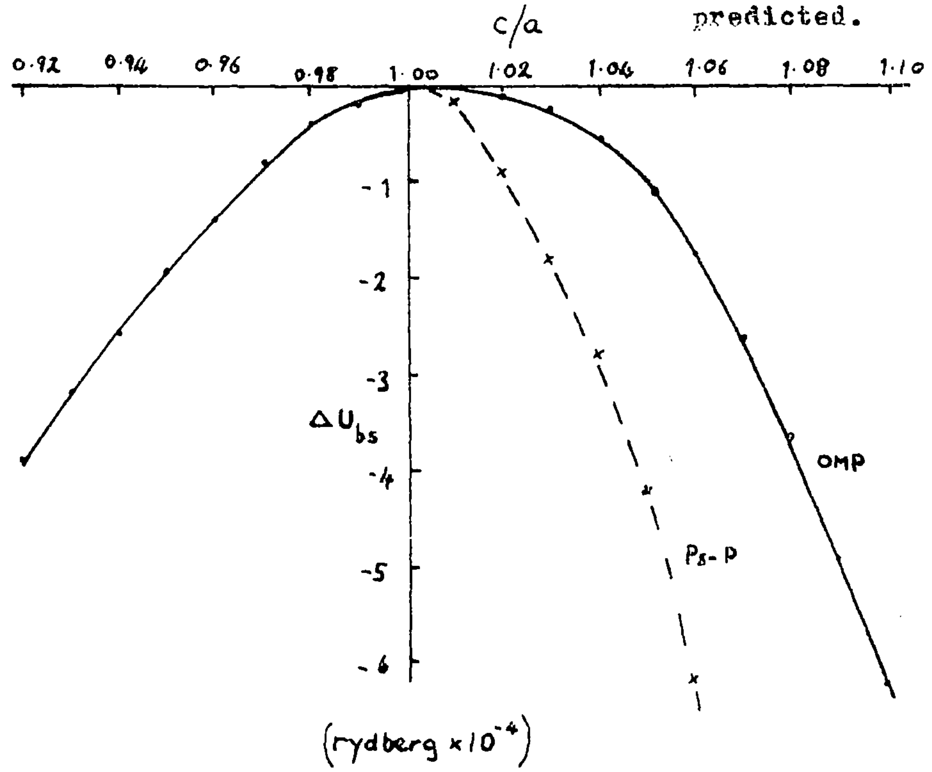

Figure 7.12(b) The curve shown in (a) is replotted here on an expanded scale, and the value of U at c/a = 1 has been subtracted off. The dashed line shows the variation given by the $F_N(q)$ of Animalu (1966).

energy for a tetragonal distortion of a cubic structure. They write this energy (U_s) as the sum of three terms: the band structure energy (U_{bs}), the Ewald energy (U_e) and another, as yet unspecified, contribution (Δ).

$$U_s = U_{bs} + U_e + \Delta$$

The sum $U_{bs} + U_e$ was found to give a minimum at $c/a = 1.0$. The energy U_s was calculated from the observed c/a ratio and experimental elastic constants, and thus it had a minimum at $c/a = 1.08$. From this a variation in Δ with c/a could be calculated. Matsuo and Katada find that the value of Δ is comparable to, and opposite in sign to, the band structure energy and also that its value is affected little when thallium is added to indium. From this they conclude that its source is an exchange interaction. Now the model on which Matsuo and Katada's work is based is the pseudopotential of Animalu (1966). We have recalculated U_{bs} with the $F_N(q)$ used in this work for indium, and also with that of Shaw (1968) for indium, and find that both give values for U_{bs} smaller by a factor of about five compared with the Animalu potential results. (See figure 7.12.) Thus the particular model used affects the result of this calculation quite drastically; a recalculation of Δ results in a change of sign in that quantity, and in a reduction in its magnitude. It would seem, then, that this approach is not a particularly profitable one to follow, although it may well be true that there is another contribution to the total energy of indium and the alloys which, when included, would allow the correct crystal structures to be predicted.

7.5.3 Further work and summary

It is possible in priciple, given a F(q) for indium and the alloys, to calculate other physical properties, such as the phonon density of states and the Grüneisen parameter. In view of the nature of the doubt surrounding the extent of the applicability of the energy-wavenumber characteristics we have not performed these calculations. It is obvious that before much more theoretical work can be performed on indium and the alloys a model must be constructed which satisfactorily resolves the problem of the structure of indium. In the mean time the limitations on the model must be borne in mind.

The test of a theoretical model is its ability to predict observable physical properties. Although we have seen that the crystal structures of indium and its alloys with thallium are not yet accounted for, yet the work presented here shows that as far as the prediction of sound velocities in these materials is concerned the optimised model potential has met with more success. Of particular interest to this work has been the finding that one particular phonon mode — that for propagation in the $[110]$ direction with polarisation $[1\bar{1}0]$ — has a small value of $\partial\omega/\partial Q$ near to $\underline{Q} = 0$ in indium, and that on addition of thallium its slope passes through a minimum at a thallium concentration corresponding to that for the fct to fcc martensitic transition. Both the form of the variation of the slope and the magnitude of the elastic constant associated with that mode — $\frac{1}{2}(C_{11}-C_{12})$ — are in quite good agreement with observation.

CHAPTER 8

DISCUSSION OF THE RESULTS, AND CONCLUSIONS

Introduction

In the previous three chapters the various experimental and theoretical results obtained for those indium-thallium alloys studied have been presented. A certain amount of discussion of the findings of the calculations has already been given in Chapter 7, and so in part A of this chapter we discuss the experimental results. Part B consists of a more general consideration of the conclusions reached. A discussion of the experimental results has been left until this point because it leads quite directly into the concluding remarks.

The experimental results will be discussed in the order in which they are presented in Chapter 5, that is first the thermal expansion of the alloys, then the ultrasound velocity and elastic constant behaviour, followed by a brief evaluation of the attenuation mechanisms found in these materials.

Part A

8.1 Thermal expansion of indium-thallium alloys and the Grüneisen parameter

Measurement of the thermal expansion of the alloys was undertaken primarily in order to make corrections for the change in sample thickness with temperature when calculating the velocity of sound in these materials from measured ultrasound pulse transit times. However, the behaviour of the thermal expansion tensor component is of some interest in itself.

The most remarkable feature of the results is the negative value of the tensor component α_{33} over a wide temperature range above about 200K almost to the melting point. This feature was found for both of the tetragonal alloys measured. The finding is in qualitative agreement with results for indium by Collins et al. (1967) who found that α_{33} became negative above about 220K and remained so at least as far as 300K — the highest temperature for which they give results. Munn (1970) has discussed the negative coefficient in indium in terms of variation of the Grüneisen parameter and the elastic constants. He concludes that the effect is seen because of the magnitudes of the elastic constants, (in particular the small size of $\frac{1}{2}(C_{11}-C_{12})$), and not because of any large anisotropy in the Grüneisen parameter, for he found the latter to be almost isotropic.

The thermal expansion of a tetragonal material can be expressed in the form (Baron and Munn, 1967; Munn, 1968)

$$\begin{aligned} \alpha_{11} &= (C_\eta/V)\,(C_{33}\gamma_{11}-C_{13}\gamma_{33})/\ C_{33}(C_{11}+C_{12})-2C_{13}^{\,2} \\ \alpha_{33} &= (C_\eta/V)\,(C_{11}+C_{12})\gamma_{33}-2C_{13}\gamma_{11}\ /\ C_{33}(C_{11}+C_{12})-2C_{13}^{\,2} \end{aligned} \qquad (8.1)$$

in which C_η/V is the heat capacity (at constant strain) per molar volume. The two independent components of the Grüneisen tensor are γ_{11} and γ_{33}. From equations 8.1 the ratio γ_{11}/γ_{33} is given by

$$\frac{\gamma_{11}}{\gamma_{33}} = \frac{\alpha_{33}C_{13} + \alpha_{11}(C_{11}+C_{12})}{\alpha_{33}C_{33} + 2C_{13}\alpha_{11}} \,. \qquad (8.2)$$

Munn gives a value of 1.05 for this ratio in indium at 284K. For the In-11.5 at.% Tl alloy we have calculated γ_{11}/γ_{33} over the temperature range 150 to 410K and find little variation from unity, consistent with Munn's result for indium. Figure 8.1 shows the calculated variation of the anisotropy ratio γ_{11}/γ_{33} for the In-11.5 at.% Tl alloy. (In a cubic alloy the ratio is always unity, by symmetry.) Thus the analysis of Munn for indium would appear to hold for the alloys also, and so we can conclude that, as in indium, it is possible to have highly anisotropic, and even negative, thermal expansion coefficients for the tetragonal alloys without a similar anisotropy in the Grüneisen coefficients.

A determination of the absolute values of γ_{11} and γ_{33} is made difficult by the paucity of specific heat data. However, an estimate can be made based on the values of C_p given by Schwartz (1970) for three alloys containing 18.8, 28.9 and 34.6 at.% Tl. He finds that at 300K each one has a value of C_p of 28.0 joule mole^{-1} $^oK^{-1}$, with a variation in this figure between the three compositions of only 0.3%. If we assume a value of 28.0 joule mole^{-1} $^oK^{-1}$ for C_p in the alloys studied here, and if we use the measured results of thermal expansion coefficients at 300K, then we can use equations 8.1 to obtain values for γ_{11} and γ_{33}. The results are: γ_{11}= 2.4, γ_{33}= 2.2 for 11.5 at.% Tl; γ_{11}= 2.3, γ_{33}=2.2 for 15 at.% Tl; γ = 2.0 for 25 at.% Tl. The cubic alloy has only one thermal expansion and Grüneisen coefficient; no negative value of α was observed, although in the transition region a temperature hysteresis was seen. The values of α for the fcc and fct sides of the transition temperature were different (by a factor of almost two).

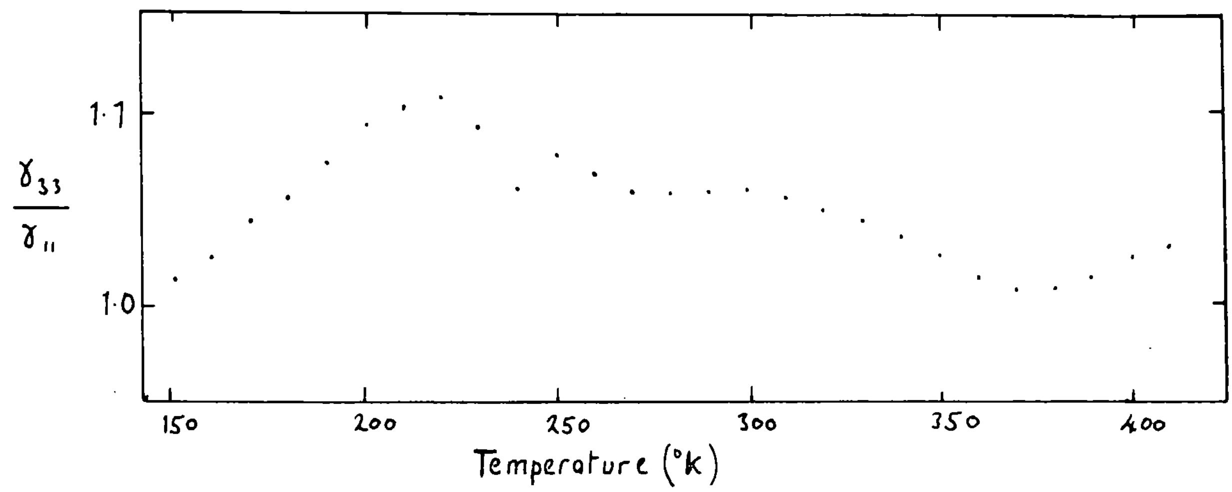

Figure 8.1 The temperature variation of γ_{11}/γ_{33} for an In-11.5 at.% Tl alloy.

8.2 Temperature variation of the observed ultrasound velocities and elastic constants

The first part of this section will deal with the variation with temperature of ultrasound velocity observed in the In-Tl alloys; it will be followed by a discussion of the elastic constants.

8.2.1 Ultrasound velocity changes

In the absence of phase transitions most solids have a velocity of sound which is almost temperature independent close to 0 K, and which varies approximately linearly with temperature (with a negative gradient) above about 20K; the variation continues in this fashion until near to the melting point. The tetragonal alloys studied had a temperature variation of this form: the few measurements which were possible at very low temperatures (to 4.2K) showed that the slope $\partial v/\partial T$ indeed approached zero as T tended to zero, while the remainder of the measurements, obtained within the range 77 to 423K, showed an almost linear variation. However, there were deviations from linearity in longitudinal velocities near to the melting point. Figure 8.2 shows a collection of results for both of the tetragonal alloys (11.5 and 15 at.% Tl) of longitudinal and shear velocities near to T_m (melting point about 425K). Certain of these curves have a slope which is tending towards zero as the melting point is approached. We can associate this with a pre-melting effect rather than a pre-transition or mode-softening one, since it has been seen to a similar extent in both the 11.5 and 15 at.% Tl alloys, even though the former

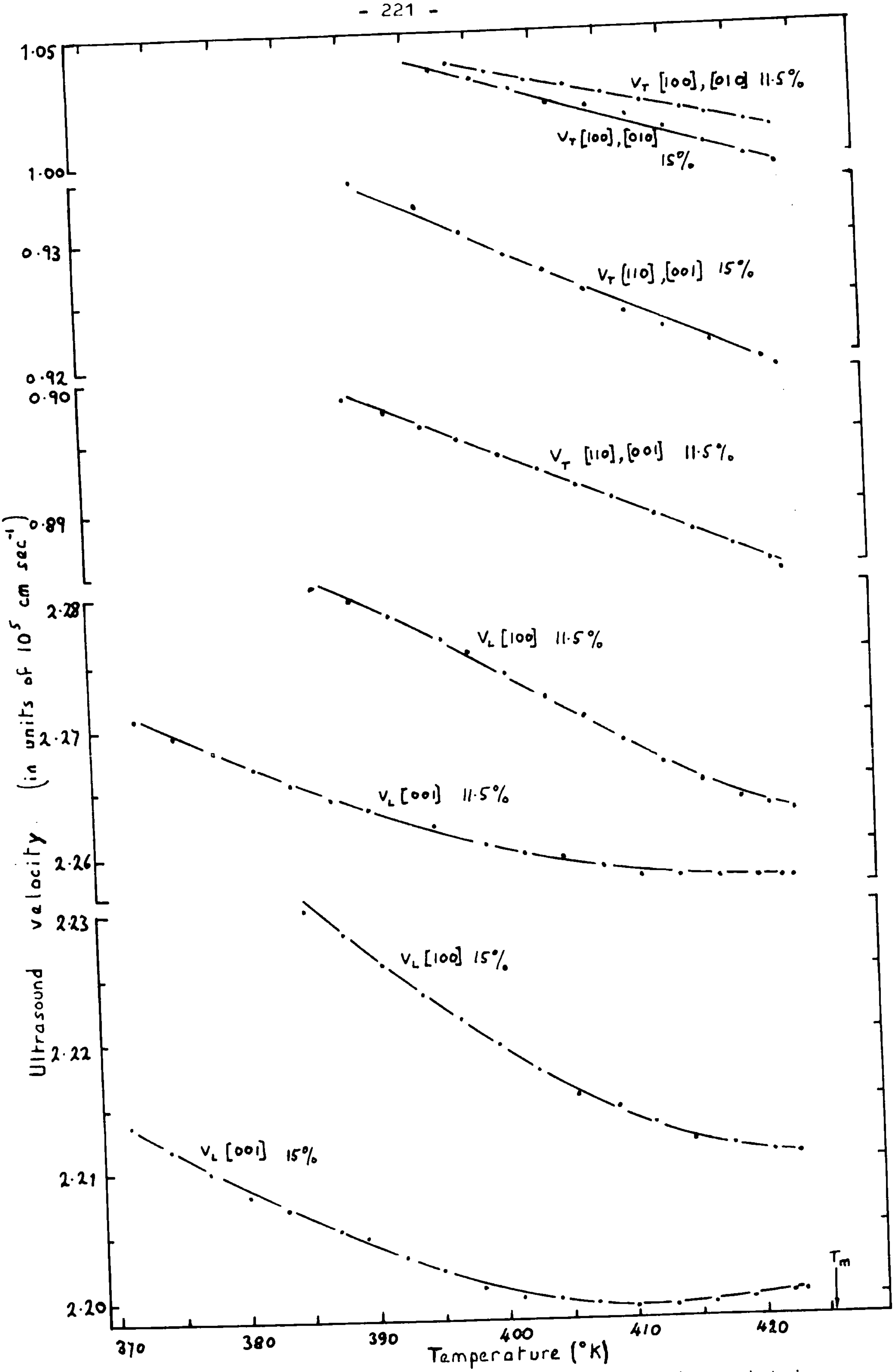

Figure 8.2 Ultrasound velocity near the melting point in In-11.5 and 15 at.% Tl.

is further from the fct/fcc boundary at the melting point than is the latter. The effect has also been seen in the In-25 at.% Tl alloy (Chung, 1973, private communication), in which mode softening of the slow shear mode in the [110] direction is almost certainly becoming reduced for an increase in temperature towards T_m.

The slopes $\partial v/\partial T$ vary somewhat between orientations, and for the In-11.5 at.% Tl alloy range from 3.45×10^2 cm sec^{-1} $^oK^{-1}$ for the shear wave velocities leading to C_{44}, to 1.88×10^3 cm sec^{-1} $^oK^{-1}$ for the slow shear mode propagating in the [110] direction. (Both figures apply to the linear portions of the variation), and for the In-15 at.% Tl alloy the corresponding values are 2.85×10^2 and 2.0×10^3, respectively.

The sound velocity in a perfectly harmonic solid would not change with temperature, and any variation found in practice is a reflection of the anharmonic contributions to the binding energy. Thus the slope of a velocity-temperature curve is related to the anharmonicity in the binding forces appropriate to the polarisation of the particular mode. From the results for the tetragonal materials the greatest slope was found for the mode polarised [$1\bar{1}0$] and propagating in the [110] direction.

The velocity changes seen in the cubic alloys 25 and 27 at.% Tl fall into two sections: temperatures near to the martensitic transition region and temperatures remote from that region. In the latter section the behaviour was similar to that for the tetragonal alloys, and need not be discussed further at this stage.

In the vicinity of the martensitic transition there were deviations in sound velocity from the curve produced by an extrapolation of the variation in the cubic phase. There was a depression in the velocity-temperature curves of between 0.2 and 0.3%. The depression was greater for the higher T_c 25 at.% alloy. This dip was seen in each of the measured curves, for polarisations [110], [1̄10]; [110], [001]; [100], [100]. However, in the case of the last the higher attenuation caused the precision in the measurements to be greatly reduced and the form of the dip is not so well established. Also, the twinned tetragonal form which existed below T_c had a changed orientation with respect to the original cubic one, so that the direction of propagation had effectively changed.

We can sum up the temperature variation in the transition region of the 25 and 27 at.% Tl alloys by enumerating four features of interest. Firstly, there was no obvious discontinuity in the velocity-temperature curve at the fcc-fct transformation. Secondly, the variation has been described as a dip because the velocity curve eventually returned to the line extrapolated from the cubic region. (This could only be seen with confidence in the [11̄0] measurements because of the difficulty with [100] propagation in the tetragonal phase of these alloys, as discussed above.) Thirdly, the magnitude of the dip and the temperature range over which it occurred differed for the two alloys, being sharper for the higher T_c 25% alloy. Fourthly, the variation was rather different from that observed in a 21 at.% Tl alloy by Pace and Saunders (1972), in which a much more pronounced dip was seen in the fast shear mode propagating along [110], of about $2\frac{1}{2}$%, and extending over only about 10°K, compared with 30° or 40° for those reported here. These results will be discussed further in section B.

8.2.2 Variation of elastic constants

For all of the six independent elastic constants for the tetragonal alloys, except C_{12} and C_{13}, and for all three of the cubic ones except C_{12} there are modes of sound propagation which give their values directly. Thus the temperature variation of these moduli can also be found directly. The moduli C_{12} and C_{13} depend on a knowledge of more than one velocity for their determination. The variation of elastic constants for the tetragonal alloys is shown in figures 5.13 and 5.14; figure 5.8 gives the details for the cubic alloys.

Considering first the tetragonal alloys we observe two effects. As the melting point is approached both the 11.5 and 15 % alloys are becoming closer to the fcc/ fct boundary. These particular alloys melt and do not transform to the cubic phase, but nevertheless the moduli are changing with temperature in a way which suggests that a transformation would occur if it were not for the melting process. From figures 5.13 and 5.14 the pairs of moduli C_{11} and C_{33}, C_{44} and C_{66} are tending to the same value. (In a cubic phase each pair is equal.) The moduli C_{12} and C_{13} are also expected to tend to the same value, but the larger error on the value of C_{13} means that no definite conclusion can be drawn from this result. In any material which transforms from tetragonal to cubic this overall trend would be expected. But it can also be seen that the moduli C_{11} and C_{12} are becoming more nearly equal. This is not an automatic feature of a tetragonal to cubic transition, but would result from a softening of the phonon mode whose slope near to $\underline{Q} = 0$ gave the modulus $\frac{1}{2}(C_{11}-C_{12})$. Once again, no conclusions can be reached for the variation of $C_{33}-C_{13}$.

At a given temperature the 15 at.% Tl alloy is closer to the phase boundary than is the 11.5at.% one, and the elastic constant values reflect this fact. We find that the differences between C_{11} and C_{33}, and between C_{44} and C_{66} are smaller for the former composition alloy than for the latter near the melting point. Also, $C_{11}-C_{12}$ is less. Because of the low value of the ultrasound velocity which led to a determination of $\frac{1}{2}(C_{11}-C_{12})$, experimental difficulties prevented its measurement in the 15% alloy above 378K, but an extrapolation to 423K shows that its value at that temperature is very small, and is about 65% of its room-temperature value. It is interesting that the temperature variations of the moduli C_{11} and $\frac{1}{2}(C_{11}-C_{12})$ are such as to give an almost temperature-independent value of C_{12}.

We now turn briefly to the cubic alloys. Only three elastic constants are involved, and their temperature dependence has been shown in figure 5.8 for the 25 and 27 at.% Tl samples, after a thermal expansion correction to the sample thicknesses has been applied. In the cubic region the values of C_{11} and C_{12} are tending to the same value at the transition temperature T_c, within the limits of experimental error. (T_c has been taken as the temperature corresponding to the top of the peak in ultrasonic attenuation.) In the tetragonal phase the curves diverge again. However, as remarked previously, the slight change in orientation of atomic planes in the twinned tetragonal form means that the measured velocities are no longer governed by the same elastic constant combinations as they were in the single crystal cubic modification. As a result the elastic constant variations below T_c must be treated with caution. The elastic constant C_{44} derives directly from a measured velocity, so that its variation is similar to that of the velocity from which it is calculated (the [001] polarised shear wave propagating in the [110] direction). But here again, we can only be sure that the measured velocity gives a value of C_{44} in the region above T_c.

8.3 Ultrasound attenuation in In-Tl alloys

The two main features of the temperature dependence of the measured attenuation of indium-thallium alloys mentioned in Chapter 5 — the peaks at the phase transition and the overall rise, seen in all alloys, towards lower temperatures — will be discussed separately.

The attenuation peak at the phase transition has been observed in other alloy compositions (18 and 21 at.% Tl) and its origin has been discussed by Pace and Saunders (1972a). It may be attributed to an increased coupling between ultrasonic waves and the lattice vibrations in the vicinity of T_c brought about by anharmonic interactions. Fleury (1971) discusses the effect for soft optic modes. The temperature of the observed peak was used to characterise the transition temperatures of the cubic alloys, and to check any hysteresis in T_c between warming and cooling. The results of the measurements have been given in figures 5.18 and 5.19 . An increased attenuation for higher frequencies was observed, but no satisfactory study was possible of the frequency dependence of the attenuation because the high values of attenuation found at relatively low ultrasound frequencies (15MHz) meant that values too large to measure occured above about 50MHz. In a similar way to the trend found in the extent of sound velocity deviations at T_c for these alloys and for those measured by Pace and Saunders (1972), the attenuation peaks also spanned a smaller temperature range for higher values of T_c; figure 8.3(b) shows the attenuation behaviour at the phase transition for 21, 25 and 27 at.% Tl alloys. At temperatures below T_c a further rise was observed. A similar effect has been seen following the transition in $SrTiO_3$, and in that case it has been suggested (Rehwald, 1970) that the rise is due to grain boundary scattering. Such a mechanism, though possibly a contributor, is probably not the predominant one here, for a similar rise was also seen in the 11.5 and 15 at.% samples below $\simeq$220K: these alloys do not transform. Moreover, the transition peaks appeared to be superimposed on a rising background attenuation which had a similar form for all of the alloys studied.

The mechanism of the attenuation in the tetragonal alloys, and in the temperature regions of the cubic ones remote from the transition region, is far from clear. The features to be explained are:

1) At low temperatures ($\lesssim$20K) the attenuation is very high, and almost temperature independent. (Measurements were made to 4.2K on several samples, and at $\simeq$2K on one of those no reduction was observed from the value at 4.2K.)

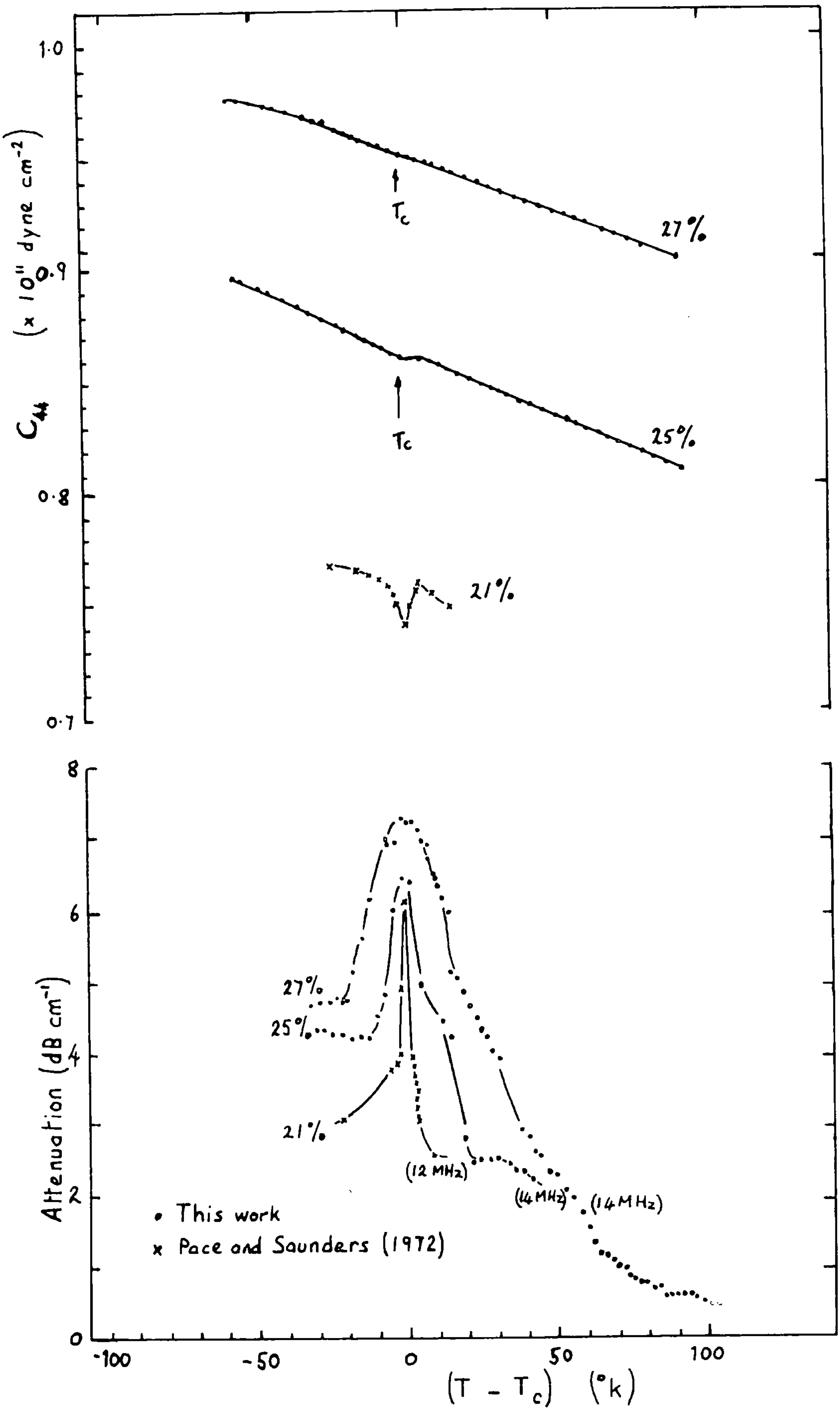

Figure 8.3 Velocity and attenuation in the vicinity of the martensitic transition in three In-Tl alloys.

2) In the temperature range of approximately 40K to 200K the measured attenuation fell to a value of about 0.1 of its 4.2K figure. The steepness of the slope varied between samples. Just before the fall a small peak was seen at between 20 and 40K.
3) From $\simeq$200K to $\simeq$350K there was an almost temperature independent region.
4) As the melting point was approached a gradual rise in attenuation was found, until within a few degrees of T_m it had approximately doubled its 350K value.

The preceding four observations apply to longitudinal wave attenuation; the directions studied were [100], [001], and [110], although the effects did not appear to depend on propagation direction. Shear wave attenuation was not studied extensively, and not at all at low temperatures.

The phonon-phonon, or Akhieser type, mechanism for damping depends on phonon populations of the various modes. These vary with temperature according to the Bose-Einstein distribution function, and at low temperatures the decrease in population results in a drop in attenuation as the number of phonons for interaction with the ultrasound wave decreases. But if there is a very soft phonon mode, that is, one of very low energy, then it would be possible to have a significant number of phonons available for interaction at much lower temperatures than for most solids. Consequently, the ultrasound attenuation could be large, even at very low temperatures, and thus the low-temperature attenuation behaviour seen in the alloys could result from the presence of a soft phonon mode.

As far as the sharp fall at between 40 and 200K is concerned, there are several mechanisms which could be responsible and which would lead to the observed variation in α_L with temperature.

First we consider the Woodruff and Ehrenreich (1961) expression for damping of a longitudinal mode.

$$\alpha_L = \frac{8.68\,\gamma^2\omega^2\,kT}{\rho v^5}\ \mathrm{dB\ cm^{-1}} \qquad (8.3)$$

in which γ is the Grüneisen parameter, ρ is the density, v is the sound velocity, ω is the ultrasound frequency, T is temperature, and k is thermal conductivity. Equation 8.3 predicts a constant value of attenuation α_L above Θ_D when $k \propto 1/T$. 8.3 can also be written as

$$\alpha_L = \frac{C_v T \gamma^2 \tau_{th} \omega^2}{3\rho v^3} \qquad (8.4)$$

since $k = \frac{1}{3} C_v v^2 \tau_{th}$. If τ varies with temperature, and, specifically, decreases for increase of temperature, then α_L will also decrease.

Alternatively, one could look to the work of Mason and Rosenberg on Al, Pb, Nb and Cu (Mason and Rosenberg, 1966, 1967; Mason and MacDonald, 1971).

These workers were able to identify two components in the observed sound attenuation measurements. One was a dislocation component, and the other a square-law component (it varied as ω^2). The latter was shown to be made up of an electron viscosity inversely proportional to resistivity, and a (smaller) phonon viscosity. Their results show that the square-law component has a temperature dependence in Pb and Al very similar in form to that seen in the indium-thallium alloys, in that it had a large rise on decrease of temperature (exponential) with a small turnover at about 30K. Mason and Rosenberg reference results for propagation in the [001] direction in zinc, for which the slip plane for dislocation motion is (001). Propagation in [001] thus gave no dislocation component, and only the square-law one was seen. However, it is unlikely that such a simplification is possible in the indium-thallium alloys, and before either this or the previous mechanism can be tested further a study of frequency dependence must be performed.

The final region of interest is that near to the melting point, at which a rise in α_L is again seen. Saunders, Pace and Alper (1967) have described a rise in α_L in In_2Bi which occurred within about 1^{o} of the melting point. As in the case of the 40 to 200K region in the alloys we can only speculate, but the Woodruff and Ehrenreich expression of equation 8.3 shows an increase in α_L for a rise of thermal conductivity. A sharp rise in k for both metals and alloys has been observed (Pashaeev, 1962) near the melting point, and the specific heat anomaly has been described (Borelius, 1963). Thermal data near the melting point is needed to test this hypothesis, but if the cause is, in fact, an increase in k or C_v then the latter appears to take place starting at about 20 or $30^{o}K$ from T_m.

Part B

In this part we shall discuss the bearing of the experimental and theoretical results for the indium-thallium alloys on the lattice properties of those materials, with particular reference to the martensitic phase transition.

8.4 Anharmonic effects in indium-thallium alloys

8.4.1 Experimental observations

If the internal energy of a crystal lattice U is expressed in terms of strain components then we may write an expression for U involving products of strain components to any order desired. The harmonic approximation involves only second order combinations. As a simple example we consider one strain component only; let this be denoted by x. We may write

$$U = ax^2 - bx^3 - cx^4 - \ldots \qquad (8.5)$$

in which the coefficients are all positive. The first term represents a symmetrical, harmonic potential well, while the other terms modify the well shape to make it asymmetrical. A simplified account of the effect of anharmonicity on an elastic constant can be seen as follows. The second order elastic constant when the strain is x is given by $\partial^2 U/\partial x^2$. If x is a longitudinal strain the result is a constant such as C_{11} or C_{33}. The shear constants involve shear strains in the second derivative. From equation 8.5 $\partial^2 U/\partial x^2$ is equal to $2a - 6bx - 12cx^2 - \ldots$ The strain x is proportional to temperature (see, for example, Kittel, 1966), and when quartic and higher terms are ignored the elastic constant is also proportional to temperature. This results in the linear variation of elastic constant with temperature seen in most solids. An increase in anharmonicity can be represented by an increase in the coefficient b in equation 8.5, and in consequence of this the elastic constant will be reduced. Moreover, if the range of temperature for which b has a larger value is small, then the corresponding elastic modulus will show a dip. Similar considerations apply for shear moduli.

The variation of elastic constants with temperature through the martensitic transition in both the 25 and 27 at.% Tl alloys shows a slight dip in the vicinity of T_c. The dip is larger for the higher T_c alloy of 25 at.%. In figure 8.3(a) is shown the temperature variation of the modulus C_{44} in the vicinity of T_c for these alloys, and also that for 21 at.% Tl reported by Pace and Saunders (1972). The results suggest an increased anharmonic effect for alloys of lower thallium content and higher transition temperatures. The attenuation peak at T_c can also be considered to be a result of enhanced anharmonic interaction, and in figure 8.3(b) is shown the variation in longitudinal wave attenuation in the [110] direction in the same three alloys. The fractional increase in attenuation from the 'base level' is seen to be greatest for the 21 at.% Tl alloy.

The variation in temperature range over which the enhanced anharmonic effects are seen for the three alloys could be due to the fact that the apparent 'two-phase' region of the phase diagram (figure 2.1(b), and Pollock and King, 1968) is wider at lower temperatures.

At this stage it begins to appear that a larger variation of observed properties near the phase transition for higher values of T_c might be a general feature of the alloys. The magnitude of the peak in thermal expansion, as reported by Pahlman and Smith (1968), appears to follow this trend. To examine the hypothesis further we show in figure 8.4 the values of elastic moduli for various compositions at various temperatures. The moduli concerned are those for propagation of longitudinal and fast shear waves in the [110] direction. (Figure 8.4 represents an extension, made possible by the results of the present work, of a collection of data given by Pace and Saunders (1972).) The data for 290K shows a fairly well-established variation, and we see a dip in both the moduli shown at about 22 at.% Tl. If the above reasoning is correct, then we should expect a variation in modulus-composition curves for different temperatures of the form shown in the sketch below.

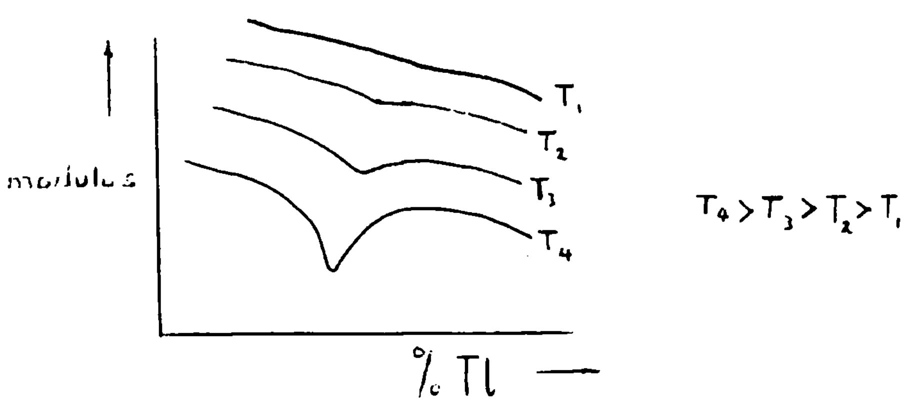

We now look to see whether the curves joining points representing lower temperature values have smaller dips in them than that for 290K. The points shown for 200K and 100K are not inconsistent with this idea, but there is still insufficient data to form a definite conclusion for this aspect of the problem.

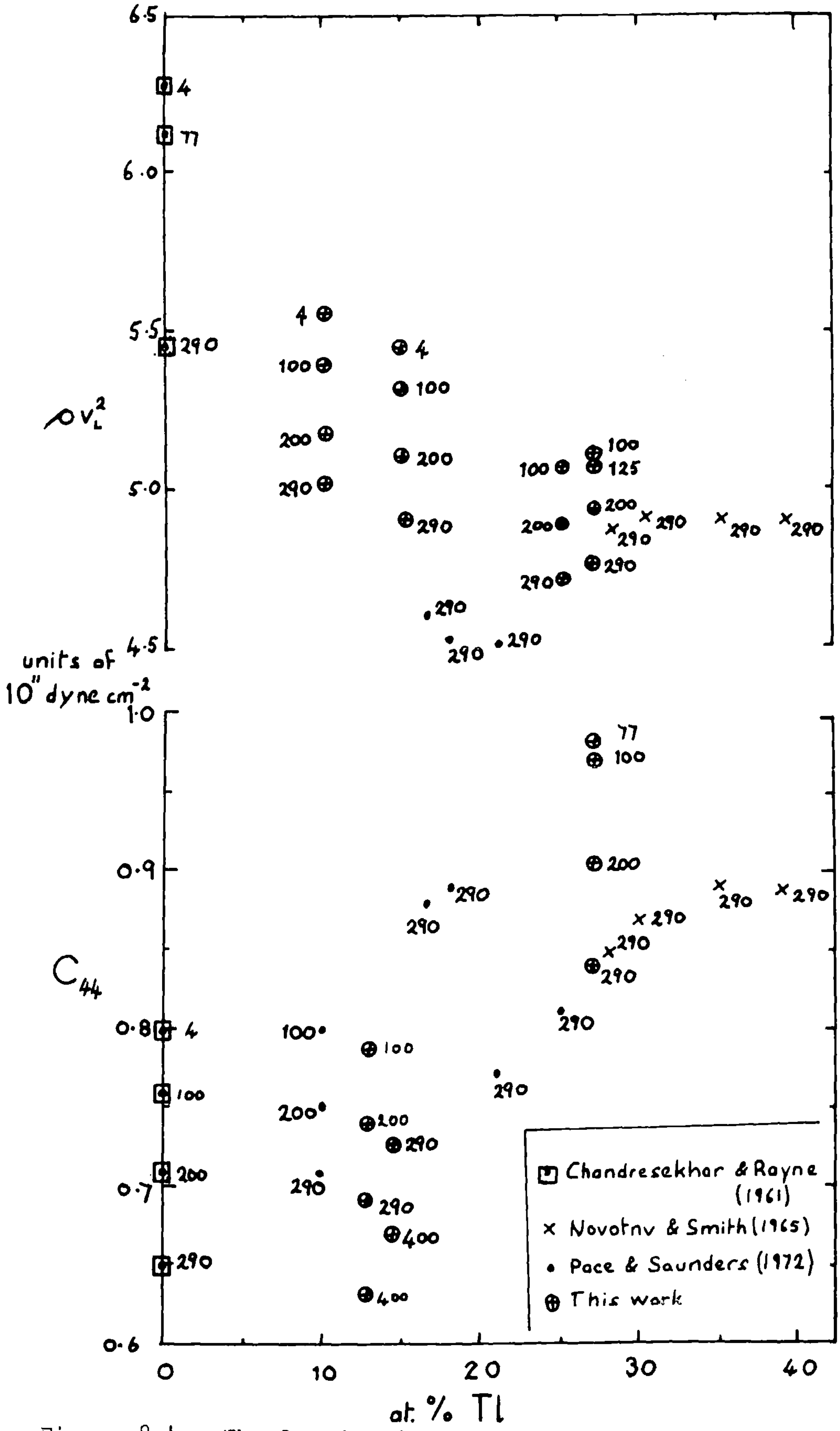

Figure 8.4 The longitudinal and one of the shear moduli for propagation in the [110] direction. The temperature corresponding to each point is shown adjacent to the point (the units are degrees Kelvin).

Further work on the temperature dependence of elastic moduli for other compositions is obviously needed here.

8.4.2 Debye temperatures and specific heat

The Debye theory of solids makes it possible to calculate a value for the specific heat of a material from a knowledge of the sound velocities. The theory is based on a harmonic approximation to the lattice energy dependence on strain, so that differences between observation and calculation would be expected to arise whenever there is an appreciable anharmonic contribution. For example, a harmonic solid has a constant value of specific heat at high temperatures (greater than the Debye temperature). In the Debye theory the lattice frequencies are assumed to take on a continuous range of values up to a cut-off frequency ν_D: the frequency ν_D is such that the total number of lattice modes is 3n for a solid containing n atoms. If the density of states function is $N(\nu)$, this condition can be expressed as

$$\int_0^{\nu_D} N(\nu)\, d\nu \quad = \quad 3n \quad . \qquad (8.6)$$

To the cut-off frequency ν_D there corresponds a temperature Θ_D, known as the Debye temperature, and related to ν_D by $\Theta_D = h\nu_D/k$. In terms of sound velocities, the Debye temperature is given by

$$\Theta_D \quad = \quad \frac{h}{k}\left(\frac{9n}{4\pi V}\right)^{\frac{1}{3}} \Bigg/ \left[\int\left(\frac{1}{v_1^3} + \frac{1}{v_2^3} + \frac{1}{v_3^3}\right) \frac{d\Omega}{4\pi}\right]^{\frac{1}{3}} \qquad (8.7)$$

where v_1, v_2 and v_3 are the three velocities of wave propagation in some direction, and V is the crystal volune. The integral is over all solid angle.

Three mode Debye temperatures can also be defined, and are given by

$$\Theta_i = \frac{h}{k}\left(\frac{3n}{4\pi V}\right)^{\frac{1}{3}} \Big/ \left[\int \frac{1}{v_i^3} \quad \frac{d\Omega}{4\pi}\right]^{\frac{1}{3}} \quad . \tag{8.8}$$

For a real solid there is no one cut-off frequency, but a tail on the high frequency end of the density of states function; an effective Debye temperature Θ_e can be defined, (see Liebfried and Ludwig, 1961).

We have calculated total and mode Debye temperatures for indium-thallium alloys. In figure 8.5 are shown the fast shear, slow shear and total Debye temperatures for alloys containing different amounts of thallium. The room temperature sound velocities for the calculations come from elastic constants given by Chandresekhar and Rayne (1961), Novotny and Smith (1965) and by this work. Figure 8.6 shows the results of a similar calculation for one alloy — In-27 at.% Tl — as a function of temperature (including its transition temperature of 125K).

The computation of Θ_D from sound velocities by means of 8.7 or 8.8 centres around evaluation of the integral. Alers (1965) reviews several methods available. These are approximational methods, and require a knowledge of sound velocities in a small number of predetermined directions. Such methods were found to be insufficiently accurate for the indium-thallium alloys on account of the large anisotropy of the velocity surface of the slow shear mode, and its close proximity to zero in ⟨110⟩ directions. Figure 8.7 shows the (110) cross-section for several alloys, including the 27 at.% one. The method used here for evaluation of the integrals in equations 8.7 and 8.8 has been to approximate them by a sum

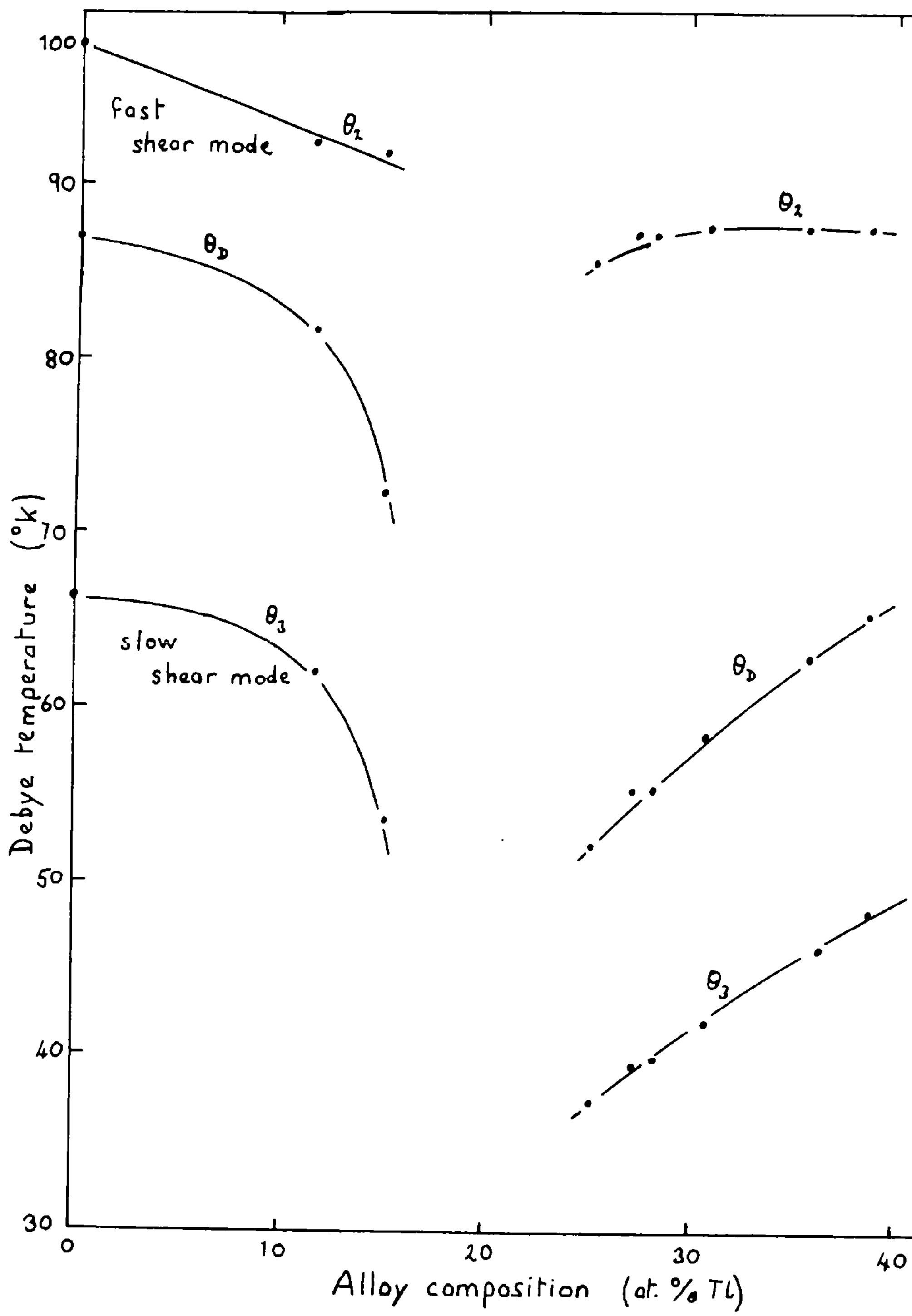

Figure 8.5 Calculated Debye temperatures from sound velocity data of several alloys at 290K. The sources of the data are given in the text.

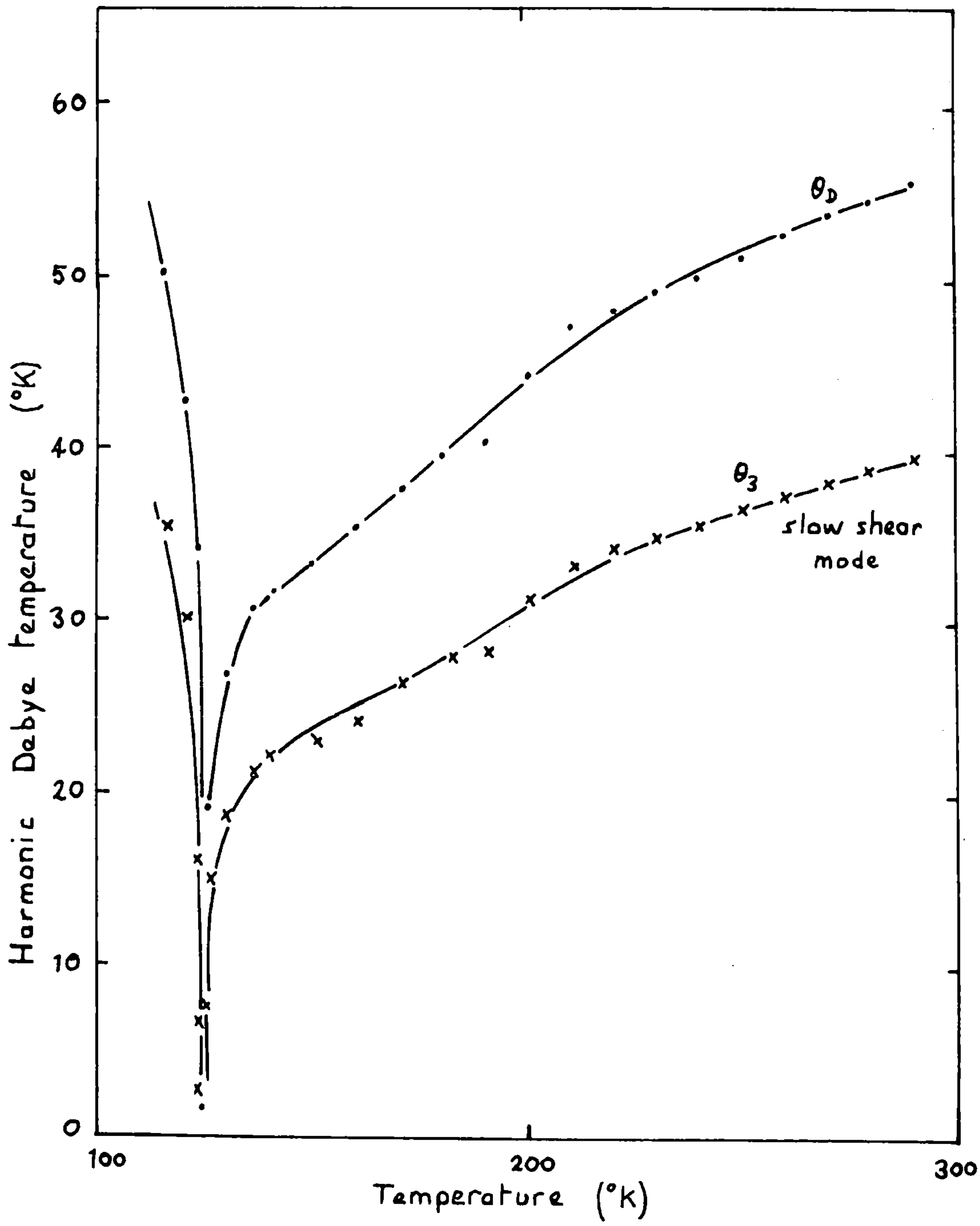

Figure 8.6 Calculated Debye temperatures for In-27 at.% Tl as a function of temperature.

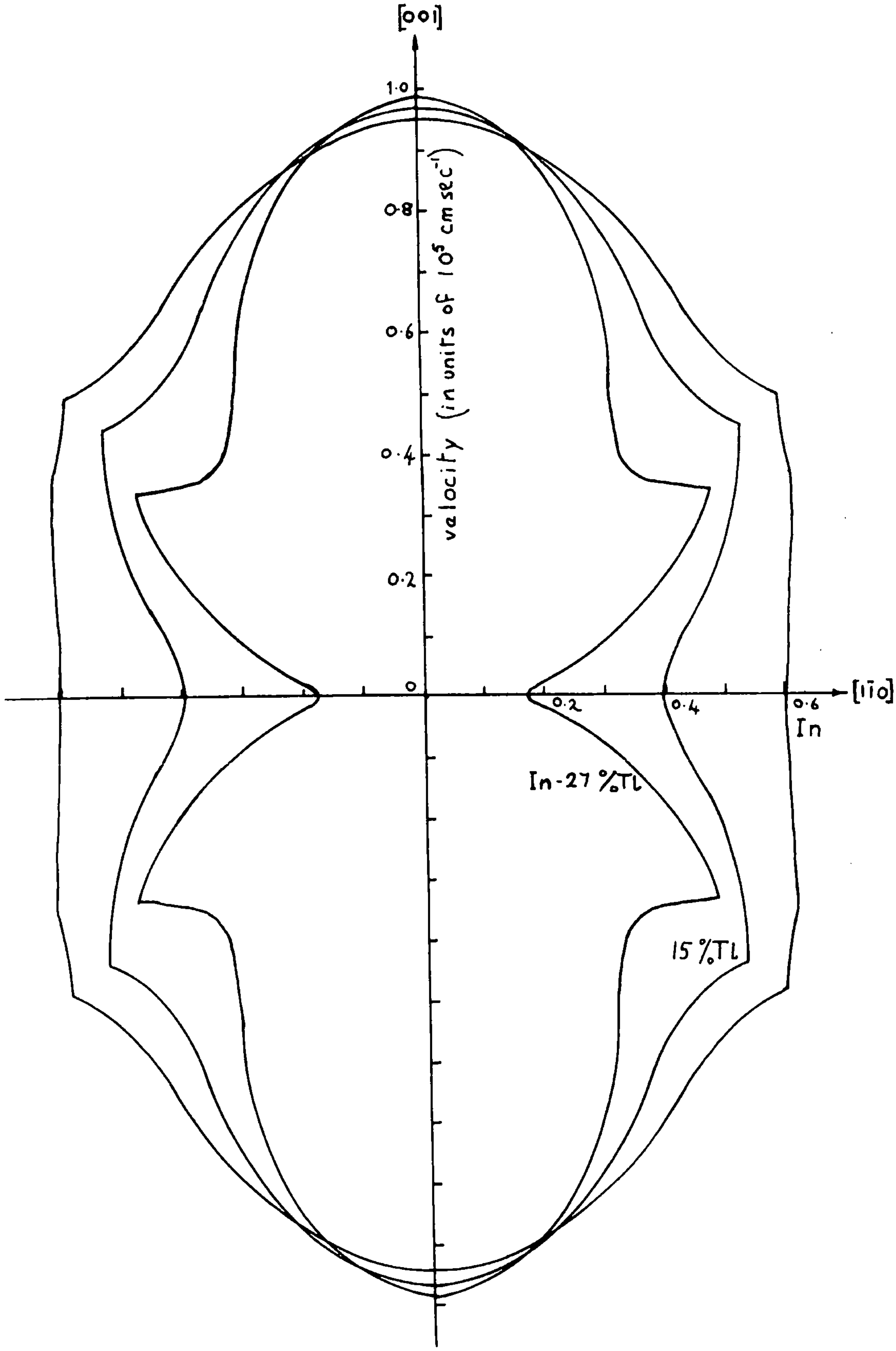

Figure 8.7 Cross-sections of the slow shear mode velocity surfaces for In, In-15 at.% Tl and In-27 at.% Tl at room temperature (290K). The cross-sections are for wave propagation in the (110) plane.

with a small value of $\Delta\Omega$. The Christoffel equations were solved to find the velocities of sound propagation along 643 directions, each subtending an equal solid angle, in half of the first quadrant of space. An angular spacing between directions of 2° was used, which corresponded to a value of $\Delta\Omega$ of 1.218×10^{-3} steradians.

A comparison between the theoretical results and experimental ones is possible if the specific heat C_v is computed from the values of Θ_D obtained. The expression for C_v is

$$C_v = 9nk\left(\frac{T}{\Theta_D}\right)^3 \int_0^{x_D} \frac{x^4 e^x}{(e^x-1)^2} dx \quad , \qquad (8.9)$$

in which $x = \frac{h\nu}{kT}$ and $x_D = \Theta_D/T$. Tables are available for evaluation of this integral, and Beattie (1926-7) gives values of $C_v/3k$ as a function of Θ_D/T. C_v has been calculated for In-27 at.% Tl over the temperature range 117 to 300K. Unfortunately there are no specific heat data available for this composition, but Schwartz (1970) has reported the temperature variation of C_p for In-28.9 at.% Tl. We have applied a correction to his results to obtain C_v, using the method of Clusius and Schachinger (1952). The correction takes the form $C_p - C_v = A C_p^2 T$, with a value for A of 8.03×10^{-6} mole joule^{-1} $^{\circ}K^{-1}$. Figure 8.8 shows the experimental results of Schwartz for C_p and the corrected curve for C_v. The small variation in specific heat at the transition in the 28.9% alloy (at about 90K) can be seen. Superimposed on the experimental curves is the calculated variation in C_v for the 27% alloy. The calculated decrease of Θ_D with temperature leads to a value of C_v which is almost independent of temperature, and very close to the value 3R

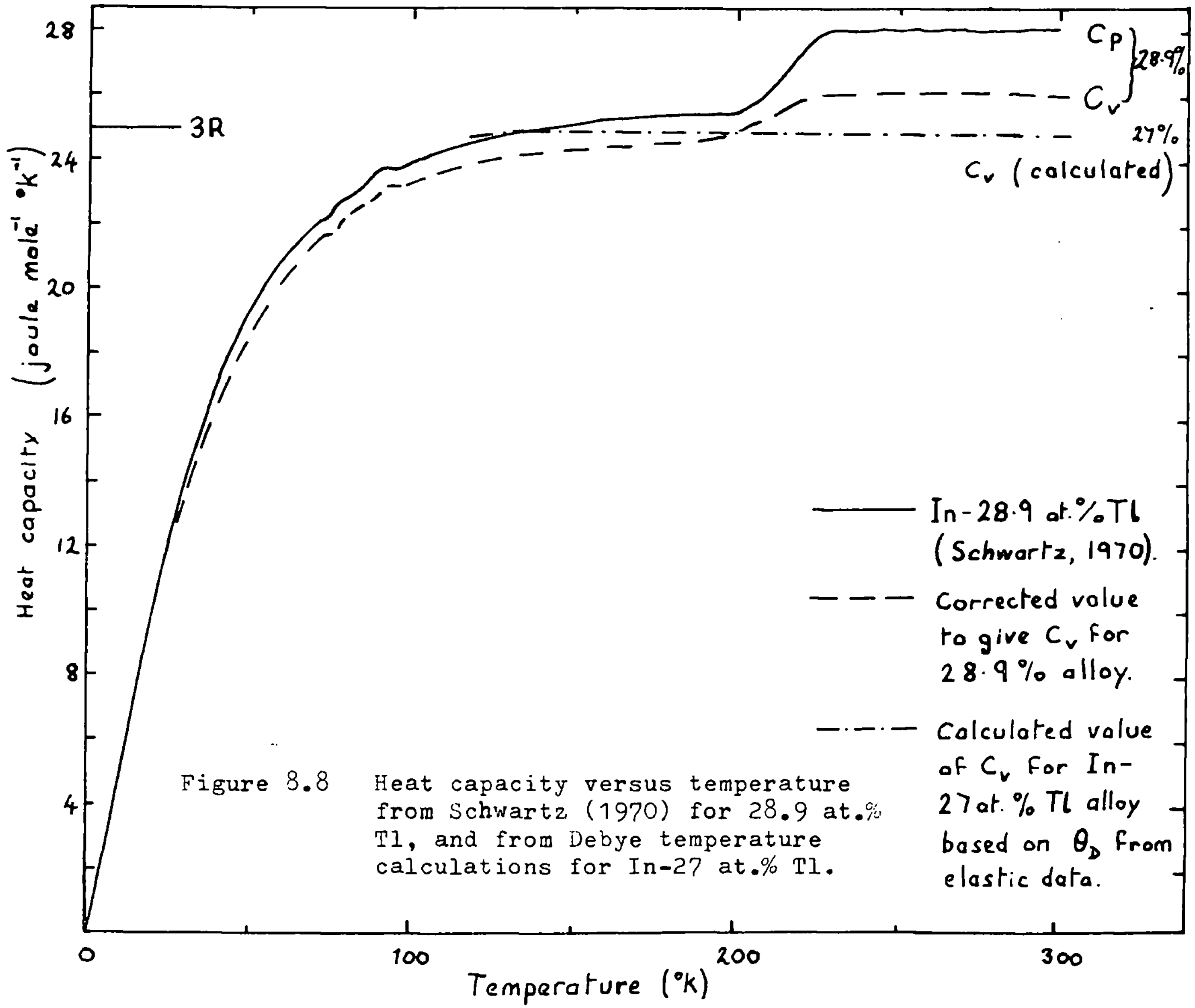

Figure 8.8 Heat capacity versus temperature from Schwartz (1970) for 28.9 at.% Tl, and from Debye temperature calculations for In-27 at.% Tl.

(= 24.94 joule mole^{-1} $^{o}K^{-1}$). The interpretatation of figure 8.8 is complicated somewhat by the use of data for two different compositions, but if we assume that the Debye model results in a very small value of Θ_D at T_c (because of the very low velocity of one of the modes of wave propagation), then the resulting specific heat should be very close to 3R. The fact that the observed specific heat is less than this value in the 28.9 at.% Tl alloy means that its effective Debye temperature does not, in reality, fall to zero. Thus we find another limitation on the harmonic model in the vicinity of the transition temperature.

8.5 Order of the phase transition in indium-thallium alloys

8.5.1 First and second order transitions

A first order phase transition is one which involves a discontinuity in first derivatives of the free energy, while a second order one is accompanied by discontinuities in second derivatives ; in both cases the free energy itself is continuous. (See, for example, Zemansky, 1951.) On that basis there are discontinuities in volume and entropy at a first order phase change and there is a latent heat associated with it, while a second order one has continuous variations in volume and entropy but discontinuities in specific heat, thermal expansion and bulk modulus. (See, for example, Roberts and Miller, 1960.) The elastic constants are related to the internal energy U by $C_{ij} = \partial^2 U/\partial x_i \partial x_j$, in which x_i and x_j are strains. We would thus expect a discontinuous change in elastic constants at a second order transition.

There is a type of second order transition at which specific heat, bulk modulus and thermal expansion all change very rapidly, but not discontinuously. Such a type is known as a λ- transition. At a λ- transition the elastic constants also change very rapidly: Garland (1970) reviews the effects on ultrasonic attenuation and velocity seen at many λ-transitions. In some materials, such as NH_4Cl, the change in modulus can be very pronounced, while in others it can be much smaller. The fractional change seen in the velocity of a longitudinal wave in [100] in $RbMnF_3$ is only about 0.05%. For a λ- transition the Pippard equations relate specific heat, thermal expansion and bulk modulus to the change in transition temperature with pressure. Garland (1964) has applied these equations to elastic properties of crystals, and has shown that at a λ- transition the modulus $\frac{1}{2}(C_{11} - C_{12})$ should be constant.

8.5.2 Application to indium-thallium

Both first and second order transitions have been proposed for the fcc to fct transformation in indium-thallium alloys. The work of Guttman (1950) on X-ray measurements of lattice parameters and on the nature of the region of the phase diagram close to the phase boundary led him to conclude that the transition was of second order because he found (i) that any discontinuity in volume did not exceed 0.1% (and probably not more than 0.03%), and (ii) that all X-ray powder photographs at room temperature had lines from one or other structure and never both, suggesting no two-phase region on the phase diagram. On the other hand, Burkart and Read (1953), who measured the change in length of specimens on transformation, pointed to the discontinuity in Gibbs free energy implied by their findings of discontinuities in strain at the transition, and considered it to be of first order. The room temperature variation of lattice parameters with composition (shown in figure 4.11) was also considered to suggest a first order process. Anderson and Blount (1965) considered the question of a cubic to tetragonal phase transition on general, and found that such a change ought to be first order, but were unable to come to any definite conclusion concerning that in In-Tl. The work of Pollock and King (1968) and their description of the phase diagram as a 'realisation' one has already been discussed in Chapter 2. As a result of their work we might describe the transition as of 'pseudo-first' order when a macroscopic sample is considered, but of second order for a region around a nucleation centre where the transformation proceeds by a single interface.

The results of the present work can usefully be used to extend this discussion. However, in the interpretation of the temperature variation of various parameters the effects of anharmonicity must be kept separate.

Of the experimentally observable quantities mentioned in section 8.5.1, namely the thermal expansion, specific heat, bulk modulus and the elastic moduli, results are available from this work for thermal expansion and elastic moduli. Considering first the thermal expansion component of the 25 at.% Tl alloy in the two phases, we find that in the temperature regions remote from the transformation its values in the two phases are almost indpendent of temperature and differ by a factor of about 2. The results of Pahlman and Smith (1968) for thermal expansion of other compositions also show a step, but of a smaller magnitude than that seen here.

The ultrasound velocity data in the vicinity of the phase transition have been discussed briefly in section 8.2.1, in which it was remarked that no obvious discontinuity was seen. These results are reminiscent of those found at a λ- transition, although the variation of the modulus $\frac{1}{2}(C_{11}-C_{12})$ with temperature is not consistent with Garland's result, mentioned in the previous section, that $\frac{1}{2}(C_{11}-C_{12})$ should have a constant value. In figure 8.9 we show the variation with temperature of sound velocity in the [110] direction for In-25 at.% Tl near to T_c, after a correction has been made for thermal expansion of the sample. An extrapolation has been made of the velocity in the cubic phase and, neglecting the dip at T_c, we can detect a small step in the experimental curve. Hardly any step-like effect was seen in In-27 at.% Tl. The data of Pace and Saunders (1972) for a 21 at.% Tl alloy shows a slightly larger step between velocity values in the two phases. In each of these cases the changes seen were very small ($\lesssim$ 0.3%), and when taken together reinforce the notion that the transition in in indium-thallium from fcc to fct is of second order and not first. The specific heat data of Schwartz (1970) in which there is hardly any change ($\simeq$ 1%) in C_p at the transformation for a 28.9 at.% Tl alloy is in line with this conclusion, although it would be useful to have heat capacity data near T_c for other alloy compositions to provide additional evidence.

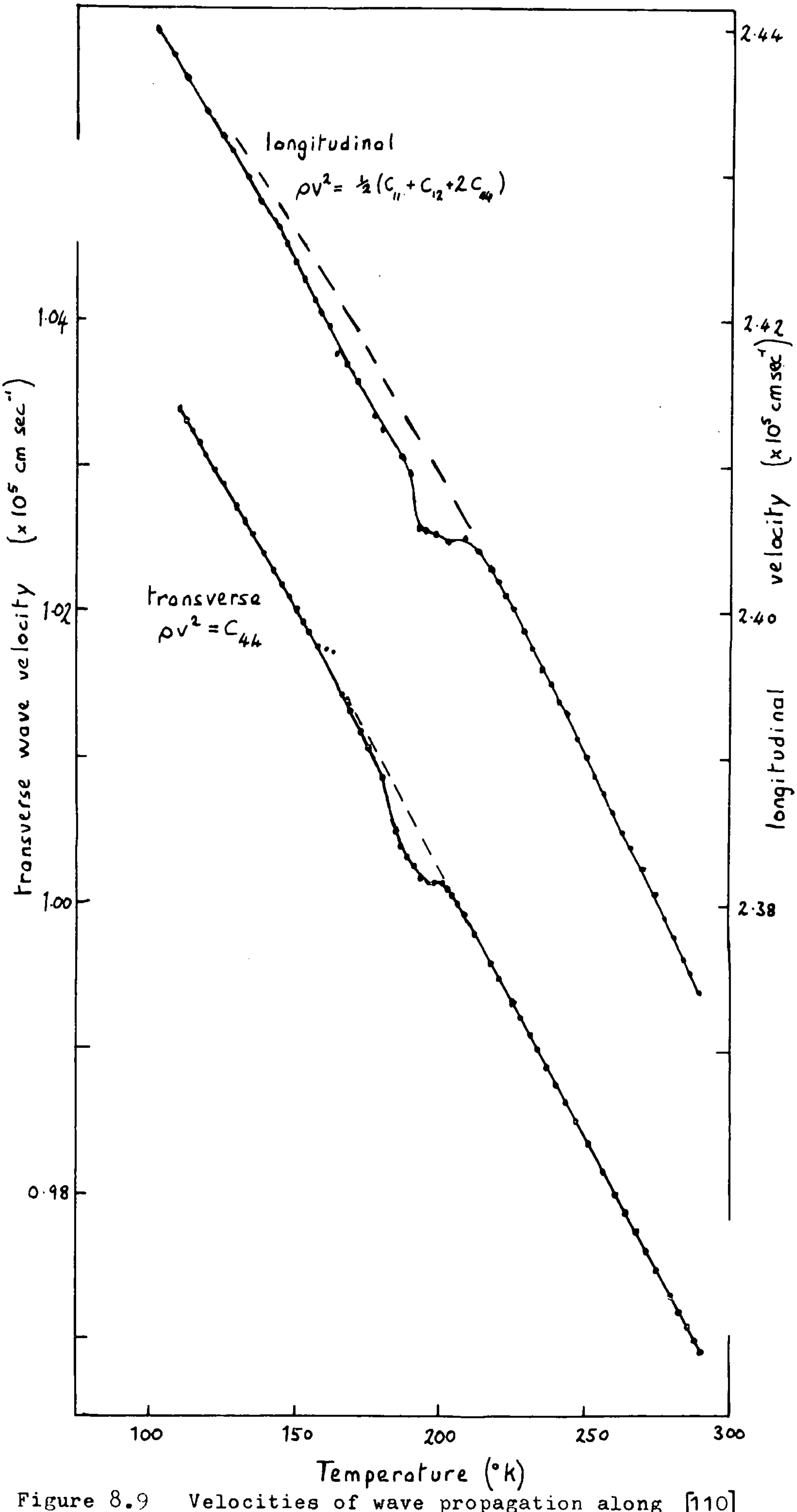

Figure 8.9 Velocities of wave propagation along [110] for In-25 at.% Tl, after a thermal expansion correction has been made.

In summarising this section, we find further evidence to that already presented by other workers to suggest that the fcc to fct transition is of second order. Ignoring anharmonic effects near to T_c we have observed steps in thermal expansion and in sound velocity (and hence in elastic constant), but in the latter case the steps were very small in magnitude. A λ- transition has been considered as a possibility, although the variation in C' with temperature is not entirely consistent with such a model.

8.6 Soft modes and the martensitic phase transition — a summary

The softening of an acoustic phonon mode as the martensitic transition is approached has been the central theme of this thesis, and we now bring together the experimental and theoretical findings. Experimentally, it was the variation of $\frac{1}{2}(C_{11} - C_{12})$ (or C') as a function of composition, which led Pace and Saunders (1972) to propose as the transition mechanism the softening of the [110], [1$\bar{1}$0] polarised mode. In the more controlled experiments made possible by use of temperature as the variable, we have been able to confirm the decrease towards zero of the modulus C'; we present in figure 8.10 a summary of the temperature variation of C' for the alloys studied, together with the variation in indium of that modulus (from Chandresekhar and Rayne, 1961). Figure 8.10 shows quite clearly the effect for the 25 and 27 at.% Tl alloys, while the variation of C' for the 11.5 and 15 at.% Tl alloys shows for the first time its behaviour in single crystal tetragonal

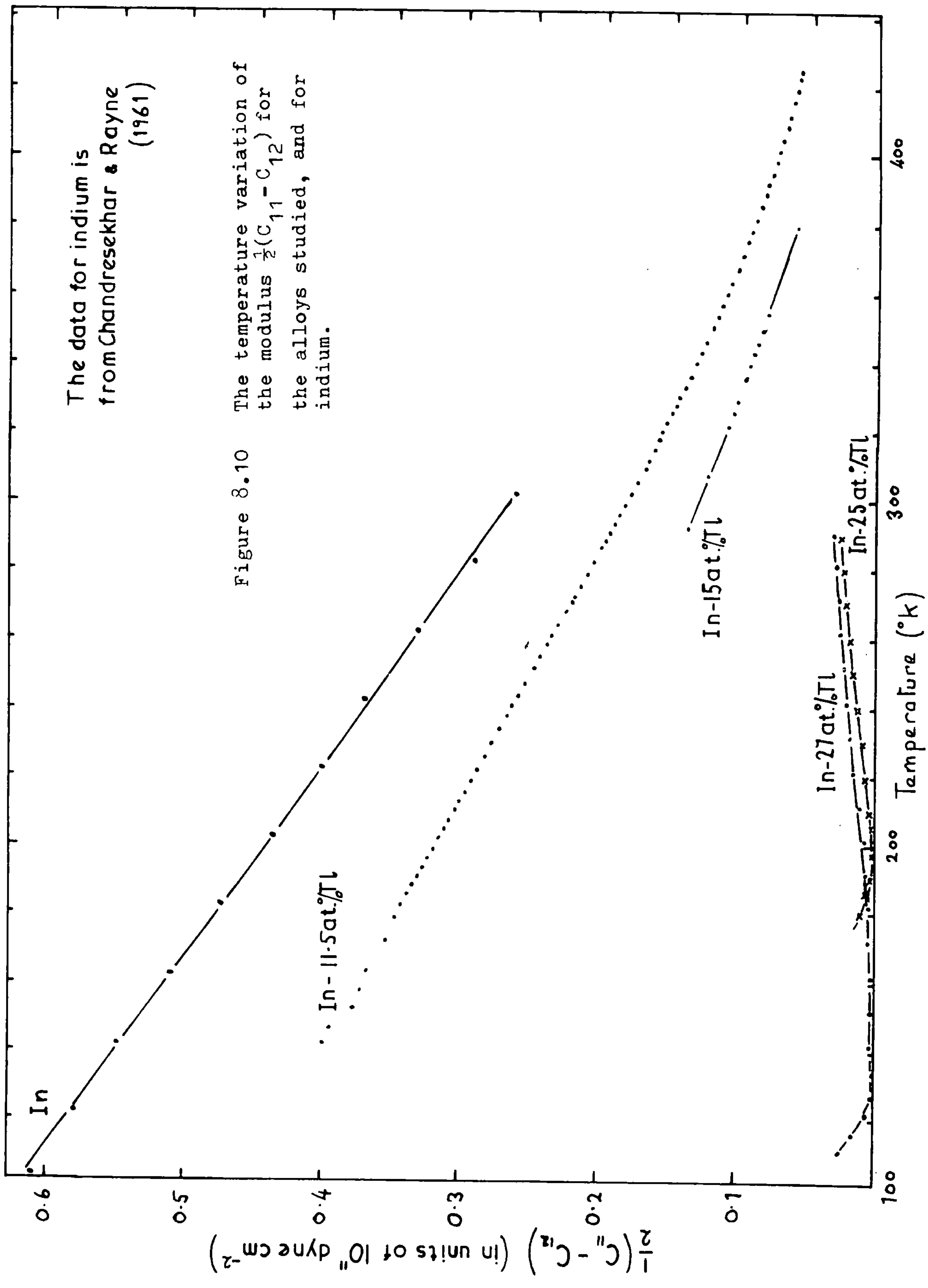

Figure 8.10 The temperature variation of the modulus $\frac{1}{2}(C_{11} - C_{12})$ for the alloys studied, and for indium.

materials as the phase boundary is approached. (If an extrapolation of the phase division line is made into the liquid phase then at 423K the 15 at.% Tl alloy is about 25^{o}K from the boundary.) From a theoretical point of view it has also been possible to show a mode softening, within the limitations on the model potential theory discussed in Chapter 7. The theory took as its starting points very basic atomic and lattice parameters; the calculations showed that the stability of the slow shear mode in the [110] direction was very sensitive to small changes in these, particularly to variation in lattice parameter values. Other modes were affected very little by these changes, and it would seem that the mode which becomes unstable does so as small changes occur in lattice dimensions on change of temperature. But the postulate of mode softening has been shown to be theoretically viable, as well as experimentally so.

The experimental results for mode softening at the transition are, qualitatively, in accord with the soft mode theory of Cochran (1960) and its developments as outlined in Chapter 2, for not only do we find that the slope of a dispersion curve tends to zero at T_c, but also that the atomic displacements required to form the new phase correspond to the eigenvector of the unstable mode. The transition temperature of a soft mode process is that at which thermal fluctuations are no longer able to stabilise the lattice against the instability of one or more of the modes. The ability of fluctuations to produce stability depends on anharmonic interactions; since the transition temperature for In-Tl can vary between 0 and 425K there must be a variation in its anharmonic properties if a soft mode is, indeed, the mechanism of the transition. Evidence has been found for such a variation, as described in section 8.4.

The theoretical part of the present work has shown that the lattice dynamics associated with the martensitic phase transition in indium-thallium alloys are far from being completely understood or accounted for, but that results obtained so far suggest that further investigation should prove profitable.

8.7 Suggestions for further work

The study of indium-thallium alloys described in this thesis has brought to light a number of interesting features which could be usefully pursued further.

The question of the mechanism or mechanisms responsible for the ultrasonic attenuation variation with temperature has not been satisfactorily resolved. Experiments to measure accurately the frequency dependence of attenuation both in the vicinity of the phase transition and remote from it would be required. Around T_c one might look for a variation of attenuation with frequency of the form $\alpha = (T-T_c)^n f(\nu)$, and the exponent n and the function f could be found. Such an investigation has not been possible in the present work because of the high values of attenuation encountered at T_c in the alloys investigated, but the results obtained for temperature dependence of attenuation would suggest that a suitable alloy composition to use for a frequency study would be one which transformed at between 250 and 270K, or one containing about 23 at.% Tl. This alloy would have its attenuation peak at the phase transition superimposed on a lower background value; it could also be prepared in single crystal form.

Further investigation is suggested, too, into the idea that physical phenomena associated with the phase transition occur more sharply at a higher T_c. In this connection it would be interesting to study the specific heat variation near the transition temperature in the 18.8 at.% Tl alloy which Schwartz (1970) investigated. Unfortunately his data did not extend to temperatures greater than 300K (the 18.8% composition transforms at about 350K).

Mention has already been made of the desirability of producing the elastic constant variation with temperature for compositions other than those already reported. Such results would enable figure 8.4 to be extended, and the compositional dependence of elastic moduli at temperatures other than 290K to be found.

On the theoretical side a better model for indium would allow the calculation of phonon density of states and specific heats to be made. In the light of the discussion of Chapter 7 a better model would be one which predicted the observed tetragonal crystal structure. A further study of anharmonic properties could usefully be made, leading to values of the effective Debye temperature. Experimentally, the pressure variation of elastic constants to obtain the third order moduli would yield valuable information, and the validity of Pippard's equations (1956) in these materials could then be assessed to determine better whether a λ-transition was involved.

8.8 Summary

Lattice properties of In-Tl alloys have been studied in the vicinity of the fcc to fct martensitic transition. The experimental aspects have been investigated by ultrasonic and thermal expansion methods, while a theoretical approach has resulted in the calculation of phonon dispersion curves for the alloys starting from optimised model potential theory. In addition a method of deriving the stability limits of Poisson's ratio has been applied to the crystal structures as the transition is approached, using elastic constant data; the onset of instability has been found to give a Poisson's ratio which approaches its lower limit only in the direction of the shear responsible for the structure change. The softening of the phonon mode for propagation in the [110] direction, polarised $[1\bar{1}0]$ has been shown to occur both experimentally and theoretically; the transition mechanism has been interpreted as consistent with the soft-mode theory normally applied to soft optic mode transitions. Ultrasonic attenuation peaks have been found to accompany the phase transition, and are attributed to enhanced anharmonic interactions. However, no satisfactory explanation has been found for a large and rapid rise in attenuation seen in all alloys below about 220K. An increased anharmonic contribution to the strain energy can be identified for alloys with a higher transformation temperature. Evidence has been found to support the notion that the martensitic phase transformation in In-Tl alloys is of second order.

Appendix I

Determination of the angle between two crystallographic planes given the goniometer settings for X-ray beam incidence along their normals.

1) Sign convention for goniometer angles.

a) Rotation about vertical axis is positive if anticlockwise when viewed from above.

b) Rotation about either of the other two axes is positive if anticlockwise when viewed with the X-ray beam normal or from the left.

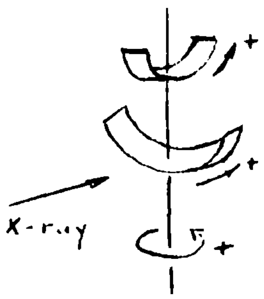

(Figure A1.1)

2) Two axial sets considered:

i) A set x_i with x_3 vertical and x_1 along the X-ray beam.

ii) A set x_i' with x_3' perpendicular to the goniometer platform and x_1' in the direction of the X-ray beam when $\theta=\phi=\gamma=0$; θ, ϕ, γ as defined in figure A1.1.

3) Method of calculation.

Let the goniometer settings be θ, ϕ, γ, as defined in figure A1.1, when a crystal has been oriented so that the X-ray beam is incident normally to a set of lattice planes. These angles then give the Euler angles of the transformation of the axial set x_i'. We require the direction cosines of x_1 with respect to x_i'. The procedure is repeated for another set of planes. Then the angle required is that between two lines whose orientation with respect to a set of orthogonal axes is given by the two sets of direction cosines calculated.

4) Procedure

Let x' be defined by the angles α and β in figure A1.2. The y' axis is perpendicular to x' and makes an angle of δ with the tangent to a circle, centre O, in the x'-z plane.

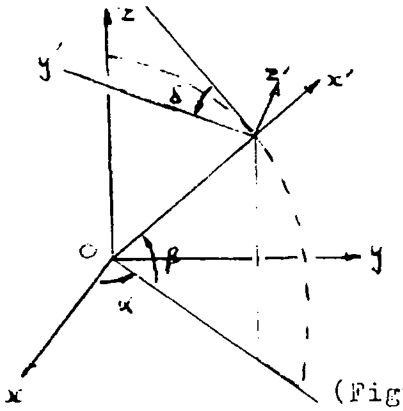

(Figure A1.2)

The direction cosines of x',y' and z' with respect to x,y,z are[1]

$$\begin{pmatrix} A & B & C \\ D\cos\delta - E\sin\delta & F\cos\delta - G\sin\delta & H\cos\delta \\ -E\cos\delta - D\sin\delta & -F\sin\delta - G\cos\delta & -H\sin\delta \end{pmatrix}$$

where
$A = \cos\alpha\cos\beta$ $\quad E = -\sin\alpha$
$B = \sin\alpha\cos\beta$ $\quad F = -\sin\alpha\sin\beta$
$C = \sin\beta$ $\quad G = \cos\alpha$
$D = -\cos\alpha\sin\beta$ $\quad H = \cos\beta$

For the present case $x_1' \equiv x'$, $x_2' \equiv -z'$, $x_3' \equiv y'$ and consequently the direction cosines of x_1 with respect to x_i' are

$$\begin{pmatrix} \cos\theta\cos\phi \\ -\sin\theta\cos\gamma - \cos\theta\sin\phi\sin\gamma \\ -\cos\theta\sin\phi\cos\gamma + \sin\theta\sin\gamma \end{pmatrix}$$

Let these direction cosines be p_1, p_2, p_3; let another set be p_1', p_2', p_3'. The angle between the unit vectors $\underline{r}_1 = p_1\underline{i} + p_2\underline{j} + p_3\underline{k}$ and $\underline{r}_2 = p_1'\underline{i} + p_2'\underline{j} + p_3'\underline{k}$ is given by $\sin\eta = |\underline{r}_1 \times \underline{r}_2|$

The cross product is $\begin{vmatrix} \underline{i} & \underline{j} & \underline{k} \\ p_1 & p_2 & p_3 \\ p_1' & p_2' & p_3' \end{vmatrix}$

If this result is $t_1\underline{i} + t_2\underline{j} + t_3\underline{k}$, then $\sin\eta = \sqrt{t_1^2 + t_2^2 + t_3^2}$.

(1) Turley and Sines (1972)

Appendix II

Determination of relationships between dependent and independent elastic constants

The number of independent components of the elastic compliance tensor in a crystal of a given symmetry is invariant under coordinate transformations (Fumi 1952). For crystals of the tetragonal (TI) Laue group, taken here as an example, there are six independent constants. Let any general, unspecified, compliance constant be denoted by S_i when referred to conventional crystallographic axes, or by S_i' when referred to transformed axes; any symbol S_{ij} with two suffixes represents a specific compliance tensor component in the usual matrix notation of Voigt. For a tetragonal crystal, let the six independent compliances be S_1', S_2', S_3', S_4', S_5' and S_6'. S_{22}' is a typical compliance constant whose dependence on the S_i' is required; we treat this case specifically as an example. Then we can write

$$S_{22}' = f_1S_1' + f_2S_2' + f_3S_3' + f_4S_4' + f_5S_5' + f_6S_6' \qquad (A2.1)$$

and the dependence is established once the coefficients f_i are known. The component S_{22}' can also be written in terms of the unprimed compliances:

$$S_{22}' = \alpha_1S_1 + \alpha_2S_2 + \alpha_3S_3 + \alpha_4S_4 + \alpha_5S_5 + \alpha_6S_6 \qquad (A2.2)$$

and S_i' can be similarly related to the S_i by

$$\left.\begin{aligned} S_1' &= A_1S_1 + A_2S_3 + A_3S_3 + A_4S_4 + A_5S_5 + A_6S_6 \\ S_2' &= B_1S_1 + B_2S_2 + B_3S_3 + B_4S_4 + B_5S_5 + B_6S_6 \\ &\cdot \\ &\cdot \\ &\cdot \\ S_6' &= F_1S_1 + F_2S_2 + F_3S_3 + F_4S_4 + F_5S_5 + F_6S_6 \;. \end{aligned}\right\} \quad (A2.3)$$

The coefficients α_i in equation A2.2 and $A_i, B_i, \ldots F_i$ in A2.3 are fourth order combinations of the direction cosines corresponding to the transformation under consideration, and are determined from the tensor transformation rule of equation 3.16 . Substituting A2.3 into A2.1 and using A2.2, we have

$$\left.\begin{aligned} S_{22}' &= \alpha_1S_1 + \alpha_2S_2 + \alpha_3S_3 + \alpha_4S_4 + \alpha_5S_5 + \alpha_6S_6 \\ &= f_1(A_1S_1 + A_2S_2 + A_3S_3 + A_4S_4 + A_5S_5 + A_6S_6) \\ &\quad + f_2(B_1S_1 + B_2S_2 + B_3S_3 + B_4S_4 + B_5S_5 + B_6S_6) \\ &\quad + f_3(C_1S_1 + \;\ldots\ldots \\ &\quad \cdot \\ &\quad \cdot \\ &\quad + f_6(F_1S_1 + F_2S_2 + F_3S_3 + F_4S_4 + F_5S_5 + F_6S_6) \end{aligned}\right\} \quad (A2.4)$$

Now the S_i are independent (by definition) and hence we can compare their coefficients in this equation, and we have

$$\left.\begin{aligned} \alpha_1 &= f_1A_1 + f_2B_1 + f_3C_1 + f_4D_1 + f_5E_1 + f_6F_1 \\ \alpha_2 &= f_1A_2 + f_2B_2 + f_3C_2 + f_4D_2 + f_5E_2 + f_6F_2 \\ \alpha_3 &= f_1A_3 + \ldots\ldots \\ &\cdot \\ &\cdot \\ \alpha_6 &= f_1A_6 + f_2B_6 + f_3C_6 + f_4D_6 + f_5E_6 + f_6F_6 \end{aligned}\right\} \quad (A2.5)$$

Values of α_i, A_i, B_i, $\ldots F_i$ can be evaluated from equation 3.16

using the appropriate direction cosines: equation A2.5 is a set of six equations in the six coefficients f_i and can be solved by, for example, Gauss elimination to give the required relation between the dependent compliance constant S_{22}' and the chosen six independent ones S_i'. The same method can be readily applied in the calculation of any other dependent constant.

The choice of independent elastic compliances is governed by the requirement that the relations A2.5 must themselves be independent, and thus lead to a unique determination of the coefficients f_i. In practice, this means that for tetragonal TI crystals any six compliances can be considered as independent provided that the transformation is such that there is no coincidence between any transformed axis and either an original axis or a direction midway between. Equations A2.5 can become unstable, however, even if the coincidence of axes is not actually obtained but is nearly so. The choice of independent compliances to be used for a given axial orientation can usually be made by inspection if these considerations are borne in mind.

For example: S_{11} and S_{33} are independent, but after a rotation about the x axis of $\pm 90^{\circ}$ S_{11}' and S_{33}' are equal and independent of S_{22}'. If the rotation is again about the x axis, but is of 45° then S_{13}' and S_{12}' become equal, and are independent of S_{23}', while S_{22}' equals S_{33}' and both of these are independent of S_{11}'. Therefore, a suitable compliance set for calculations of the limits on Poisson's ratio at 45° to the z axis when the applied stress is along the x axis would be S_{11}', S_{12}', S_{23}', S_{22}', S_{44}' and S_{55}'.

APPENDIX III

The computer programmes

PRATIO

The programme takes as input data the direction cosines of the direction which is perpendicular to the plane in which the variation of Poisson's ratio and its limits is sought. Only two of the direction cosines are read in: the third is calculated from $L_3 = \sqrt{1 - (L_1^2 + L_2^2)}$, and the integer variable NORP is set at 0 if L_3 is negative and at 1 if it is positive. Up to the CONTINUE statement labelled 28 the direction cosines for the y' and z' axes (P_1, P_2, P_3 and T_1, T_2, T_3, respectively), are calculated as y' moves around in the y'z' plane in 5° steps. The method of calculation is as described in section 6.2, and all direction cosines are referred to the untransformed axes x, y, z. For each set of x', y', z' the programme produces the dependences of two or more primed compliances on a specified set of six other primed ones. The matrix C contains 9×6 elements which give the direction cosine combinations for the way in which 9 primed compliances can be found from the six unprimed ones of the normal crystallographic set. The ordering within C is as shown below — subscripts only are listed.

	11	12	13	33	44	66
11'						
12'						
13'						
33'						
44'						
66'						
22'						
23'						
55'						

Thus $S_{13}' = C(3,1)S_{11} + C(3,2)S_{12} + \dots + C(3,6)S_{66}$.

The simplification possible for cubic materials is made in the first four lines of the CUBIC form of the programme on page 0003A. The coefficients A_i, B_i, ... F_i and α_i of Appendix II can be obtained as the appropriate lines or columns of the matrix C. In solving the six equations A2.5 for f_i the coefficients of the RHS are put into the matrix AV, and those of the LHS into the matrix S. A scientific subroutine GELG served to solve the set of 6 equations by Gauss elimination. The particular compliances whose dependence on another six is required govern the contents of AV, while the rows of C appropriate to the compliances selected as independent fill the matrix S. As given here the CUBIC form on page 0003A gives results for three sets of independent compliances: S_{11}', S_{12}', S_{44}'; S_{11}', S_{12}', S_{55}'; S_{11}', S_{12}', S_{66}'; in each case the dependent moduli considered were S_{13}', S_{33}', S_{22}' and S_{23}'. The corresponding ones for the TETRAGONAL version, on page 0003B were: S_{23}' and S_{33}' in terms of S_{11}', S_{12}', S_{13}', S_{22}', S_{44}' and S_{55}', and S_{22}' and S_{13}' in terms of S_{11}', S_{12}', S_{23}', S_{33}', S_{44}' and S_{66}'. If the dependences of any other primed compliances are required, it is thus necessary to change the statements in the loop ending at the label 59 so as to put the appropriate components of C into AV and S. If numerical values of any of the primed compliances are required, it is a trivial matter to insert a READ statement near the beginning of the programme to read in values of the unprimed compliances, and then a set of statements of the form

```
      DO 250 I=1,6
      S11D=C(1,I)*COMP(I)+S11D
  250 S12D=C(2,I)*COMP(I)+S12D   .
```

The example given produces values for S_{11}' and S_{12}'.

PRATIO


```
      INTEGER H
      REAL L1,L2,L3,L12,L22,L32
      DIMENSION C(9,6),AV(3,4),S(3,3),COMP(6)
C
C   L1,L2,L3 ARE D.C.'S OF APPLIED STRESS DIRECTION. IF L3 IS NEGATIVE NORP IS 0
C
C     COMP(1) - COMP(6) ARE THE COMPLIANCES IN THE ORDER:
C                       S11, S12, S13, S33, S44, S66.
C
      READ(5,2)L1,L2,NORP
    2 FORMAT(2F6.3,I2)
      L12=L1**2
      L22=L2**2
      L3=SQRT(1.0-L12-L22)
      IF(NORP.EQ.0)L3=-L3
      L32=L3**2
      SA=L2/SQRT(L12+L22)
      CA=L1/SQRT(L12+L22)
      SB=L3
      CB=SQRT(L12+L22)/SQRT(L12+L22+L32)
      A=CA*CB
      B=SA*CB
      C1=SB
      D1=-CA*SB
      E=-SA
      F=-SA*SB
      G=CA
      H1=CB
      WRITE(6,101)L1,L2,L3
  101 FORMAT(///'      H,K,L =',F6.2,',',F6.2,',',F6.2)
      DO 31 IANG=5,175,5
      DO 29 II=1,2
      R=IANG
      IF(II.EQ.1)GO TO 11
      R=R+90.0
   11 P=R/57.296
      IF(R-90.0) 3,31,3
    3 IF(R-180.0) 4,31,4
    4 IF(R-270.0) 5,31,5
    5 W=TAN(P)
      CG=1.0/SQRT(1.0+W*W)
      SG=SQRT(1.0-CG*CG)
      IF(R-180.0) 12,12,13
   13 IF(R-360.0)20,20,12
   20 SG=-SG
   12 IF(270.0-R) 14,14,15
   15 IF(R-90.0) 14,14,16
   16 CG=-CG
   14 CONTINUE
      IF(II.EQ.2)GO TO 84
      P1=D1*CG-E*SG
      P2=F*CG-G*SG
      P3=H1*CG
      P12=P1**2
      P22=P2**2
```



```
      P32=P3**2
      GO TO 28
   84 T1=D1*CG-E*SG
      T2=F*CG-G*SG
      T3=H1*CG
      T12=T1**2
      T22=T2**2
      T32=T3**2
   28 CONTINUE
      C(1,1)=L12*L12+L22*L22
      C(2,1)=L12*P12+L22*P22
      C(3,1)=L12*T12+L22*T22
      C(4,1)=T12*T12+T22*T22
      C(5,1)=4.0*(P12*T12+P22*T22)
      C(6,1)=4.0*(P12*L12+P22*L22)
      C(7,1)=P12*P12+P22*P22
      C(8,1)=P12*T12+T22*P22
      C(1,2)=2.0*L12*L22
      C(2,2)=P12*L22+L12*P22
      C(3,2)=T12*L22+L12*T22
      C(4,2)=2.0*T12*T22
      C(5,2)=8.0*P1*T1*P2*T2
      C(6,2)=8.0*P1*L1*P2*L2
      C(7,2)=2*P12*P22
      C(8,2)=P12*T22+T12*P22
      C(1,3)=2.0*L32*(1.0-L32)
      C(2,3)=P32*(L12+L22)+L32*(P12+P22)
      C(3,3)=T32*(L12+L22)+L32*(T12+T22)
      C(4,3)=2.0*T32*(1.0-T32)
      C(5,3)=8.0*P3*T3*(P1*T1+P2*T2)
      C(6,3)=8.0*P3*L3*(P1*L1+P2*L2)
      C(7,3)=2*P32*(1.0-P32)
      C(8,3)=P32*(T12+T22)+T32*(P12+P22)
      C(1,4)=L32*L32
      C(2,4)=P32*L32
      C(3,4)=T32*L32
      C(4,4)=T32*T32
      C(5,4)=4.0*P32*T32
      C(6,4)=4.0*P32*L32
      C(7,4)=P32*P32
      C(8,4)=P32*T32
      C(1,5)=L32*(1.0-L32)
      C(2,5)=L3*P3*(L2*P2+L1*P1)
      C(3,5)=L3*T3*(L2*T2+L1*T1)
      C(4,5)=T32*(1.0-T32)
      C(5,5)=(P3*T2+P2*T3)**2+(P1*T3+P3*T1)**2
      C(6,5)=(P3*L2+P2*L3)**2+(P1*L3+P3*L1)**2
      C(7,5)=P32*(1.0-P32)
      C(8,5)=T3*P3*(T2*P2+T1*P1)
      C(1,6)=L12*L22
      C(2,6)=P1*P2*L1*L2
      C(3,6)=T1*T2*L1*L2
      C(4,6)=T12*T22
      C(5,6)=(P1*T2+T1*P2)**2
      C(6,6)=(P1*L2+L1*P2)**2
```

PAGE 0003A

CUBIC

```
      C(7,6)=P12*P22
      C(8,6)=P1*P2*T1*T2
      C(9,1)=4.0*(L12*T12+L22*T22)
      C(9,2)=9.0*L1*T1*L2*T2
      C(9,3)=8.0*L3*T3*(L1*T1+L2*T2)
      C(9,4)=4.0*L32*T32
      C(9,5)=(L3*T2+L2*T3)**2+(L1*T3+L3*T1)**2
      C(9,6)=(L1*T2+T1*L2)**2
      DO 17 I=1,9
      C(I,1)=C(I,1)+C(I,4)
      C(I,2)=C(I,2)+C(I,3)
   17 C(I,3)=C(I,5)+C(I,6)
      WRITE(6,151)
  151 FORMAT( /////T10,'MATRIX OF DIRECTION COSINES.        (C2)'/)
      WRITE(6,107)C
  107 FORMAT(9E12.3)
C                        L.H.S. COEFFICIENTS PUT INTO AV
      NCOUNT=0
  150 NCOUNT=NCOUNT+1
      IF(NCOUNT-2)200,210,220
  200 K=5
      GOTO 90
  210 K=5
      GOTO 90
  220 K=6
   90 DO 59 I=1,3
      S(I,1)=C(1,I)
      S(I,2)=C(2,I)
      S(I,3)=C(K,I)
      AV(I,1)=C(3,I)
      AV(I,2)=C(4,I)
      AV(I,3)=C(7,I)
   59 AV(I,4)=C(8,I)
      WRITE(6,152)
  152 FORMAT(///T10,'MATRIX OF COEFFS. OF R.H.S. (TRANSPOSED)'/)
      WRITE(6,100) S
  100 FORMAT(3E13.4)
C                              EQUATIONS SOLVED BY GAUSS ELIMINATION.
      CALL GELG(AV,S,3,4,1.0E-05,IER)
      WRITE(6,154)IANG,AV
  154 FORMAT(  'ANGLE TO MERIDIANAL TANGENT =',I5,' DEGREES'//
     2        '  S13''= ',F8.3,'*S11''',F8.3,'*S12''',F8.3,'*S44'''/
     3        '  S33''= ',F8.3,'*S11''',F8.3,'*S12''',F8.3,'*S44'''/
     4        '  S22''= ',F8.3,'*S11''',F8.3,'*S12''',F8.3,'*S44'''/
     5        '  S23''= ',F8.3,'*S11''',F8.3,'*S12''',F8.3,'*S44'''/)
      IF(NCOUNT.NE.3)GOTO 150
   31 CONTINUE
      STOP
      END
```

PAGE 0003B

TETRAGONAL

```
      NCOUNT=0
  150 CONTINUE
      NCOUNT=NCOUNT+1
      WRITE(6,151)
  151 FORMAT( /////T10,'MATRIX OF DIRECTION COSINES.        (C2)'/)
      WRITE(6,107)C
  107 FORMAT(9E12.3)
C                        L.H.S. COEFFICIENTS PUT INTO AV
      DO 59 I=1,6
      DO 59 J=1,6
      AV(I,1)=C(4,I)
      AV(I,2)=C(8,I)
      S(I,J)=C(J,I)
      S(I,4)=C(7,I)
      S(I,6)=C(9,I)
      IF(NCOUNT.EQ.1)GOTO 59
      AV(I,1)=C(7,I)
      AV(I,2)=C(3,I)
      S(I,J)=C(J,I)
      S(I,3)=C(8,I)
      S(I,4)=C(4,I)
   59 CONTINUE
      WRITE(6,152)
  152 FORMAT(///T10,'MATRIX OF COEFFS. OF R.H.S. (TRANSPOSED)'/)
      WRITE(6,100) S
  100 FORMAT(6E13.4)
C                              EQUATIONS SOLVED BY GAUSS ELIMINATION.
      CALL GELG(AV,S,6,2,1.0E-05,IER)
      IF(NCOUNT.EQ.2)GOTO 40
      WRITE(6,154)IANG,AV
  154 FORMAT(  'ANGLE TO MERIDIANAL TANGENT =',I5,' DEGREES'//
     2        '  S33''= ',F8.3,'*S11''',F8.3,'*S12''',F8.3,'*S13''',F8.3,
     3'*S22''',F8.3,'*S44''',F8.3,'*S55'''/
     4        '  S23''= ',F8.3,'*S11''',F8.3,'*S12''',F8.3,'*S13''',F8.3,
     5'*S22''',F8.3,'*S44''',F8.3,'*S55'''/)
      GOTO 150
   40 WRITE(6,153)IANG,AV
  153 FORMAT(  'ANGLE TO MERIDIANAL TANGENT =',I5,' DEGREES'//
     2        '  S22''= ',F8.3,'*S11''',F8.3,'*S12''',F8.3,'*S23''',F8.3,
     3'*S33''',F8.3,'*S44''',F8.3,'*S66'''/
     4        '  S13''= ',F8.3,'*S11''',F8.3,'*S12''',F8.3,'*S23''',F8.3,
     5'*S33''',F8.3,'*S44''',F8.3,'*S66'''/)
   31 CONTINUE
      STOP
      END
```

DISPS

The programme calculates the phonon dispersion curves in three crystal directions: [001], [110] and [100]. The output lists the band structure and electrostatic energy changes and the lattice frequencies for the three modes of propagation in each direction, at equally-spaced values of $\underline{Q}$ up to the zone boundary at $2\pi/a$. The input parameter SIZE is the fraction of the origin to zone boundary distance between successive values of $\underline{Q}$. The programme starts by reading in values for valency (Z), effective valencies of indium and thallium (ZS1 and ZS2), the lattice parameters in angstrom units (AL and CL), the atomic weight of the alloy in atomic units (AM), the atomic volumes of indium and thallium in atomic units (OM1 and OM2) and the alloy composition in percentage thallium (COMP). The energy-wavenumber characteristic is read into F. The reciprocal lattice dimensions and the fermi wavevector FWN are calculated. The direction of propagation is taken as the z-direction, with x- and y-directions in the plane perpendicular to z and oriented along simple directions in the lattice. The reciprocal lattice point spacings along the x, y and z axes are labelled A, B and C, followed by the Miller indices of the propagation direction. For each value of $\underline{Q}$ the band structure and electrostatic energy changes are evaluated according to equations 7.45 and 7.47; the last part of the programme obtains the lattice frequencies from $\omega = \sqrt{(\delta E_{bs} + \delta E_{es})/M}$, (equation 7.49).

The sum over $\underline{q}$ for the band structure energy change is taken at all lattice points (except $\underline{q}=0$) for which the argument of $F_N(q)$ does not exceed 7.0, ($F_N(q) = 0$ when $q > 7.0$).

The points are taken from a simple rectangular mesh of 9^3 points of spacing π/a, π/a and π/c. Each point is tested to determine whether its co-ordinates place it on the bct reciprocal lattice under consideration. If so, equation 7.45 is evaluated and the result, labelled DEBSL or DEBST for a longitudinal or a transverse mode, respectively, is added to the sum. (See lines 5, 9, 13 and 14 of page 3.) A set of logical IF statements performs the task of sorting out the points required from those which are not; (the IF statements follow label 7 on page 2). Interpolation of $F_N(q)$ is performed by the subroutine INTER, which uses a four-point Stirling central-difference formula over most of the range of q, and a Newton forward method for $q/k_f < 0.1$; (see, for example, Fröberg, 1965).

The procedure for evaluating the electrostatic energy change (equation 7.47) is rather more involved, and sums over parallel and perpendicular components of $\underline{q}_o$ are taken separately. The reciprocal lattice points are projected onto the xy plane and for each value of $\underline{q}_o{}^{\perp}$ an analytical expression is used to evaluate the sum over $\underline{q}_o{}''$. Adaptation of a result of Harrison (1966) gives, for a particular value of $\underline{q}_o{}^{\perp}$, the sum over $\underline{q}_o{}''$ extending from $+\infty$ to $-\infty$, and including $\underline{q}_o{}'' = 0$.

$$\sum_{\underline{q}_o{}''} \left[\frac{1}{(\underline{Q}+\underline{q}_o{}'')^2 + \underline{q}_o{}^{\perp 2}} + \frac{1}{(\underline{Q}-\underline{q}_o{}'')^2 + \underline{q}_o{}^{\perp 2}} - \frac{2}{\underline{q}_o{}^{\perp 2} + \underline{q}_o{}''^2} \right]$$

$$= \frac{\pi}{q_o{}^{\perp}\, q_o{}''} \left[\frac{2e^{A}\cos B}{e^{2A}-2e^{A}\cos B+1} - \frac{2e^{-A}\cos B}{e^{-2A}-2e^{-A}\cos B+1} - \frac{e^{A}+1}{e^{A}-1} \right]$$

in which $A = 2\pi q_o{}^{\perp} / \underline{q}_o{}''$ and $B = 2\pi \underline{Q} / \underline{q}_o{}''$. In the programme this is the function SM in lines 5 to 7 of page 1. When the values of $\underline{q}_o{}''$ to be summed did not include $\underline{q}_o{}'' = 0$ the result was

DISPS


```
      IMPLICIT REAL*8(A-H,O-Z)
      DIMENSION DEBSL(150),DEBST(150,2),DEESL(150),DEEST(150,2),
     2SUMT(150,2),SUML(150),WT(150,2),AN(150),WL(150)
      COMMON F(73),CONST,PI,FWN
      SM(F,PI,CO,C,CT,A)=(P*PI/(CO*C))*((CT*2.*DEXP(A)-2.)/(DEXP(2.*A)-2
     2.*DEXP(A)*CT+1.)-(2.*DEXP(-A)*CT-2.)/(DEXP(-2.*A)-2.*DEXP(-A)*CT+1
     3.)-2.*(1.+2./(DEXP(A)-1.)))
      READ(5,100)     Z,AM,AL,CL,ZS1,ZS2,CM1,CM2,CCMP
  100 FORMAT(      F4.2,D11.4,2F7.4,4F8.5,F5.1)
C
C     READ IN VALUES OF FERMI WAVE NUMBER, VALENCY,EFFECTIVE VALENCY,
C              IONIC MASS(IN A.U.),LATTICE PARAMETERS A & C.
C
      READ(5,201)SIZE
  201 FORMAT(F6.3)
      DO 306 J=59,73
  306 F(J)=0.
      F(1)=1.
      READ(7,200)(F(I),I=2,51)
      READ(7,200)(F(I),I=55,71,4)
      F(72)=0.00005
      F(53)=0.00005
      F(54)=0.00004
      F(56)=0.00001
      F(57)=0.00000
      F(58)=0.00000
  200 FORMAT(F8.5)
      PI=3.141593
      A001=2.*PI*0.529/AL
      B001=A001
      C001=2.*PI*0.529/CL
      A110=1.4162*PI/AL
      B110=1.058*PI/CL
      C110=A110
      A100=A001
      B100=C001
      C100=B001
      OM=AL*AL*CL/(4.*0.529**3)
      FWN=0.529*(36.*PI*PI/(AL*AL*CL))**0.3333
      T=CCMP/100.
      OM=DSQRT(CM1*CM2)
      CONST=2.*PI*((1.-T)**2*ZS1*ZS1/OM1+T*T*ZS2*ZS2/CM2+2.*T*(1.-T)*OM
     2*ZS1*ZS2/(OM1*OM2))
      P=8.0
C
C       CALCULATION OF CHANGE IN BAND STRUCTURE ENERGY OWING TO
C                      DISTURBANCE OF LATTICE.
C
      A=A001
      B=B001
      C=C001
      NC=1
      NSTEP=1+1./SIZE
      WRITE(6,107)
```



```
  107 FORMAT(//'1      PROPAGATION IN (001) DIRECTION.')
   40 IF(NC-2)150,39,150
   39 WRITE(6,106)
  106 FORMAT(//'1      PROPAGATION IN (110) DIRECTION')
      A=A110
      B=B110
      C=C110
      NSTEP=1+1.414/SIZE
  150 IF(NC-3)151,149,151
  149 WRITE(6,108)
  108 FORMAT(//'1       PROPAGATION IN (100) DIRECTION')
      A=A100
      B=B100
      C=C100
  151 DO 33 I=1,NSTEP
      DEBSL(I)=0.0
      DEBST(I,1)=0.0
   33 DEBST(I,2)=0.0
      DO 22 L=1,NSTEP
      Q=1.058*SIZE*L*PI/AL
      IF(NC.EQ.1)Q=Q*AL/CL
   49 AN(L)=L*SIZE
      DO 2 I=1,9
      DO 2 J=1,9
      DO 2 K=1,9
      IT=I-(I/2)*2
      JT=J-(J/2)*2
      KT=K-(K/2)*2
    7 ISUM=IT+JT+KT
      IF(NC.NE.2.AND.(IT.EQ.JT.AND.IT.EQ.KT))GOTO 91
      IF(NC.EQ.2.AND.(ISUM.EQ.3.OR.ISUM.EQ.1))GOTO 91
      GOTO 2
   91 FI=I-1
      FJ=J-1
      FK=K-1
      X=FI*A
      Y=FJ*B
      Z=FK*C
      QO=DSQRT(X**2+Y**2+Z**2)
      ETA=QO/FWN
      IF(ETA-7.0)5,5,2
    5 IF(QO)2,55,6
   55 CALL INTER(C,FQ,C,FR,Q,FS)
      DEBSL(L)=2.*C**2*FQ
      GOTO 2
    6 IF(I.EQ.1.OR.J.EQ.1.OR.K.EQ.1)P=4.0
      IF(I.EQ.1.AND.(J.EQ.1.OR.K.EQ.1).OR.(J.EQ.1.AND.K.EQ.1))P=2.0
   60 CT2=Z**2/(X**2+Y**2+Z**2)
      ST2=1.0-CT2
      CT=DSQRT(CT2)
      QOPQ=DSQRT(Q**2+QO**2+2.*Q*QO*CT)
      QOMQ=DSQRT(Q**2+QO**2-2.*Q*QO*CT)
      SA2M=QO**2*ST2/QOMQ**2
      CA2M=1.-SA2M
      QOMQA=QOMQ**2*CA2M
```

```
   50 SA2P=QO**2*ST2/COPC**2
      CA2P=1.-SA2P
      COPCA=COPQ**2*CA2P
      CALL INTER(QOPQ,FQOPQ,QOMQ,FQOMQ,CO,FQO)
      DEBL=COPCA*FCOPQ+COMQA*FCOMC-2.*QC**2*FQC*CT2
      CP2=1.0
      IF(I.NE.1.OR.J.NE.1)CP2=X**2/(X**2+Y**2)
      N=1
      DEBSL(L)=DEBSL(L)+P*DEBL
   13 COPCA=COPQ**2*CP2*SA2P
      COMCA=COMQ**2*CP2*SA2M
      CALL INTER(COPC,FCOPQ,COMQ,FCOMC,CO,FQO)
      DEBT=COPCA*FCOPQ+COMCA*FCOMC-2.*CO**2*FCO*ST2*CP2
      DEBST(L,N)=DEBST(L,N)+P*DEBT
      IF(N-1)2,21,2
   21 CP2=1.0
      IF(I.NE.1.OR.J.NE.1)CP2=Y**2/(X**2+Y**2)
      N=2
      GOTO 13
    2 P=8.0
   22 CONTINUE
      WRITE(6,102)
  102 FORMAT(//'      BAND STRUCTURE ENERGY CHANGE'//15X,'QA/2*PI',10X,
     2'TRANSVERSE(1)',9X,'TRANSVERSE(2)',9X,'LONGITUDINAL')
   15 WRITE(6,101)(AN(I),DEBST(I,1),DEBST(I,2),DEBSL(I),I=1,NSTEP)
  101 FORMAT(17X,F4.2,10X,D12.5,10X,D12.5,10X,D12.5)
C
C        CALCULATION OF CHANGE IN ELECTROSTATIC ENERGY OWING TO DISTURBANCE
C                 OF LATTICE.
C
      DO 20 L=1,NSTEP
      DEESL(L)=0.0
      DEEST(L,1)=0.0
      DEEST(L,2)=0.0
      SUML(L)=0.0
      SUMT(L,1)=0.0
   20 SUMT(L,2)=0.0
      P=4.0
      DO 23 L=1,NSTEP
      Q=1.058*SIZE*L*PI/AL
      IF(NC.EQ.1)Q=Q*AL/CL
   36 DO 3 I=1,9
      DO 3 J=1,9
      SUMC11=0.
      FI=I-1
      FJ=J-1
      IT=I-(I/2)*2
      JT=J-(J/2)*2
      IF(NC-2)32,95,32
   32 IF(IT-JT)3,95,3
   95 X=FI*A
      Y=FJ*B
      COX=X
      COY=Y
      COPER=DSQRT(COX**2+COY**2)
```



```
      IF(QOPER)3,3,68
   68 IF(QOPER-6.)8,8,3
    8 AA=PI*COPER/C
      TH=PI*Q/C
      CTH=DCOS(TH)
      C1=2.*C
      IF(I.EQ.1.OR.J.EQ.1)P=2.0
      SUM=SM(P,PI,COPER,C1,CTH,AA)
      IF(NC.NE.2.AND.IT.EQ.0)GOTO 56
      IF(NC.EQ.2.AND.IT.NE.JT)GOTO 56
      SUMC11=SUMQ11+SUM
      GOTO 57
   56 SUMQ11=SUMQ11-SUM
      AA=AA*2.
      TH=TH*2.
      CTH=DCOS(TH)
      SUM=SM(P,PI,COPER,C,CTH,AA)
      SUMC11=SUMC11+SUM
   57 SUML(L)=SUML(L)+SUMC11*COPER**2
      DEESL(L)=CONST*(2.0-SUML(L))
      A1=1.0
      A2=0.0
      N=1
   25 SUMT(L,N)=SUMT(L,N)+SUMC11*(A1*COX+A2*COY)**2
      DEEST(L,N)=CONST*SUMT(L,N)
      IF(N-1)3,26,3
   26 A1=0.0
      A2=1.0
      N=2
      GOTO 25
    3 P=4.0
   23 CONTINUE
      WRITE(6,103)
  103 FORMAT(//' ELECTROSTATIC ENERGY CHANGE'//15X,'QA/2*PI',10X,
     2'TRANSVERSE(1)',9X,'TRANSVERSE(2)',9X,'LONGITUDINAL')
      WRITE(6,101)(AN(I),DEEST(I,1),DEEST(I,2),DEESL(I),I=1,NSTEP)
C                                                        2
C        CALCULATION OF VIBRATION SPECTRUM.            W  =(E   + E  )/M
C                                                            BS    ES
      DO 1 L=1,NSTEP
      WL(L)=DSQRT(DABS(1.715D33*(DEBSL(L)+DEESL(L))/AM))
      DO 1 J=1,2
    1 WT(L,J)=DSQRT(DABS(1.715D33*(DEBST(L,J)+DEEST(L,J))/AM))
      WRITE(6,105)
  105 FORMAT(//'      PHONON CURVES'//15X,'QA/2*PI',23X,'TRANSVERSE FREQUE
     2NCIES',25X,'LONGITUDINAL FREQUENCY')
      WRITE(6,104)(AN(I),WT(I,1),WT(I,2),WL(I),I=1,NSTEP)
  104 FORMAT(17X,F4.2,15X,D12.5,19X,D12.5,19X,D12.5)
      IF(NC-3)80,27,27
   80 NC=NC+1
      NSTEP=1+1./SIZE
      GOTO 40
   27 STOP
      END
```

```
      SUBROUTINE INTER(Q,FQ,R,FR,S,FS)
      IMPLICIT REAL*8(A-H,O-Z)
      COMMON F(73),CONST,PI,FWN
      N=1
      QF=Q
    7 ETA=QF/FWN
      P=-CONST/QF**2
      JF=(10.*ETA)/1+1
      H=10.*ETA+1.-JF
      Y=0.0
      IF(ETA-7.0)1,1,2
    1 IF(JF.LE.2)GOTO 3
      A=F(JF-1)
      B=F(JF)
      C=F(JF+1)
      D=F(JF+2)
      Y=(B+C)/2.+(H-.5)*(C-B)+H*(H-1.)*(A+D-B-C)/4.+H*(H-1.)*(H-.5)*
     2(D-3.*C+3.*B-A)/6.
      GOTO 2
    3 A=F(JF)
      B=F(JF+1)
      C=F(JF+2)
      D=F(JF+3)
      Y=A+H*(B-A)+H*(H-1.)*(C-2.*B+A)/2.+H*(H-1.)*(H-2.)*(D-3.*C+3.*B-A)
     2/6.
    2 IF(N-2)4,5,6
    4 FQ=P*Y
      N=N+1
      QF=R
      GOTO 7
    5 FR=P*Y
      N=N+1
      QF=S
      GOTO 7
    6 FS=P*Y
      RETURN
      END
```

COMBINE

```
C         THIS PROGRAMME COMBINES F(Q) FUNCTIONS FOR INDIUM AND
C          THALLIUM TO PRODUCE F(Q) FOR ALLOYS.  RESULTS ARE
C          GIVEN FOR 5 AT.% TL STEPS.
      REAL KF,KF1,KF2
      DIMENSION F1(55),F2(55),G1(55),G2(55),H1(55),H2(55),FQ1(55),
     1FQ2(55),WQ1(55),WQ2(55),EPS1(55),EPS2(55),ETA(55)
      XW(C,X1,X2)=(1.-C)*X1+C*X2
      READ(5,101)OM1,OM2,KF1,KF2,ZS1,ZS2
  101 FORMAT(2F8.3,2F7.4,2F8.5)
      DO 2 I=1,55
    2 READ(7,103)ETA(I),WQ1(I),FQ1(I),EPS1(I),F1(I),G1(I),H1(I)
      DO 3 I=1,55
    3 READ(7,103)ETA(I),WQ2(I),FQ2(I),EPS2(I),F2(I),G2(I),H2(I)
  103 FORMAT(T22,F3.1,7X,F9.6,5X,F8.6,9X,F9.5,3(4X,F8.5))
      PI=3.14159
      DO 1 J=1,8
      C1=(J-1)*5.
      C=C1/100.
      ZS=XW(C,ZS1,ZS2)
      OMD=XW(C,OM1,OM2)
      KF=XW(C,KF1,KF2)
      Y=2.*PI*((1.-C)*ZS1/SQRT(OM1)+C*ZS2/SQRT(OM2))**2
      OM=SQRT(OM1*OM2)
      OM=OMD
      WRITE(6,120)C1,OM,ZS,Y
  120 FORMAT('1     ALLOY COMPOSITION: INIUM -',F5.1,' AT.% THALLIUM',
     210X,'WEIGHTED MEAN OF ATOMIC VOLUME =',F7.2,/77X,'EFFECTIVE VALENC
     3E =',F7.5,/ 8X,' NORMALISING FACTOR =',F9.5,'*C*C*F(Q)',//8X,
     4' WQ(AV)            FNQ(AV)          ETA           FQ(AV)')
      DO 1 I=1,55
      Q1=ETA(I)*KF1
      Q2=ETA(I)*KF2
      Q=ETA(I)*KF
      EPS=(EPS1(I)+EPS2(I))/2.
      H=(H1(I)+H2(I))/2.
      FUNQ1=-2.*ZS1**2*PI*FQ1(I)/(Q1**2*OM1)
      FUNC2=-2.*ZS2**2*PI*FQ2(I)/(Q2**2*OM2)
      FQUNAV=2.*PI*ZS1*ZS2*(1.-EPS-(1.-EPS1(I))*(1.-EPS2(I)))/(OM*EPS1(I
     2)*EPS2(I)*Q*Q)+(EPS1(I)+EPS2(I)-EPS)*16./(OM*Q*Q*EPS1(I)*EPS2(I))*
     3(8.*G1(I)*G2(I)/PI-G1(I)*ZS2-G2(I)*ZS1)-16.*H/OM
      FQUNAV=FQUNAV*2.*C*(1.-C)+(1.-C)**2*FUNC1+C*C*FUNC2
      FNQAV=-FQUNAV*OM*Q/Y
      WQAV=XW(C,WQ1(I),WQ2(I))
      WRITE(8,111)FNQAV
    1 WRITE(6,110)WQAV,FNQAV,ETA(I),FQUNAV
  110 FORMAT(2(7X,F9.5),F9.1,3(7X,F9.5))
  111 FORMAT(F8.5)
      STOP
      END
```

obtained from two applications of SM using different reciprocal lattice point spacings and taking the difference of the two results; (see lines 3 to 19 on page 4: NC has the value 1, 2 or 3 for propagation in the [001], [110] or [100] directions). The sum was found to have converged sufficiently by $\underline{q}_o{}^{\perp} = 6\,k_f$. In order to reduce the computing time the sums are only evaluated in the first quadrant and a multiplicative factor P is used to correct the results. When SIZE was 0.05 the programme took about 60 sec. C P U time on an IBM 360/67.

COMBINE

This programme evaluates normalised energy-wavenumber characteristics for the alloys starting from certain functions obtained for each element from MODPOT, namely F, G, H, $F_n(q)$, ϵ, Z* and Ω. Also the fermi wavevector k_f is required. The analysis outlined in section 7.3.2 has been carried out and the un-normalised energy-wavenumber characteristics FUNQ1 and FUNQ2 are computed. FQUNAV is based on the product of matrix elements for the two metals. The average energy-wavenumber characteristic $F_{av}(q)$ is obtained from C^2FUNQ2 + $(1-C)^2$FUNQ1 + 2C(1-C)FQUNAV, in which C is the percentage of thallium. Renormalisation is performed to give FNQAV. The programme is designed to carry out this procedure for steps in thallium concentration of 5% up to 35%.

MODPOT

MODPOT is a slightly modified version of the PL/1 programme given by Shaw (1968a) to calculate normalised energy-wavenumber characteristics and form factors for metals. It requires as input data the fermi wavevector (KF), the valency (Z), the maximium value of l for which the potential has been modelled (LO) and the well depths and their energy derivatives (AO,A1,A2, DAODE,DA1DE,DA2DE). The output consists of the normalised energy-wavenumber characteristic FQ and form factor WQ tabulated at q/k_f values in steps of 0.1 up to 5.0 and in steps of 0.4 up to 7.0. In addition, the functions EPS, F, G and H are given for each value of q/k_f. The calculation of FQ in lines 541-3 is the form to which the expression in COMBINE for FQUNAV reduces in the case of pure indium.

For further details of the procedures used see Shaw (1968a); the information given here is sufficient to enable the programme to be used. On an IBM 360/67 the running time was approximately 1400 seconds.

MODPOT

```
APN9:MODPOT
      /* OPTIMIZED MAIN PROGRAM / COMPUTATION OF W(K,Q)
      F(Q) AND VEFF(R) USING OPTIMUM PARAMETERS        */
      L1: PROCEDURE OPTIONS (MAIN);
      DCL(I,N,LO,ETA1) FIXED BIN,
      (EPS,WO,FQ,VEFF,PI,ETA,VO,AO,A1,A2,DAODE,DA1DE,DA2DE,RHO,ZSTAR,
      K,K1,RO,R1,R2,CS,KKF,KRO,KR1,KR2,K1RO,K1R1,K1R2,ARG,ARG1,
      (FLO,FL1,FL2,FKLO,FKL1,FKL2,FKFLO,FKFL1,FKFL2,FALO,FAL1,FAL2)(0:10)
      ,KF,R,G1,H1,ETO                              ) FLOAT DEC,
      FCA(1:70) FLOAT DEC, Z FLOAT DEC EXTERNAL,
      ELEMENT CHAR(12) VARYING,
      (VINC,IO,I1,I2,FKF,DCZ,G,CHZ,H,FA) ENTRY(FLOAT DEC)
      RETURNS (FLOAT DEC),
      (DFDZ,GZ,HZ,FK) ENTRY(FLOAT DEC, FLOAT DEC) RETURNS(FLOAT DEC),
      F ENTRY(FLOAT DEC,FLOAT DEC,FLOAT DEC) RETURNS(FLOAT DEC);

      /* IO,I1,AND I2 ARE PROCEDURES FOR EVALUATING INTEGRALS
      WHICH ENTER IN THE COMPUTATION OF THE DEFLETION HOLE */
      IO: PROC (PK) FLOAT DEC;
      DCL X FIXED BIN, (PK,ANSWER,FUNC(0:10),KR) FLOAT DEC;
      DO X=1 TO 9 BY 2;
      KR=PK*Z/(AO+(X**2/100-1)*PK**2*DAODE/2);
      FUNC(X)=4*(KR-5*SIN(2*KR*X/10)/X);    END;
      DO X=2 TO 8 BY 2;
      KR=PK*Z/(AO+(X**2/100-1)*PK**2*DAODE/2);
      FUNC(X)=2*(KR-5*SIN(2*KR*X/10)/X);    END;
      KR=PK*Z/AO;
      FUNC(10)=KR-SIN(2*KR)/2;
      FUNC(0)=0;
      ANSWER= SUM(FUNC)/30;
      RETURN(ANSWER);  END IO;
      I1: PROC(PK) FLOAT DEC;
      DCL X FIXED BIN, (PK,ANSWER,FUNC(0:10),KR) FLOAT DEC;
      DO X=1 TO 9 BY 2;
      KR=PK*Z/(A1+(X**2/100-1)*PK**2*DA1DE/2);
      FUNC(X)=4*(KR+5*SIN(2*KR*X/10)/X-200*(SIN(KR*X/10))**2/(KR*X**2));
      END;
      DO X=2 TO 8 BY 2;
      KR=PK*Z/(A1+(X**2/100-1)*PK**2*DA1DE/2);
      FUNC(X)=2*(KR+5*SIN(2*KR*X/10)/X-200*(SIN(KR*X/10))**2/(KR*X**2));
      END;
      KR=PK*Z/A1;
      FUNC(10)=KR+SIN(2*KR)/2-2*(SIN(KR))**2/KR;
      FUNC(0)=0;
      ANSWER= SUM(FUNC)/30;
      RETURN(ANSWER);  END I1;
      I2: PROC(PK) FLOAT DEC;
      DCL X FIXED BIN, (PK,ANSWER,FUNC(0:10),KR) FLOAT DEC;
      DO X=1 TO 9 BY 2;
      KR=PK*Z/(A2+(X**2/100-1)*PK**2*DA2DE/2);
      FUNC(X)=4*(KR-5*SIN(2*KR*X/10)/X-600*(COS(KR*X/10)-10*SIN(KR*X/10)/
      (KR*X))**2/(KR*X**2));    END;
      DO X=2 TO 8 BY 2;
      KR=PK*Z/(A2+(X**2/100-1)*PK**2*DA2DE/2);
      FUNC(X)=2*(KR-5*SIN(2*KR*X/10)/X-600*(COS(KR*X/10)-10*SIN(KR*X/10)/
      (KR*X))**2/(KR*X**2));    END;
      KR=PK*Z/A2;
      FUNC(10)=KR-SIN(2*KR)/2-6*(COS(KR)-SIN(KR)/KR)**2/KR;
      FUNC(0)=0;
      ANSWER= SUM(FUNC)/30;
      RETURN(ANSWER);  END I2;

      /* F IS A PROCEDURE FOR EVALUATING THE GENERAL NON-LOCAL
         MATRIX ELEMENT F(K,Q). AN INTEGRAL OVER RADIUS IS
         INVOLVED IN THIS AND THE FOLLOWING THREE PROCEDURES */
      F: PROC (PU,PZ,PETA) FLOAT DEC;
      DCL(F1,PU,PZ,PETA,N) FLOAT DEC,
      Z FLOAT DEC EXTERNAL, M FIXED BIN;
      K=KF*SQRT(PU+PZ**2);    KKF=K**2-KF**2;
      K1=KF*SQRT(PU+(PZ+PETA)**2);
      RO=Z/(AO+KKF*DAODE/2);  KRO=K*RO;  K1RO=K1*RO;
      DO M=1 TO 9 BY 2;  N=M;
      FLO(M)=4*((N-10)/N)*SIN(KRO*N/10)*SIN(K1RO*N/10);
      END;
      DO M=2 TO 8 BY 2;  N=M;
      FLO(M)=2*((N-10)/N)*SIN(KRO*N/10)*SIN(K1RO*N/10);
      END;
      FLO(0),FLO(10)=0;
      IF LO=0 THEN GO TO LFO ;
      CS=(PU+PZ*(PZ+PETA))/SQRT((PU+PZ**2)*(PU+(PZ+PETA)**2));
      R1=Z/(A1+KKF*DA1DE/2);  KR1=K*R1;  K1R1=K1*R1;
      DO M=1 TO 9 BY 2;  N=M;
      ARG=KR1*N/10;   ARG1=K1R1*N/10;
      FL1(M)  =4*((N-10)/N)*(SIN(ARG)/ARG-COS(ARG))*
      (SIN(ARG1)/ARG1-COS(ARG1));
      END;
      DO M=2 TO 8 BY 2;  N=M;
      ARG=KR1*N/10;   ARG1=K1R1*N/10;
      FL1(M)  =2*((N-10)/N)*(SIN(ARG)/ARG-COS(ARG))*
      (SIN(ARG1)/ARG1-COS(ARG1));
      END;
      FL1(0),FL1(10)=0;
      IF LO=1 THEN GO TO LF1;
      R2=Z/(A2+KKF*DA2DE/2);  KR2=K*R2;  K1R2=K1*R2;
      DO M=1 TO 9 BY 2;  N=M;
      ARG=KR2*N/10;   ARG1=K1R2*N/10;
      FL2(M)  =4*((N-10)/N)*((3/ARG**2-1)*SIN(ARG)-3*COS(ARG)/ARG)*
      ((3/ARG1**2-1)*SIN(ARG1)-3*COS(ARG1)/ARG1);
      END;
      DO M=2 TO 8 BY 2;  N=M;
      ARG=KR2*N/10;   ARG1=K1R2*N/10;
      FL2(M)  =2*((N-10)/N)*((3/ARG**2-1)*SIN(ARG)-3*COS(ARG)/ARG)*
      ((3/ARG1**2-1)*SIN(ARG1)-3*COS(ARG1)/ARG1);
      END;
      FL2(0),FL2(10)=0;
      IF LO=2 THEN GO TO LF2;
      LFO:  F1=(Z/(K*K1))*SUM(FLO)/30;
      GO TO LF;
      LF1:  F1=(Z/(K*K1))*(SUM(FLO)+3*CS*SUM(FL1))/30;
      GO TO LF;
      LF2:  F1=(Z/(K*K1))*(SUM(FLO)+3*CS*SUM(FL1)
       +2.5*(3*CS**2-1)*SUM(FL2))/30;
      LF: RETURN(F1);   END F;
```

```
   /* FK IS A PROCEDURE WHICH EVALLATES F(K,Q) WHEN K=K' */
FK: PROC (PU,PETA) FLOAT DEC;
DCL(FK1,PU,PETA,N) FLOAT DEC,
 Z FLOAT DEC EXTERNAL, M FIXED BIN;
K=KF*SQRT(PU+(PETA/2)**2);
KKF=K**2-KF**2;
RO=Z/(AO+KKF*DAODE/2);  KRO=K*RO;
DO M=1 TO 9 BY 2; N=M;
FKLO(M) =4*((N-10)/N)*(SIN(KRO*N/10))**2;
END;
DO M=2 TO 8 BY 2;  N=M;
FKLO(M) =2*((N-10)/N)*(SIN(KRO*N/10))**2;
END;
FKLO(0),FKLO(10)=0;
IF LO=0 THEN GO TO LFKO;
CS=(PU-(PETA/2)**2)/(PU+(PETA/2)**2);
R1=Z/(A1+KKF*DA1DE/2);  KR1=K*R1;
DO M=1 TO 9 BY 2;  N=M;
ARG=KR1*N/10;
FKL1(M)=4*((N-10)/N)*(SIN(ARG)/ARG-COS(ARG))**2;
END;
DO M=2 TO 8 BY 2;  N=M;
ARG=KR1*N/10;
FKL1(M) =2*((N-10)/N)*(SIN(ARG)/ARG-COS(ARG))**2;
END;
FKL1(0),FKL1(10)=0;
IF LO=1 THEN GO TO LFK1;
R2=Z/(A2+KKF*DA2DE/2);  KR2=K*R2;
DO M=1 TO 9 BY 2;  N=M;
ARG=KR2*N/10;
FKL2(M) =4*((N-10)/N)*((3/ARG**2-1)*SIN(ARG)-3*COS(ARG)/ARG)**2;
END;
DO M=2 TO 8 BY 2;   N=M;
ARG=KR2*N/10;
FKL2(M) =2*((N-10)/N)*((3/ARG**2-1)*SIN(ARG)-3*COS(ARG)/ARG)**2;
END;
FKL2(0),FKL2(10)=0;
IF LO=2 THEN GO TO LFK2;
LFKO: FK1=(Z/K**2)*SUM(FKLO)/30;
GO TO LFK;
LFK1: FK1=(Z/K**2)*(SUM(FKLO)+3*CS*SUM(FKL1))/30;
GO TO LFK;
LFK2: FK1=(Z/K**2)*(SUM(FKLO)+3*CS*SUM(FKL1)
  +2.5*(3*CS**2-1)*SUM(FKL2))/30;
LFK: RETURN(FK1);  END FK;

   /*  FKF IS A PROCEDURE WHICH EVALLATES F(K,Q) WHEN K=K'=KF  */
FKF: PROC(PETA) FLOAT DEC;
 DCL(PETA,FKF1,N) FLOAT DEC,
 Z FLOAT DEC EXTERNAL, M FIXED BIN;
K=KF;  CS=1-PETA**2/2;
 KRO=KF*Z/AO;
 DO M=1 TO 9 BY 2;  N=M;
   FKFLO(M)=4*((N-10)/N)*(SIN(KRO*N/10))**2;
 END;
 DO M=2 TO 8 BY 2;  N=M;
   FKFLO(M)=2*((N-10)/N)*(SIN(KRO*N/10))**2;
END;
FKFLO(0),FKFLO(10)=0;
 IF LO=0 THEN GO TO LFKFO;
 KR1=KF*Z/A1;
 DO M=1 TO 9 BY 2;  N=M;
 ARG=KR1*N/10;
 FKFL1(M)=4*((N-10)/N)*(SIN(ARG)/ARG-COS(ARG))**2;
 END;
 DO M=2 TO 8 BY 2;   N=M;
 ARG=KR1*N/10;
 FKFL1(M)=2*((N-10)/N)*(SIN(ARG)/ARG-COS(ARG))**2;
 END;
 FKFL1(0),FKFL1(10)=0;
 IF LO=1 THEN GO TO LFKF1;
 KR2=KF*Z/A2;
 DO M=1 TO 9 BY 2;  N=M;
 ARG=KR2*N/10;
 FKFL2(M)=4*((N-10)/N)*((3/ARG**2-1)*SIN(ARG)-3*COS(ARG)/ARG)**2;
 END;
 DO M=2 TO 8 BY 2;   N=M;
 ARG=KR2*N/10;
 FKFL2(M)=2*((N-10)/N)*((3/ARG**2-1)*SIN(ARG)-3*COS(ARG)/ARG)**2;
 END;
 FKFL2(0),FKFL2(10)=0;
 IF LO=2 THEN GO TO LFKF2;
 LFKFO:  FKF1=(Z/K**2)*SUM(FKFLO)/30;
 GO TO LFKF;
 LFKF1: FKF1=(Z/K**2)*(SUM(FKFLO)+3*CS*SUM(FKFL1))/30;
 GO TO LFKF;
 LFKF2: FKF1=(Z/K**2)*(SUM(FKFLO)+3*CS*SUM(FKFL1)
   +2.5*(3*CS**2-1)*SUM(FKFL2))/30;
 LFKF: RETURN(FKF1);  END FKF;

    /* FA IS A PROCEDURE WHICH EVALUATES F(K,Q) WHEN K AND K'
         ARE ANTI-PARALLEL, K=KF, AND K'>KF    */
 FA: PROC(PETA) FLOAT DEC;
  DCL(PETA,FA1,N) FLOAT DEC,
 Z FLOAT DEC EXTERNAL, M FIXED BIN;
 K=KF;   K1=KF*(PETA-1);
 KRO=Z*KF/AO;  K1RO=Z*K1/AO;
 DO M=1 TO 9 BY 2;  N=M;
 FALO(M)=4*((N-10)/N)*SIN(KRO*N/10)*SIN(K1RO*N/10);
 END;
 DO M=2 TO 8 BY 2;   N=M;
 FALO(M)=2*((N-10)/N)*SIN(KRO*N/10)*SIN(K1RO*N/10);
 END;
 FALO(0),FALO(10)=0;
 IF LO=0 THEN GO TO LFAO;
 KR1=Z*KF/A1;  K1R1=Z*K1/A1;
 DO M=1 TO 9 BY 2;  N=M;
 ARG=KR1*N/10;    ARG1=K1R1*N/10;
 FAL1(M) =4*((N-10)/N)*(SIN(ARG)/ARG-COS(ARG))*
 (SIN(ARG1)/ARG1-COS(ARG1));
 END;
 DO M=2 TO 8 BY 2;    N=M;
 ARG=KR1*N/10;    ARG1=K1R1*N/10;
 FAL1(M) =2*((N-10)/N)*(SIN(ARG)/ARG-COS(ARG))*
 (SIN(ARG1)/ARG1-COS(ARG1));
 END;
 FAL1(0),FAL1(10)=0;
 IF LO=1 THEN GO TO LFA1;
```

```
KR2=2*KF/A2;  K1R2=2*K1/A2;
DO M=1 TO 9 BY 2;  N=M;
ARG=KR2*N/10;    ARG1=K1R2*N/10;
FAL2(M) =4*((N-10)/N)*((3/ARG**2-1)*SIN(ARG)-3*COS(ARG)/ARG)*
((3/ARG1**2-1)*SIN(ARG1)-3*COS(ARG1)/ARG1);
END;
DO M=2 TO 8 BY 2;   N=M;
ARG=KR2*N/10;    ARG1=K1R2*N/10;
FAL2(M) =2*((N-10)/N)*((3/ARG**2-1)*SIN(ARG)-3*COS(ARG)/ARG)*
((3/ARG1**2-1)*SIN(ARG1)-3*COS(ARG1)/ARG1);
END;
FAL2(0),FAL2(10)=0;
IF LO=2 THEN GO TO LFA2;
LFA0: FA1=(Z/(K*K1))*SUM(FAL0)/30;
GO TO LFA;
LFA1: FA1=(Z/(K*K1))*(SUM(FAL0)-3*SUM(FAL1))/30;
GO TO LFA;
LFA2: FA1=(Z/(K*K1))*(SUM(FAL0)-3*SUM(FAL1)+5*SUM(FAL2))/30;
LFA:  RETURN(FA1);  END FA;

    /*  DFDZ IS A PROCEDURE FOR EVALUATING THE DERIVATIVE OF
        F(K,Q) WITH RESPECT TO Z=K2/KF AT Z=-Q/2    */
DFDZ: PROC(PU,PETA) FLOAT DEC;
DCL(PU,PETA,DFDZ1) FLOAT DEC,
Z FLOAT DEC EXTERNAL;
K=KF*SQRT(PU+(PETA/2)**2);
KKF=K**2-KF**2;
RO=Z/(A0+KKF*DA0DE/2);    KRO=K*RO;
DFDZ1=-(KF**2*PETA/4)*RO**3*DA0DE*(1/(KRO)**2-SIN(2*KRO)/
(2*KRO**3));     IF LO=0 THEN GO TO LDFDZ;
R1=Z/(A1+KKF*DA1DE/2);  KR1=K*R1;
CS=(PU-(PETA/2)**2)/(PU+(PETA/2)**2);
DFDZ1=DFDZ1-(KF**2*PETA/4)*3*CS*R1**3*DA1DE*(1/(KR1)**2
  +SIN(2*KR1)/(2*KR1**3)-2*(SIN(KR1))**2/(KR1)**4);
IF LO=1 THEN GO TO LDFDZ;
R2=Z/(A2+KKF*DA2DE/2);    KR2=K*R2;
DFDZ1=DFDZ1-(KF**2*PETA/4)*(2.5*(3*CS**2-1)*R2**3*DA2DE*
(1/(KR2)**2-9*(COS(KR2))**2/(KR2)**4-6*(SIN(KR2))**2
/(KR2)**6+(6/(KR2)**5-1/(2*(KR2)**3))*SIN(2*KR2)));
LDFDZ:  RETURN(DFDZ1);  END DFDZ;

    /* HZ IS A PROCEDURE FOR INTEGRATING THE SQUARE OF F(K,Q)
        OVER THE RANGE U=0 TO 1-Z**2    */
HZ: PROC (PZ,PETA) FLOAT DEC;
DCL (M,N) FIXED BIN, (ANSWER,PZ,PETA,A,H,ALO,RO) FLOAT DEC,
Z FLOAT DEC EXTERNAL,
FUNC(0:20) FLOAT DEC;
FUNC=0;
A=1-(PZ)**2;
M=2*CEIL(10*A);
H=A/M;
DO N=1 TO (M-1) BY 2;
FUNC(N)=4*(F(N*H,PZ,PETA))**2;    END;
IF M>2 THEN
DO N=2 TO (M-2) BY 2;
FUNC(N)=2*(F(N*H,PZ,PETA))**2;  END;
FUNC(M)=(F(A,PZ,PETA))**2;
IF PETA>=1 THEN DO;
IF PZ>1E-3 THEN
FUNC(0)=(F(0,PZ,PETA))**2; ELSE
IF PZ<-1E-3 THEN
FUNC(0)=(F(0,PZ,PETA))**2; ELSE DO;
ALO=A0-KF**2*DA0DE/2;  RO=Z/ALO;
FUNC(0)=(ALO*SIN(KF*PETA*RO)/(KF*PETA)**3-Z/(KF*PETA)**2)**2; END;
END; ELSE DO;
IF PZ>1E-3 THEN
FUNC(0)=(F(0,PZ,PETA))**2;  ELSE
IF PZ<-1E-3 THEN DO;
IF PZ>-PETA+1E-3 THEN
FUNC(0)=(F(0,PZ,PETA))**2;  ELSE
IF PZ<-PETA-1E-3 THEN
FUNC(0)=(F(0,PZ,PETA))**2; ELSE DO;
ALO=A0+(PETA**2-1)*KF**2*DA0DE/2;   RO=Z/ALO;
FUNC(0)=(ALO*SIN(KF*PETA*RO)/(KF*PETA)**3-Z/(KF*PETA)**2)**2;  END;
END; ELSE DO;
ALO=A0-KF**2*DA0DE/2;  RO=Z/ALO;
FUNC(0)=(ALO*SIN(KF*PETA*RO)/(KF*PETA)**3-Z/(KF*PETA)**2)**2;  END;
END;
ANSWER=(H/3)*SUM(FUNC);
RETURN(ANSWER);  END HZ;

    /* DHZ IS A PROCEDURE FOR INTEGRATING 2*F(K,Q)*DF(K,Q)/DZ
        OVER THE RANGE U=0 TO 1-(Q/2*KF)**2  */
DHZ:  PROC(PETA) FLOAT DEC;
DCL (M,N) FIXED BIN, (PETA,A,H,ANSWER) FLOAT DEC,
FUNC(0:20) FLOAT DEC;
FUNC=0;
A=1-(PETA/2)**2;
M=2*CEIL(10*A);
H=A/M;
DO N=1 TO (M-1) BY 2;
FUNC(N)=8*FK(N*H,PETA)*DFDZ(N*H,PETA);   END;
IF M>2 THEN
DO N=2 TO (M-2) BY 2;
FUNC(N)=4*FK(N*H,PETA)*DFDZ(N*H,PETA); END;
FUNC(M)=2*FKF(PETA)*DFDZ(A,PETA);
FUNC(0)=2*FK(0,PETA)*DFDZ(0,PETA);
ANSWER=(H/3)*SUM(FUNC);
RETURN(ANSWER);  END  DHZ;

    /*  H IS A PROCEDURE FOR INTEGRATING THE FUNCTION
        H(Z)/(Z+ETA/2) OVER THE RANGE Z=-1 TO 1    */
H: PROC (PETA) FLOAT DEC;
DCL (Z,PETA,ANSWER) FLOAT DEC, FUNC(-40:40) FLOAT DEC,
N FIXED BIN;
IF PETA<2-1E-3 THEN GO TO CASE1;
ELSE IF PETA>2+1E-3 THEN GO TO CASE3;
ELSE GO TO CASE2;
CASE1:  DO;
DO N=-39 TO 39 BY 2;  Z=N;
IF Z<-20*PETA-1E-3 THEN
FUNC(N)=4*HZ(.025*Z,PETA)/(.025*Z+PETA/2);  ELSE
IF Z>-20*PETA+1E-3 THEN
FUNC(N)=4*HZ(.025*Z,PETA)/(.025*Z+PETA/2);  ELSE
FUNC(N)=4*PETA*(FKF(PETA))**2+4*DHZ(PETA);
END;
```

```
DO N=-38 TO 38 BY 2;  Z=N;
IF Z<-20*PETA-1E-3 THEN
FUNC(N)=2*HZ(.025*Z,PETA)/(.025*Z+PETA/2);  ELSE
IF Z>-20*PETA+1E-3 THEN
FUNC(N)=2*HZ(.025*Z,PETA)/(.025*Z+PETA/2);  ELSE
FUNC(N)=2*PETA*(FKF(PETA))**2+2*DHZ(PETA);
END;
FUNC(40),FUNC(-40)=0;
ANSWER=(KF/(4*PETA))*(.025/3)*SUM(FUNC);
RETURN(ANSWER);  END;  GO TO ENDH;
CASE2:  DO;
FUNC=0;
DO N= -19 TO 19 BY 2;  Z=N;
FUNC(N)=4*HZ(.05*Z,2)/(.05*Z+1);
END;
DO N= -18 TO 18 BY 2; Z=N;
FUNC(N)=2*HZ(.05*Z,2)/(.05*Z+1);
END;
FUNC(20)=0;  FUNC(-20)= 2*(FKF(2))**2;
ANSWER= (KF/8)*(0.05/3)*SUM(FUNC);
RETURN(ANSWER);  END;  GO TO ENDH;
CASE3:  DO;
FUNC=0;
DO N= -19 TO 19 BY 2; Z=N;
FUNC(N)=4*HZ(.05*Z,PETA)/(.05*Z+PETA/2);
END;
DO N= -18 TO 18 BY 2; Z=N;
FUNC(N)=2*HZ(.05*Z,PETA)/(.05*Z+PETA/2);
END;
FUNC(20),FUNC(-20)=0;
ANSWER= (KF/(4*PETA))*(0.05/3)*SUM(FUNC);
RETURN(ANSWER);  END;  GO TO ENDH;
ENDH:  END H;

    /* GZ IS A PROCEDURE FOR INTEGRATING F(K,C) OVER THE
       RANGE U=0 TO 1-Z**2    */
GZ: PROC (PZ,PETA) FLOAT DEC;
DCL (M,N) FIXED BIN, (ANSWER,PZ,PETA,A,H,ALO,RO) FLOAT DEC,
Z FLOAT DEC EXTERNAL,
FUNC(0:20) FLOAT DEC;
FUNC=0;
A=1-(PZ)**2;
M=2*CEIL(10*A);
H=A/M;
DO N=1 TO (M-1) BY 2;
FUNC(N)=4*F(N*H,PZ,PETA);  END;
IF M>2 THEN
DO N=2 TO (M-2) BY 2;
FUNC(N)=2*F(N*H,PZ,PETA);   END;
FUNC(M)= F(A,PZ,PETA);
IF PETA>=1 THEN DO;
IF PZ>1E-3 THEN
FUNC(0)= F(0,PZ,PETA);   ELSE
IF PZ<-1E-3 THEN
FUNC(0)=  F(0,PZ,PETA);   ELSE DO;
ALO=AO-KF**2*DAODE/2;  RO=Z/ALO;
FUNC(0)=ALO*SIN(KF*PETA*RO)/(KF*PETA)**3-Z/(KF*PETA)**2;  END;
END; ELSE DO;
IF PZ>1E-3 THEN
FUNC(0)= F(0,PZ,PETA);   ELSE
IF PZ<-1E-3 THEN DO;
IF PZ>-PETA+1E-3 THEN
FUNC(0)= F(0,PZ,PETA);   ELSE
IF PZ<-PETA-1E-3 THEN
FUNC(0)= F(0,PZ,PETA);   ELSE DO;
ALO=AO+(PETA**2-1)*KF**2*DAODE/2;   RO=Z/ALO;
FUNC(0)=ALO*SIN(KF*PETA*RO)/(KF*PETA)**3-Z/(KF*PETA)**2; END;
END; ELSE DO;
ALO=AO-KF**2*DAODE/2;  RO=Z/ALO;
FUNC(0)=ALO*SIN(KF*PETA*RO)/(KF*PETA)**3-Z/(KF*PETA)**2;  END;
END;
ANSWER=(H/3)*SUM(FUNC);
RETURN(ANSWER); END GZ;

    /* DGZ IS A PROCEDURE FOR INTEGRATING DF(K,C)/DZ OVER
       THE RANGE U=0 TO 1-(Q/2*KF)**2    */
DGZ:  PROC(PETA) FLOAT DEC;
DCL (M,N) FIXED BIN, (PETA,A,H,ANSWER) FLOAT DEC,
FUNC(0:20) FLOAT DEC;
FUNC=0;
A=1-(PETA/2)**2;
M=2*CEIL(10*A);
H=A/M;
DO N=1 TO (M-1) BY 2;
FUNC(N)=4*DFDZ(N*H,PETA);  END;
IF M>2 THEN
DO N=2 TO (M-2) BY 2;
FUNC(N)=2*DFDZ(N*H,PETA);   END;
FUNC(M)= DFDZ(A,PETA);
FUNC(0)= DFDZ(0,PETA);
ANSWER=(H/3)*SUM(FUNC);
RETURN(ANSWER);  END DGZ;

    /* G IS A PROCEDURE FOR INTEGRATING THE FUNCTION
       G(Z)/(Z+ETA/2) OVER THE RANGE Z=-1 TO 1   */
G: PROC (PETA) FLOAT DEC;
DCL (Z,PETA,ANSWER) FLOAT DEC, FUNC(-40:40) FLOAT DEC,
N FIXED BIN;
IF PETA<2-1E-3 THEN GO TO CASE1;
ELSE IF PETA>2+1E-3 THEN GO TO CASE3;
ELSE GO TO CASE2;
CASE1:  DO;
DO N=-39 TO 39 BY 2;  Z=N;
IF Z<-20*PETA-1E-3 THEN
FUNC(N)=4*GZ(.025*Z,PETA)/(.025*Z+PETA/2);  ELSE
IF Z>-20*PETA+1E-3 THEN
FUNC(N)=4*GZ(.025*Z,PETA)/(.025*Z+PETA/2);  ELSE
FUNC(N)=4*PETA*FKF(PETA)+4*DGZ(PETA);
END;
DO N=-38 TO 38 BY 2;  Z=N;
IF Z<-20*PETA-1E-3 THEN
FUNC(N)=2*GZ(.025*Z,PETA)/(.025*Z+PETA/2);  ELSE
IF Z>-20*PETA+1E-3 THEN
FUNC(N)=2*GZ(.025*Z,PETA)/(.025*Z+PETA/2);  ELSE
FUNC(N)=2*PETA*FKF(PETA)+2*DGZ(PETA);
END;
FUNC(40),FUNC(-40)=0;
```

```
ANSWER=(KF/(4*PETA))*(.025/3)*SUM(FUNC);
RETURN(ANSWER);  END;  GO TO ENDG;
CASE2:  DO;
FUNC=0;
DO N= -19 TO 19 BY 2;  Z=N;
FUNC(N)=4*GZ(.05*Z,2)/(.05*Z+1);
END;
DO N= -18 TO 18 BY 2;  Z=N;
FUNC(N)=2*GZ(.05*Z,2)/(.05*Z+1);
END;
FUNC(20)=0;  FUNC(-20)= 2*FKF(2);
ANSWER=(KF/8)*(0.05/3)*SUM(FUNC);
RETURN(ANSWER); END;  GO TO ENDG;
CASE3:  DO;
FUNC=0;
DO N= -19 TO 19 BY 2;  Z=N;
FUNC(N)=4*GZ(.05*Z,PETA)/(.05*Z+PETA/2);
END;
DO N= -18 TO 18 BY 2;  Z=N;
FUNC(N)=2*GZ(.05*Z,PETA)/(.05*Z+PETA/2);
END;
FUNC(20),FUNC(-20)=0;
ANSWER= (KF/(4*PETA))*(0.05/3)*SUM(FUNC);
RETURN(ANSWER); END; GO TO ENDG;
ENDG: END G;
   /*  VIND IS A PROCEDURE FOR EVALUATING THE INTEGRAL OF

        F(Q)*SIN(C*R)/C*R OVER THE RANGE Q=0 TO 5*KF.  THIS
        INTEGRAL REPRESENTS THE INDIRECT PART OF THE
        EFFECTIVE INTERACTION BETWEEN IONS   */
VIND: PROC(PR) FLOAT DEC;
DCL N FIXED BIN, (PR, ANSWER) FLOAT DEC,
FUNC(0:50) FLOAT DEC;
DO N=1 TO 49 BY 2;
FUNC(N)=(40/(N*PR))*FQA(N)*SIN(N*KF*PR/10);
END;
DO N=2 TO 48 BY 2;
FUNC(N)=(20/(N*PR))*FQA(N)*SIN(N*KF*PR/10);
END;
FUNC(50)= FQA(50)*SIN(5*KF*PR)/(5*PR);
FUNC(0)=KF;
ANSWER=(0.1/3)*SUM(FUNC);
RETURN(ANSWER); END VIND;

   /*  THE MAIN PROGRAM BEGINS HERE. DATA FOR AN ELEMENT
       IS READ IN AND THE ATOMIC VOLUME COMPUTED   */
I=1;  PI=3.141593;
N=1;
FQA=0;
L2: GET FILE(SCARDS) DATA(ELEMENT,Z,KF,LO,AO,A1,A2,DAODE,DA1DE,DA2DE);
VO=(3*PI**2*Z)/KF**3;
   /* THE DEPLETION HOLE IS NOW CALCULATED AND ZSTAR DETERMINED */
IF LO=0 THEN
RHO=(2/PI)*DAODE*IO(KF);
ELSE IF LO=1 THEN
RHO=(2/PI)*(DAODE*IO(KF)+3*DA1DE*I1(KF));
ELSE IF LO=2 THEN
RHO=(2/PI)*(DAODE*IO(KF)+3*DA1DE*I1(KF)+5*DA2DE*I2(KF));
ZSTAR=Z-RHO  ;
   /* CRITICAL DATA FOR THE ELEMENT IS PRINTED OUT  */
PUT FILE(SPRINT) PAGE;
PUT FILE(SPRINT) EDIT('ELEMENT','Z','KF','VO','RHO','ZSTAR')
(SKIP(5),X(10),A,X(4),A,X(6),A,X(9),A,X(9),A,X(7),A);
PUT FILE(SPRINT) EDIT(ELEMENT,Z,KF,VO,RHO,ZSTAR)
(SKIP(3),X(12),A(2),X(7),F(1),X(4),F(6,5),X(4),F(7,3),X(4),
F(8,5),X(4),F(7,5));
PUT FILE(SPRINT) EDIT('ETA','WQ','FQ','EPS','F','G','H')
(SKIP(10),X(20),A,(2)(X(11),A),X(16),A,(3)(X(11),A));
PUT FILE(SPRINT) SKIP;

   /* THE FORM FACTOR WQ AND THE BAND STUCTURE ENERGY FQ
      ARE EVALUATED FOR ETA=Q/KF FROM 0.1 TO 5 IN STEPS
      OF 0.1. FIRST THE DIELECTRIC FUNCTION EPS(Q) IS
      DETERMINED. VALUES FOR WQ AND FQ ARE PRINTED OUT   */
DO ETA1=1 TO 50 BY 1,54 TO 70 BY 4;
ETA=ETA1*1.000000000000E-1;
ETO=ETA+1E-2;
IF ETA<2-1E-3 THEN
EPS=1+(2/(PI*KF*ETA**2))*(((1-(ETA/2)**2)/ETA)
*LOG(ABS((1+ETA/2)/(1-ETA/2)))+1);  ELSE
IF ETA>2+1E-3 THEN
EPS=1+(2/(PI*KF*ETA**2))*(((1-(ETA/2)**2)/ETA)
*LOG(ABS((1+ETA/2)/(1-ETA/2)))+1);  ELSE
EPS = 1+1/(2*PI*KF);
G1=G(ETA);
H1=H(ETA);
IF ETA<=2 THEN
F1=FKF(ETA); ELSE
F1=FA(ETA);
WQ=-4*PI*ZSTAR/(VO*(KF*ETA)**2*EPS)
-(4*PI/VO)*F1+(32/(VO*(ETA*KF)**2))*G1/EPS;
FQ=(EPS-1)/EPS+(16/(PI*EPS*ZSTAR))*G1
-64*(G1)**2/(EPS*(PI*ZSTAR)**2)
+8*(ETA*KF/ZSTAR)**2*H1/PI;
FQA(ETA1)=FQ;
PUT FILE(SPRINT) EDIT(ETO,WQ,FQ,EPS,F1,G1,H1)
(SKIP,X(20),F(3,1),X(7),F(9,6),X(5),F(8,6),X(6),(4)F(12,5));
END; END L1;
```

REFERENCES

Abarenkov I V, 1965, Technical Report of the Cavendish Laboratory, No.2.

Alers G A, 1965, Physical Acoustics Vol IIIB, Ed. W P Mason Academic Press, New York.

Anderson P W and Blount E J, 1965, Phys. Rev. Lett. 14,217

Animalu A O E, 1965, Phil. Mag. 11,379

Animalu A O E, 1966, Proc. Roy. Soc. A294,376

Animalu A O E and Heine V, 1965, Phil. Mag. 12,1249

Appapillai M and Heine V, 1972, Technical Report of the Cavendish Laboratory, No.5.

Appapillai M and Williams A R, 1973, J. Phys. F 3,4,759

Bacher R F and Goudsmit S, 1932, Atomic Energy States, McGraw-Hill, New York.

Bichowsky F R and Rossini F D, 1936, The Thermodynamics of Chemical Substances, Reinhold, New York.

Barron T H K and Munn R W, 1967, Phil. Mag. 15,85

Basinski Z S and Christian J W, 1954, Acta Met. 2,2 148

Beattie J A, 1926-7, J. Maths. Phys. (M.I.T.) 6,1

Bliss E S and Rayne J A, 1969, Phys, Rev. 177,2,673

Bordoni P G, Nuovo M and Verdini L, 1960, Nuovo Cim. Suppl. 18,55

Borelius G, 1963, Sol. St. Phys. Vol 15, Ed. F Seitz and D Turnbull, Academic Press, New York.

Bowles J S, Barrett C S and Guttman L, 1950, Trans. A I M E 188,1478

Brillouin L, 1938, Les Tenseurs, 1st American Edition, 1946, Dover, New York

Burkart M W and Read T A, 1953, Trans. A I M E 197,1516

Chandresekhar B S and Rayne J A, 1961, Phys. Rev. 124,4,1011

Chatterjee D, 1972, Thesis, University of Durham

Clapp P C, 1973, Phys. Stat. Sol.(b) 57,561

Clark J A and Dawber P G, 1972, J. Phys. F 2,930

Clusius K and Schachinger L, 1952, Z. für angew. physik 4,442

Cochran W, 1960, Advan. Phys. 9,387

Cohen M H and Heine V, 1961, Phys. Rev. 122,1821

Collins J G, Cowan J A and White G K, 1967, Cryogenics,7,219

Connell R A, 1963, Phys. Rev. 129,5,1952

Cottam R I, 1973, Thesis, University of Durham

Cousins C S G, 1970, J. Phys. C 3,1677

Doidge P R and Sik-Hung K, 1964, Phys. Lett. 12,2,82

Drude P, 1900, Ann. der Physik 1,3,566

Dynes R C, 1970, Phys. Rev. B 2,3,644

Eckert R E and Drickamer H G, 1952, J. Chem. Phys. 20,13

Farley J M, 1973, Thesis, University of Durham

Farley J M and Saunders G A, 1972, J. Phys. C 5,3021

Fischer E and Vieli H P, 1967, Phys. Lett. 26A,1,35

Fischer E and Olsen P L, 1968, Phys. Lett. 26A,8,379

Fleury P A, 1971, J. Acoust. Soc. Amer. 49,1041

Fleury P A, 1972, Comments on Sol. St. Phys. IV,149

Fröberg C-E, 1965, Introduction to Numerical Analysis, Addison-Wesley, London

Fuchs K, 1935, Proc. Roy. Soc. A151, 585

Fumi F G, 1952, Nuovo Cim. 9,9,739

Garland C W, 1964, J. Chem. Phys. 41,4,1005

Garland C W, 1970, Physical Acoustics Vol. VII, Ed. W P Mason and R N Thurston, Academic Press, New York.

Garwood R D, 1970, Martensite: Fundamentals and Technology, Ed. E R Petty, Longmans, London

Glazer A M and Megaw H D, 1972, Phil. Mag. 25,5,1119

Gubser D U, Mapother D E and Connelly D L, 1970, Phys. Rev. B 2,7,2547

Gunton D J and Saunders G A, 1972, J. Mat. Sci. 7,1061

Guttman L, 1950, Trans. A I M E 188,1472

Halder N C, 1969, Phys. Rev. 177,2,471

Ham F S, 1955, Solid State Physics Vol I, Ed. F Seitz and D Turnbull

Hansen M and Anderko K, 1958, Constitution of Binary Alloys, McGraw Hill, New York, 2nd Edn, p.864.

Harrison W A, 1966, Pseudopotentials in the Theory of Metals, Benjamin, New York.

Hearmon R F S, 1961, Applied Anisotropic Elasticity, Oxford

Heine V, 1969, Physics of Metals Vol I, Ed. J M Ziman, Cambridge

Heine V and Abarenkov I V, 1964, Phil. Mag. 9,451

Heine V and Weaire D, 1966, Phys. Rev. 152,603

Heine V and Weaire D, 1970, Solid State Physics Vol 24, Ed. F Seitz

Hill E R, 1970, Thesis, Case Western Reserve University

Inglesfield J, 1969, J. Phys. C 2,1285

Inglesfield J, 1972, J. Phys. F 2,5,878

Kaye G W C and Laby T H, 1966, Tables of Physical and Chemical Constants, 13th edn, Longmans, London.

Khayutin S G and Spichivetskii E S, 1966, Phys. Met. Metallog. 22,3 (English translation, published 1967).

Kittel C, 1966, Introduction to Solid State Physics, 3rd edn. Wiley, New York

Kogachi M and Matsuo Y, 1971, J. Phys. Chem. Solids 32,2393

Kumar A and Sharan B, 1972, J. Phys. C 5, 3161

Ledbetter H M, 1973, J. Phys. Chem. Solids 34,4,721

Liebfried G and Ludwig W, 1961, Solid State Physics Vol 12, Ed. F Seitz and D Turnbull

Lipson H and Stokes A R, 1941, Nature 1481,437

Luo H L, Hagen J and Merriam M F, 1965, Acta Met, 13,1012

Mason W P and MacDonald D E, 1971, J. Appl. Phys. 42,5,1836

Mason W P and Rosenberg A, 1966, Phys. Rev. 151,2,434

Mason W P and Rosenberg A, 1967, J. Appl. Phys. 38,1929

Matsuo Y and Katada K, 1973, Acta Met. 21,6,829

Matsuo Y and Kogachi M, 1971, Acta Met. 19,1287

Maynell C A, 1972, Thesis, University of Durham

McSkimin H J, 1961, J. Acoust. Soc. Amer. 33,12

Meriam M F, Hagen J and Luo H L, 1967, Phys. Rev. 154,2,424

Meriam M F, Hagen J and Luo H L, 1967a, Phys. Rev. 154,2,438

Meyerhoff R W and Smith J F, 1963, Acta Met. 11,529

de Morton M, 1969, J. Appl. Phys. 40,1,208

Munn R W, 1968, Phil. Mag. 17,433

Munn R W, 1969, Adv. Phys. 18,75,515

Munn R W, 1970, Acta Crystall. A26,6,161

Nagasawa A, 1971, Phys. Stat. Sol.(a) 8,2,531

Niblett D H, 1966, Physical Acoustics Vol IIIA, Ed W P Mason, Academic Press, New York.

Novotny D B and Smith J F, 1965, Acta Met. 13,881

Nye J F, 1957, Physical Properties of Crystals, Oxford.

Pace N G, 1970, Thesis, University of Durham

Pace N G and Saunders G A, 1970, Phil. Mag. 22,175,73

Pace N G and Saunders G A, 1972, Proc. Roy. Soc. A326,521

Pace N G and Saunders G A, 1972a, Nature Phys. Sci. 237,72,47

Pahlman J E and Smith J F, 1968, J. Less-Common Met. 16,397

Pashaeev B P, 1962, Sov. Phys. Sol. State 3,303,1773

Petty E R, 1970, Ed. Martensite: Fundamentals and Technology, Longmans, London

Phillips N E, 1955, Phys. Rev. 100,6,1719

Pindor A J and Pynn R, 1969, J. Phys. C 2,1037

Pippard A, 1956, Phil. Mag. 1,473

Poisson S D, 1829, Memoire de l'Academie de Paris t.8

Pollock J T and King H W, 1968, J. Mat. Sci. 3,372

Postnikov V S, Zolotuin I V, Burmistrov U N and Sharshakov I M, 1969, Fiz. Metallov. Metallog. 28,4,766

Predel B and Sandig H, 1970, Z. für Metallkunde 61,5,387

Pytte E, 1971, Structural Phase Transitions and Soft Modes, Ed. E J Samuelson et al., Universiteitsforlaget, Oslo.

Pytte E, 1973, Comments on Solid State Physics 5,41

Rehwald W, 1968, Phys. Lett. 27A,5

Rehwald W, 1970, Sol. Stat. Comm. 8,8,607

Roberts J K and Miller A R, 1960, Heat and Thermodynamics, 5th edn. Blackie, London

Rowell J M and Dynes R C, 1971, Proc. of Int. Conf. on Phonons, Rennes, France, p.150

Salmon G, 1912, Lessons Introductory to the Modern Higher Algebra, Hodges, Foster and Co., Dublin.

Saunders G A, Pace N G and Alper T, 1967, Nature 216,5122

Scheel K and Heaus W, 1914, Verhandl. Deut. Phys. Ges. 16,1

Schwartz R G, 1970, Thesis, U S Atomic Energy Commission IS-T-362

Seeger A, Donth H and Pfaff F, 1957, Disc. Faraday. Soc. 23,19

Seitz F, 1940, The Modern Theory of Solids, McGraw-Hill, New York

Shaw R W, 1968, Phys. Rev. 174,769

Shaw R W, 1968a, Thesis, W W Hansen Lab. Rep. No. 1666, Stanford University

Shaw R W and Pynn R, 1969, J. Phys. C 2,2071

Shirane G, 1971, Structural Phase Transitions and Soft Modes, Ed. E J Samuelson et al., Universiteitsforlaget, Oslo.

Shiozaki I and Sato T, 1967, J. Phys. Soc. Jap. 22,1,105

Silverman B D and Joseph R I, 1963, Phys. Rev. 129,2062

Sladek R J, 1953, Phys. Rev. 91,1280

Sladek R J, 1954, Phys. Rev. 97,4,902

Southwell R V, 1941, Theory of Elasticity, 2nd edn., Oxford.

Stout J W and Guttman L, 1950, Phys. Rev. 79,396

Stout J W and Guttman L, 1952, Phys. Rev. 88,703

Stout J W and Guttman L, 1952a, Phys. Rev. 88,713

Taylor D W and Vashishta P, 1972, Phys. Rev. B 5,11,4410

Tilley D R and Doidge P R, 1966, Phil. Mag. 13,795

Truell R, Elbaum C and Chick B B, 1969, Ultrasonic Methods in Solid State Physics, Academic Press, New York.

Turley J and Sines G, 1971, J. Phys. D 4,264

Valentiner S, 1940, Z. für Metallkunde 32,244

Wechsler M S, Lieberman D S and Read T A, 1953, Trans. A I M E 197,1503

Wertheim 1848, Ann. de Chimie t.23

White G K, 1959, Low Temperature Physics, Oxford.

Winder D R and Smith C S, 1958, J. Phys. Chem. Solids 4,128

Woodruff T C and Ehrenreich H, 1961, Phys. Rev. 123,1553

Wraight P C, 1968, Phys. Lett. 26A, 4,140

Wright R B and Stuart D M, 1931, Bureau of Standards J. of Res. 7,3,519

Yarnell J L, Warren J L and Koenig S H, 1965, Lattice Dynamics, ed. R F Wallis, Pergamon, New York.

Yonemitsu K, Takano K, Hishiyama Y, Matsuda T and Shiozaki I, 1965, J. Phys. Soc. Jap. 20,10,1797

Zemansky M W, 1951, Heat and Thermodynamics, McGraw-Hill, London

Ziman J M, 1960, Electrons and Phonons, Oxford.

Austin B J, Heine V and Sham L J, 1962, Phys. Rev. 127,1,276

Cohen M H and Heine V, 1961, Phys. Rev. 122,6,1821

Phillips J C and Kleinman L, 1959, Phys. Rev. 116,2,287

Shaw R W and Harrison W A, 1967, Phys. Rev. 163,3,604